

**VOID CONSOLIDATION OF THERMOPLASTIC COMPOSITES VIA NON-  
AUTOCLAVE PROCESSING**

by

Danning Zhang

A dissertation submitted to the Faculty of the University of Delaware in partial fulfillment of the requirements for the degree of Doctor of Philosophy in Materials Science and Engineering

Summer 2017

© 2017 Danning Zhang  
All Rights Reserved

**VOID CONSOLIDATION OF THERMOPLASTIC COMPOSITES VIA NON-  
AUTOCLAVE PROCESSING**

by

Danning Zhang

Approved: \_\_\_\_\_  
Darrin Pochan, Ph.D.  
Chair of the Department of Materials Science and Engineering

Approved: \_\_\_\_\_  
Babatunde Ogunnaike, Ph.D.  
Dean of the College of Engineering

Approved: \_\_\_\_\_  
Ann L. Ardis, Ph.D.  
Senior Vice Provost for Graduate and Professional Education

I certify that I have read this dissertation and that in my opinion it meets the academic and professional standard required by the University as a dissertation for the degree of Doctor of Philosophy.

Signed:

---

John W. Gillespie, Jr., Ph.D.  
Professor in charge of dissertation

I certify that I have read this dissertation and that in my opinion it meets the academic and professional standard required by the University as a dissertation for the degree of Doctor of Philosophy.

Signed:

---

Michael Mackay, Ph.D.  
Member of dissertation committee

I certify that I have read this dissertation and that in my opinion it meets the academic and professional standard required by the University as a dissertation for the degree of Doctor of Philosophy.

Signed:

---

Suresh G. Advani, Ph.D.  
Member of dissertation committee

I certify that I have read this dissertation and that in my opinion it meets the academic and professional standard required by the University as a dissertation for the degree of Doctor of Philosophy.

Signed:

---

Dirk Heider, Ph.D.  
Member of dissertation committee

## ACKNOWLEDGMENTS

During my time here at UD-CCM, I have learned a lot from the books, research, and the wonderful people around me. Here I am going to thank those who helped and supported me along the way.

First, I would like to thank my advisor Professor John W. Gillespie, Jr. who influenced me the most during my Ph.D.. I highly appreciate his guidance throughout my research. Professor Gillespie has taught me so much about identifying problems, solving problems, and thinking logically. There were tough times during my Ph.D. that I thought I would never have finished. Prof. Gillespie encouraged me and given his time and helped me with his knowledge and experience. I deeply appreciate his support, patience, and true care.

I am grateful to Dr. Dirk Heider for his help and support to my research. Dr. Heider has provided me his expertise and experience. He is very busy, and I really appreciate his time and advice.

I would also like to thank Prof. Suresh G. Advani for his discussion and advice. I am also grateful to Prof. Michael Mackay to be one of my committee members. Thank you for your time and support.

I would like to thank Dr. Pavel Simacek and Dr. Tom Cender for their help on the permeability related issues. Special thanks to Dr. Steve Sauerbrunn for his training and discussion on thermal analysis topics. I would also like to thank Dr. John Tierney, Dr. Joseph Deitzel, Dr. Nickolas Shevchenko, David Roseman for all your support during the years.

I feel lucky to have the past and present CCM graduate students who have crossed the path with me. Dr. Jennifer Mueller was like a sister, shared with me her valuable experience. Dr. Hatice Sinem Sas is a great friend and always encouraged me. Sandeep Tamrakar, Raja Ganesh, Hong Yu, Dr. Subramani Sockalingam, Dr. Preston McDaniel, Min-young Yun, Maxime Dempah, Dr. Cedric Jacob, Dr. Michael Yeager, and Albraa Jaber, I appreciated your discussion about work and life and the fun times we spent together.

I could not finish without the help from our great technicians including Johnny Thiravony, Steven Durbano, Touy Thiravong, John Morris and Philip Roach. I also want to thank Corinne Hamed, Robin Mack, Penny O'Donnel, Megan Hancock and Therese Stratton for their support.

I appreciate the friendship with Xiaocao Hu, Yingying Zeng, Cijing Zhang, Lu Wang, Howard Yang, Yujun Zhong, Yao Yao, Jing Qu, and Chuan Qin. You have made my life in Newark colorful. I want to thank my friends Jie Meng, Xiaolei Geng, Ying Zhu, and Huan Jin. Thank you for your lifetime friendship and support.

I want to thank my lovely parents who let me choose my own path and tried to help me with their best. Thank you for your endless love. I am very grateful to my parents in law to their love and support.

Lastly, I want to thank the most important person and the love of my life, my husband Yi Zou. I feel very lucky to have Yi with me. Yi has always been there with me no matter the good times or the bad times. I am deeply grateful to his companionship, support, encouragement, and love. Together we have overcome many difficulties. I believe we will create a bright future.

## TABLE OF CONTENTS

LIST OF TABLES .....	xi
LIST OF FIGURES .....	xii
ABSTRACT .....	xxi

### Chapter

1	INTRODUCTION .....	1
1.1	Motivation and Significance of the Research.....	1
1.1.1	Preliminary Study of OVB Consolidation of Thermoplastic Laminates .....	2
1.2	Literature Review .....	4
1.2.1	Voids in Thermoplastic Prepreg.....	4
1.2.2	Manufacturing of High Performance Thermoplastic Composites .....	5
1.2.3	Mechanisms of Void Dynamics .....	7
1.2.3.1	Coupled mechanism of Stress Equilibrium and Gas Molecule Diffusion.....	7
1.2.3.2	Void Compression by High Applied Pressure.....	10
1.2.3.3	Void Filling with Resin Flow .....	12
1.2.3.4	Moisture/Gas Nucleation and Diffusion Controlled Void Dynamics .....	13
1.2.3.5	Void Escaping through Buoyancy Force.....	14
1.2.3.6	Influence of Air Permeability on Void Reduction .....	15
1.3	Research Objectives .....	16
1.4	Unique Contribution.....	17
1.5	Dissertation Outline.....	18
2	MICROSTRUCTURE OF THERMOPLASTIC PREPREG.....	21
2.1	Introduction .....	21
2.2	Microstructure of Voids in Thermoplastic Prepreg.....	22

2.2.1	3D Characterization Techniques and X-ray Micro-CT ( $\mu$ -CT)...	22
2.2.2	SRVE of the Microstructure of Composite Materials .....	23
2.2.3	Thermoplastic Prepreg Material .....	24
2.2.4	Set-up of X-Ray Micro-CT Characterization .....	24
2.2.5	Results of Void Geometry .....	27
	2.2.5.1 3D Void Geometry .....	27
	2.2.5.2 Void Length.....	27
2.2.6	Void Statistics and Determination of SRVE for Void Microstructure .....	29
	2.2.6.1 3D Void Content.....	30
	2.2.6.2 Void Length.....	33
	2.2.6.3 Equivalent Diameter of voids.....	37
	2.2.6.4 Void Aspect Ratio .....	40
	2.2.6.5 Sub-SRVEs and the SRVE.....	43
2.3	Characterization of Tape Surface .....	45
	2.3.1 Experimental procedure.....	45
	2.3.2 Determination of SRVE of Tape Surface .....	45
2.4	Summary.....	48
3	<b>INTERLAYER AIR PERMEABILITY OF THERMOPLASTIC PREPREG STACKS.....</b>	<b>50</b>
3.1	Introduction .....	50
3.2	Test Set-up for In-plane Air Permeability Measurements.....	51
3.3	Stacking Orientation Dependence of Interlayer Permeability before Processing.....	55
3.4	Interlayer Permeability during Processing Cycles .....	64
	3.4.1 Phase Transitions of PEEK Resin in the Raw Tape during Processing.....	65
	3.4.2 Effect of Processing Cycle on Interlayer Permeability .....	66
	3.4.2.1 Effect of Temperature Ramp .....	67
	3.4.2.2 Effect of Dwell Time.....	69
3.4.3	Characterization of Surface Topology of OVB Processed Tapes.....	71

3.4.3.1	Surfaces from 0°/0° Samples.....	72
3.4.3.2	Surfaces from 0°/90° Samples.....	75
3.5	Summary.....	79
4	DETERMINATION OF KEY VOID REDUCTION MECHANISMS.....	81
4.1	Introduction .....	81
4.2	Viable Mechanisms in Thermoplastic OVB Processing .....	81
4.3	Discussion of Key Void Reduction Mechanisms during OVB Processing.....	86
4.4	Experimental procedure.....	90
4.4.1	Laminate fabrication.....	90
4.4.2	Void inspection.....	92
4.4.2.1	X-Ray micro-CT.....	92
4.4.2.2	Optical microscopy.....	93
4.5	Results of voids in processed laminates and discussion.....	93
4.6	Summary.....	101
5	MODELS FOR VOID AIR REMOVAL .....	102
5.1	Introduction .....	102
5.2	Model Set-up .....	104
5.2.1	Single Layer Air Diffusion Followed by Interlayer Air Flow... 104	
5.2.1.1	Non-isothermal Diffusion through Single Layer Prepreg.....	104
5.2.1.2	Model for In-plane Interlayer Air Flow.....	108
5.2.1.2.1	General Model Set-up.....	108
5.2.1.2.2	Klinkenberg Effect .....	110
5.2.2	Through Thickness Diffusion in Prepreg Stacks.....	112
5.3	_Modeling Results for Consolidation Experiments .....	113
5.3.1	Air Removal in Laminates with Perimeter Open to Vacuum....	114
5.3.1.1	Results of Single Layer Diffusion .....	114
5.3.1.2	Characteristic Time for Interlayer Air Flow.....	116

5.3.2	Diffusion through Prepreg Stacks during Processing.....	117
5.4	Summary.....	121
6	MODEL FOR MATERIAL BEHAVIOR OF INTERLAYER REGION BEFORE RESIN MELT IN THE OVB PROCESSING .....	123
6.1	Introduction .....	123
6.2	Related Mechanical Properties of PEEK resin.....	125
6.3	General Approach and Model set-up for Kh Prediction.....	126
6.4	Resin Behavior Model.....	131
6.5	Input of Material Properties and Parameters .....	135
6.6	Results and Discussion of Material Behavior of Interlayer Region .....	141
6.6.1	General resin behavior.....	141
6.6.2	Behavior of the interlayer region.....	144
6.6.3	Effect of processing conditions to the interlayer permeability..	150
6.7	Summary.....	153
7	DESIGN AND OPTIMIZATION OF PROCESSING CYCLE OF THERMOPLASTIC OVB PROCESSING .....	154
7.1	Introduction .....	154
7.2	Parametric Study of the Model of Single Layer Diffusion.....	154
7.2.1	Effect of Raw Tape Properties .....	154
7.2.2	Effect of Processing Conditions .....	155
7.3	Parametric Study of the Air Flow Model through Permeable Interlayer Region .....	159
7.4	Discussion of Design and Optimization of the Processing Cycle .....	161
7.5	Summary.....	167
8	SUMMARY AND FUTURE WORK .....	168
8.1	Research Summary .....	168
8.2	Future Work.....	170
	REFERENCES .....	173
Appendix		
A	COMPARISON ON VOID STATISTICS BETWEEN X-RAY MICRO-CT AND OPTICAL MICROSCOPY.....	185

A.1	Method for sample preparation and optical microscopy inspection.....	185
A.2	2D Results Comparison.....	185
<b>B</b>	<b>DETERMINATION OF MICRO-CT RESOLUTIONS FOR VOID INSPECTION.....</b>	<b>189</b>
B.1	Effect of Scanning Resolution on Void Content.....	189
B.2	Effect of scanning resolution on void length.....	191
B.3	Effect of scanning resolution on void equivalent diameter.....	192
<b>C</b>	<b>Determination of Settings for Tape Surface Characterization with Confocal Microscope.....</b>	<b>194</b>
C.1	Definitions of Surface Roughness Parameters.....	194
C.2	Selection of Surface Scanning Parameters.....	194
<b>D</b>	<b>Calculation of Characteristic time for Voids Escaping through Buoyancy ...</b>	<b>197</b>
<b>E</b>	<b>Solubility and Diffusion Coefficient of O<sub>2</sub> and N<sub>2</sub> in APC2 Composites.....</b>	<b>199</b>
<b>F</b>	<b>ESTIMATION OF SUPER-SATURATION RATIO AND PROBABILITY OF NUCLEATION OF AIR DISSOLVED IN THE COMPOSITE DOMAIN OF PREPREG TAPE.....</b>	<b>203</b>
<b>G</b>	<b>KUNDSSEN NUMBER, FLOW REGIMES AND KLINKENBERG PARAMETERS FOR INTERLAYER AIR FLOW.....</b>	<b>207</b>
G.1	Knudsen Number and Flow Regime.....	207
G.2	Klinkenberg Effect.....	209
<b>H</b>	<b>FITTING PARAMETERS FOR TEMPERATURE PROFILES MEASURED IN CONSOLIDATION EXPERIMENTS.....</b>	<b>211</b>
<b>I</b>	<b>DERIVATION OF NON-ISOTHERMAL VISCOELASTIC CONSTITUTIVE EQUATION.....</b>	<b>212</b>
<b>J</b>	<b>PERMISSIONS.....</b>	<b>214</b>

## LIST OF TABLES

Table 2.1 X – ray micro CT scanning parameters .....	26
Table 2.2 Information of voids with L=Sample length in three samples .....	28
Table 2.3 Sub-SRVEs for void properties with corresponding fitting parameters of distribution functions.....	44
Table 3.1 Stacking orientation configurations for the measurements of interlayer permeability of raw tapes .....	57
Table 3.2 Results of Permeability thickness products for all measured lay-up configurations (each is tested with 3 specimens containing 3 identical interlayers).....	58
Table 3.3 Principal permeability thickness products for interlayer included angle of 0°, 30°, 60°, and 90° .....	59
Table 6.1 Material parameters in the viscoelastic compliance and time-temperature shift factor of PEEK in Equation 6.23 and 6.24.....	138
Table 6.2 Temperature dependent material parameters in the viscoplastic model.....	140
Table C.1 Scanning Settings.....	195
Table C.2 Roughness results after surface scanning with the six settings .....	196
Table E.1 $S_0$ , $D_0$ , $\Delta H_s$ , and $ED$ of $N_2$ and $H_2O$ in amorphous PEEK [93].....	199
Table G.1 Knudsen number and flow regimes .....	207
Table G.2 $K$ , $r$ and $Kn$ estimated from the measured $Kh$ .....	209
Table G.3 $b$ , $K \propto h$ and $K \propto h/Kh$ for some measured interlayer in Chapter 3.....	210
Table H.1 Fitting parameters of Gauss functions for temperature profiles used for non-isothermal diffusion analysis .....	211

## LIST OF FIGURES

Figure 1.1 Schematic of vacuum bag assembly in OVB processing of thin thermoplastic laminates .....	3
Figure 1.2 Micro images show nearly void free cross-ply laminates are obtained after 1 hr dwell at 380 °C.....	3
Figure 1.3 Less than 1% void content was achieved for 2-layer and 4-layer thin cross-ply laminates after 0 min and 10 mins dwell cycle at 380 °C.....	3
Figure 1.4 Cross sectional micrograph show voids (black area in the tape, $V_v = 7.8\%$ ) in thermoplastic prepreg tape, Solvay AS4/APC2 prepreg, 6 consecutive images stitched large image of prepreg tape under 200X magnification with sample width of 3.4 mm.....	5
Figure 1.5 Schematics of (a) autoclave, (b) oven vacuum bag (OVB), (c) ATP process, (d) compression molding.....	7
Figure 1.6 Schematic of a cell of polymer shell containing a void [26] .....	9
Figure 1.7 Geometry of void reduction model of ATP process [36,37].....	11
Figure 1.8 Schematic of void filling model.....	13
Figure 2.1 Processing of X-ray cross-sectional micrographs.....	26
Figure 2.2 3D voids in an AS4/PEEK prepreg sample (2.1 mm × 1.8 mm × 0.18 mm) from X-ray $\mu$ -CT. (a) 3D view of prepreg sample, (b) Extracted voids in the sample (colors are to separate individual voids).....	28
Figure 2.3 Volume distributions of voids with different length in the total void volume in three samples of 2.14 mm (width) × 1.87 mm (length), 4 mm (width) × 3.7 mm (length) and 4 mm (width) × 9.18 mm (length). L is the length of the voids, in the unit of mm. ....	29
Figure 2.4 Error of void content. (a) Along the tape length direction of 8 samples of 4.5 mm × 9.2 mm × 0.18 mm, (b) along the tape width direction of sample volume of 36 mm × 5.3 mm × 0.18 mm .....	32

Figure 2.5 Empirical and fitted normalized cumulative distributions of voids in different void lengths in a tape sample of 4.5 mm wide with varying length. ....	33
Figure 2.6 Fitting parameters of 3-parameter Weibull distribution for void length distribution along sample length direction. (a) Shape factor and (b) scale factor. ....	35
Figure 2.7 Fitting parameters of 3-parameter Weibull distribution for void length along sample width direction with sub-SRVE length of 6.1 mm. (a) Shape factor and (b) scale factor. ....	36
Figure 2.8 Normalized frequency distribution of void length in the sub-SRVE of void length and total examined volume. ....	36
Figure 2.9 Empirical and fitted normalized cumulative distributions of voids in different void equivalent diameters in a tape sample of 4.5 mm wide with varying length. ....	37
Figure 2.10 Fitting parameters of 3-parameter Gamma distribution for void equivalent diameter distribution along sample length direction. (a) Shape factor and (b) scale factor. ....	39
Figure 2.11 Fitting parameters of 3-parameter Gamma distribution for void equivalent diameter along sample width direction with sub-SRVE length of 6.1 mm. (a) Shape factor and (b) scale factor. ....	40
Figure 2.12 Normalized numbers of voids in equivalent diameters ranges in prepreg tape. ....	40
Figure 2.13 Fitting parameters of 3-parameter lognormal distribution for void aspect ratio distribution along sample length direction. (a) Location factor and (b) scale factor. ....	42
Figure 2.14 Location and scale factors of 3-parameter lognormal distribution for void aspect ratio along sample width direction with sub-SRVE length of 5.2 mm. ....	43
Figure 2.15 Normalized numbers of voids in aspect ratio ranges in prepreg tape. ....	43
Figure 2.16 Error of surface parameters along (a) tape width and (b) length direction. ....	47

Figure 2.17 3D display of AS4/APC2 prepreg tape surface with tape width of 13975.8 $\mu\text{m}$ and length of 2997.25 $\mu\text{m}$ .....	48
Figure 3.1 Schematic of permeable interlayer region formed between two prepreg layers .....	51
Figure 3.2 Top view of experimental set-up of air permeability test .....	52
Figure 3.3 schematic of 1D Darcy's flow through the prepreg stacks .....	55
Figure 3.4 The coordinates and angles for the measurements of interlayer permeability of an arbitrary lay-up $\theta_1/\theta_2$ .....	56
Figure 3.5 $Khxy$ for $\omega = 0^\circ$ . Predicted $Khxx$ is in excellent agreement with measured $Khxx$ values for the $\theta/\theta$ interlayers ( $\theta = \alpha$ in this case).....	60
Figure 3.6 $Khxy$ for $\omega = 60^\circ$ . Predicted $Khxx$ is in excellent agreement with measured $Khxx$ values for interlayers listed in Table 3.1.....	61
Figure 3.7 Results of permeability thickness products of $0^\circ/\theta$ interlayers .....	62
Figure 3.8 Results of permeability thickness products of $\theta/90^\circ$ interlayers .....	63
Figure 3.9 Comparison of the $Khx$ results for $\theta/\theta$ , $0^\circ/\theta$ , $\theta/90^\circ$ and $\pm \theta$ interlayers at room temperature .....	63
Figure 3.10 Plot of transverse storage modulus versus temperature of raw tape showing phase transitions and different stages of the resin .....	66
Figure 3.11 Permeability thickness products along x direction of (a) $0^\circ/0^\circ$ , (b) $90^\circ/90^\circ$ , and (c) $0^\circ/90^\circ$ interlayers at elevated temperature .....	68
Figure 3.12 Permeability thickness products along x direction of (a) $0^\circ/0^\circ$ , (b) $90^\circ/90^\circ$ , and (c) $0^\circ/90^\circ$ interlayers under dwell at 240 $^\circ\text{C}$ .....	70
Figure 3.13 3D surface profiles of the tapes from $0^\circ/0^\circ$ after OVB processing to different temperature at ramp rate of 2.8 $^\circ\text{C}/\text{min}$ .....	73
Figure 3.14 3D surface profiles of the tapes from $0^\circ/0^\circ$ after OVB processed with different time at 240 $^\circ\text{C}$ .....	74

Figure 3.15 RMS roughness and average height between tape surface and a flat surface of the tapes from 0°/0° lay-ups at (a) different temperature at the heating ramp rate of 2.8 °C/min and (b) different dwell time at 240 °C during the OVB processing.....	75
Figure 3.16 RMS roughness and average height between tape surface and a flat surface of the tapes from 0°/90° lay-ups at (a) different temperature and (b) different dwell time under 240 °C during the OVB processing..	76
Figure 3.17 Laser intensity images showing the surface patterns of tapes from 0°/90° lay-ups during temperature ramping .....	77
Figure 3.18 Laser intensity images showing the surface patterns of tapes from 0°/90° lay-ups at different dwell time under 240 °C during the OVB processing .....	78
Figure 4.1 Schematic of void removal mechanisms.....	86
Figure 4.2 Intra- and interlayer voids in AS4/APC2 laminates.....	88
Figure 4.3 Diffusion time of N <sub>2</sub> depend on laminate thickness, from 9.4 s for 0.18 mm, to 18.6hrs for 15mm laminates.....	89
Figure 4.4 Schematic of vacuum bag assembly in the oven.....	91
Figure 4.5 Measured bulk temperature of 2-layer and 72-layer laminates during processing.....	92
Figure 4.6 3D volume and voids in prepreg and processed laminates with edges open condition from X-ray micro-CT. 72-layer thick laminate is void free as the 2-layer thin laminate .....	94
Figure 4.7 3D volume and voids in prepreg and processed laminates with edges sealed condition from X-ray micro-CT. Significant voids were trapped in the 72-layer thick laminate under the edges sealed condition.....	95
Figure 4.8 Microscopy images of the 2-layer laminates after consolidation (Vv: void content; dark black regions are voids).....	96
Figure 4.9 Optical micrographs of the 72-layer laminates after processing (Vv: void content; dark black regions are voids).....	97

Figure 4.10 Average void contents of the processed laminates from more than 40 cross-sectional images along the width direction (more than 28 mm) in the center region of each laminate. Error bars are the standard deviation of the void content in all the images for each laminate. <1% void contents were obtained in 2-layer and 72-layer in the condition of open edges. ....	98
Figure 4.11 Void contents at different through thickness locations of the 72-layer edge sealed laminate. At each location, more than 40 cross-sectional images along the width direction (more than 28 mm) were examined. The error bars are the standard deviation of the void content in all the images for each through thickness location. Large error bars are due to the highly non-homogeneous void content along the width direction of the laminate. ....	99
Figure 5.1 Schematic of void air removal mechanisms (a) void air diffusion through single layer prepreg followed by extraction through permeable interlayer regions, (b) void air diffusion through the thickness direction of a prepreg stack. ....	103
Figure 5.2 Air in voids and composite domains in the raw prepreg tape .....	105
Figure 5.3 Simplified geometry for single layer diffusion model .....	105
Figure 5.4 Schematic of air flow model in an interlayer cavity. L is the length of the interlayer cavity that air flow through; the transient flow is solved with finite difference method with element length of $\Delta L$ , and m is the total number of elements. i denotes the $i_{th}$ number of element ( $i=1, \dots, m$ ) and the $i_{th}$ point along the panel length ( $i=0, \dots, m$ ). $P(L_i, t)$ and $n(L_i, t)$ are the pressure (Pa) and amount of molecules (mol/m) of air in the $i_{th}$ element. ....	109
Figure 5.5 Simplified geometry for the model of diffusion through the thickness of prepreg stack with an example of a 3-layer laminate .....	113
Figure 5.6 Evolution of number of moles of air normalized by the initial amount in voids in single layers of 2-layer and 72-layer laminates with perimeter open to vacuum, showing diffusion of single layer for thin and thick laminates completes at 200 °C and 197 °C during the heating ramps, respectively.....	115
Figure 5.7 Concentration gradient of N <sub>2</sub> in the composite domain in the model of single layer diffusion during the heating ramp of 72-layer thick laminates.....	116

Figure 5.8 Concentration profile of $N_2$ in a 5-layer laminates during the heating ramp of consolidation experiment cycle for thick laminates .....	118
Figure 5.9 Normalized amount of air in each intra- and inter- layer void domain of a 5-layer laminate during the heating ramp of consolidation experiment for thick laminates .....	119
Figure 5.10 Thickness of each intra- and inter- layer void domain of a 5-layer laminate during the heating ramp of consolidation experiment for thick laminates.....	120
Figure 5.11 Diffusion time to achieve 1% void content in a laminate of the 1 to 72 - layer laminates. With the intra and interlayer voids inside of the laminates, the diffusion time required to remove air inside of the voids is much longer than that with homogeneously distributed $N_2$ and no voids in the tape.....	121
Figure 6.1 Constant force $F$ per unit tape length applied through vacuum bag on top of the prepreg layers .....	127
Figure 6.2 Simplified geometry and unit cell of the interlayer region along the tape width direction with a constant force $f$ per unit length of the tape on each unit cell.....	128
Figure 6.3 Unit cell of interlayer region before and after deformed with processing time and temperature .....	128
Figure 6.4 strain of $h$ derived from measured $Kh$ for $0^\circ/0^\circ$ and $0^\circ/90^\circ$ interlayers at elevated temperature and dwell time in OVB processing, showing large permanent strain and cut-off strains for both interlayers .....	130
Figure 6.5 General approach to determine the model of $Kh$ for a lay-up configuration .....	131
Figure 6.6 The Derived elastic modulus of PEEK in prepreg and consolidated laminates and measured transverse modulus $E_{22}$ of APC2 unidirectional laminates at elevated temperature .....	137
Figure 6.7 Viscoelastic creep compliance of PEEK in prepreg tape at temperature from $25^\circ\text{C}$ to $200^\circ\text{C}$ for $t = 1\text{s}$ at each temperature plotted with Equation 6.23 and 6.24 with the material parameters from literature listed in Table 6.1. ....	139

Figure 6.8 Time dependence of viscoelastic creep compliance of PEEK in prepreg tape at temperatures under isothermal condition plotted with Equation 6.23 and 6.24 with the material parameters from literature listed in Table 6.1.....	139
Figure 6.9 Temperature dependent yield stress (threshold stress for viscoplastic deformation) of PEEK used in the viscoplastic model.....	140
Figure 6.10 The elastic-viscoelastic strain of $h$ under constant stress of 5 MPa at temperatures up to 165 °C from model calculation, showing increasing viscoelastic strain with temperature and time especially during the glass transition of the PEEK resin.....	142
Figure 6.11 Elastic-viscoelastic strain of $a$ during temperature ramp to 170 °C with a heating rate of 2.8 °C/min under the stress level of 1, 3, and 5 MPa from model calculation, showing the strain depends on the local stress of the interlayer region. ....	142
Figure 6.12 Viscoplastic strain rate with increasing temperature under different $\sigma/\sigma_y$ ratio.....	143
Figure 6.13 Comparison of $\epsilon h$ from material response model under different initial stress and calculation from measured $Kh$ during temperature ramp for 0°/0° interlayer, showing the curve with $\sigma_0 = 11 MPa$ fits the experimental results best .....	144
Figure 6.14 Comparison of $\epsilon h$ from material response model under different initial stress and calculation from measured $Kh$ during temperature ramp for 0°/90° interlayer, showing the curve with $\sigma_0 = 12 MPa$ fits the experimental results best .....	145
Figure 6.15 Comparison of $\epsilon h$ from material response model under different initial stress and calculation from measured $Kh$ during temperature dwell cycle for 0°/0° interlayer, showing the curve with $\sigma_0 = 11 MPa$ fits the experimental results best .....	146
Figure 6.16 Comparison of $\epsilon h$ from material response model under different initial stress and calculation from measured $Kh$ during temperature dwell cycle for 0°/90° interlayer, showing the curve with $\sigma_0 = 12 MPa$ fits the experimental results best .....	147

Figure 6.17 A typical cross-sectional micrograph of the AS4/APC2 tape with width of 1.35mm, showing wedge-like surface bumps, and few fibers locating close to the surface in the resin rich surface region.....	147
Figure 6.18 Predicted $Kh$ of $0^\circ/0^\circ$ and $0^\circ/90^\circ$ interlayers by applying the initial $h_0$ calculated from measured $Kh$ with Equation 6.4 to the strain curves with $\sigma_0 = 11 \text{ MPa}$ and $\sigma_0 = 12 \text{ MPa}$ , respectively. ....	149
Figure 6.19 Evolution of interlayer permeability products $Kh$ of (a) $0^\circ/0^\circ$ and (b) $0^\circ/90^\circ$ interlayers under different heating rate at elevated temperature, showing less reduction of interlayer permeability is obtained with relatively higher heating rate at a certain temperature before plateau $Kh$ .....	151
Figure 6.20 Evolution of interlayer permeability products $Kh$ of (a) $0^\circ/0^\circ$ and (b) $0^\circ/90^\circ$ interlayers under different dwell cycles at elevated temperature with a heating rate of $5 \text{ }^\circ\text{C}/\text{min}$ , showing less reduction of interlayer permeability can be achieved at same processing time with lower dwell temperature before plateau $Kh$ .....	152
Figure 7.1 Temperature and processing time for removing the amount of void air to reach 1% void content through single layer diffusion with different initial void content with heating rate of $2.8 \text{ }^\circ\text{C}/\text{min}$ .....	155
Figure 7.2 Temperature and processing time for removing 99.9% void volatiles through single layer diffusion during heating ramps with different heating rate with initial $V_v=7.77\%$ .....	156
Figure 7.3 Total processing time required for removing 99.9% void volatiles through single layer diffusion at different dwell temperature with heating rate of $2.8 \text{ }^\circ\text{C}/\text{min}$ and initial $V_v=7.77\%$ .....	157
Figure 7.4 Temperature for removing 99.9% void volatiles through single layer diffusion with different vacuum levels with initial $V_v=7.77\%$ and heating rate of $2.8 \text{ }^\circ\text{C}/\text{min}$ .....	158
Figure 7.5 Air flow time with different initial void content in a part size of 1m. ....	159
Figure 7.6 Air evacuation times for different part in-plane sizes under permeability thickness products of $8.0\text{E-}16 \text{ m}^3$ to $1\text{E-}14\text{m}^3$ . Laminates of any thickness can be OVB processed successfully. ....	160

Figure 7.7 Chart for determination of the air removal strategy in OVB processing for AS4/APC2 laminates with initial $V_v=7.77\%$ with (a) given part in-plane dimension and thickness (b) allowable processing time (c) allowable processing time and part-in plane dimension. ....	163
Figure 7.8 Interlayer permeability thickness products of $0^\circ/90^\circ$ lay-up in the processing cycle with different dwell temperature and heating rate of $5^\circ\text{C}/\text{min}$ .....	164
Figure 7.9 Interlayer permeability thickness products of $0^\circ/0^\circ$ lay-up in the processing cycle with different dwell temperature and heating rate of $5^\circ\text{C}/\text{min}$ .....	165
Figure A.1 Basic procedures for image processing .....	186
Figure A.2 2D and 3D average void content of prepreg tape.....	187
Figure A.3 Comparison of void equivalent diameter distribution per mm tape across the fiber direction .....	188
Figure B.1 Voids in the sample scanned with different resolutions of $\mu\text{-CT}$ .....	190
Figure B.2 Number of voids in different length ranges in a sample of $2.1\text{ mm} \times 1.8\text{ mm} \times 0.18\text{ mm}$ under different scanning resolution. ....	191
Figure B.3 Number of voids in different equivalent diameter ranges in a sample of $2.1\text{ mm} \times 1.8\text{ mm} \times 0.18\text{ mm}$ under different scanning resolution.....	192
Figure C.1 Schematics of surface roughness parameters $R_a$ , $R_q$ , and $R_z$ .....	194
Figure C.2 Laser intensity image of the tape sample (from scanning setting 4) .....	196
Figure F.1 Supersaturation ratios of $\text{N}_2$ , and $\text{O}_2$ during temperature ramping in OVB processing .....	204
Figure F.2 Term A and Term B of the nucleation rates of $\text{N}_2$ , $\text{O}_2$ and $\text{H}_2\text{O}$ with increasing temperature in OVB processing .....	206
Figure G.1 Prepreg tape surface in contact with a flat surface showing the ratio of interlayer region height and width of porous channels can be in the order of 0.01 .....	208

## **ABSTRACT**

High quality continuous fiber reinforced thermoplastic composite materials can be obtained with autoclave processing that utilizes vacuum and high levels of positive pressure to achieve very low void content materials. Due to the high cost of autoclave, there is a strong demand to develop cost effective out of autoclave (OOA) alternatives that provide equivalent properties. Oven vacuum bag (OVB) processing is inherently low cost and scalable to large part manufacturing. One of the most important criteria to achieve autoclave equivalent properties is void reduction. Preliminary consolidation experiments achieved void free thin AS4/APC2 carbon PEEK thermoplastic laminates in the OVB processing. However, the methods and the mechanisms for void reduction are not fully understood. The goal of this research is to develop a fundamental understanding of the void reduction mechanisms and develop process models that can be used to design and optimize the OVB processing cycle for thermoplastic laminates of varying thickness and in-plane dimensions.

The microstructure of the voids in AS4/APC2 carbon PEEK thermoplastic prepreg is critical to the initial condition of void reduction and the understanding of the void reduction mechanism. Spherical voids were assumed based on the 2D characterization in the literature. In this study, high resolution 3D X-ray micro-CT was employed to obtain 3D information of voids in a large volume of prepreg tape. Representative properties including void content, geometry and dimensions were obtained through statistical study. The statistical representative volume element (SRVE) of the void microstructure was determined. The majority of the voids were

found to be rod-like with aspect ratio from 2 to 150 and finite lengths smaller than 1 mm. The voids are encapsulated in the prepreg tape and do not form porous pathways along the fiber direction.

Due to the rough surfaces of the thermoplastic prepreg tapes, porous interlayer regions are formed when prepreg tapes are stacked, which is another important property that may affect the void reduction. With a 1D flow experimental set-up, the product of the in-plane air permeability and thickness ( $Kh$ ) of a wide range of lay-up configurations of AS4/APC2 before and after processing were investigated. The interlayer permeability from the raw tape lay-ups is about 1-2 orders higher than the reported permeability of some partially impregnated thermosetting prepreg designed for vacuum bag processing. The interlayer permeability exhibits directional dependency, and 2D rotation transformation matrix can be used for predicting the  $Kh$ s of different lay-ups. Different lay-ups show different extent of reduction with the increasing temperature and dwell time during processing. Fiber –fiber contacts limit the contact between layers and prevents significant drop of the permeability during processing.

With the encapsulated voids and highly viscous resin in the AS4/APC2 prepreg tape, and vacuum bag pressure, the driving force for void reduction can only be provided by reducing the internal pressure of voids through the removal of air from the void. Through the consolidation experiments of 72-layer thick laminates, a combined mechanism that air diffusion from the void through a single layer prepreg followed by interlayer air evacuation is validated to be the key mechanism to achieve low void content in thick laminates via OVB processing. Analytical models for single layer diffusion and interlayer air flow are developed to simulate the air removal during

OVB processing. With the inputs of the consolidation experiments, the modeled results are in line with the experimental results, further validating the combined mechanism for void air removal.

The air flow time through the interlayer region highly depends on the interlayer permeability and the part in-plane dimensions. Maintaining the interlayer permeability during the heating ramps of the processing is critical especially for large parts. A model based on the time and temperature dependent elastic-viscoelastic-viscoplastic behavior of the PEEK resin is established to describe the deformation of the interlayer region formed by the resin rich surface region of the prepreg tapes. The modeled strains are compared with the strain calculated from the measured  $Kh$ , and the difference is discussed with the microstructure of the prepreg tape and the surface characteristics of the tapes from processed lay-ups. It is found that the deformation of the interlayer is initially governed by the resin response. Fiber-fiber contacts then supports the local stress and result in a strain plateau, preventing further deformation and reduction of the interlayer permeability.

With the air removal models and the interlayer material response, parametric studies were conducted to investigate the effects of tape properties, processing conditions and part sizes. Lower initial void content, high level of vacuum, and relatively high heating rate are favorable to reduce the processing time. Low temperature dwell cycle may be included in the heating ramp to optimize the processing cycle. Based on the combined mechanism for air removal, very thick section large parts can be OVB processed (75 m parts in 8 hours with no thickness limitations based on the design of the processing cycle).

# Chapter 1

## INTRODUCTION

### 1.1 Motivation and Significance of the Research

High quality high performance continuous fiber reinforced thermoplastic composite materials can be obtained with autoclave processing that utilizes both vacuum and high levels of positive pressure to achieve very low void content composites. The autoclave process has been developed over the past 50 years in the space and aerospace industries and is known to provide the highest level of structural material properties [1–3]. However, the manufacturing cost using high pressure autoclave is very high and part sizes are limited by the expensive equipment. There is a strong demand to develop cost effective out of autoclave alternatives that provide equivalent properties. One of the most important requirements to achieve equivalent properties for out of autoclave processing is reducing the void content in thermoplastic composites to less than 1% to meet the aerospace autoclave standards. The fundamental mechanisms of void reduction in thermoplastic composites are not fully understood, especially in the low pressure vacuum assisted non-autoclave processing methods.

In this study, oven vacuum bag (OVB) processing (i.e. no external pressure) is chosen as our out of autoclave process. OVB is inherently low cost and scalable to large part manufacturing. Exploratory consolidation trials were conducted for thin laminates and showed that void reduction under vacuum is possible for thermoplastic composites. From the literature, a comprehensive list of void dynamics mechanisms is

reviewed. Generally, void reduction depends on the void origins, microstructure of the voids in prepreg materials, and processing conditions. This thesis develops a fundamental understanding of void dynamic mechanisms of thermoplastic composites through experimentation and formulate validated process models that can be used for OVB process optimization of laminates of varying thickness and in-plane dimensions.

### **1.1.1 Preliminary Study of OVB Consolidation of Thermoplastic Laminates**

Preliminary OVB consolidation trials were conducted for AS4/APC2 carbon fiber reinforced PEEK prepreg from Solvay which is a high performance continuous thermoplastic composite prepreg material widely used in aerospace industry. Thin 2-layer  $0^\circ/90^\circ$ , 4-layer  $[0^\circ/90^\circ]_s$ , and 8-layer  $[0^\circ/90^\circ]_{2s}$  cross-ply laminates with 300 mm by 300mm in dimension were vacuum bagged as shown in Figure 1.1. The laminates were heated to 380 °C with standard heating and cooling rate of 2.7 °C/min (5 °F/min) and dwelled for different time periods. After the consolidation, voids were examined with an optical microscope. It was found that all cross-ply laminates were void free after 1 hour of dwell with the typical cross-sectional images shown in Figure 1.2. Average void content of the 2-layer and 4-layer laminate after the processing cycles of 0 min and 10 min dwell at 380°C were obtained and presented in Figure 1.3. Less than 1% voids were achieved for all laminates (presented in Figure 1.3) with slightly higher void content in the 0 min dwell cycle than the 10 mins longer dwell cycle.

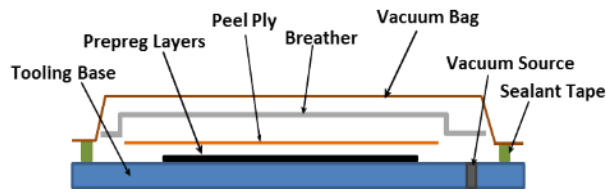


Figure 1.1 Schematic of vacuum bag assembly in OVB processing of thin thermoplastic laminates

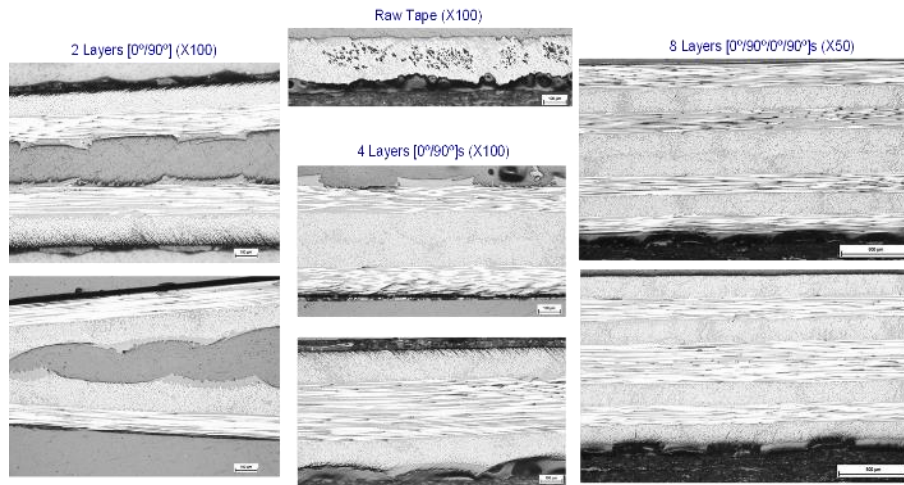


Figure 1.2 Micro images show nearly void free cross-ply laminates are obtained after 1 hr dwell at 380 °C

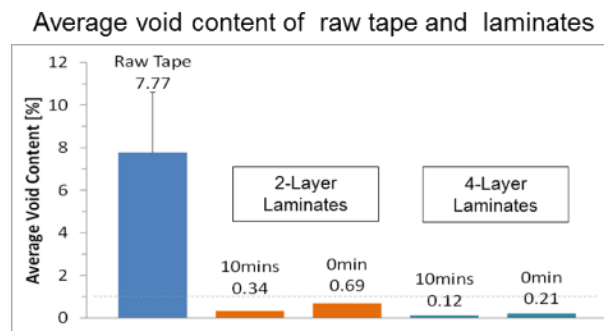


Figure 1.3 Less than 1% void content was achieved for 2-layer and 4-layer thin cross-ply laminates after 0 min and 10 mins dwell cycle at 380 °C

The preliminary consolidation experiments showed that void free thin laminates can be achieved with OVB processing. OVB processing is a promising low cost alternative for autoclave process for high performance thermoplastic composites. The void reduction mechanism will be investigated in this research. The methods to process thick section thermoplastic composites and large dimensions will be established in this research. In the next section, the origins of the voids, the processes to consolidate voids in thermoplastic composites, and the void dynamic mechanisms in composites are reviewed.

## **1.2 Literature Review**

### **1.2.1 Voids in Thermoplastic Prepreg**

Voids in high performance thermoplastic composites can originate from voids that pre-exist in the thermoplastic prepreg layers (Figure 1.4) or by air entrapped between layers during lamination. Voids in the prepreg are generated during the manufacture of the prepreg. In a hot melt prepreg process, voids can be created by entrapped air, dissolved and adsorbed moisture and volatiles (plasticizers) in the resin that may nucleate and grow voids during processing [1,4–8]. In addition, voids can be created by inadequate wetting of the fibers by the resin, or insufficient infiltration of the resin into the fiber tows. [9] Consequently, voids within the prepreg can be in resin rich area and also within the fiber tow regions. Voids can vary in size (submicron in the resin rich regions to 3-5 fiber diameters (20-50 microns) in regions of poor infiltration) and spatial location and across the width and along the length of the prepreg. The void microstructure has three dimensional attributes that is best quantified through statistical means. Mechanisms of void reduction are sensitive to

these microstructural details. [1,10–13] A robust OVB process must eliminate all types of voids present in the prepreg or composite properties will be degraded. Studies have shown that the compression strength/strain to failure of thermoplastic composite cylinders reduces 50%-86% when the void content in the carbon fiber or glass fiber thermoplastic parts increase from about 1% to 5%~7%. [13]

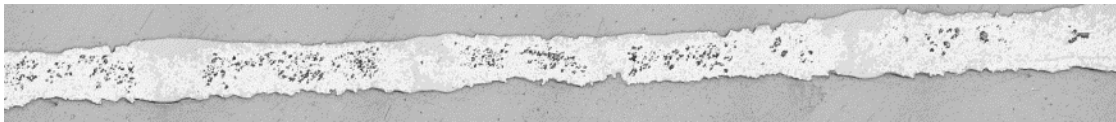


Figure 1.4 Cross sectional micrograph show voids (black area in the tape,  $V_v = 7.8\%$ ) in thermoplastic prepreg tape, Solvay AS4/APC2 prepreg, 6 consecutive images stitched large image of prepreg tape under 200X magnification with sample width of 3.4 mm.

### 1.2.2 Manufacturing of High Performance Thermoplastic Composites

Voids in thermosetting composites can be eliminated with resin flow or bleeding introduced by high pressure and vacuum in various manufacturing processes. [14–16] Intralayer and interlayer voids in high performance thermoplastic composites are difficult to be removed because of the high viscosity of thermoplastic resins ( $10^2 \sim 10^6 \text{ Pa}\cdot\text{s}$  for thermoplastic melt vs.  $0.05 \sim 0.5 \text{ Pa}\cdot\text{s}$  for thermoset [17]) that results in and significantly less resin flow comparing to that of thermosetting resins. The manufacturing methods of thermoplastic composites with prepreg are usually autoclave processing, in-situ consolidation processing such as automated tow/tape placement (ATP) and filament winding, and compression molding (Figure 1.5). High pressure (can be 500 psi) and vacuum in autoclave processing can significantly reduce the void content in continuous thermoplastic composite parts. [2,3] Although

compression molding with high pressure can also reduce the voids, it is not a cost effective method for large complex shaped parts due to the cost of complex mold and application of high pressure. [18] Non-autoclave in-situ consolidation methods using robotics can significantly reduce the labor time for hand lay-up by increasing material deposition rates while improving placement accuracy and repeatability between parts. This process can also be used for parts with curved surfaces or complex shapes. However, in-situ consolidation does not consistently achieve less than 1% void content. Typically, post processing with an autoclave is still required to achieve high quality parts with low void content. [19–21] Because the manufacturing cost of autoclave processing is very high, a growing and strong demand in the industry is to develop non-autoclave processing that produce affordable high performance parts. One possible processing route to replace the autoclave is the oven vacuum bag (OVB) process (Figure 1.5), also as introduced in the preliminary study. For aerospace applications one could combine robotics for rapid, accurate and repeatable placement of prepreg for large complex shapes with low cost OVB consolidation process to achieve low void content high performance composite structures. However, the scientific basis for void reduction in high viscosity thermoplastic composites under vacuum pressure is not well understood.

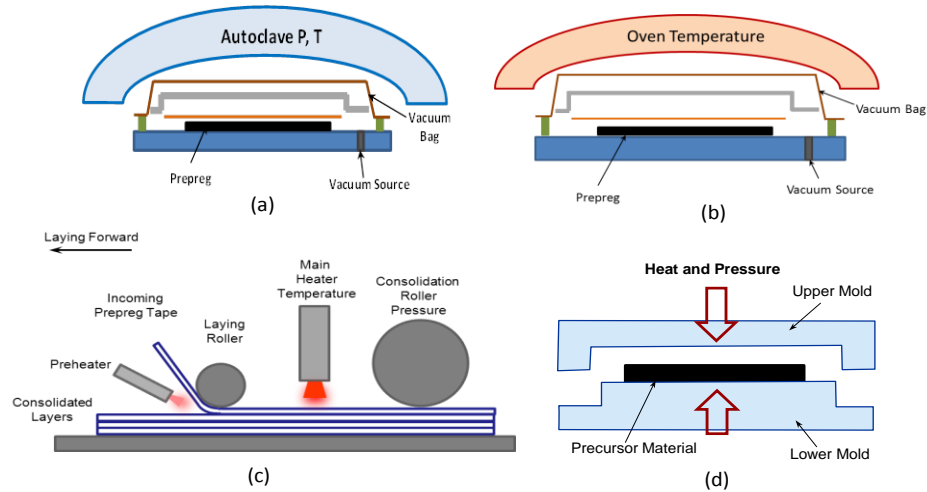


Figure 1.5 Schematics of (a) autoclave, (b) oven vacuum bag (OVB), (c) ATP process, (d) compression molding

### 1.2.3 Mechanisms of Void Dynamics

Voids are seen in both thermoplastic and thermosetting composites. The mechanisms of void formation and elimination in polymer or polymer composites found in the literature include coupled mechanism of stress equilibrium at void boundary and gas molecule diffusion, void compression by applied pressure, void filling with resin flow, moisture/gas nucleation and diffusion, and void escaping through buoyancy. Air permeability of prepeg is found to be important for void reduction during composite processing as well. Each mechanism may be suitable for certain types of voids and processing conditions.

#### 1.2.3.1 Coupled mechanism of Stress Equilibrium and Gas Molecule Diffusion

Before composite processing, void formation was studied in polymeric foaming process involving diffusion of void gas molecules. An early cell model of isothermal growth of spherical gas bubble in an infinite sea of viscous fluid involving

diffusion and mechanical equilibrium was developed by Amon et al [22]. Arefmanesh and Advani [23,24] extended the model for a large number of simultaneously growing bubbles with limited availability of diffusing species in highly viscous fluid.

Roychowdhury and coworkers [25,26] applied this idea to their study of volatile (moisture)-induced void formation in amorphous PEI for structural applications. A comprehensive model was developed including moisture desorption during temperature ramp, void nucleation after glass transition temperature and isothermal void growth. Keeping the cell model concept, a spherical void grows within a polymer cell was used as shown in Figure 1.6. All the voids are assumed spherical. The void radius was obtained by solving the momentum equation at void boundary, the Fickian diffusion equation of volatile species, and the mass conservation equation at the void polymer interface in a coupled fashion. It is found that: (1) with a fixed moisture content, the void size and void fraction increase with processing time; (2) the applied pressure results in a decreasing nucleation density and hinders void growth; (3) larger void can grow within thinner polymer shell. This work stressed the importance of applied pressure, void internal pressure, volatile concentration and diffusion, and processing time. Ledru et al. [27] applied this coupled model of pure polymer to composites in his recent work on void growth in thermosetting composite in an autoclave process. He pointed out that the applied pressure, the concentration of diffusive species and the diffusion coefficient, are the three major factors for void control.

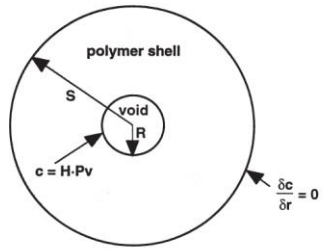


Figure 1.6 Schematic of a cell of polymer shell containing a void [26]

Their work also indicates the importance of composite and resin material properties. The resin viscosity changing with processing temperature largely affects the rate of resin flow and critical time for void reduction. Surface tension between the void and resin works together with void internal pressure and the applied pressure, governing the stress equilibrium and whether the void should collapse or grow. The solubility of the volatiles or gases in the resin determines the initial concentration in the resin under a certain condition. As the temperature changing, the solubility at temperature also changes, governing the direction of the gas diffusion and void dynamics. The glass transition temperature and/or melting temperature of thermoplastic resin/composite are also important material properties, determining the starting point of resin softening and void behavior. The void reduction and process optimization cannot be done without knowing the effect of these important material properties.

This mechanism may be applicable for voids in the resin rich area where diffusion is important in OVB process. Diffusion coupled with resin flow might be needed for larger voids in the fiber tows. Since OVB only has low pressure due to applied vacuum, gas diffusion becomes more important for void reduction. The real void geometry and spatial distribution (local content), and the gas transportation

between the materials and processing environment which would affect the void reduction were not considered.

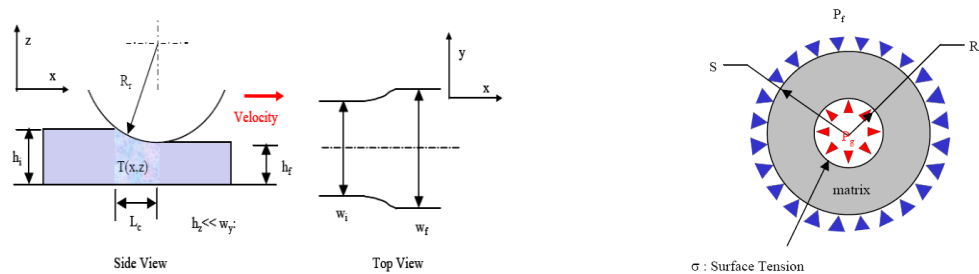
### **1.2.3.2 Void Compression by High Applied Pressure**

Studies have shown that the high applied pressure in autoclave process can effectively reduce the void content of both thermosetting and thermoplastic composites. [2,3,14,28,29]. Non-autoclave in situ processing method of thermoplastic composites such as filament winding and ATP can provide high productivity, and reduce manufacturing cost.[30,31] However, ATP is a highly non isothermal process, and the consolidation time of local prepreg positions are very short compared with autoclave process. The layers below the top layers experience reheating, where deconsolidation of the layers could occur.

Modeling and experimental work have been done by researches to understand the complex ATP process and control the part quality. The voids in the laminates can be categorized into intralayer voids which presented within a prepreg layer, and interlayer voids that between two layers due to the rough surface of the prepreg. The inter-layer voids can be predicted with models for intimate contact developed by Lee and Springer[32] and Mantell and Springer[33], and modified for ATP process by Pitchumani et al [31,34] and Tierney and Gillespie[35,36]. The rough surface topology is idealized as a periodic array of the identically sized element. Under the applied temperature and pressure, the surface elements undergo squeeze flow and spread along the interface between layers. The time required to achieve fully intimate contact decreases with increasing applied pressure and temperature.

The reduction of intralayer voids during ATP process is dominated by the void consolidation under the effect of compaction and cooling of consolidation rollers. Two

models are well developed for the void reduction of ATP process: a macroscopic model for void transport, and a microscopic model for void compression. [31,34,36–40] Because thermoplastic resins exhibit a high viscosity as a result that the fibers move along the resin rather than relative to the resin, the process is described as a squeeze flow rather than Darcian flow. The fibers and resin are modeled as an equivalent homogeneous fluid to compress the void. In the macroscopic void transport model, the fluid motion is due to the thickness decreasing and width increasing of the tape under the compaction of the roller (Figure 1.7(a)). In the microscopic void consolidation model, a void at any location is modeled as a sphere with a radius  $R$  surrounded by a composite shell of outer radius  $S$  (Figure 1.7(b)). Void growth or collapse is governed by the stress equilibrium between the voids internal pressure, the pressure outside and the surface tension. Therefore, if the outside pressure is very small, the voids would grow. In the region away from the compaction rollers where the fluid pressure decreases to atmospheric pressure, the deconsolidation occurs.



(a) Macroscopic void transport model

(b) Microscopic void consolidation model

Figure 1.7 Geometry of void reduction model of ATP process [36,37]

Large gradients of void fraction through the thickness of ATP parts due to the repeated processing through multiple lay-up and heat sink effect at the tool interface, were observed and simulated by both Tierney et al.[36,39] and Kan et al. [41]. It is very common that the void content of the part after ATP is still higher than required. Lamontia and coworkers revealed the effect of the initial tape properties on ATP parts and showed the benefit of using smooth tape with low initial void fraction on processing and part quality.[21,42–44]. Although good correlations were obtained between experimental results and model prediction, the void reduction model may be only applied for processing methods with high pressure and fast speed, such as ATP where the high pressure is the key to reduce voids, which is not possible in OVB process. Similarly as the coupled mechanism, the void geometry and spatial distribution were not considered in the model.

### **1.2.3.3 Void Filling with Resin Flow**

For voids present in the fiber tow region, resin flow to infuse the fiber tow and close the voids will be needed. A resin infusion model was developed by Simacek for in-situ consolidation processes [45,46], taking the distance between the voids and the void sizes into account in a unit cell containing voids and composite (Figure 1.8). After the pressure is applied on the prepreg tape, the tape thickness is changing, and the resin flows through the fiber bed to fill the voids. The net driving force for void filling is reduced by the pressure that builds up within the void boundary as temperature is increased or void volume decreases (e.g. ideal gas law). This model and the ATP microscopic void consolidation model both show the significance of initial conditions within the voids. In this model, the spatial distribution and local content of

voids within fiber tows are incorporated and shown to be important. However, the gas transportation which may be important in low pressure OVB process was ignored.

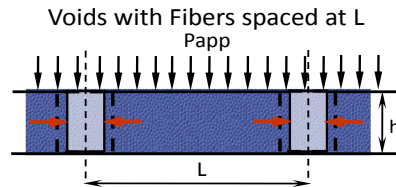


Figure 1.8 Schematic of void filling model

#### 1.2.3.4 Moisture/Gas Nucleation and Diffusion Controlled Void Dynamics

Although the source of voids may be different, the nucleation and diffusion related void dynamics has been studied extensively in the literature. An early study by Kardos et.al [47] was about moisture induced void generation and growth in thermosetting composite. In his modeling work, no void pre-exists in the composite; critical – sized nuclei formed from water or air at the early stage. The following void growth is considered in an isotropic pseudo-homogeneous medium via diffusion of air or vapor. He pointed out that the initial resin moisture content and the resin pressure early in the cycle are critical in producing a void – free laminate. Once the voids are formed and stabilized, he concluded that voids can only be removed with resin flow. However, this modeling work was not validated with detailed experiments. A recent study by Grunenfelder et.al adopted the diffusion controlled model to predict the void content and obtained good correlation with experimental results. [15] In Roychowdhury's study [28] , void nucleation and growth due to the volatiles was the origin of the voids in the polymers which had no pre-existing voids as well.

Nevertheless, the moisture desorption during the non-isothermal temperature ramps was considered and set the initial concentration profile in the material.

Through the experimental investigation in short glass fiber thermoplastic composites, Vaxman et.al [48] suggested that voids are formed by the entrapped air during the compounding and processing stages, and nucleate at short fiber ends. Leterrier et.al [49] found that the expansion of a composite sheet under atmospheric pressure at high temperature is largely induced by the gases previously dissolved in the polymeric matrix, and proposed that the voids were closed under the high pressure by means of void dissolving into the resin as individual molecules, through his study of thermoplastic stamping process and a scaled-up experiment with polypropylene. In OVB processing of thermoplastic composites, void air may also dissolve into the resin or the air dissolves in the resin may also nucleate new voids, which can affect the void reduction, and require further analysis.

#### **1.2.3.5 Void Escaping through Buoyancy Force**

Muric-Nesic et al.[50] studied void reduction of thermosetting composite with vibration and vacuum assisted curing system. He proposed that the voids escape by means of buoyancy and assisted by the effect of applied pressure, solubility and diffusion, and vibration. The buoyancy effect and the time for a void to float up highly depend on the viscosity of the resin and the size of the void. In high viscosity fluids such as thermoplastic polymer melt, the void movement relative to resin could be difficult. This mechanism may not be viable in thermoplastic OVB processing.

### **1.2.3.6 Influence of Air Permeability on Void Reduction**

Studies have shown that air permeability is a crucial element for gas venting off from thermosetting prepreg stack during curing, especially in the thick composite manufacturing [51–54]. Nam et al.[51] found that the inter-laminar voids in a plain weave carbon fiber prepreg stack initially form a porous network due to the undulation of the fiber tow and uneven prepreg surfaces for gas to flow through, reducing the intralayer voids; as the autoclave pressure increases, the open pores began to be disconnected and sealed in the laminates. Shim and Seferis [52] found that interlaminar permeability appear to be more important than intralaminar permeability when prepreg was laminated and vacuum applied in the processing could eliminate significant porosity. Besides the in-plane permeability, through thickness permeability of thermosetting prepreg was also studied by researchers[54–56] . Xin et al. found that the air entrapped in prepreg stack with higher air permeability can be vented off more easily than with lower air permeability, and stressed the impact of air permeability on voids reduction in vacuum bag only process. Recent years, partial/semi impregnated thermosetting prepreg were developed for vacuum bag process. The dry fiber region was designed to provide porous path for gas evacuation and produce void free part more cost efficiently than autoclave. [53,57]

Although not studied by any researcher so far, permeability of thermoplastic prepreg may also be an important factor for void reduction during processing, especially OVB process with prepreg which has inherent voids in the solid prepreg microstructure. If the single layer prepreg is permeable in thickness or fiber directions with inter-connected voids, the void gases could be evacuated when the vacuum applied in the bag before softening of the resin, resulting in vacuum inside of the voids, which provides the driving force for void closing under the low pressure. If no

apparent permeability were found for single layer prepreg, then gas can only escape via diffusing to the prepreg surface. The diffusion time highly depends on the thickness of stacking material. This indicates that in OVB process, thick laminates may need extremely long time to reduce voids or end up with high void content in short time. Then, the diffusion dominated gas evacuation mechanism will be one of the key technical challenges for OVB. However, porous paths can be formed by the interlayer region due to the rough prepreg surfaces will play an important role for rapid escape of the gases. The interface permeability could reduce when the intimate contact between layers develops. Therefore, possible process optimization for thick laminates may be achieved by controlling the processing temperature, dwell segments and time in OVB process.

From the above review, it is seen that the void consolidation mechanism in thermoplastic composite processing is still not fully understood, especially for OVB consolidation of thermoplastics composites. Although models were established to describe the proposed mechanisms, factors such as void geometry, size and spacial distribution and the microstructure of prepreg tape, the processing environment (vacuum, venting) were not considered. Those factors could have important impact on void consolidation and gas molecules escaping. The detailed initial properties of the voids and prepreg should be characterized, which has not been done for thermoplastic prepreg tape so far.

### **1.3 Research Objectives**

This research focuses on the fundamental science of void consolidation in thermoplastic composites during OVB processing. The objectives of this research are as follows:

- Investigate the microstructure of the thermoplastic prepreg tape and the interlayer permeability of prepreg stacks as they provide the initial conditions and important input for void reduction
- Identify and validate the key mechanism for void reduction in OVB processing of high performance thermoplastic composites
- Develop models for the void reduction mechanism, integrating the initial tape properties, processing conditions and final void content
- Optimize the overall OVB process for laminates of any thickness and in-plane dimensions.

#### **1.4 Unique Contribution**

This research provides a fundamental understanding of the void air removal mechanism and void reduction in highly viscose thermoplastic composite consolidations, specifically the OVB process which is a potential alternative of the autoclave for aerospace applications.

The 3D characterization of the void properties and the statistical approach of determining the SRVE of the microstructure of voids in thermoplastic prepreg material provides the unknown knowledge for this widely used AS4/APC2 prepreg tape and the methodology that can be widely used for investigating the microstructures of other materials.

For the first time, the interlayer air permeability of thermoplastic prepreg lay-ups is investigated. Its importance to the void air removal and void reduction is pointed out, which may provide a starting point for the future research on controlling and designing the thermoplastic prepreg tape with interlayer permeability more favorable for the OVB processing. The experimental set-up for the permeability measurement provides a direct way for obtaining the effect in-plane permeability in OVB processing, and can be widely adopted as well.

The combined mechanism of void air diffusion through single layer prepreg followed by air flow through interlayer region fills the unknown knowledge of the void consolidation in thermoplastic composite, and proves the capability of OVB processing to achieve the aerospace requirements for void content. The models developed shows that the OVB processing can be designed and optimized for a particular part size and initial tape properties to achieve low void content, which have a significant impact on the thermoplastic processing in quality and cost wise.

## **1.5 Dissertation Outline**

In Chapter 2, two important features of the thermoplastic prepreg tape are investigated: the microstructure of voids and the surface roughness of the tape. The microstructure of voids is characterized with 3D high resolution 3D X-ray micro-CT, and the detailed void properties such as 3D void fraction, dimensions, number density and aspect ratios are quantified. Statistical error analysis and distribution functions are applied for the void analysis and the statistical representative volume element (SRVE) of void microstructure is determined. The obtained void information provides important information on determination of void reduction mechanism in Chapter 4, and input for the void reduction model in Chapter 5. Surface roughness of the tape is characterized and the representative tape dimensions are determined. The roughness information is correlated to the interlayer permeability in Chapter 3.

In Chapter 3, the in-plane interlayer permeability of the prepreg stacks is measured experimentally. The principal of the experimental set-up is Darcy's law. The interlayer permeability of raw prepreg tape with a wide range of lay-up configurations is measured. In order to study the effect of processing cycle to the interlayer permeability, typical interlayers are OVB processed to different temperature and dwell

times before the permeability measurement. The surface roughness of processed tapes with same condition is correlated to the permeability changes, providing more insight of the interaction of the contact layers. The measured permeabilities are applied in the air evacuation model in Chapter 5.

In Chapter 4, void reduction mechanisms are analyzed and discussed with the microstructure of prepreg and processing conditions in OVB processing. A designed consolidation experiment shows that aerospace requirement of low void content can be obtained in thick section thermoplastic composite via OVB processing, and validates that void air removal through single layer diffusion followed by interlayer air evacuation is the key mechanism to achieve low void content.

In Chapter 5, models for void air removal mechanisms based on the combined mechanism of air diffusion through single layer of the prepreg tape followed by air evacuation through the permeable interlayer regions, and the diffusion mechanism through the thickness of the laminates are developed. With the input of the initial void content in AS4/APC2 prepreg and the temperature profiles of the consolidation experiment in Chapter 4, the characteristic time and temperature from the model calculation are correlated to the experimental results in Chapter 4, further validates the mechanism for void reduction in OVB processing.

In Chapter 6, a material behavior model was developed to investigate the deformation of the interlayer region and the evolution of the interlayer permeability. The modeling results are compared with the experimental results from the interlayer permeability thickness products. The behavior of the interlayer region are also discussed with the microstructure of the prepreg tape and the surface characterization results from Chapter 3.

With the models of diffusion, air flow, and material behavior, the design and optimization of the processing cycle is introduced in Chapter 7. The effect of initial void content, processing conditions, interlayer permeabilities and part sizes on void air removal are investigated through parametric studies. The guidelines for designing the proper heating ramp for air removal is provided.

Finally, Chapter 8 summarizes the conclusions of this research. The major contributions and potential applications of the methodology and models in this work are reviewed. Topics of future research are proposed.

## Chapter 2

### MICROSTRUCTURE OF THERMOPLASTIC PREPREG

#### 2.1 Introduction

Thermoplastic prepreg materials for high performance thermoplastic composite parts contain a relatively high level of initial void content (5%-10%). From the typical cross sectional micro image in Figure 1.4, voids inside the prepreg vary in size and mainly non-uniformly locate within the fiber tow region. The microstructure and the status of voids in the prepreg determine the initial conditions of the void reduction in the OVB processing of thermoplastic composite parts, and need to be investigated. Voids in the composites are usually characterized in 2D. However, in real prepreg system, they are 3D objects, and have 3D geometry and distributions. Therefore, the detailed 3D void content, geometry, sizes and number densities are investigated systematically and statistically in this chapter. The surfaces of the thermoplastic prepreg are very rough (Figure 1.4) and can form interlayer voids or form permeable interlayer region when laid-up, which may significantly affect the void reduction. Therefore, as another important feature of the microstructure, surface roughness of the thermoplastic prepreg tape is also characterized.

## **2.2 Microstructure of Voids in Thermoplastic Prepreg**

### **2.2.1 3D Characterization Techniques and X-ray Micro-CT ( $\mu$ -CT)**

To experimentally characterize the voids in composite materials, 2D optical microscopy (OM) and scanning electron microscopy (SEM) are commonly used.[2,10,15,50,58,59] However, the information about void shape and sizes in the 3<sup>rd</sup> dimension (i.e. fiber direction) has not been thoroughly quantified.

Therefore, a 3D inspection technique is needed. Automated serial sectioning which is commonly used for 3D microstructural characterization of metals can be used for thermoplastic matrix composites, but sectioning and polishing is quite time consuming (up to 0.2  $\mu\text{m/hr}$  for high precision milling).[60–62]. X-ray computed micro tomography (Micro-CT), originally used for medical imaging, has been applied on the microstructures of composite materials in recent years. Several studies showed the capability of high resolution micro-CT on inspecting voids, internal damages, in-situ damage development inspection during testing and microstructures of fiber reinforced polymer matrix composites. [63–69] Unlike serial sectioning, micro-CT scans provide 3D microstructure information with fast speed and high resolution. To examine large sample volume for statistical study, thousands of cross-sectional images are needed to construct 3D volume. With automated serial sectioning together with traditional imaging techniques such as OM or SEM, it is impractical to inspect the same volume of prepreg with the same precision as  $\mu$ -CT scanning. [70] Additionally,  $\mu$ -CT does not involve any specimen preparation, avoiding the possible errors introduced during the polishing and sample preparation step in OM. Therefore, for statistical characterization of 3D void microstructure in the thermoplastic prepreg,

high resolution X-ray  $\mu$ -CT is the most accurate and practical inspection technique currently available.

### **2.2.2 SRVE of the Microstructure of Composite Materials**

SRVEs of the microstructure of composite materials based on statistics of reinforcing fibers were investigated in the literature. Through quantitative characterization, micro-structure modeling and finite element method (FEM) based simulation, Shan et al. determined the RVE of glass fiber ceramic composite materials which contains fiber poor and rich region, and provide Young's modulus and local stress distribution comparable to those in the real composites.[71]. Using FEM, Grufman and Ellyin compared the transverse damage behavior with different microstructure sample size of fiber composites, and determined the SRVE with Kolmogorov goodness of fit statistical test.[72] Based on the random distribution of fibers, the SRVEs of typical unidirectional carbon fiber reinforced polymer (CFRP) was established by Trias et al.[73] and Zangenberg and Brondsted[74], and it is shown that the sizes of SRVE defined varies with different criterion and applications. Side length larger than 600  $\mu\text{m}$  was found for square-shaped SRVE[74], and the ratio of SRVE side length and equivalent fiber radius was found to be 60 based on numerically generated SRVEs and mechanical performance of composites[73]. RVE was also investigated and applied to the study of mechanical properties and piezoelectric properties of nanocomposites[75–77]. However, the study on SRVEs of void microstructure in composite materials and the related knowledge are lacking. Consolidation models using statistical input parameters are just now advancing to the level of detail that has been seen in mechanics. In this chapter, statistical error analysis and distribution functions are applied for void analysis, from which the sub-SRVE for

each void property were determined. The overall SRVE of the void microstructure was constructed from the maximum dimensions of individual sub-SRVEs for each void property.

### **2.2.3 Thermoplastic Prepreg Material**

The thermoplastic prepreg material used throughout this thesis is the unidirectional AS4/APC2 Carbon/PEEK prepreg from Solvay with a width of 30cm, areal weight 145 g/m<sup>2</sup>, resin weight fraction of 32%, nominal tape thickness of 0.17 mm, nominal fiber diameter of 7 μm, and a nominal void volume content range of 5% to 10%. Samples were cut from the central region of the prepreg tape and examined with X-ray micro CT technique.

### **2.2.4 Set-up of X-Ray Micro-CT Characterization**

The X-Ray micro CT system used in this study is Skyscan's 1172 high resolution μ-CT from Bruker. The system operates at 20-100 KV /0-250 μA with a maximum power of 10 W. The maximum image size of 4000 × 2096 pixels was chosen. For initial void geometry study, the highest resolution of 0.74 μm/pixel was chosen and 10 samples with the size of 2.2mm×1.8mm×0.18 mm were scanned. In order to assess the accuracy of the μ-CT measurements, 2D statistical results are compared to those from 2D optical microscopy (Appendix A). And it shows that 2D cross-sections from micro-CT provide accurate void content information which ensures the accuracy for 3D void information.

The micro-CT detector's field of view defines the maximum sample width (along the transverse direction of the prepreg tape) at different resolution. The scanning resolutions of 0.74 μm/pixel, 1.48 μm/pixel, and 2.96 μm/pixel were used to

inspect a prepreg sample of 2.2 mm×1.8mm×0.18mm to study the effect of scanning resolution on the quantitative results of void characteristics. (Appendix B) In order to study the void length and statistical distribution of voids, large and long samples need to be inspected. Considering the practical scanning time and relative accuracy of the statistical results, 1.48 μm/pixel was used to scan all the samples with a maximum single sample width of 4.5 mm. Since the full prepreg thickness is smaller than the maximum width to be accommodated, all the prepreg samples were scanned with full thickness (0.18mm). To examine the length of the voids, maximum scanning length along the fiber direction of 9.2 mm was achieved with oversize scanning function.

In Section 2.2.5.2, it will show that 9.2mm exceeds all length range of voids. Therefore, for the study of the statistical representative volume of void microstructure, a maximum sample size of 36 mm (width, across fiber direction) × 9.2 mm (length, along fiber direction) is constructed from 8 samples of 4.5 mm (width) × 9.2 mm (length) with full tape thickness. A systematic statistical treatment of this data set is used to quantify the void properties and associated sub-SRVEs having in-plane length scales smaller than the 36 mm x 9.2 mm sample.

Other relevant scanning parameters are shown in Table 2.1. The noise of μ-CT were reduced by increasing frame averaging, maintaining good contrast by suitable voltage and current range, and reduced rotation steps. Voids area smaller than 1 pixel can be artifacts from noise and were neglected in this work. Skyscan NRecon software was used to reconstruct the x-ray raw images of a sample into a set of parallel 2D micrographs, providing the 3D information of the entire volume of the sample, which were processed and thresholded into binary images (illustrated in Figure 2.1), and then

analyzed in Skyscan CTAn software for 3D void content. The number, volume and dimensions of voids were analyzed in Avizo Fire 7.0.

Table 2.1 X – ray micro CT scanning parameters

Parameters	Values
X-ray Voltage	40KV
X-ray Current	250μA
Filter	None
Rotation Steps	0.2° for 2.2mm wide samples 0.25° for 4mm wide samples
Frame Averaging	8
Random Movement	10

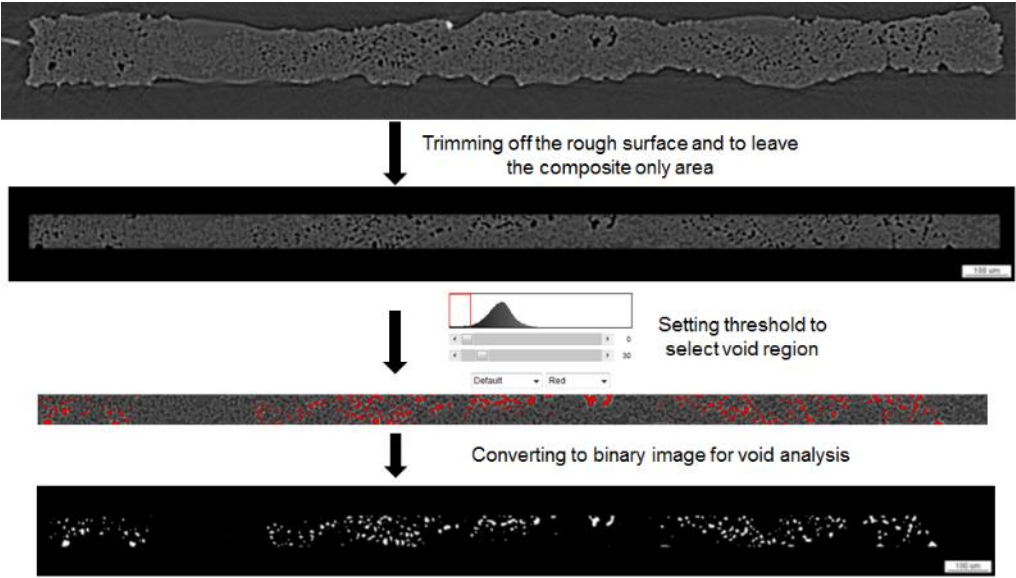


Figure 2.1 Processing of X-ray cross-sectional micrographs

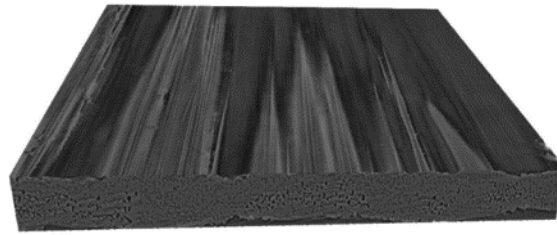
## **2.2.5 Results of Void Geometry**

### **2.2.5.1 3D Void Geometry**

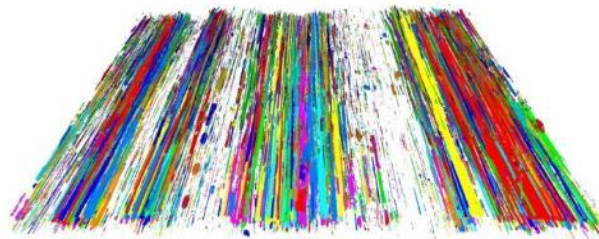
After micro-CT scanning under  $0.74\mu\text{m}/\text{pixel}$  and the reconstruction, the 3D volume of a prepreg sample can be viewed in CTVox software as seen in Figure 2.1 (a). The voids can be seen from the cross-section, and the rough surfaces of the prepreg tape were clearly evident. After extracting the voids from the volume in Figure 2.1 (b), the voids are found to have rod-like geometry that is oriented along the fiber direction as opposed to spheres assumed in 2D optical microscopy and in some modeling work. The detailed quantitative analysis of the length the rod-like voids will be given later.

### **2.2.5.2 Void Length**

Figure 2.1 shows that the majority of voids are rod-like and many have lengths approaching the sample length of 1.8 mm. Therefore, void length are studied with increasing length of samples. Three samples scanned under resolution of  $1.48\mu\text{m}/\text{pixel}$  and increased sample lengths of 1.8mm 3.7mm and 9.18mm. The detailed information of the samples is presented in Table 2.2. Only a small number percentage of voids have length equal to the sample length of 1.8mm. As the sample length increases, the number and the volume fraction of voids having length equal to sample length decreases significantly. From the volume distribution of the voids in Figure 10, the majority of the void volume is composed of voids with lengths smaller than 2mm. Given the large in-plane dimensions of prepreps, one concludes these rod-like voids do not form continuous porous pathways along the fiber length from one end to the other end.



(a)



(b)

Figure 2.2 3D voids in an AS4/PEEK prepreg sample (2.1 mm × 1.8 mm × 0.18 mm) from X-ray  $\mu$ -CT. (a) 3D view of prepreg sample, (b) Extracted voids in the sample (colors are to separate individual voids)

Table 2.2 Information of voids with L=Sample length in three samples

Sample	Sample Length [mm]	Sample Width [mm]	Total number of voids	Number of voids with L=Sample length	3D Void content [%]	Volume content of Void with L=Sample Length [%]
1	1.87	2.14	25634	12	6.56	1.05
2	3.7	4	28724	4	5.74	0.75
3	9.18	4	102595	1	5.34	0.107

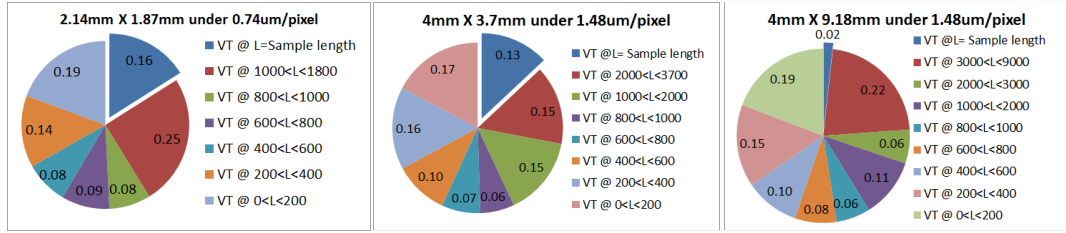


Figure 2.3 Volume distributions of voids with different length in the total void volume in three samples of 2.14 mm (width)  $\times$  1.87 mm (length), 4 mm (width)  $\times$  3.7 mm (length) and 4 mm (width)  $\times$  9.18 mm (length). L is the length of the voids, in the unit of mm.

### 2.2.6 Void Statistics and Determination of SRVE for Void Microstructure

Individual voids show local inhomogeneity but statistically distributed in a volume of thermoplastic prepreg. For each void property, i.e. void content, length, diameter and aspect ratio, there is a sub-SRVE that has the minimum volume (i.e. minimum in-plane width and length) that contain an equivalent statistical distribution of the void property as larger volume samples. Samples with smaller volumes would be statistically different and not include all of the microstructural features. The SRVE defines the length scales for modeling and simulation or experiments in which the region is considered statistically homogeneous and results would not be sensitive to sample size or location within the prepreg.

The sub-SRVE length scales for 3D average void content is determined based on the deviation (5% is used in this study) from void content of the large samples. The sub-SRVEs of void length, diameter and aspect ratios are based on the deviation of the normalized number distributions of voids compared to the distributions for the largest sample. Accurate statistical distribution functions (considerations such as Weibull, lognormal, loglogistic, Gamma, normal, logistic, and exponential) are first identified to describe the distributions for each type of void attribute. The fitting parameters are

obtained as a function of inplane dimensions. The parameters exhibit significant variability at low length scales and asymptote to the parameters for the largest sample. The length scales for the sub-SVREs are defined at the onset of the plateau region. Since the SRVE has two dimensions (all are full prepreg thickness), the minimum lengths for sub-SRVE were determined first. The minimum widths of sub-SRVEs are then determined using the SRVE lengths determined from the first step. This sequence was used for all void properties.

### 2.2.6.1 3D Void Content

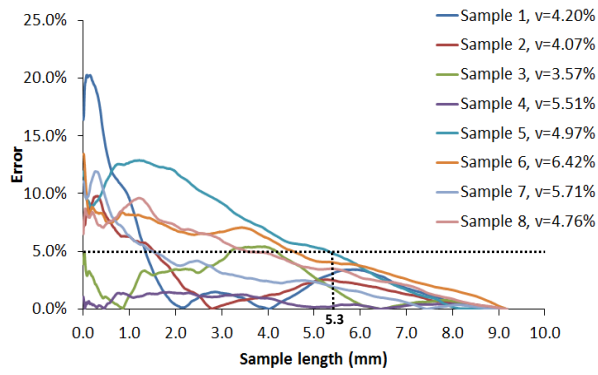
The errors of void content comparing to large samples are defined as:

$$error = \frac{|m-v|}{v} \quad (2.1)$$

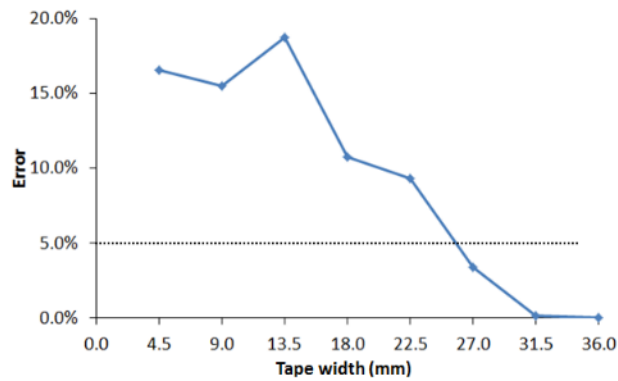
For the determination of sub-SRVE length,  $v$  is the void content of a prepreg sample with size of 4.5 mm  $\times$  9.2 mm, and  $m$  is the void content of the same sample and same width and sample length ranging from 0 to 9.2 mm. For the determination of sub-SRVE width,  $v$  is the void content of the sample volume with 36 mm  $\times$  sub-SRVE length, and  $m$  is the void content of sample volume of increasing width  $\times$  sub-SRVE length.

The errors along the length direction of 8 samples are shown in Figure 2.3. To achieve errors smaller than 5%, all the sample need to be at least 5.3 mm which is defined as the sub-SRVE length for average of void content. It is also seen that the void content for individual samples presented in Figure 2.3 (a) varies from 3.57% to 6.42% indicating more inhomogeneity of voids distributed across the width direction. The error along the width direction shown in Figure 2.3 (b) goes to zero when tape width is 31.5 mm, and is no longer sensitive to increasing tape width. The sub-SRVE

width is determined to be 27 mm at the threshold level. The dimensions of this sub-SRVE are 27 mm×5.3 mm×0.18 mm with an average void content of 4.7%. The dimensions of this sub-SRVE are less than the maximum sample size inspected.



(a)



(b)

Figure 2.4 Error of void content. (a) Along the tape length direction of 8 samples of  $4.5 \text{ mm} \times 9.2 \text{ mm} \times 0.18 \text{ mm}$ , (b) along the tape width direction of sample volume of  $36 \text{ mm} \times 5.3 \text{ mm} \times 0.18 \text{ mm}$

### 2.2.6.2 Void Length

It is found that the best fit for normalized number distribution for voids in void length is the 3-parameter Weibull distribution as seen in Figure 2.4 with its probability density function given as:

$$f(x) = \frac{\alpha}{\beta} \left(\frac{x-\mu}{\beta}\right)^{\alpha-1} e^{-\left(\frac{x-\mu}{\beta}\right)^\alpha} \quad (2.2)$$

Where  $x$  is void length in this case,  $\alpha$ ,  $\beta$ , and  $\mu$  are the shape, scale, threshold factors, respectively, the fitting parameters.

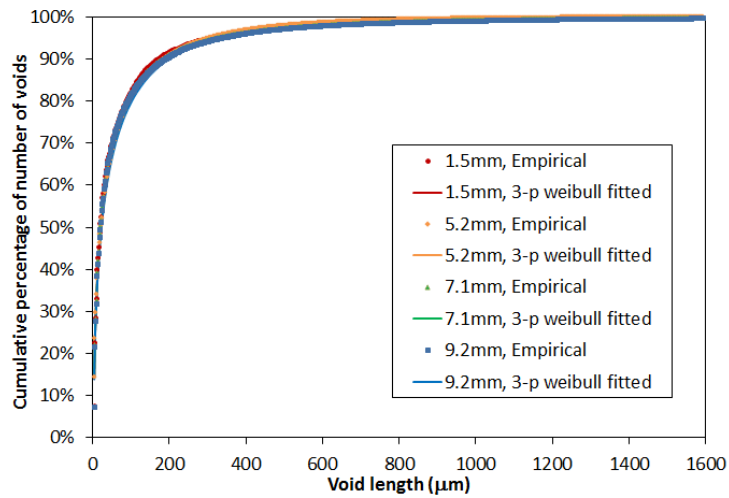
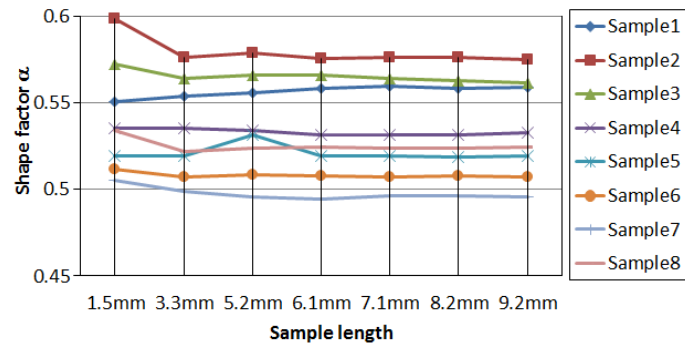


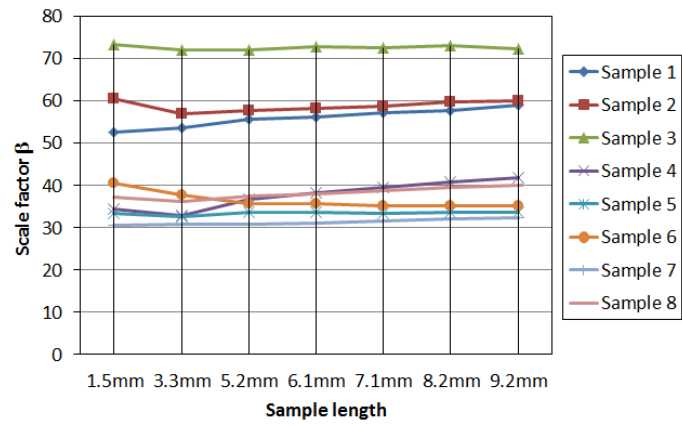
Figure 2.5 Empirical and fitted normalized cumulative distributions of voids in different void lengths in a tape sample of 4.5 mm wide with varying length.

Each of the 8 scanned samples was analyzed with sub-volume of 4.5 mm in width and length of 1.5 mm, 3.3 mm, 5.2 mm, 6.1 mm, 7.1 mm, 8.2 mm, and 9.2 mm. The threshold factor  $\mu$  for all the sub-volumes is determined to be 2.93  $\mu\text{m}$ . Both the shape and scale factors shown in Figure 2.5 are stationary when the sample length increases to 6.1 mm for all samples. With sample length of 6.1 mm, the scale and

shape factor were plotted with increasing tape width in Figure 2.6, and plateaus as the tape width increases beyond 27 mm. Therefore, the sub-SRVE based on void length distribution was determined to be 27 mm in width and 6.1 mm in length. Figure 2.7 shows the normalized frequency of voids in length range of 0 to 9.2 mm in the sub-SRVE and total examined volume from experiment and fitted statistical distribution function. 99% of the voids has void length smaller than 1 mm. The sub-SRVE based on void length (27 mm  $\times$  6.1 mm  $\times$  0.18 mm) is found to be slightly larger than that from void content (but still less than the maximum inspection volume).

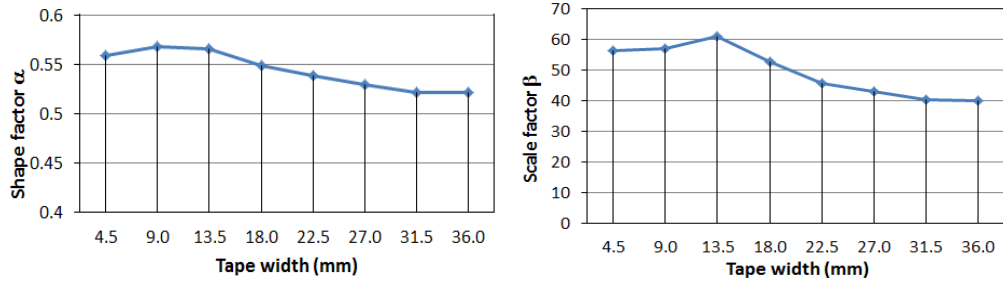


(a)



(b)

Figure 2.6 Fitting parameters of 3-parameter Weibull distribution for void length distribution along sample length direction. (a) Shape factor and (b) scale factor.



(a)

(b)

Figure 2.7 Fitting parameters of 3-parameter Weibull distribution for void length along sample width direction with sub-SRVE length of 6.1 mm. (a) Shape factor and (b) scale factor.

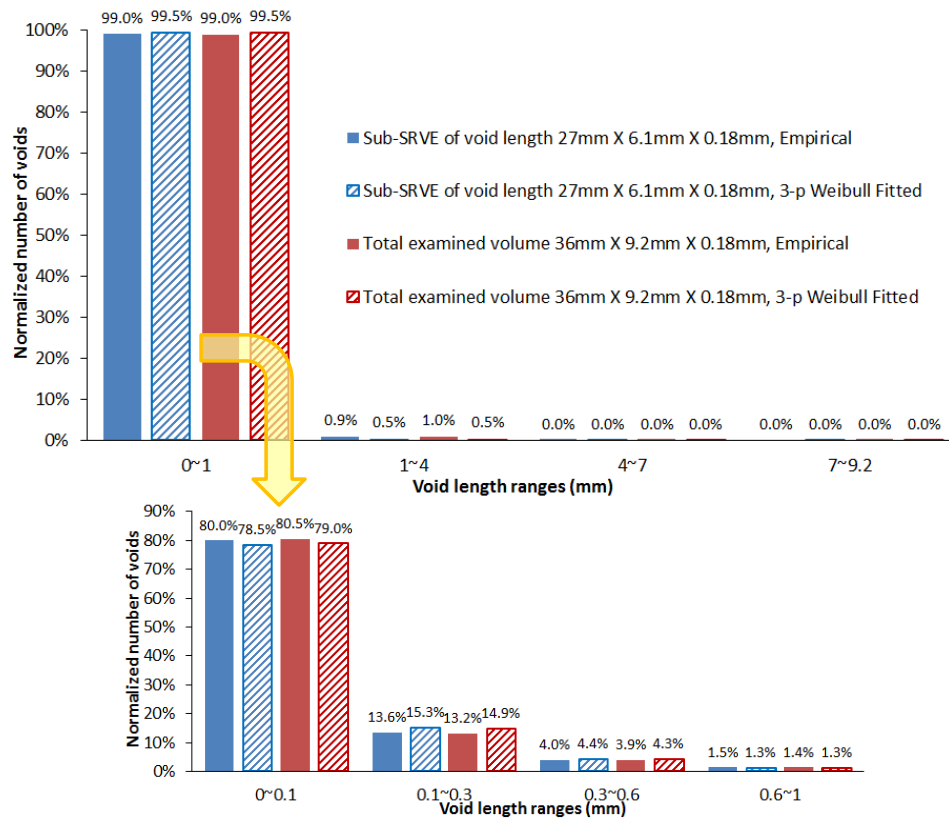


Figure 2.8 Normalized frequency distribution of void length in the sub-SRVE of void length and total examined volume.

### 2.2.6.3 Equivalent Diameter of voids

3-Parameter Gamma function provides the best fit to the void equivalent diameter distribution as seen in Figure 2.8 with the probability density function:

$$f(d) = \frac{(d-\mu)^{\alpha-1} e^{-\left(\frac{d-\mu}{\beta}\right)}}{\beta^{\alpha} \Gamma(\alpha)} \quad (2.3)$$

Where  $d$  is the equivalent diameter of voids,  $\alpha$ ,  $\beta$ , and  $\mu$  are the shape, scale, threshold factors of 3-parameter Gamma distribution, respectively.

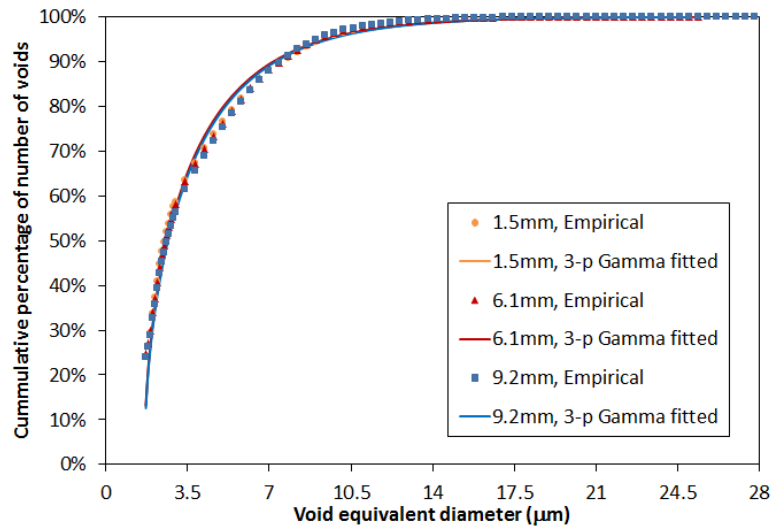
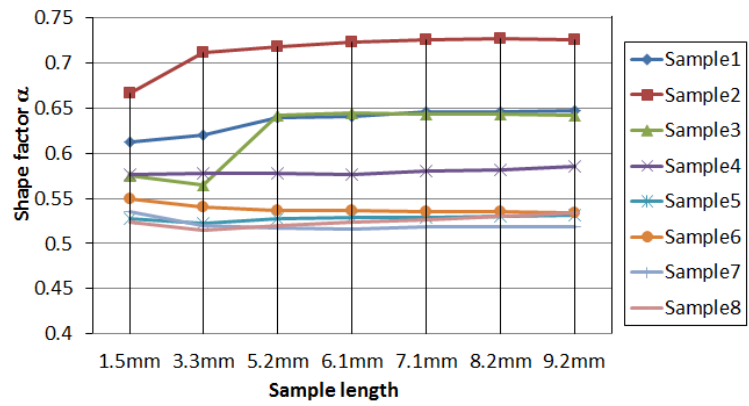


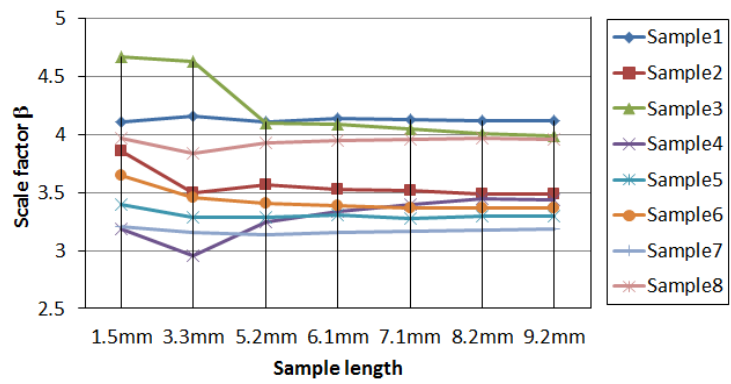
Figure 2.9 Empirical and fitted normalized cumulative distributions of voids in different void equivalent diameters in a tape sample of 4.5 mm wide with varying length.

The threshold was found to be 1.63 μm for all distributions, and the other two parameters versus sample length are shown in Figure 2.9. The shape and scale factors are stationary when sample length is longer than 6.1 mm which is defined as the sub-SRVE length for void diameter. The fitting parameters with increasing tape width

were plotted in Figure 2.10 with sample length of 6.1 mm, and the SRVE width of 27 mm was determined. The normalized number of voids in different void equivalent diameter ranges of sub-SRVE in Figure 2.11 shows that about 90% of voids have equivalent diameter smaller than the fiber diameter (7  $\mu\text{m}$ ) and less than 1% are greater than 2 times of fiber diameters. The sub-SRVE based on void equivalent diameter is the same as that from void length (i.e. 27 mm  $\times$  6.1 mm  $\times$  0.18 mm).



(a)



(b)

Figure 2.10 Fitting parameters of 3-parameter Gamma distribution for void equivalent diameter distribution along sample length direction. (a) Shape factor and (b) scale factor.

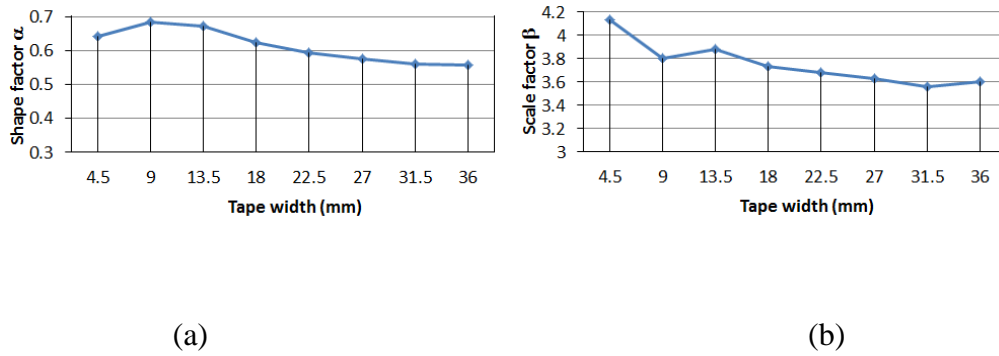


Figure 2.11 Fitting parameters of 3-parameter Gamma distribution for void equivalent diameter along sample width direction with sub-SRVE length of 6.1 mm. (a) Shape factor and (b) scale factor.

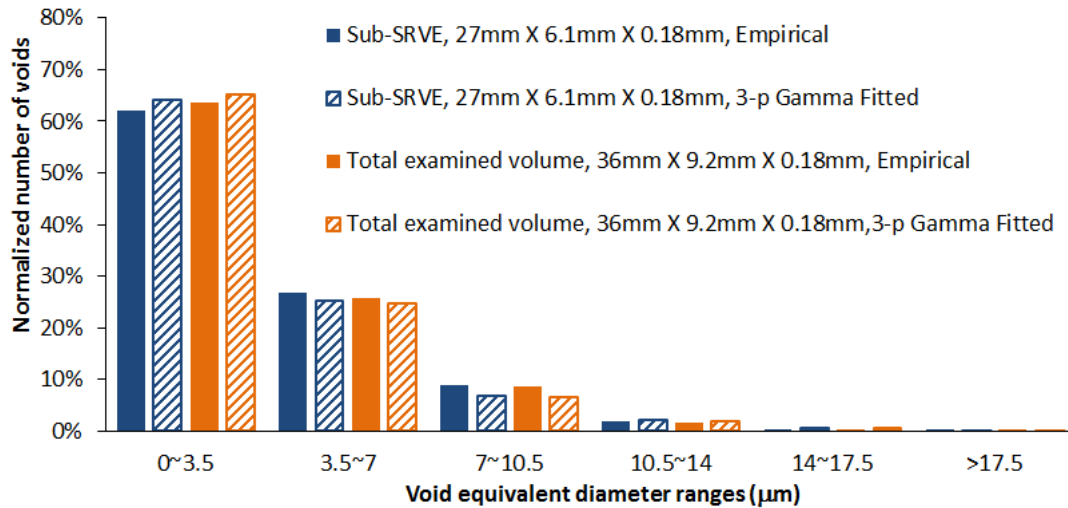


Figure 2.12 Normalized numbers of voids in equivalent diameters ranges in prepreg tape.

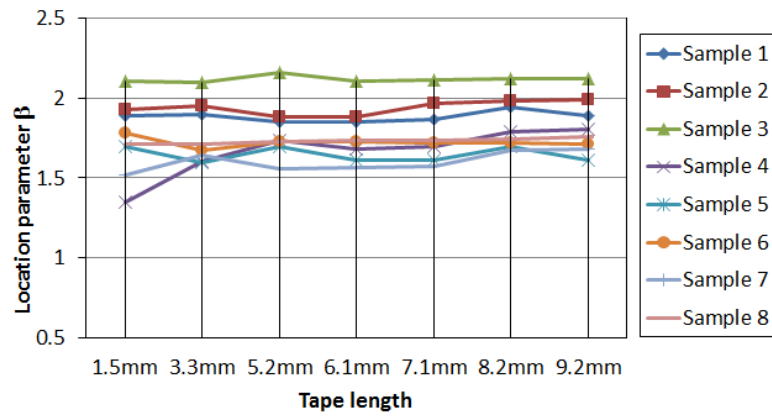
#### 2.2.6.4 Void Aspect Ratio

After analyzing the number distribution of void aspect ratio (length divided by equivalent diameters of voids), 3-parameter lognormal distribution function was found to be the best fit with the probability density function given by:

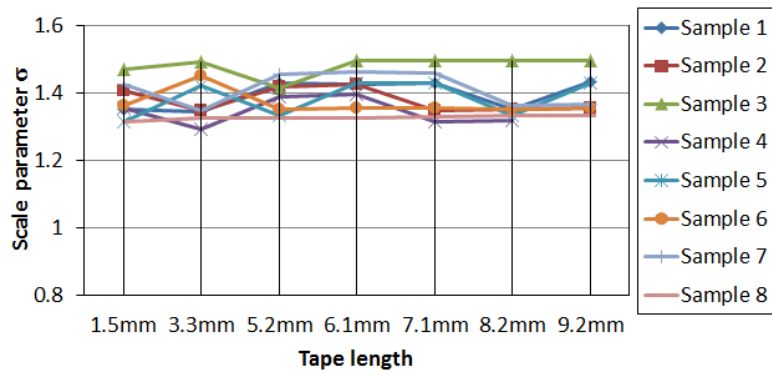
$$f(x) = \frac{1}{\sqrt{2\pi}\sigma(x-\mu)} \text{Exp}\left(-\frac{(\ln(x-\mu)-\beta)^2}{2\sigma^2}\right) \quad (2.4)$$

Where  $x$  is the aspect ratio of voids,  $\sigma$ ,  $\beta$ , and  $\mu$  are the scale, location, threshold parameters, respectively.

The threshold parameters were found to be 1.24; the scale and location parameters were presented in Figure 2.12. It is seen that the location parameter tends to be stable when sample length is larger than 5.2 mm for all samples, and the scale factors fluctuates within a very small range ( $<0.1$ ) for each sample. Therefore, the sub-SRVE length of void aspect ratio was determined to be 5.2 mm. With this sample length, the location factor and scale factor with increasing tape width was presented in Figure 2.13, where the sub-SRVE width of 22.5 mm was determined. The normalized frequency distribution of void aspect ratio of the sub-SRVE is shown in Figure 2.14. The results show that 80% of the voids have aspect ratios in the 2-50 range with approximately 4% having aspect ratios greater than 50. In addition, approximately 6.5% of the voids have an aspect ratio of 1-2 which is commonly assumed from optical 2D images.



(a)



(b)

Figure 2.13 Fitting parameters of 3-parameter lognormal distribution for void aspect ratio distribution along sample length direction. (a) Location factor and (b) scale factor.

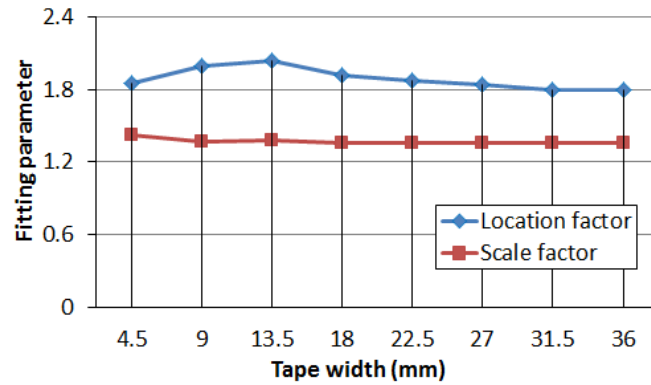


Figure 2.14 Location and scale factors of 3-parameter lognormal distribution for void aspect ratio along sample width direction with sub-SRVE length of 5.2 mm.

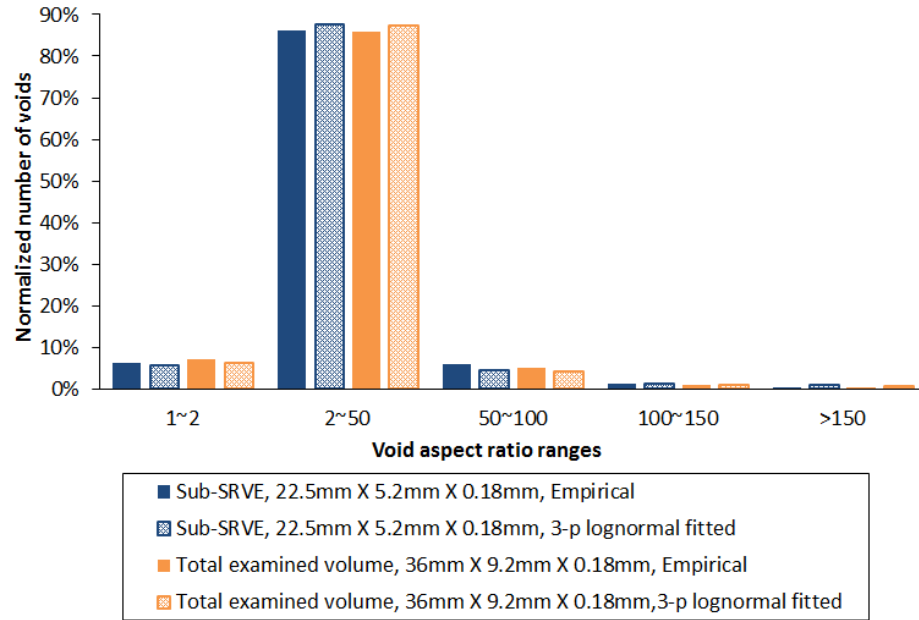


Figure 2.15 Normalized numbers of voids in aspect ratio ranges in prepreg tape.

### 2.2.6.5 Sub-SRVEs and the SRVE

Based on the above analysis, sub-SRVEs, and fitting parameters of distribution functions are summarized in Table 2.3. Taking the largest dimensions of the sub-

SRVEs, the SRVE of the AS4/APC2 tape is 6.1 mm along the fiber direction and 27 mm along the transverse direction of the full thickness of the tape.

Table 2.3 Sub-SRVEs for void properties with corresponding fitting parameters of distribution functions.

Void property	Sub-SRVE		Feature value or distribution			
	Length (mm)	Width (mm)	Value /distribution	Fitting parameters		
				Shape /Location	Scale	Threshold
Content	5.3	27	4.70%	--		
Length	6.1	27	3-p Weibull	0.53	43.18	2.93
Equivalent diameter	6.1	27	3-p Gamma	0.57	3.63	1.63
Aspect ratio	5.2	22.5	3-p lognormal	1.87	1.35	1.24

From the above statistical void study, not only the void properties but also the void features revealed provide important information for the investigation for void consolidation mechanisms. From the distribution of void aspect ratio, it is seen that only a small fraction of the voids are near spherical in shape (only 6.5% number of voids have aspect ratio smaller than 2). The majority of voids (90%) have aspect ratios between 2-150. In the case of large aspect ratio, gradients in the fiber direction can be ignored and 2D simulation of void dynamics such as the resin infusion model by Simacek et al.[46] are more realistic. In this 2D model, to obtain the 2D void content, one should examine at least 27 mm across the fiber direction, which should be slightly higher than the 3D void content 4.7% due to the limited length of voids along the fiber direction.

### **2.3 Characterization of Tape Surface**

In this section, the surface roughness of the raw prepreg tape is characterized. A SRVE for tape surface roughness is determined. The common surface roughness parameters such as arithmetic mean roughness  $R_a$ , root mean square roughness  $R_q$ , and cross point average  $R_z$  are obtained. (Definitions shown in Appendix C)

#### **2.3.1 Experimental procedure**

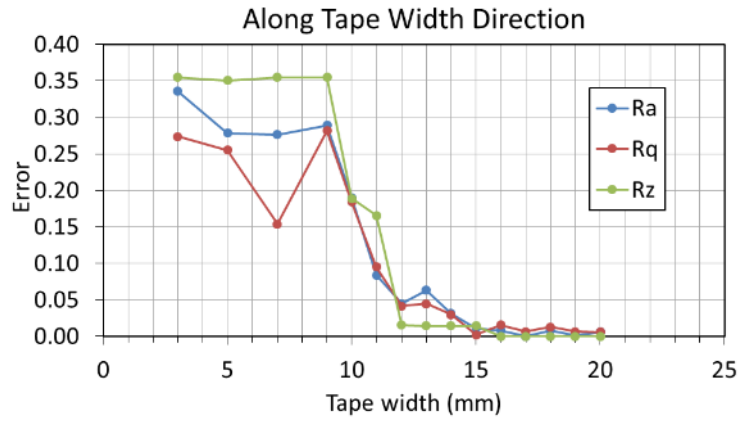
Keyence VK-X200 3D color laser scanning microscope was used for the tape surface characterization. After comparing the surface roughness from 6 scanning settings (Appendix C), a magnification of 200 with the x-y in-plane resolution of 2.77  $\mu\text{m}/\text{pixel}$  and z resolution of 0.1 nm was selected. Large tape sample of 21 mm (width)  $\times$  7 mm (length) from the center region of the tape was examined executively. The laser intensity images containing surface height information are then stitched together automatically through the Keyence analysis software.  $R_a$ ,  $R_q$ , and  $R_z$  are the surface parameters that used to represent the roughness level of the tape, and to determine the SRVE of the tape surface.

#### **2.3.2 Determination of SRVE of Tape Surface**

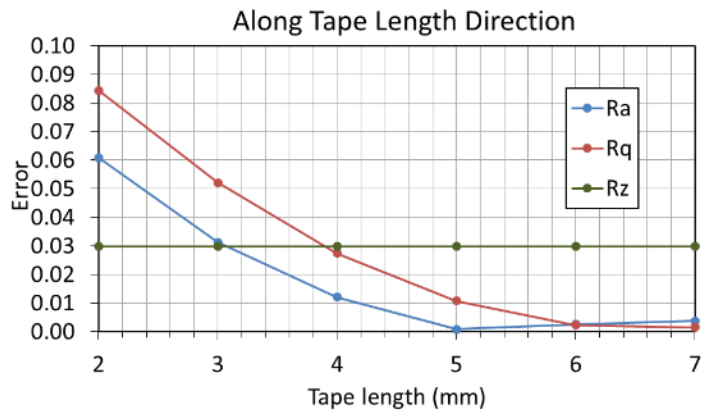
Similarly as determining the sub-SRVE of 3D void content in Section 2.2.6.1, the SRVE width and length of tape surface is based on the 5% deviation from the surface parameters ( $R_a$ ,  $R_q$ , and  $R_z$ ) of the large sample. Therefore equation 2.1 is also used here.  $v$  in this case is the result of a roughness parameter of sample size of 21 mm (width)  $\times$  7 mm (length).  $m$  is the result of the same roughness parameter from increasing sample width or increasing length. The SRVE width is firstly determined from increasing sample width up to 21 mm with tape length of 1 mm. Then, with the

determined SRVE width, surface parameters were examined with increasing tape length up to 7 mm.

The errors of Ra, Rq, and Rz with increasing sample length and width are presented in Figure 2.15. It is seen that when tape width is larger than 14mm and length larger than 3mm, all surface roughness parameters have error smaller than 5% compared to those from the largest sample size. Therefore, the SRVE of the tape surface is determined to be 14 mm (width) ×3 mm (length). And the Ra, Rq and Rz values for the prepreg tape is 14.3  $\mu\text{m}$ , 18.7  $\mu\text{m}$  and 116.3  $\mu\text{m}$  respectively. The 3D display of the tape surface is shown in Figure 2.16. It is clearly seen that the roughness along the tape width direction is much more significant than along the fiber length direction.



(a)



(b)

Figure 2.16 Error of surface parameters along (a) tape width and (b) length direction

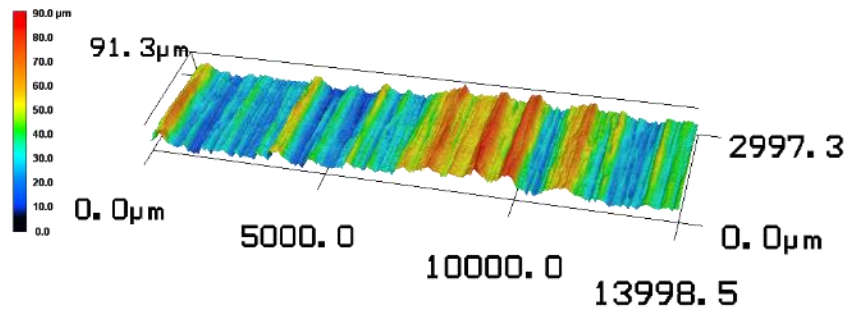


Figure 2.17 3D display of AS4/APC2 prepreg tape surface with tape width of 13975.8  $\mu\text{m}$  and length of 2997.25  $\mu\text{m}$

## 2.4 Summary

The void microstructure of the AS4/APC2 thermoplastic prepreg material was studied through high resolution 3D X-ray  $\mu$ -CT and statistical analysis. It is found that voids are rod-link in geometry and with the major axis aligning along the fiber direction. After scanning a large volume of tape, representative 3D void content was obtained. Suitable statistical distribution functions were found to describe the void length, equivalent diameter and aspect ratio distributions and sub-SRVE for each void property were determined. . From the statistical study, 99% number of voids has length smaller than 1 mm which is way smaller than the reasonable in-plane dimension of a thermoplastic composite part. Therefore, all the voids are sealed in the prepreg, and do not form porous pathways along the fiber direction. The majority of voids have aspect ratio of 2 to 150, and the use of spherical void model for void dynamics is not appropriate to the voids in this prepreg tape. The SRVE of AS4/APC2 tape is 6.1 mm in length, 27 mm in width and the full prepreg thickness (0.18 mm). Surface of the prepreg tape was also characterized. An SRVE of 14 mm in width by 3 mm in length is determined based on the surface roughness parameters. The roughness along the tape width direction is significantly higher than from the length direction.

With the rough surfaces, interlayer free space can be formed when two prepreg layers were stacked.

The study of the micro voids and the surface roughness reveals important features of microstructure of prepreg tape, and can guide the investigation of void consolidation mechanisms. The conclusions of the micro void properties may not be applied to other thermoplastic prepreg tape. However, the methodology for analyzing voids and relating the results to the void dynamics during the processing can be widely adopted.

## Chapter 3

### INTERLAYER AIR PERMEABILITY OF THERMOPLASTIC PREPREG STACKS

#### 3.1 Introduction

Most thermoplastic prepreg materials are rigid at room temperature and have rough surfaces as introduced in Chapter 1. When two prepreg layers are placed together, permeable interlayer regions may form as shown in Figure 3.1. The knowledge of the permeability of the interlayer region is lack. Since the interlayer region is configured by the two contact layers, different stacking orientations may form interlayer with different permeability levels. During the manufacturing process of thermoplastic composites, the resins get softened when the temperature is increased above their glass transition temperature and/or melting temperature. The interlayer gaps can be gradually closed and the permeability is reduced as the intimate contact between layers develops. How the permeability change during the consolidation cycles may also affect the void consolidation. In this chapter, the interlayer permeability of a wide range of interlayer configurations including unidirectional and off-axis stacking was measured before processing. Prepreg layers with different stacking orientation are also vacuum bag processed under different temperature conditions. The permeability of OVB processed interlayers is measured and the evolution of permeability during thermal processing is quantified and correlated to the changes in surface roughness.

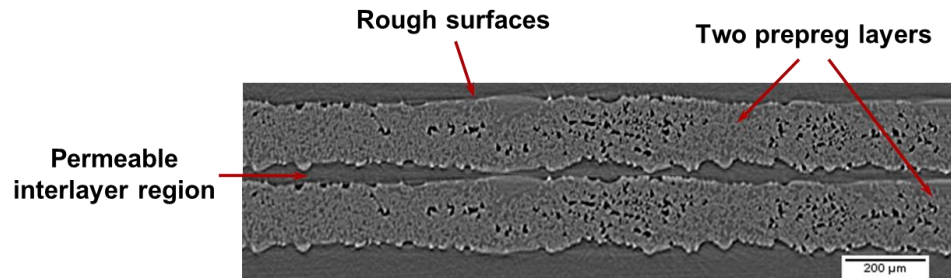


Figure 3.1 Schematic of permeable interlayer region formed between two prepreg layers

### 3.2 Test Set-up for In-plane Air Permeability Measurements

Darcy's law has been used to describe the fluid flow through fiber reinforced composites and is utilized to measure the air permeability of porous reinforcing materials used in composite processes. [54–56,78] In this study, a test set-up based on 1-D Darcy's flow was established and is shown in Figure 3.2. A stack of prepreg layers (room temperature or after OVB processing) is studied and placed on a tool with top and bottom surfaces sealed with vacuum grease to minimize surface air flow paths. In addition, the two prepreg edges parallel to the air flow direction are sealed using tacky tape to eliminating edge air flow paths (i.e. race-tracking). One end is connected to the vacuum pump and the other end to a flow meter (range: 0-10 liter/min) which measures the total flow rate through interlayer regions. Vacuum values are measured with a pressure gauge and are always below 10 kPa which is considered to be full vacuum in the processing. Therefore, pressure gradient of 1atm is used in the derivation of the permeability.

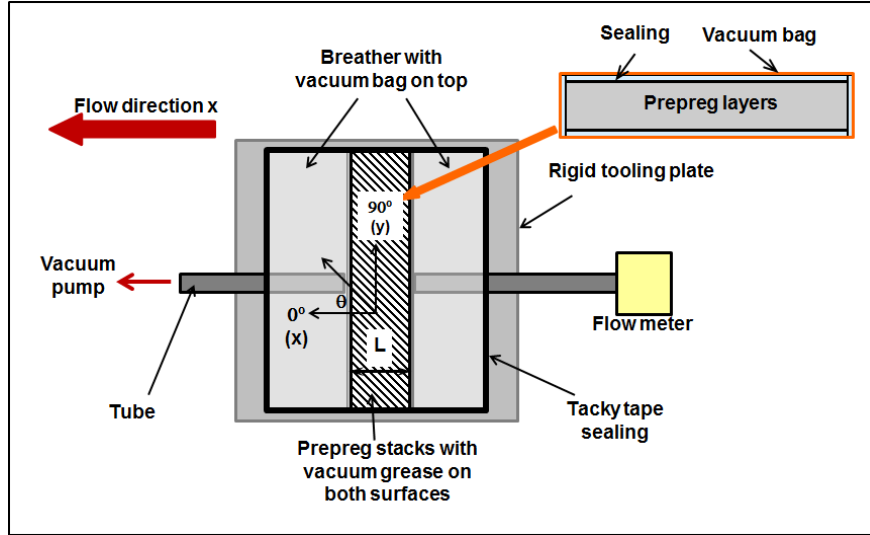


Figure 3.2 Top view of experimental set-up of air permeability test

Formed by the anisotropic unidirectional prepreg tapes, the interlayer region also possess anisotropic permeability which can be expressed by a 2D matrix in x-y coordinate (x is along the flow direction as in Figure 3.2):

$$K^{xy} = \begin{bmatrix} K_{xx} & K_{xy} \\ K_{xy} & K_{yy} \end{bmatrix} \quad (3.1)$$

With a rectangular sample, the measured permeability in 1D flow set-up depends largely on the width (W, transverse to the flow) to the length (L, along the flow) ratio.[79] The larger the W/L ratio, the local pressure gradient will be more parallel to the x axis, the measured permeability is more close to  $K_{xx}$ . In order to obtain measured permeability almost equals to  $K_{xx}$  for all angle, W of 300mm and L of 50mm (W/L ratio =6) were selected. The measured permeability may have a maximum difference of 10.5% from  $K_{xx}$  when tape fiber direction is 45° to the x axis. [79,80] This dimension also ensures that the sample size is significantly larger than the representative volume element size of the prepreg in terms of surface roughness and

internal void content determined in Chapter 2. In order to improve the reliability and the reproducibility of the test results, each sample consists of four layers of prepreg tapes forming three identical interlayer regions, producing flow rate within the measurable range of the flow meter and allowing averaging of the permeability over three layers in a single test. A high permeable breather cloth is interleaved at the prepreg edge to eliminate any pinch off points and also ensures uniform one dimensional flow conditions from the vacuum and vent ports.

The sample is bagged and placed in a mechanical testing machine (Instron 5567). Firstly, compressive load is applied on a rigid load distributor on top of the sample before opening the vacuum valve. The load head stopped when the load reaches 1570N which provides 1atm pressure as in OVB processing. The head displacement is fixed through the experiment to ensure the contact level and geometry between two layers is the same as in OVB processing. Vacuum is then applied at one side of the sample with a pressure gauge, and the flow rate is recorded at the other side open to the atmosphere. The permeability is calculated and averaged from the three interlayer regions. Three test specimens are evaluated for each room-temperature test while all measurements of higher temperature cycles are single specimen tests. Room-temperature specimen permeability is very repeatable with standard deviations of less than 10%.

The measured total flow rate  $Q_T$  for three identical interlayer regions ( $Q$  for each interlayer) based on Darcy's Law is given by:

$$Q_T = 3Q = -3 \frac{K h W}{\mu} \frac{dP}{dx} \quad (3.2)$$

Where  $K$  is the in-plane Darcy permeability of the interlayer regions;  $h$  is the effective height of the interlayer region;  $W$  is the sample width (300 mm transverse to

the flow direction);  $P$  is the pressure at location  $x$ ; and  $\mu$  is the air viscosity, (1.82E-5 Pa.s).

For gas flow in porous media, Klinkenberg effect as the slippage of the gas molecule when flowing through tight pores compared to the mean free path of the gas molecule. [81–83] Under the room temperature and atmosphere pressure, the mean free path of air is 68 nm, and the interlayer gaps of the thermoplastic prepreg could have diameters in tens of microns as in Figure 3.1 (fiber diameter is 7  $\mu\text{m}$ ). For some interlayer configurations, the interlayer gap size may be small. However, because the set-up for permeability measurement is close to the condition in vacuum bag processing condition, the measured permeability values are the effective permeability that includes the possible Klinkenberg effect already. Therefore, the Klinkenberg parameter is not included in the derivation of the permeability.

Since the surfaces of the prepreg are very rough, and statistical in nature (with large fractal dimension of 1.6 [84]), the effective gap height  $h$  can be very difficult to define explicitly. Therefore, we use the permeability thickness product  $Kh$  (unit of  $\text{m}^3$ ) to represent the permeability of the interlayer regions, which has been used in reservoir engineering to describe the drainage problem related to removal of oil and gas.[85,86] Considering the compressibility of air as developed in Ref. [78], the derivations of  $Kh$  from measured flow rate is as follows. The problem can be schematically demonstrated in Figure 3.3. At location X0, specimen is connected to the flow meter open to atmosphere. At location X1, specimen is connected to a vacuum pump. Flow rate through one interlayer region follows:

$$Q_x = -\frac{Kh*W}{\mu} \frac{dP}{dx} = \frac{nRT}{P} \quad (3.3)$$

Where  $\dot{n}$  is the rate of number of air molecules changing,  $R$  is gas constant. Local pressure  $P$  is varying along  $x$ . Integrate both side of the right part of the equation above,

$$\int_{P_1}^{P_0} P dP = -\frac{\dot{n}RT}{KhW} \int_{x_1}^{x_0} dx \quad (3.4)$$

$$\dot{n}RT = \frac{KhW(P_0^2 - P_1^2)}{2\mu L} \quad (3.5)$$

Since the air pressure at the location where flow rate  $Q$  is monitored is  $Patm$ ,

$$Q = \frac{\dot{n}RT}{Patm} \quad (3.6)$$

Inserting Equation 3.5 to Equation 3.6, with  $P_0 = Patm$  and  $P_1 = 0$  from Figure 3.3, We obtain

$$Q = \frac{KhW(P_0^2 - P_1^2)}{2\mu L Patm} = \frac{KhW Patm}{2\mu L} \quad (3.7)$$

Since the flow rate measured is from three identical interlayer regions, the permeability thickness product of each interlayer region can be calculated through:

$$Kh = \frac{2}{3} \frac{Q_T \mu L}{W Patm} \quad (3.8)$$

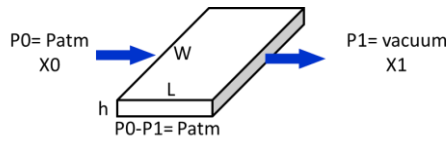


Figure 3.3 schematic of 1D Darcy's flow through the prepreg stacks

### 3.3 Stacking Orientation Dependence of Interlayer Permeability before Processing

Based on the Darcy's Law, permeability is a second order tensor. For any interlayer configuration with an included angle  $\omega$  between layers, the permeability

tensor follows the 2D rotational transformation matrix. Therefore, the permeability thickness products follow:

$$Kh^{xy} = \begin{bmatrix} Kh_{xx} & Kh_{xy} \\ Kh_{xy} & Kh_{yy} \end{bmatrix} = R \begin{bmatrix} Kh_{11} & 0 \\ 0 & Kh_{22} \end{bmatrix} R^{-1} \quad (3.9)$$

$$R = \begin{bmatrix} \cos \alpha & -\sin \alpha \\ \sin \alpha & \cos \alpha \end{bmatrix} \quad (3.10)$$

Where  $\alpha$  ( $0^\circ \leq \alpha \leq 90^\circ$ ) is the angle between the current x-y coordinate to the principal 1-2 coordinate (note that in the general case this angle is different than the angle  $\theta$  used to define the fiber orientation with respect to the flow direction (x)).

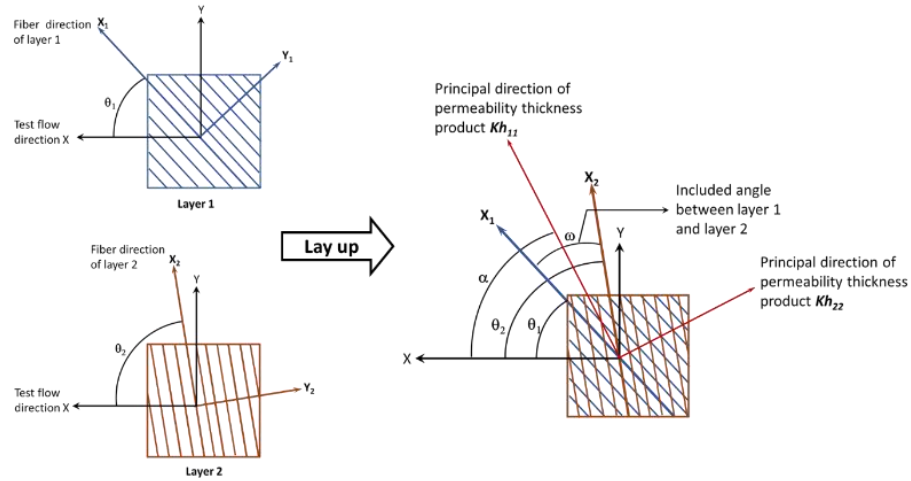


Figure 3.4 The coordinates and angles for the measurements of interlayer permeability of an arbitrary lay-up  $\theta_1/\theta_2$

The angles used in our study are defined in Figure 3.4 for an arbitrary lay-up comprised of two layers.  $\theta_1$  and  $\theta_2$  define the fiber orientation of layers 1 and 2 with respect to the flow direction (x). The included angle  $\omega$  between layer 1 and layer 2 equals  $|\theta_2 - \theta_1|$ . Lay-ups that have the same included angle can be described by a single

set of principal permeability thickness products (See Table 3.1 and 3.2).  $\alpha$  defines the angle between the direction of the principal permeability thickness product  $Kh_{11}$  and the flow direction. In order to study the interlayer permeability of various stacking orientations, lay-ups having the same included angle  $\omega$  are defined as shown in Table 3.1. In addition, Table 3.1 also defines the orientation ( $\theta$ ) of the layer fiber directions with respect to the flow direction (x) of the samples that are tested at room temperature in the test set-up (see Figure 4).  $\theta=0^\circ$  is oriented along the tested flow direction (x direction in Figure 4).

Table 3.1 Stacking orientation configurations for the measurements of interlayer permeability of raw tapes

Included angle $\omega$	Layer orientations to the test flow direction
$0^\circ$	$0^\circ/0^\circ, 15^\circ/15^\circ, 30^\circ/30^\circ, 45^\circ/45^\circ, 60^\circ/60^\circ, 75^\circ/75^\circ, 90^\circ/90^\circ$
$15^\circ$	$0^\circ/15^\circ, 75^\circ/90^\circ$
$30^\circ$	$0^\circ/30^\circ, 60^\circ/90^\circ, \pm 15^\circ, \pm 75^\circ$
$45^\circ$	$0^\circ/45^\circ, 45^\circ/90^\circ$
$60^\circ$	$0^\circ/60^\circ, 30^\circ/90^\circ, \pm 30^\circ, \pm 60^\circ$
$75^\circ$	$0^\circ/75^\circ, 75^\circ/90^\circ$
$90^\circ$	$0^\circ/90^\circ$ (same as $90^\circ/0^\circ$ ), $\pm 45^\circ$

The permeability thickness product measurements of all lay-up configurations along the flow direction  $Kh_{xx}$  are presented in Table 3.2. It is seen that the standard deviations for all interlayer configurations are below 10% and highest in the  $90^\circ/90^\circ$  case. For interlayer configurations with included angle  $\omega$  having a minimum of three  $Kh_{xx}$  measurements, it is possible to determine the corresponding principal permeability thickness products ( $Kh_{11}$  and  $Kh_{22}$ ) and the angle ( $\alpha$ ) for each lay-up using Equation 3.9 and 3.10. Therefore, for  $\omega$  of  $0^\circ, 30^\circ, 60^\circ$  and  $90^\circ$ , the  $Kh_{11}$  and

$Kh_{22}$  and the lay-ups with principal 1 direction aligning the tested flow direction are obtained and presented in Table 3.3.

Table 3.2 Results of Permeability thickness products for all measured lay-up configurations (each is tested with 3 specimens containing 3 identical interlayers)

Included angle $\omega$	Lay-up	$Kh_{xx}$ (m <sup>3</sup> )	CV (%)
0°	0°/0°	3.51E-15	3.6
	15°/15°	3.22E-15	2.1
	30°/30°	2.74E-15	0.7
	45°/45°	1.72E-15	4.7
	60°/60°	1.14E-15	8.1
	75°/75°	6.01E-16	7.3
	90°/90°	3.04E-16	9.7
15°	0°/15°	3.83E-15	5.0
	75°/90°	5.73E-16	7.6
30°	0°/30°,	3.46E-15	2.2
	60°/90°	1.10E-15	8.2
	±15°	3.54E-15	3.3
	±75°	1.01E-15	7.0
45°	0°/45°	3.24E-15	3.1
	45°/90°	1.73E-15	2.1
60°	0°/60°	3.10E-15	3.2
	30°/90°	2.42E-15	4.1
	±30°	3.29E-15	5.0
	±60°	2.10E-15	4.9
75°	0°/75°	3.05E-15	2.8
	15°/90°	2.85E-15	4.2
90°	0°/90°(same as 90°/0°)	2.98E-15	2.2
	±45°	2.89E-15	4.3

CV: coefficient of variation from 3 specimens.

Table 3.3 Principal permeability thickness products for interlayer included angle of 0°, 30°, 60°, and 90°

Included angle $\omega$	$Kh_{11}$ (m3)	$Kh_{22}$ (m3)	Lay-up with principal direction of $Kh_{11}$ along x axis
0°	3.51E-15	3.04E-16	0°/0°
30°	3.58E-15	9.71E-16	±15°
60°	3.29E-15	2.10E-15	±30°
90°	2.98E-15	2.98E-15	±45° or 0°/90°

From Table 3.3, it is seen that the principal 1 directions for  $\omega = 0^\circ, 30^\circ$  and  $60^\circ$  are all along the central line of the included angle. For  $\omega = 90^\circ$ ,  $Kh_{11}$  and  $Kh_{22}$  are the same due to symmetry. And the calculation from Equation 3.8 and 3.9 shows that  $Kh_{xx}$  and  $Kh_{yy}$  are always the same and equal to the principal  $Kh$ , and  $Kh_{xy} = 0$  in this case. Therefore, the interlayer permeability for the interlayer configuration with the fiber orientations of two layers perpendicular to each other is isotropic.

With the corresponding  $Kh_{11}$  and  $Kh_{22}$ , the 2D permeability thickness product tensor of any included angle configuration can be obtained through Equation 3.8 and 3.9. For example, the three components of  $Kh^{xy}$  for  $\omega$  of  $0^\circ$  and  $60^\circ$  are calculated and presented in Figure 3.5 and Figure 3.6. The predicted values are compared with experimentally measured  $Kh_{xx}$ . It is seen that the predicted results agree very well with the measurements for  $\omega$  equal to  $0^\circ$  and  $60^\circ$ . This comparison validates that the principal permeability thickness products and principal coordinates for an interlayer configuration with included angle  $\omega$  can be accurately determined through measurements from a minimum of three coordinate angles for this interlayer configuration. It also proves that the entire  $Kh^{xy}$  tensor for an interlayer configuration with angle  $\omega$  can be predicted accurately through the rotation transformation matrix (i.e. Equations 3.9 and 3.10).

From Figure 3.5, it is also seen that the interface with both layers oriented along the measured flow direction ( $0^\circ/0^\circ$ ) has the highest permeability. When both layers are rotated away from the flow direction, permeability decreases monotonically with the increase of  $\theta$ , and are about an order of magnitude smaller when both layers are perpendicular to the flow direction ( $90^\circ/90^\circ$ ).

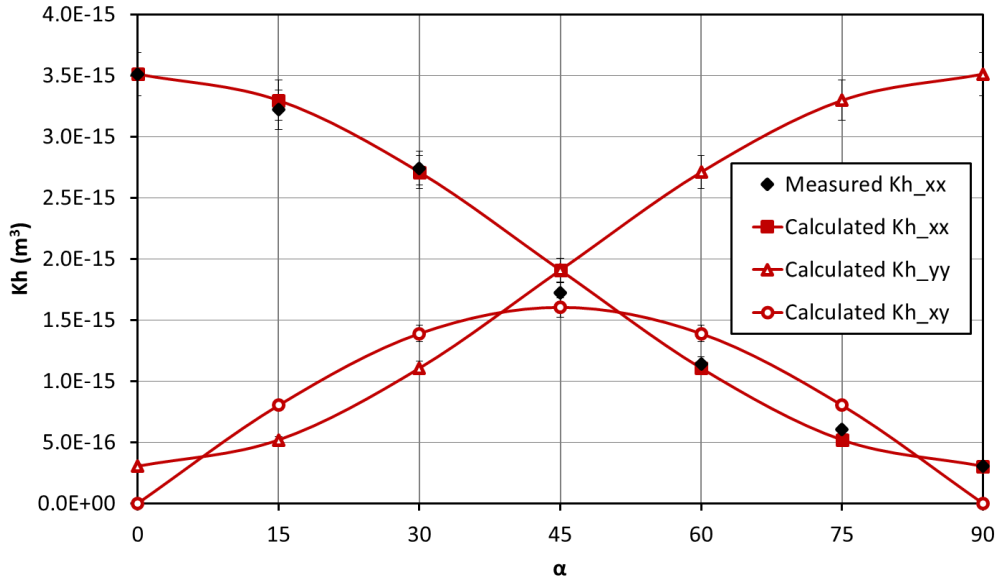


Figure 3.5  $Kh^{xy}$  for  $\omega = 0^\circ$ . Predicted  $Kh_{xx}$  is in excellent agreement with measured  $Kh_{xx}$  values for the  $\theta/\theta$  interlayers ( $\theta = \alpha$  in this case)

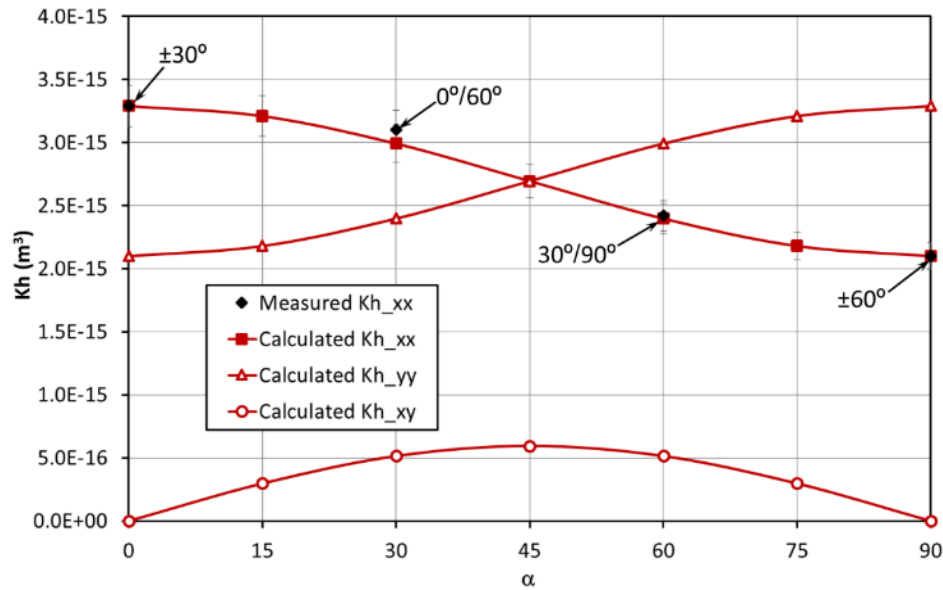


Figure 3.6  $Kh^{xy}$  for  $\omega = 60^\circ$ . Predicted  $Kh_{xx}$  is in excellent agreement with measured  $Kh_{xx}$  values for interlayers listed in Table 3.1.

It is also interesting to compare the experimental measurements of permeability in the flow direction to one another. In Figure 3.7, the results for interlayers having at least one layer with the fiber orientation in the flow direction is presented. Specifically we are plotting  $Kh_{xx}$  of interlayers of  $0^\circ/\theta$  (with different  $\omega$ ). Interestingly, as the fiber orientation of the other layer rotates away from the flow direction, the permeability shows a 10% increase at  $\theta=15^\circ$  before decreasing. This may be due to the nesting of layers with identical fiber orientation in each layer. As one layer is rotated off-axis to the  $0^\circ$  layer, the gaps in between the layers are slightly opened as nesting cannot occur, leading to the higher measured permeability. However, as the off-axis angle  $\theta$  in the second layer increases, the effective permeability reduces due to the surface roughness that resists air flow. It is also

noticed that the  $Kh_{xx}$  retains relatively high value at all  $\theta$  and changes are small (25% difference from the highest to the lowest) due to the higher permeability of the  $0^\circ$  layer that dominates in the flow direction. This will lead to primary air extraction in the  $0^\circ$  direction during OVB processing.

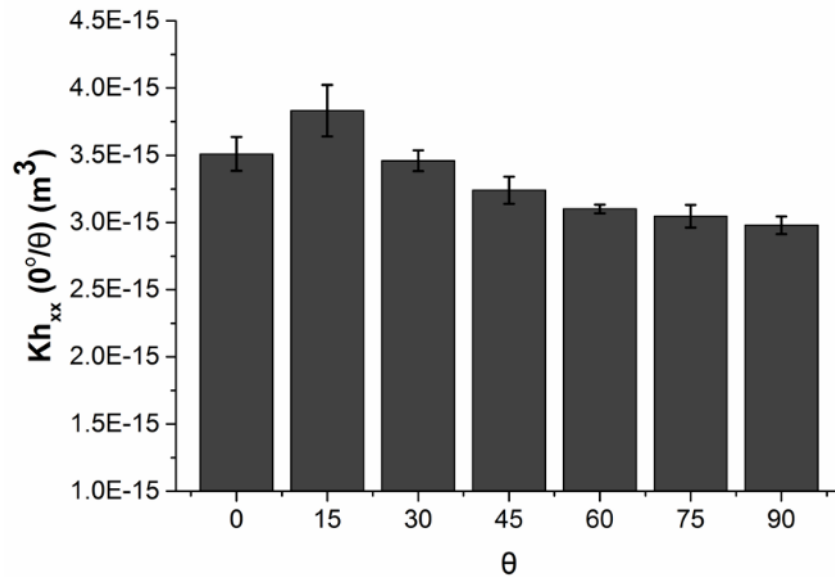


Figure 3.7 Results of permeability thickness products of  $0^\circ/\theta$  interlayers

In contrast, if one layer is fixed transverse to the measured flow direction (i.e.  $90^\circ$ ), the permeability in the flow direction becomes very sensitive to the orientation of the second layer. Figure 3.8 shows that the  $Kh_{xx}$  of  $\theta/90^\circ$  stacks decreases monotonically with increasing  $\theta$  with a minimum permeability for an all  $90^\circ$  fiber direction. Air extraction in this direction is the minimum.

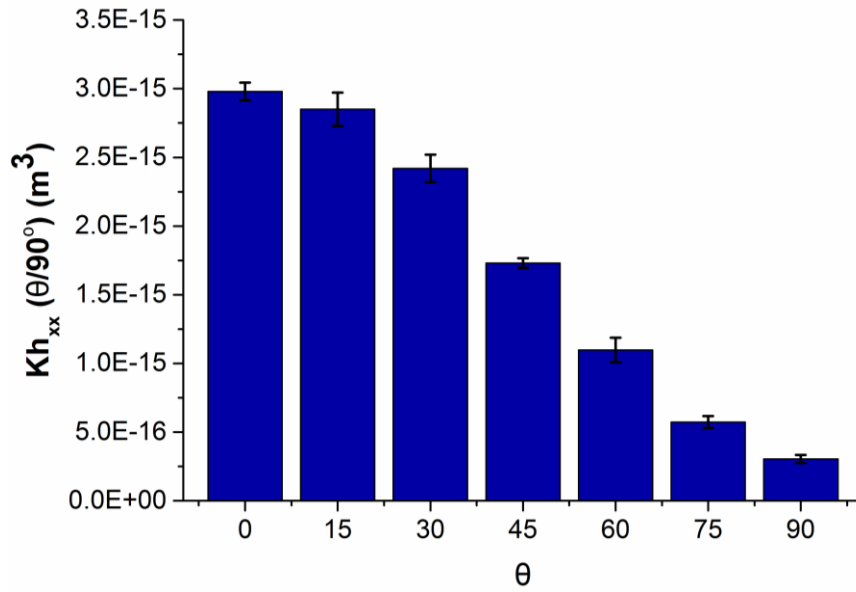


Figure 3.8 Results of permeability thickness products of  $\theta/90^\circ$  interlayers

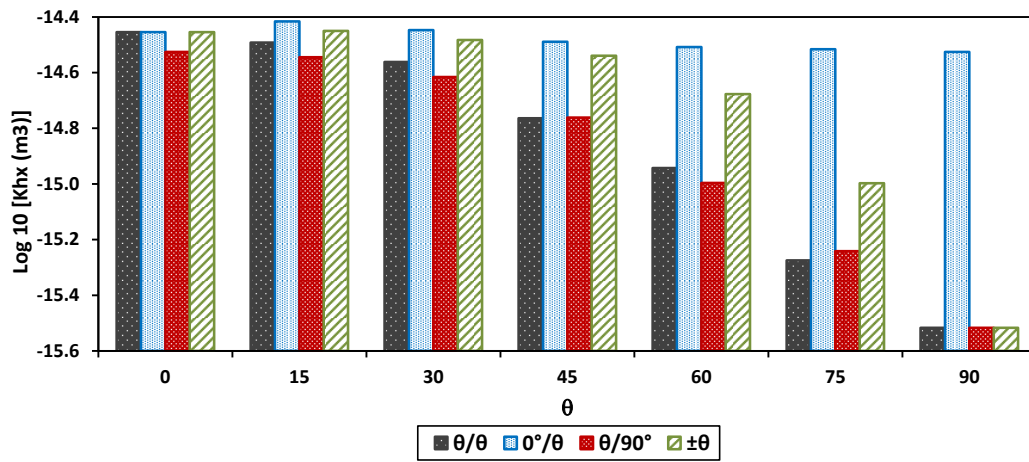


Figure 3.9 Comparison of the  $Kh_x$  results for  $\theta/\theta$ ,  $0^\circ/\theta$ ,  $\theta/90^\circ$  and  $\pm\theta$  interlayers at room temperature

The measured permeability thickness products for  $\theta/\theta$ ,  $0^\circ/\theta$ ,  $\theta/90^\circ$  and  $\pm\theta$  interlayers are compared and presented in Figure 3.9. On this log scale,  $\theta/\theta$ ,  $\theta/90^\circ$  and

$\pm\theta$  interlayers exhibit similar angular dependence and magnitude changes over the full range with a one order of magnitude reduction at  $90^\circ/90^\circ$ , with a more gradual reduction for  $\pm\theta$ . From an OVB processing perspective,  $\theta/\theta$  and  $\theta/90^\circ$  interlayers are essentially equivalent. High level of interlayer permeability in the flow direction is achieved when  $\theta$  is less than  $45^\circ$  (higher angles decrease permeability rapidly). The results for the  $0^\circ/\theta$  are interesting in that the permeability is at the highest level for all angles and is attributed to the fiber-fiber contact that are visualized in the surface images presented below.

If the interlayer height  $h$  is assumed to be  $50\ \mu\text{m}$  (see surface characterization section below), Darcy's permeability  $K$  of the interlayer regions is in the order of  $10^{-10}$  to  $10^{-12}\ \text{m}^2$ , which is higher than the permeability measured in some partially filled thermoset prepregs optimized for vacuum bag processing. [52–56,87,88] This comparison partially explains why OVB processing of thick section APC-2 laminates has been successful in achieving low void content [80]. The next section investigates the effects of processing on interlayer permeability retention.

### **3.4 Interlayer Permeability during Processing Cycles**

High performance thermoplastic prepreg materials with a resin such as poly(ether ether ketone) (PEEK) are solid in the glassy region below their glass transition ( $T_g$ ). As the temperature increases above  $T_g$ , the modulus of the thermoplastic resin decreases to a plateau level where the polymer exhibits viscoelastic response in its rubbery state. Above the melt temperature of PEEK, the resin exhibits viscous behavior, resulting in rapid loss of the interlayer permeability as material flow, and consolidation and full intimate contact develop between the prepreg layers. [11,89].

With the knowledge of this temperature dependent material behavior, it is possible to identify the process window for experiment investigation.

### **3.4.1 Phase Transitions of PEEK Resin in the Raw Tape during Processing**

Processing cycle may have a significant effect on the change of interface properties between two adjacent layers as the material consolidates due to the applied vacuum. PEEK resin has a glass transition temperature of 143 °C and melt temperature of 340 °C. [11,90] Dynamic mechanical analysis (DMA) tests are conducted in shear mode in the transverse direction of the raw prepreg tape, with temperature ramped up to 400 °C under 2.8 °C/min, and shear rate of 0.0005/s (low shear rate comparable to rate in OVB processing).

The storage modulus of the tape with increasing temperature is plotted in Figure 3.10. The resin dominated transverse shear modulus dropped significantly above the glass transition temperature, slightly increases at 160 °C due to crystallization, and then maintains a second plateau in the rubbery region prior to melting. The storage modulus is zero above the melting temperature of 340 °C where PEEK becomes a viscous fluid. (Note that the storage modulus here is significantly lower than literature reported for AS4/APC2 composite [91][92], which is mainly attributed to the voids in the prepreg and the prepreg layers were stacked layer by layer without consolidation during the test resulting higher thickness than consolidated laminates and affect the calculated modulus from measured force in DMA.) This storage modulus behavior shows that under low pressure (1atm), the deformation below T<sub>g</sub> can be ignored due to the high modulus. When the temperature is above resin melt point, the development of intimate contact can be within 2 mins under vacuum pressure at melt temperature result in rapid reduction of the interlayer

permeability [35]. Therefore, the temperature range of interest for air flow through the interlayer region is from the glass transition temperature to approximately 300 °C (i.e. end of the rubbery plateau and onset of melting). The interface properties (permeability and roughness) at room temperature (i.e. baseline), at 140 °C (slightly below the glass transition temperature) and 170°C, 240 °C, 300 °C, and dwell time ranging from 0 to 8 hrs at 240 °C are evaluated for the temperature and time dependent changes in the rubbery temperature region.

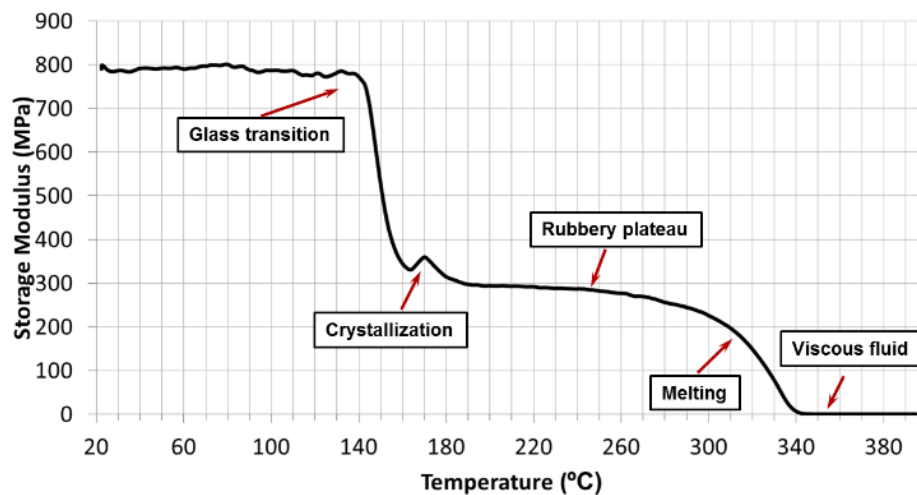


Figure 3.10 Plot of transverse storage modulus versus temperature of raw tape showing phase transitions and different stages of the resin

### 3.4.2 Effect of Processing Cycle on Interlayer Permeability

Interlayer permeability of 0°/0°, 0°/90°, 90°/90° during processing cycle were investigated. Based on the DMA results in Figure 3.10 showing different resin stages, samples were vacuum bagged and heated to the temperature of 140 °C, 170 °C, 240 °C, 300 °C with a rate of 2.8 °C/min in an oven, and then quenched with rate of 20

°C/min to room temperature. In order to investigate the effect of holding time on interlayer permeability in the rubbery state of resin, four sets of 0°/0°, 0°/90°, 90°/90° samples were also heated up to 240 °C with the same heating rate and then held for 10 min, 30 min, 1 hr and 8 hr. For each temperature and dwell cycles, one samples containing three identical interlayer regions for each interlayer configuration is measured. After the thermal cycles, each prepreg stack was tested for interlayer permeability.

#### **3.4.2.1 Effect of Temperature Ramp**

The air permeability during temperature ramp for 0°/0°, 0°/90°, and 90°/90° interlayers are presented in Figure 9. No significant reduction from room temperature measurements was found for the three interlayers permeabilities processed at 140 °C (T<sub>g</sub> for PEEK is 143 °C). Given the temperature dependent prepreg properties, this also implies no significant change would occur at lower temperatures under OVB processing.

Above T<sub>g</sub>, the permeability of 0°/0° and 90°/90° interlayer reduces monotonically with increasing temperature as shown in Figure 3.11 (a) and Figure 3.11 (b). At 300 °C, the permeability of 0°/0° decreases an order of magnitude compared to the raw tape at RT (or T<sub>g</sub>). The 90°/90° interlayer decreased to a lesser extent at 300 °C (i.e. 45%). In this temperature regime, the resin becomes rubbery and the surface topology is expected to change significantly under pressure. Contact points on the surfaces see significant local pressures well above 1atm and may be flattened quickly. This reduces the open space within the interlayer region and decreases permeability. The influence of OVB processing on the surface topology is quantified in Section 3.4.3 to provide additional insight into these mechanisms.

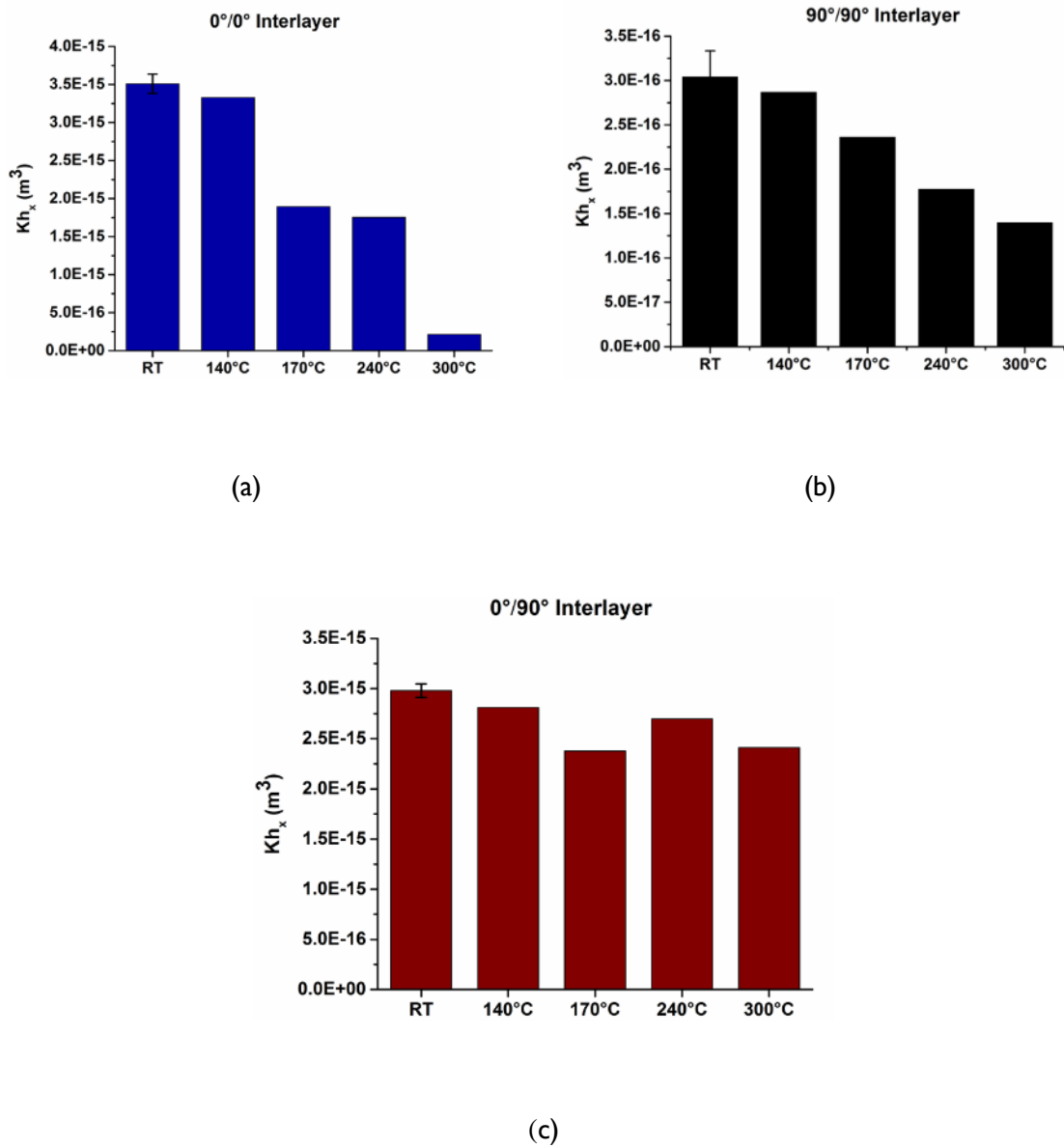


Figure 3.11 Permeability thickness products along x direction of (a) 0°/0°, (b) 90°/90°, and (c) 0°/90° interlayers at elevated temperature

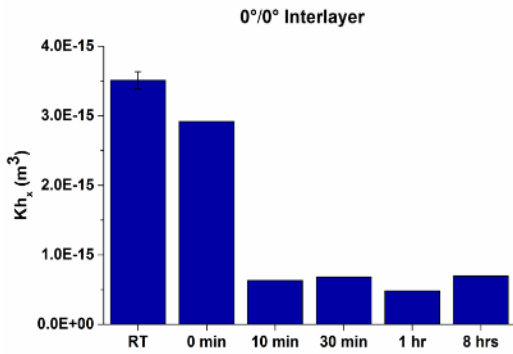
Interestingly only a slight reduction for 0°/90° interlayer is measured even when the temperature is increased to 300 °C (see Figure 3.11 (c)). Surface topology measurements after OVB processing in Section 3.4.3 show evidence of fiber-fiber

contact for off-axis layups. In this configuration, the fibers transfer load across the interface and reduce the amount of polymer movement and gap closure. A high level of permeability is retained over the entire range of temperature, which is advantageous for OVB processing.

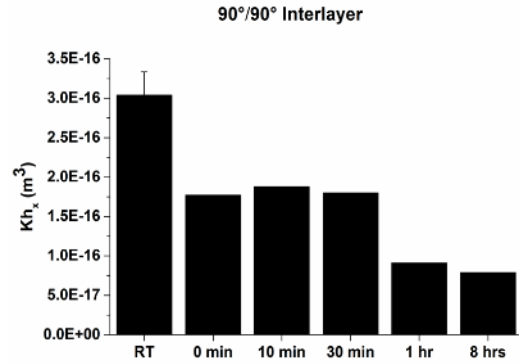
#### **3.4.2.2 Effect of Dwell Time**

The effects of dwell time on permeability of  $0^\circ/0^\circ$ ,  $90^\circ/90^\circ$ , and  $0^\circ/90^\circ$  interlayers at  $240^\circ\text{C}$  are shown in Figure 3.12. The permeability of the  $0^\circ/0^\circ$  interlayer reduces by a factor of six after the 10 min dwell to a plateau level with no further changes up to 8 hrs. The  $90^\circ/90^\circ$  interlayer permeability exhibits two plateaus with a factor of two reduction out to 30 mins followed by a factor of three reduction over 1 to 8 hrs.

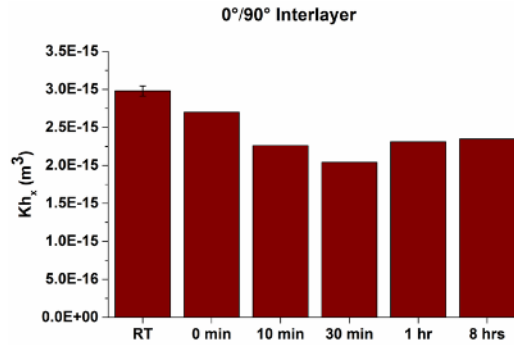
Similar to the results for the ramp study, the  $0^\circ/90^\circ$  interlayer permeability shows negligible reduction of permeability even after 8 hrs of dwell time under  $240^\circ\text{C}$  consolidation temperature (i.e. 20% to about  $2\text{E-}15\text{ m}^3$ ). This is a consequence of the fiber-fiber contact at the interface that reduces the deformation compared to the  $0^\circ/0^\circ$  and  $90^\circ/90^\circ$  interlayers. The next section characterizes the surfaces in terms of surface roughness and topology to provide insight into the origin of these changes during ramp and dwell cycles.



...(a)



(b)



(c)

Figure 3.12 Permeability thickness products along x direction of (a) 0°/0°, (b) 90°/90°, and (c) 0°/90° interlayers under dwell at 240 °C

With respect to OVB processing, the results indicate that incorporating off-axis plies in the lay-up is desirable. The 0°/90° interlayer has high initial permeability and most importantly retains the highest permeability of all of the interlayers considered even after an 8 hour dwell at 240 °C under vacuum. Based on Figure 3.9, the family of off-axis interlayers of 0°/θ exhibit significant fiber-fiber contact and may provide air

removal path at elevated temperature and during dwell for thermoplastic composite OVB processing.

### **3.4.3 Characterization of Surface Topology of OVB Processed Tapes**

After the permeability test were completed, the layers of the  $0^\circ/0^\circ$  and  $0^\circ/90^\circ$  samples processed with OVB (ramp and dwell process cycles) were separated from the stacks for surface characterization ( $0^\circ/0^\circ$  and  $90^\circ/90^\circ$  surfaces are identical). Since the melt temperature of PEEK was not exceeded, minimal bonding was observed in the  $0^\circ/0^\circ$  samples with layers being easily peeled apart by hand. Essentially no bonding occurred in the  $0^\circ/90^\circ$  samples having less contact area due to the fiber-fiber interactions. A Keyence VK-X200 3D color laser scanning microscope was used for the surface characterization. A magnification of 200 with the x-y in-plane resolution of  $2.77 \mu\text{m}/\text{pixel}$  and z resolution of 0.1 nm was used same as in Chapter 2. Samples were cut from the center region of each layer. A continuous area of 14 mm across the fiber direction by 7 mm which is the SRVE for tape surface roughness determined in Chapter was examined for each tape sample.

After microscope scanning, the 3D surface profiles and height information of the sample area were obtained. The overall observation in all samples is that the roughness along the fiber direction is much lower than transverse to the fiber direction. Since the reduction of the interlayer permeability is related to the reduction of the interlayer gaps, root mean square (RMS) line roughness transverse to the fiber direction was selected as the surface characteristic most sensitive to OVB processing. Five lines transverse to the fiber direction of each tape sample were randomly selected and averaged. In addition, the volume between a perfectly flat reference surface and the tape surface with point contact was calculated. This volume is a simple estimate of

the air flow path and should correlate with permeability. The average height of the gap was obtained by dividing this volume with the sample inspection area.

#### **3.4.3.1 Surfaces from 0°/0° Samples**

The surface profiles of the tapes from 0°/0° samples after OVB processing to different temperatures at ramp rate of 2.8 °C/min are presented in Figure 3.13. The range of surface height is approximately 100 µm in all samples including the prepreg baseline. The noticeable difference in these profiles is the reduction in the number of peaks of maximum height above 170 °C. No significant difference was observed from the surface profile of tapes processed with increasing dwell time at 240 °C (Figure 3.14). Quantitative results of averaged RMS surface roughness and gap height are given in Figure 3.15 for 0°/0° samples for both the ramp and dwell OVB process conditions. In both cases, a reduction in these quantities is measured. Increasing temperature to 300 °C under a constant temperature ramp and increasing dwell time at 240 °C up to 8 hrs reduces RMS roughness and gap height by 30 - 35 %. These trends are in qualitative agreement with the measured reduction in interlayer permeability.

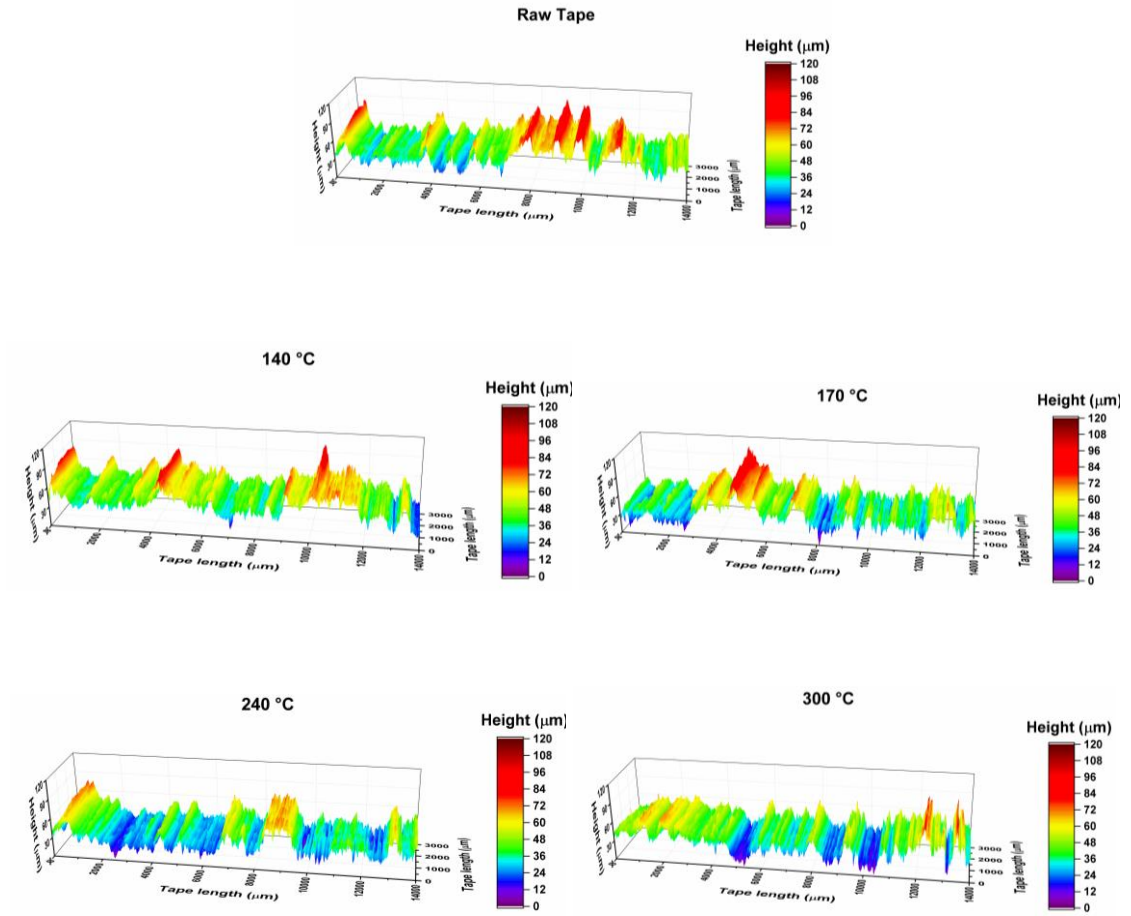


Figure 3.13 3D surface profiles of the tapes from 0°/0° after OVB processing to different temperature at ramp rate of 2.8 °C/min

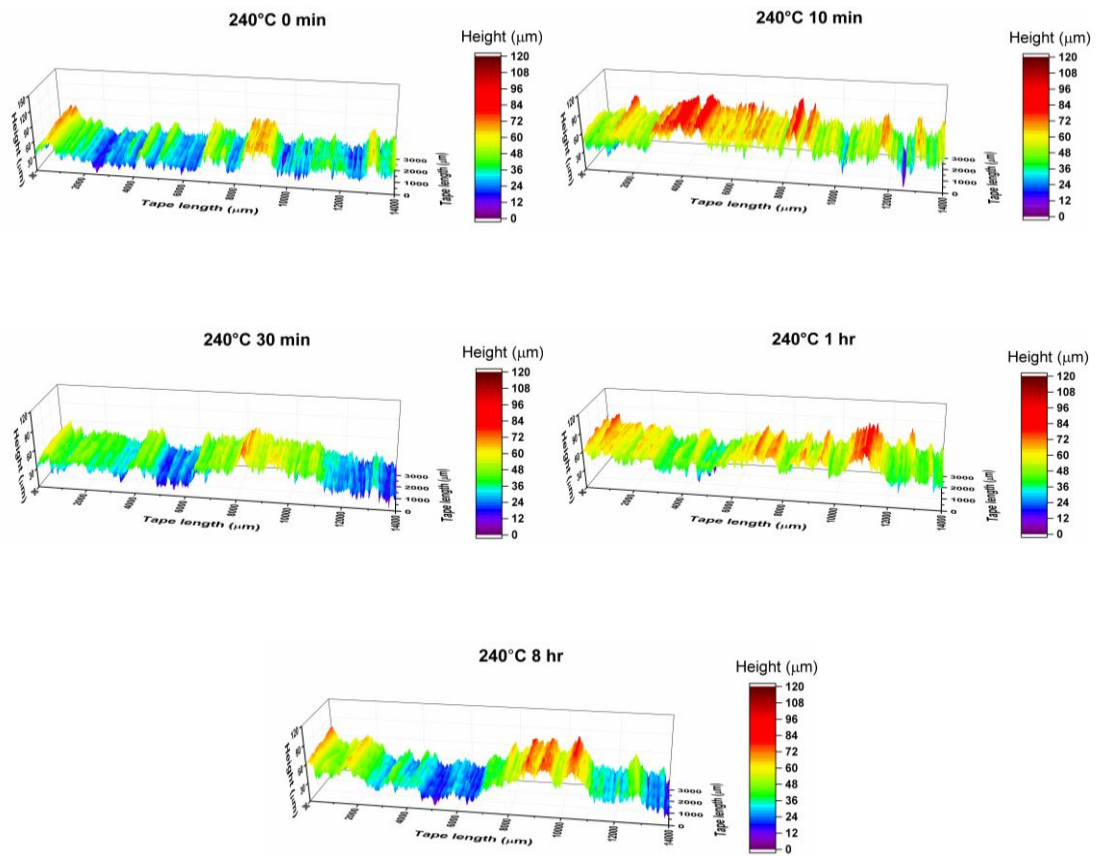


Figure 3.14 3D surface profiles of the tapes from 0°/0° after OVB processed with different time at 240 °C

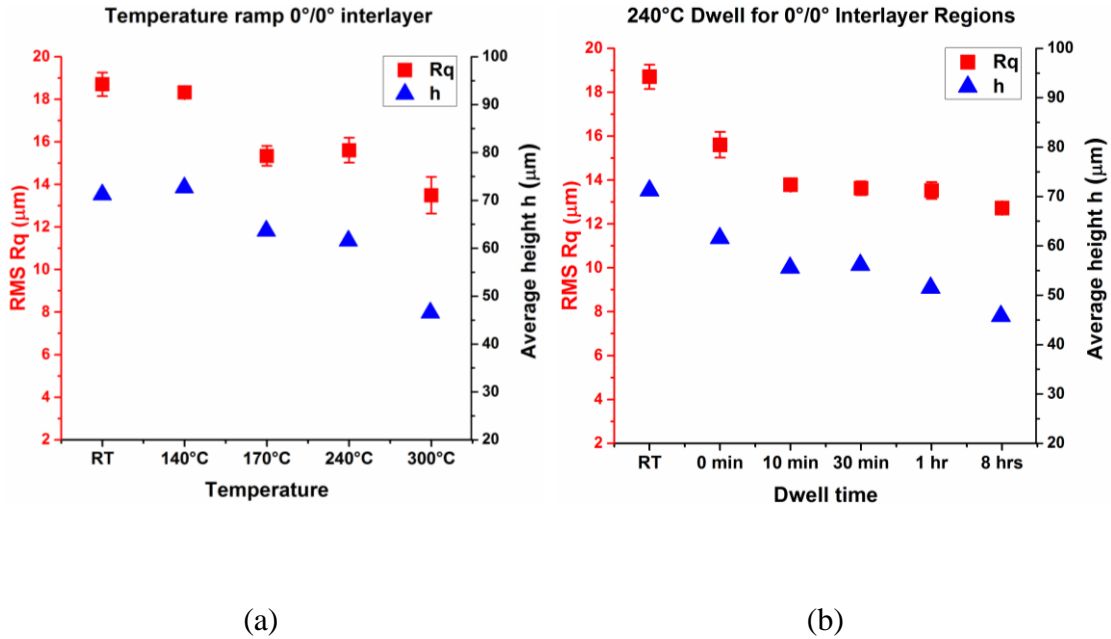


Figure 3.15 RMS roughness and average height between tape surface and a flat surface of the tapes from 0°/0° lay-ups at (a) different temperature at the heating ramp rate of 2.8 °C/min and (b) different dwell time at 240 °C during the OVB processing

### 3.4.3.2 Surfaces from 0°/90° Samples

The results of RMS roughness and the average height for the 0°/90° samples are shown in Figure 3.16. Overall trends are similar to the 0°/0° results in terms of total percentage reduction in these values. However, the height data exhibits a plateau response in terms of peak ramp temperature and dwell time at 240 °C. These results are related to air flow volume between the layers, and are very similar to the plateau behavior in the measured permeability (see Figure 3.11 (c) and 3.12 (c)). One of the reasons for this plateau behavior was due to fiber – fiber contact present in the 0°/90° samples. Evidence of this contact between orthogonal fibers at the surface is presented

in Figures 3.17 and Figure 3.18. Significant horizontal imprints on sample surfaces were observed from the laser intensity surface pattern when temperature is above  $T_g$ . The width of the imprints is of the same order of magnitude as the AS4 fiber diameter ( $8.5\ \mu\text{m}$ ). This shows clear indication of local fiber-fiber contact to the prepreg baseline. No significant difference in the number of the horizontal prints was found at temperature ramps up to  $300\ ^\circ\text{C}$  and dwell up to 8 hrs at  $240\ \text{C}$ , confirming that the majority of the surface is not in contact resulting in the higher volume at the interlayer for air transport for all temperatures and dwell time. This explains both the higher level of permeability and the plateau behavior measured for the  $0^\circ/90^\circ$  interlayer.

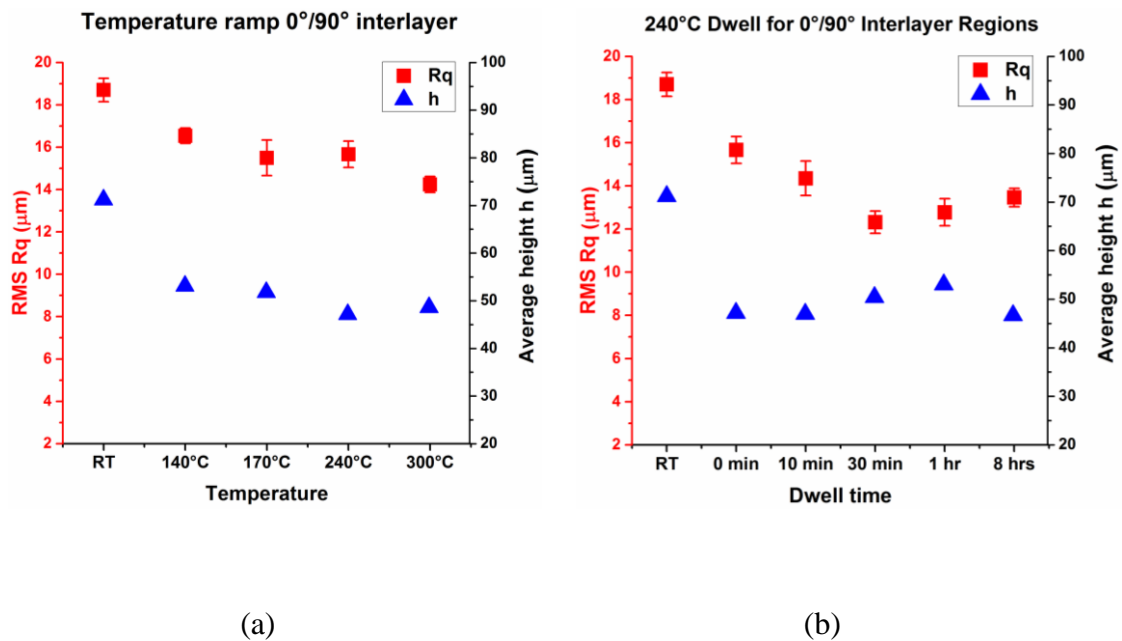
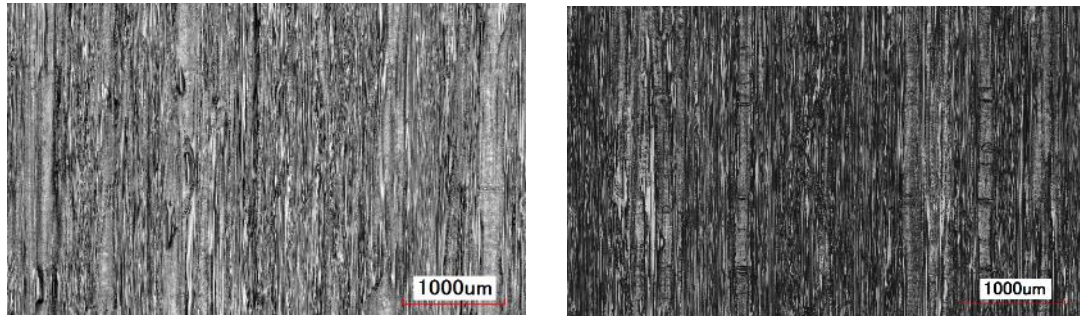
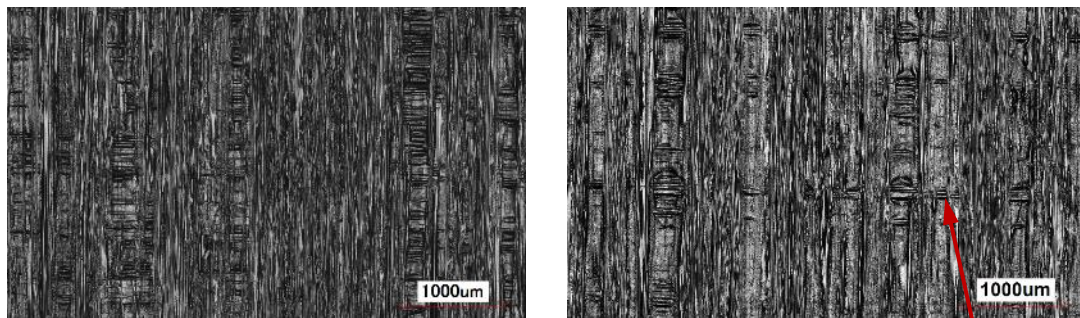


Figure 3.16 RMS roughness and average height between tape surface and a flat surface of the tapes from  $0^\circ/90^\circ$  lay-ups at (a) different temperature and (b) different dwell time under  $240\ ^\circ\text{C}$  during the OVB processing



Raw tape

140 °C



170 °C

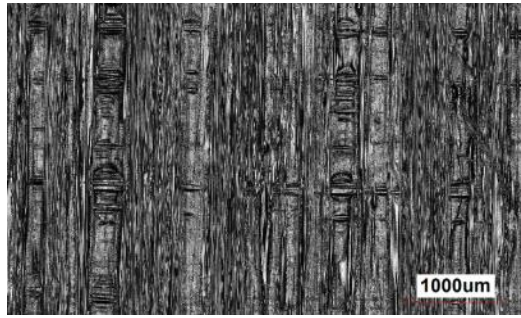
240 °C

Horizontal Imprints

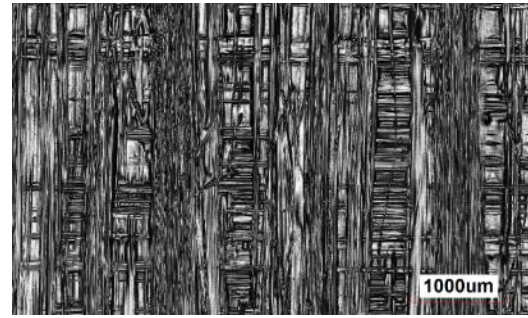


300 °C

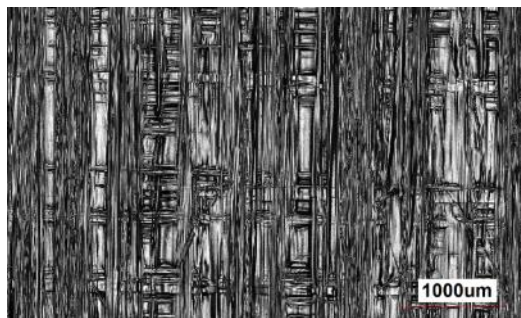
Figure 3.17 Laser intensity images showing the surface patterns of tapes from 0°/90° lay-ups during temperature ramping



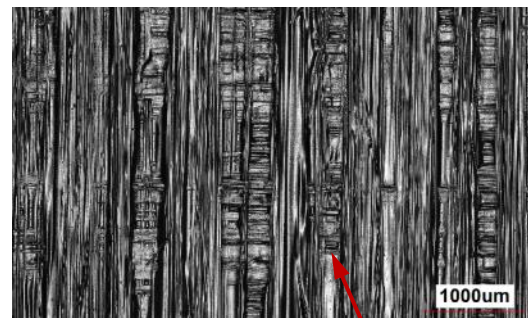
240 °C 0 min



240 °C 10 min



240 °C 30 min



240 °C 1 hr

Horizontal Imprints



240 °C 8 hr

Figure 3.18 Laser intensity images showing the surface patterns of tapes from 0°/90° lay-ups at different dwell time under 240 °C during the OVB processing

### 3.5 Summary

In this Chapter, the interlayer permeability of AS4/APC2 before and after processing at temperature ramp and dwell cycles is investigated. The permeability thickness products of  $\theta/\theta$ ,  $0^\circ/\theta$ ,  $\theta/90^\circ$  and  $\pm\theta$  (x direction flow aligned with  $0^\circ$  orientation) were measured with an experimental set-up based on 1D Darcy's flow. Before processing, room temperature results of the interlayer permeability were found to be higher than the thermoset partially impregnated prepreg systems. The interlayer permeability exhibit directional dependency and are uniquely determined by the orientation of the two adjacent prepreg layers. Since the permeability is a second order tensor, when the angle between two adjacent layers is fixed, the 2D permeability tensor follows rotation matrix for different coordinates of interest. The principal permeability thickness products for interlayer angle between  $0^\circ$  to  $90^\circ$  were determined and the full tensor can be calculated. The tensor predictions were validated with the full range of interlayer configuration of  $\theta/\theta$ . It also shows very good agreement with the measurement results of  $0^\circ/\theta$ ,  $\theta/90^\circ$  interlayers. For the latter configurations, simple equations were found to conservatively and relatively accurately calculate the permeability with only the interlayer permeability of  $0^\circ/0^\circ$ ,  $0^\circ/90^\circ$  and  $90^\circ/90^\circ$ , which is more efficient than the rotation matrix method.

Permeability of  $\theta/\theta$ ,  $\theta/90^\circ$  and  $\pm\theta$  interlayers decreases one order of magnitude when  $\theta$  increases from  $0^\circ$  to  $90^\circ$ . The  $0^\circ/\theta$  interlayers have high level interlayer permeability (x direction flow) and essentially independent of  $\theta$ . As the temperature ramps up above  $T_g$  and to a maximum of  $300^\circ\text{C}$ , the permeability of unidirectional interlayers reduces monotonically. Significant reduction of permeability was measured for unidirectional interlayers held at intermediate temperature in the resin rubbery region  $240^\circ\text{C}$  for extended dwell times. Negligible reduction was obtained for the

permeability of 0°/90° interlayer when temperature ramps up to 300 °C and after 8 hrs dwell at 240 °C due to fiber-fiber contacts between the surfaces. The surface roughness was quantified and shows trends qualitatively in line with the measured permeability thickness products. The surface pattern of 0°/90° interlayers above T<sub>g</sub> confirms the local orthogonal fiber-fiber contacts limits the contact between layers and results in higher interlayer volume for air transport.

After understanding the interlayer permeability of the thermoplastic prepreg stacks, in the next chapter, the void reduction mechanisms will be analyzed and the key mechanism will be determined. It will show that the interlayer permeability plays an important role on void reduction especially in thick thermoplastic composite OVB processing. Based on the results of this chapter, generally, the off-axis interlayer can retain high levels of permeability over a wide range of temperatures and dwell times due to fiber-fiber contact which may allow volatiles to be removed through the interlayer porous pathways during processing so that processing cycles may be optimized.

## **Chapter 4**

### **DETERMINATION OF KEY VOID REDUCTION MECHANISMS**

#### **4.1 Introduction**

From the investigation of the void microstructure of thermoplastic prepreg in the Chapter 1, the initial void conditions were obtained. Chapter 3 shows the interlayer regions are permeable. The permeable interlayer regions of thermoplastic prepreg may have significant effect on the void reduction in thermoplastic composite during OVB processing. In this Chapter, the mechanisms for void reduction are discussed based on the microstructure of the thermoplastic prepreg and the processing condition in OVB processing. Dominate mechanism is determined and validated through OVB consolidation experiments.

#### **4.2 Viable Mechanisms in Thermoplastic OVB Processing**

In Chapter 1, mechanisms of voids dynamics in the manufacturing of both thermosetting and thermoplastic composites were reviewed and include: void compression by the applied pressure, void filling with resin flow, moisture/gas nucleation and diffusion, void escaping through buoyancy force, coupled mechanism of stress equilibrium at void boundary and gas molecule diffusion, and air removal through permeable prepreg materials. These mechanisms are discussed next with the processing condition of OVB processing and the microstructure of thermoplastic prepreg tape, and the relevant mechanisms can be determined.

Previous study of void microstructure shows that voids are encapsulated in the thermoplastic prepreg tapes (Chapter 2). Prior storage of the prepreg tapes under ambient condition ensures that the concentration of air dissolved in the resin and air pressure within the void can be assumed to reach equilibrium under room temperature and atmospheric pressure. In the case of no air molecules diffusing out from voids, as the temperature increases during OVB processing, the air pressure within the voids will be larger than 1 atm based on the ideal gas law. With the 1 atm net pressure on top of the prepreg layers in vacuum bag, the voids cannot be compressed, and there is no positive driving force for resin to flow and fill the void space. Therefore, voids cannot be removed without reducing the void internal pressure.

With the porous peel plies on top and bottom surfaces of prepreg stacks, the application of vacuum removes air at the surfaces of the prepreg layers, creating concentration gradient for air within the prepreg to diffuse out. Since the prepreg interlayer regions are permeable, vacuum can also remove air between layers when the edges of the prepreg stacks are open to vacuum. The diffusion coefficients of gases increase exponentially with increasing temperature. [89] The diffusion time is a function of temperature and diffusion length. For a certain laminate thickness, if the diffusion time at a temperature is long enough, the air dissolved in the resin can be removed by diffusion and the concentration within the voids can then be reduced. Therefore, diffusion is a possible mechanism for void air removal in OVB processing.

Void escaping by means of buoyancy were proposed for low viscosity thermosetting composite processing. [50]. Based on Archimedes principle, Stokes law and Newton's law, the characteristic steady state velocity can be calculated. Voids can be assumed cylindrical, and the maximum diameter (14  $\mu\text{m}$ ) and length (1 mm) of

99% voids from the statistical study in Chapter 2 are used for conservative estimation. The calculation shows that at the processing temperature of 380 °C, the characteristic time for this void to reach surface of 0.15 mm apart requires 87 hrs. (Appendix D) The void rising time can be much longer than this if the voids are embedded deep inside the laminate, and smaller in size. Therefore, void escaping through buoyancy effect is not possible in the OVB processing of highly viscose thermoplastic composites.

Mechanism of moisture or gas nucleation can generate voids in the composites and affect the final void content. [26]. Nucleation can be categorized in to homogeneous nucleation the nuclei generated in homogenous solution. When there are impurities/defects/surfaces in the solution, nuclei can be generated along the surfaces. This process is generally easier than the homogenous nucleation. In order to analyze whether the air molecules dissolve in the resin can generate nuclei, the super – saturation ratio and the nucleation rates (number of nuclei /m<sup>3</sup>/s, representing the probability of forming nuclei) are calculated. The temperature dependent solubility of N<sub>2</sub> and H<sub>2</sub>O in amorphous PEEK resin were obtained from literature [93] and that of O<sub>2</sub> is estimated from solubility of N<sub>2</sub> following the method introduced in Ref.[89]. With 10.5% crystallinity of PEEK resin in the prepreg tape, and 35% resin volume fraction, the solubility of N<sub>2</sub>, O<sub>2</sub> and H<sub>2</sub>O in the prepreg tape were estimated, as seen in Appendix E. If assuming air is 79% N<sub>2</sub> and 21% O<sub>2</sub>, 40% relative humidity and constant amount of gas in the resin, calculation shows that the super-saturation ratio for N<sub>2</sub> and O<sub>2</sub> is smaller than 3 even at the processing temperature of 380 °C. H<sub>2</sub>O has a super saturation ratio of 926 which is significant higher than the other two gases, and may have higher possibility to form new nuclei. (Appendix F) The probability of creating nuclei or the nucleation rate is further calculated. The details are included in

Appendix F. With the highest vapor pressure at the temperature of 380 °C, the probability to observe a nucleus for N<sub>2</sub> and O<sub>2</sub> are extremely low ( $3.89 \times 10^{-5e4}$  and  $4.95 \times 10^{-2e7}$  for a sample size of 1 m<sup>3</sup> volume and time of 10000 s for N<sub>2</sub> and O<sub>2</sub> respectively). The nucleation rate for moisture is 4 nuclei /m<sup>3</sup>/s at temperature of 340 °C which is still very low. As the diffusion process occurs after vacuum is applied during the processing, it is highly possible that the moisture molecules diffuses out during the processing before reaching 340 °C. The local vapor pressure of moisture can be even lower than the current calculation. The probability of creating new nuclei can still be very low. Therefore, nucleation of new voids due to moisture can be ignored. However, the dissolved gas molecules can diffuse into the voids if local concentration in the resin is higher than at the void boundary. In this case, the internal pressure of voids will increase, or the voids may grow. Therefore, the diffusion of air in the resin can affect the void reduction.

From Chapter 3, the interlayer region of prepreg tapes is permeable and the permeability are generally higher than the in-plane permeability of partially impregnated thermosetting prepreg tape. The interlayer permeability may also affect the void reduction in thermoplastic composites.

From the above analysis, it is seen that void filling with resin flow, void air removal through diffusion, and gas escaping laterally through the permeable interlayer region are the possible mechanisms for void reduction in the OVB consolidation of thermoplastic composites. For high performance melt-impregnated AS4/APC2 prepreg tape, the initial void content is 7.77% and 4.70% from 2D and 3D measurements, respectively (Chapter 2). Statistical 3D X-ray micro-CT characterization shows that the voids are encapsulated in thermoplastic prepreg.

(Chapter 2) [94,95] In contrast to partially impregnated thermoset prepreg which are air permeable in-plane and often in the through - thickness direction, voids in thermoplastic prepreg have no direct path ways to transport air to the prepreg surfaces other than diffusing through the thermoplastic matrix. Since diffusion time is proportional to the square of diffusion length, the time for void air evacuation through moderate to thick laminates can be extremely long. [80,96,97] Therefore, in OVB processing of thick laminates, relying solely on diffusion mechanism to achieve low void content is not practical except in thin laminates. A second mechanism utilizes the permeable interlayer regions formed by the rough surfaces of thermoplastic prepreg as shown in Figure 4.1. In the case of AS4/PEEK prepreg, the in-plane air interlayer permeability is measured to be 1-2 orders higher than some partially impregnated thermosetting prepreps optimized for vacuum bag processing (Chapter 3) [52–56,87,88,98] The mechanism of void air diffusion through single layer prepreg followed by transport through interlayer regions can provide an opportunity to significantly reduce processing times needed to reduce voids in thick thermoplastic laminates during OVB processing. In the next section, the key mechanisms will be discussed in depth along with the processing cycle.

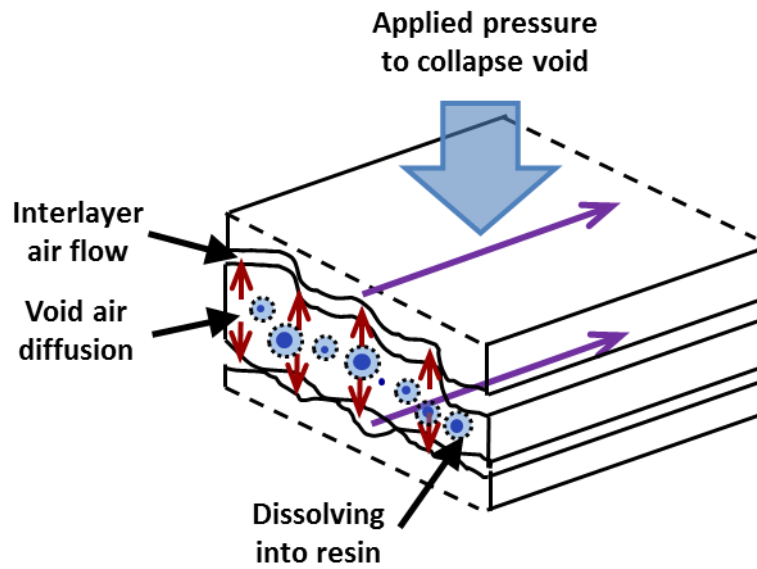


Figure 4.1 Schematic of void removal mechanisms

#### 4.3 Discussion of Key Void Reduction Mechanisms during OVB Processing

As the temperature cycle during OVB processing is followed, gas concentration and pressure will evolve, resulting in the following stages of void reduction in thermoplastic composite laminates:

- Initial application of vacuum removes air between layers in case the edges open. In the case of edges sealed air remains trapped between layers. Air diffusion commences but at low temperatures, diffusion times are very long even in a single layer compared to the process cycle.
- As the temperature is increased to levels below the resin softening temperature, the void volume is constant (resin doesn't flow) and the internal pressure ( $P$ ) changes with temperature according to the ideal gas law.

- As temperature rises above the resin softening temperature (250-340 °C for semicrystalline PEEK [11]), the void changes volume to achieve equilibrium between the applied (i.e. 1 atm) and the internal void pressure.
- During the entire process, the air concentration (C) at the void boundary with the matrix follows Henry's Law ( $C=HP$ ) [89], resulting in gas molecules within the voids to dissolve into the resin or diffuse from resin into the voids to maintain equilibrium.
- Diffusion of the gases towards the vacuum surfaces reduces the gas concentration in the matrix, and in turn reduces the concentration within the voids according to Henry's Law. To maintain pressure equilibrium between the applied pressure and the pressure within the void, the void volume reduces according to the ideal gas law when temperature is above resin softening temperature.
- In the case with edges open, the vacuum surface is the surface of each individual layer and the permeable interface between prepreg layers allows air transport out to the part edges within the vacuum bag. In the case of edges sealed, the vacuum surfaces are the laminate surfaces in contact with the peel ply, breather and vacuum bag and air must diffuse through the entire laminate thickness.

The sequence above is highly transient and dependent on the process cycle since the key properties are dependent on temperature and pressure. Diffusivity of air molecules ( $N_2$  and  $O_2$ ) typically exhibits an exponential dependence on temperature. Solubility of gases in resin changes with temperature [89,93,99]. And the concentration of gases in resin depends on solubility (Temperature dependent) and local vapor pressure.

All of these mechanisms contribute to void content reduction during OVB processing. In the case of edges sealed, two classes of voids can occur: intralayer voids within a layer discussed above and air that is trapped between the rough surfaces of adjacent layers during lay-up that may create interlayer voids (see Figure 4.2) unless sufficient time is allowed for this additional air to diffuse through the entire laminate thickness. In the case of edges open to vacuum, part consolidation also depends on interlayer permeability and inplane dimensions of the part where sufficient time is needed for air flow to the perimeter.

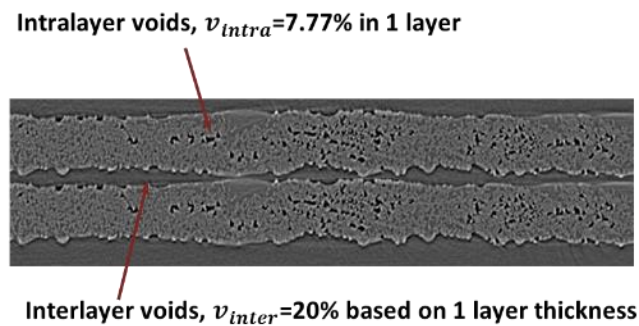


Figure 4.2 Intra- and interlayer voids in AS4/APC2 laminates

Taking the processing temperature of 380 °C for PEEK as an example, the diffusion coefficient of N<sub>2</sub> and O<sub>2</sub> are 2.29E-9 m<sup>2</sup>/s and 9.24E-10 m<sup>2</sup>/s, respectively (Appendix E). The dependence of diffusion time on laminate thickness at 380 °C for homogeneously distributed N<sub>2</sub> without voids in the laminate and symmetric boundary condition is shown in Figure 4.3. It is seen that the time for volatile removal can vary from seconds (9 s) for thin laminates (1 layer or 0.18 mm) to around 10 hours for a 72 layer thick laminates (i.e. 11 mm), and 18.6 hrs for laminate thickness of 15 mm. To

remove the air inside of the voids, the diffusion time also depends on the concentration gradient from void boundary to the surrounding resin, which can be significantly increased. In addition, lower temperatures and one sided diffusion reflecting tool surface would dramatically increase diffusion time. Nevertheless, void volatiles removal time in a single layer or thin laminates can be still short.

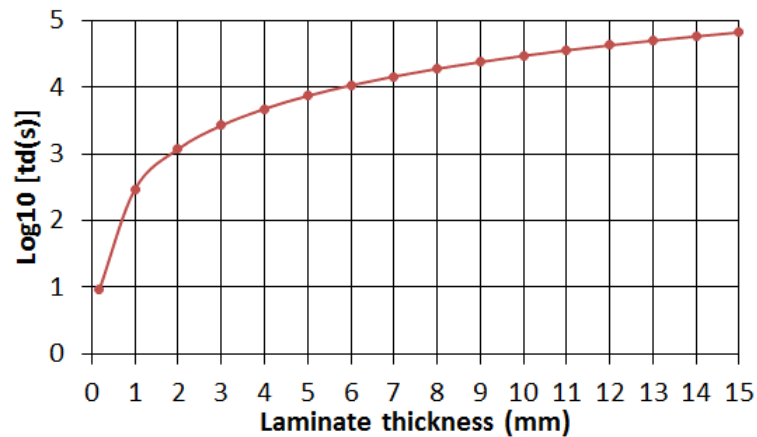


Figure 4.3 Diffusion time of N<sub>2</sub> depend on laminate thickness, from 9.4 s for 0.18 mm, to 18.6hrs for 15mm laminates

Therefore, the key mechanisms for volatile removal and void content reduction during OVB processing considered are the diffusion of void air within single layer prepreg tape to the surfaces and the flow of void air to the perimeter under vacuum through the permeable interlayer regions created between two prepreg layers. In order to validate this mechanism, designed experiments are conducted through: 1) sealing the edges (i.e. the dominant mechanism is diffusion through the full laminate thickness); 2) leaving edges open to vacuum (i.e. the dominant mechanisms is

diffusion through a single layer followed by removal through the permeable rough interlayer between two layers).

#### **4.4 Experimental procedure**

Various flat panels were fabricated to separate diffusion and the interlayer permeability mechanism experimentally. Processing conditions were designed to enable/disable gas flow out to the part edges. Part thickness was controlled to ensure full or partial air evacuation through diffusion through the surface only. Void content in the OVB processed part were spatially measured to obtain insight in the void distribution as a function of through-thickness location. The temperature cycle was shortened to allow void content gradients through the thickness to be measured to prove out the consolidation mechanism.

##### **4.4.1 Laminate fabrication**

Same AS4/APC2 prepreg tape from Solvay is used in this experiments. The tape information can be seen in Chapter 2 section 2.2.3. 300 mm × 300 mm 2-layer cross-ply ([0/90]) and 72-layer symmetric balanced ( $[(0_4/90_4)_4]_s$ ) laminates were fabricated with OVB processing. The vacuum bag assembly in the OVB processing is shown in Figure 4.4. In order to keep the edges of thick laminates from getting pinched inadvertently, a steel bar was placed 25 mm from each lateral edge of the thick laminates. Peel plies and breathers were placed on top and bottom of the laminates to generate symmetric vacuum surface conditions for air diffusion. Two edge conditions were evaluated for the thick laminates: 1) in the open edge condition, breather cloths were placed between the laminate edges and the steel bars to keep the path open to vacuum. This allowed air evacuation through all interfaces and the

effectiveness of single layer diffusion and the interface permeability mechanism to be evaluated, and 2) in the closed edge condition, the 4 lateral perimeter edges of one 72-layer laminate were sealed with thick layers of tacky tapes (Figure 4.4) eliminating interface air flow into the vacuum source so that air removal by diffusion through the entire laminate thickness under symmetric condition is the dominant mechanism.

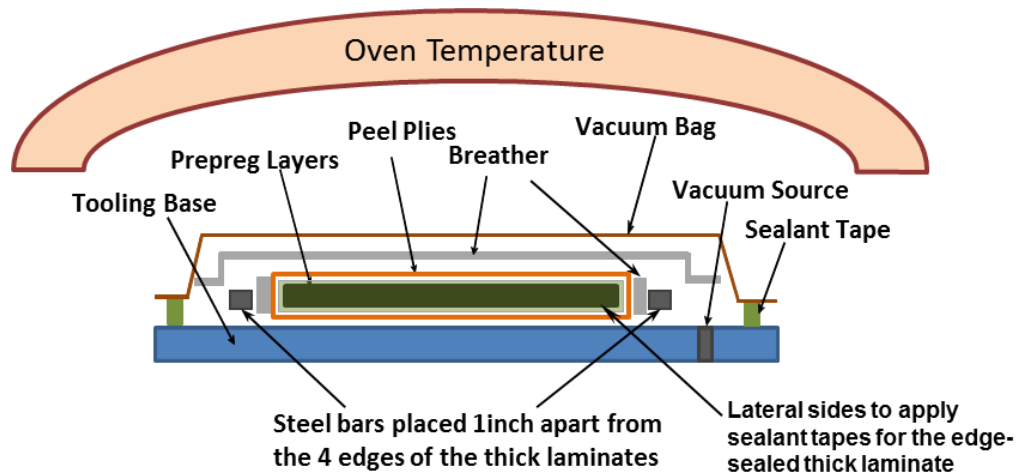


Figure 4.4 Schematic of vacuum bag assembly in the oven.

The laminates were consolidated with triangular heating and cooling cycle (ramp of 2.8 °C/min). No dwell time at 380°C was used to provide maximum sensitivity to gradients in void content reduction through the thickness. Recorded vacuum level in the bag for the laminates during the entire processing time was within the range of 27-28 inHg. Temperature gradients measured with thermocouples placed on the surface and centerline during the consolidation were found to be negligible in both thin and thick laminates due to the relatively high thermal diffusivity of the carbon/PEEK prepreg. The maximum percentage deviation of the surface to the bulk

temperature (average of the surface and centerline temperature) of the thick laminate was less than 5%. The measured bulk temperature of thick and thin laminates are presented in Figure 4.5.

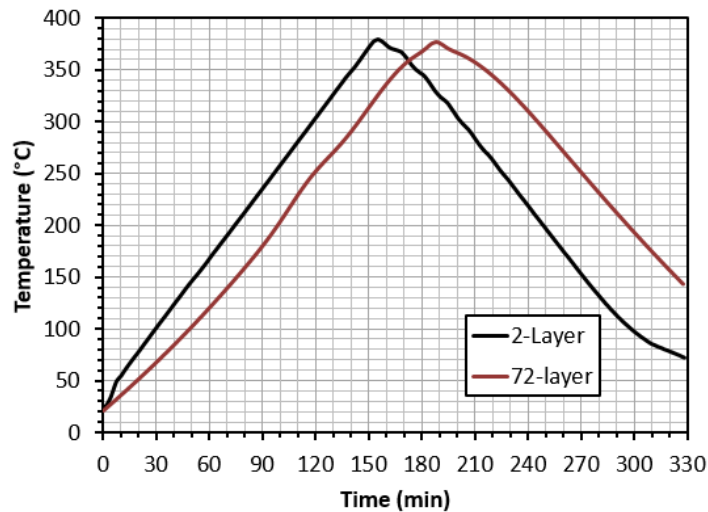


Figure 4.5 Measured bulk temperature of 2-layer and 72-layer laminates during processing.

## 4.4.2 Void inspection

### 4.4.2.1 X-Ray micro-CT.

The raw prepreg tape and processed laminates were examined with SkyScan's 1172 high resolution micro-CT to visualize 3D internal void content. The image size is 4000×2096 pixels. Samples were taken from the central region of the prepreg tapes and the laminates. Scissors were used to obtain the samples from single layer prepreg and the 2-layer laminate, and a diamond saw was used to cut the thick laminate samples. For prepreg tape and 2-layer laminates, sample sizes are 4.5 mm (width) × 3.6 mm (length) × full laminate thickness. Since the 72-layer laminates are thick (10

mm), samples were sectioned at about mid-thickness and the sample sizes are 6.4 mm (width)  $\times$  6 mm (length)  $\times$  5.4 mm (thickness) and 6 mm (width)  $\times$  4 mm (length)  $\times$  5.4 mm (thickness). The raw X-ray images were constructed with Skyscan NRecon into a set of parallel 2D tomograms, forming the 3D volumetric information of the samples.

#### **4.4.2.2 Optical microscopy**

To obtain and compare the void contents in the processed laminates, optical microscopy with higher resolution than x-ray micro-CT are used. Samples from the central region (approximately 150 mm from the panel edges representing the longest permeability interface path length) of the consolidated laminates were prepared along two directions to examine the voids in both 0° and 90° layers over 20 mm lengths, and were observed with Keyence VK-X200 confocal microscope with an image size of 2048  $\times$  1536 pixels at 400 $\times$  magnification. Images were taken with a resolution of 0.34  $\mu\text{m}/\text{pixel}$ . More than 40 single images along each cross-sectional direction were processed with Image J to obtain representative measurement. The detailed image processing method is provided in [100]. The void content of the entire laminate were obtained from averaging the void content measurements from all of the images.

### **4.5 Results of voids in processed laminates and discussion**

The 3D views from micro-CT inspection for the single layer prepreg before processing and OVB processed laminate samples are presented in Figure 4.6 and 4.7, and the 2D cross sectional images for 2-layer and 72 layer laminates under optical microscope are presented in Figure 4.8 and 4.9.

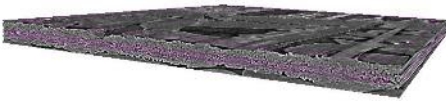
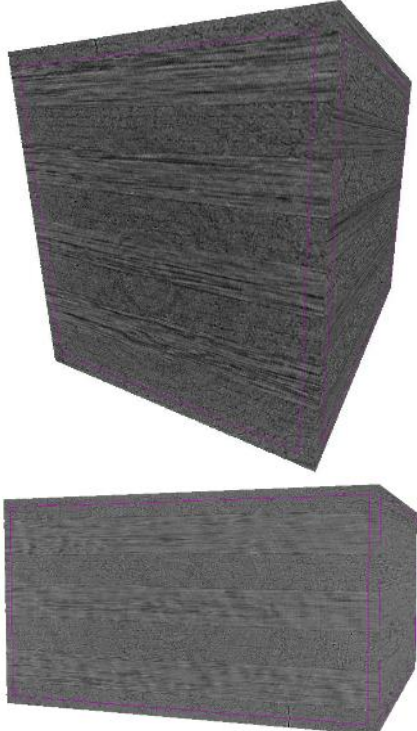
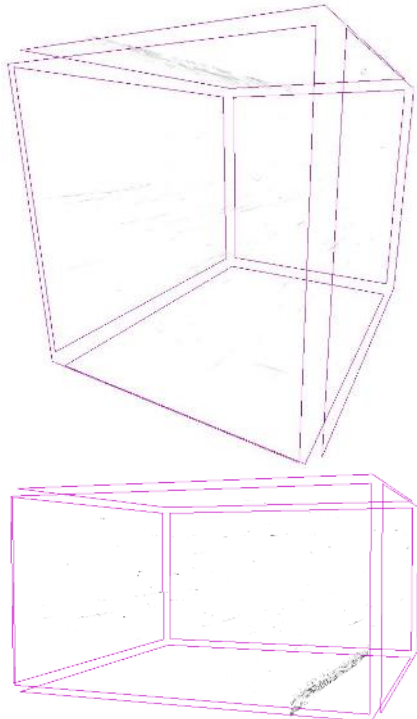
3D volume	Voids in sample
Prepreg, 1.48 $\mu$ m/pixel, sample width – 4.5mm	
	
2-layer, 1.48 $\mu$ m/pixel, sample width – 4.5mm	
	
72-layer with perimeter open to vacuum, 2.6 $\mu$ m/pixel, sample width = 6.4mm	
	

Figure 4.6 3D volume and voids in prepreg and processed laminates with edges open condition from X-ray micro-CT. 72-layer thick laminate is void free as the 2-layer thin laminate

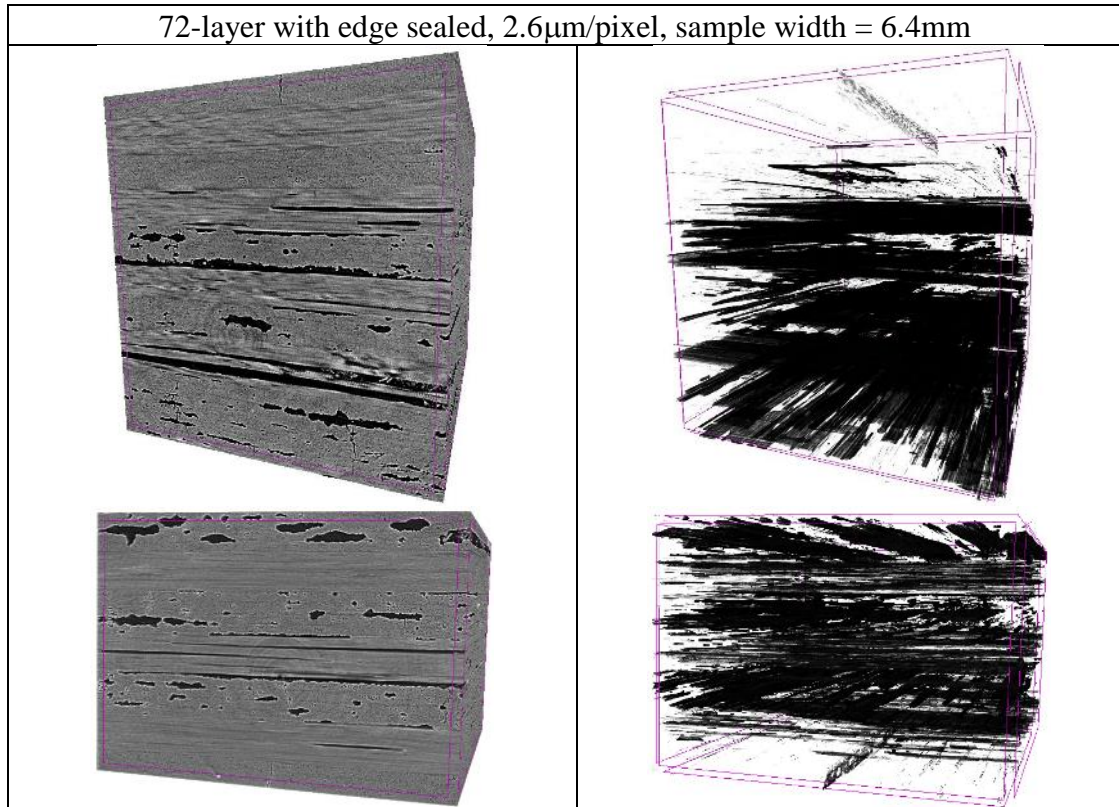


Figure 4.7 3D volume and voids in prepreg and processed laminates with edges sealed condition from X-ray micro-CT. Significant voids were trapped in the 72-layer thick laminate under the edges sealed condition

The prepreg shows rod-like voids parallel to the fiber direction with void content of 7.77%. The intralayer and interlayer voids in laminates vanish in the experiments with edges opened for both the 2-layer and 72-layer laminates due to the combined mechanism of diffusion and interlayer permeability. Significant voids remain in the edge sealed 72-layer laminates processed under identical conditions since diffusion is the only mechanism. In Figure 4.9, micrographs of 72-layer laminates were compared at three locations through the thickness: surface, quarter and mid-thickness. It is seen that when the edges were sealed to restrict the in-plane

interface permeable paths, significant amount of inter - and intra - layer voids are trapped in the inside layers of 72-layer laminates with local void content as high as 10%. Only the first 8 layers are void free (0.41%) due to diffusion and proximity to the vacuum surface. On the contrary, when the perimeters are open to vacuum, the 72-layer laminate is almost void free with homogeneous cross-section through thickness as also seen in the micro-CT 3D volume in Figure 4.6.

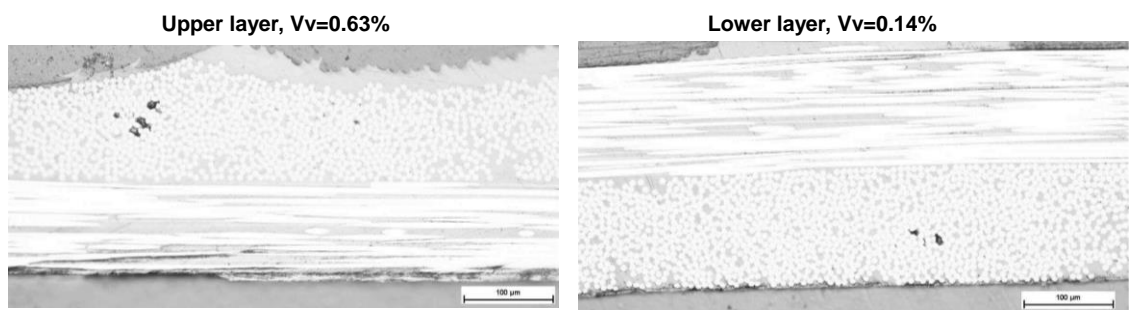


Figure 4.8 Microscopy images of the 2-layer laminates after consolidation (Vv: void content; dark black regions are voids).

The average void content of the laminates obtained from optical microscopy is shown in Figure 4.10. After processing with perimeter open to vacuum, void content was significantly reduced to 0.69% and 0.57% in 2-layer and 72-layer laminates, respectively. When the perimeters were sealed to prevent the air flow through interlayer regions, voids in the 72 layer laminate only reduced to a void content of 3.81% (averaged over the entire laminate).

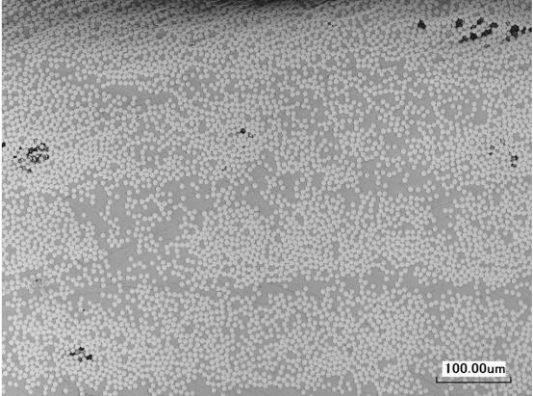
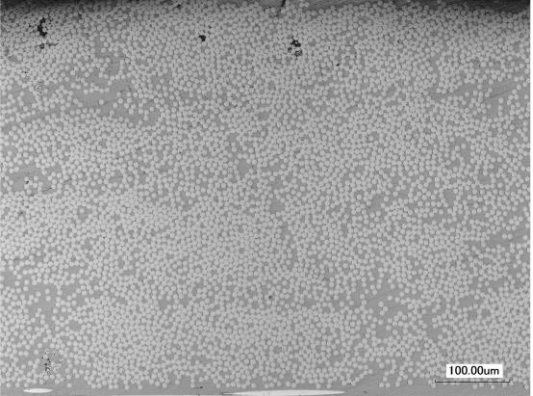
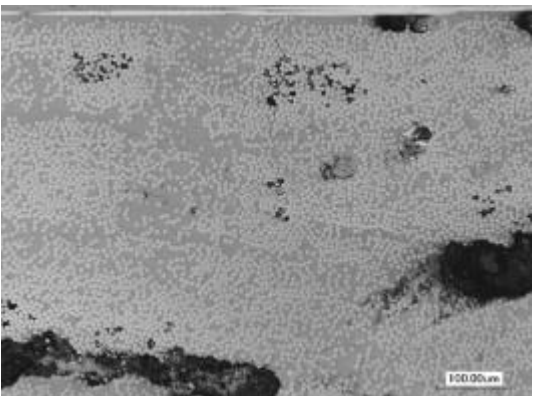
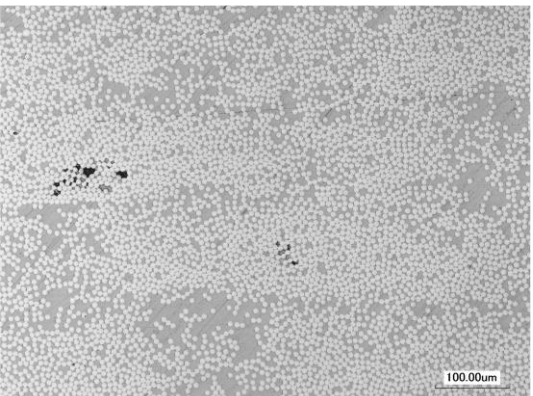
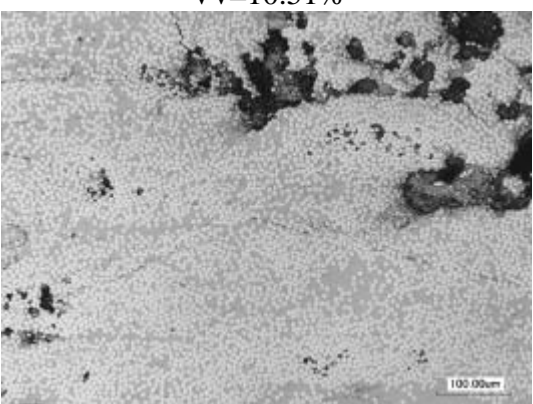
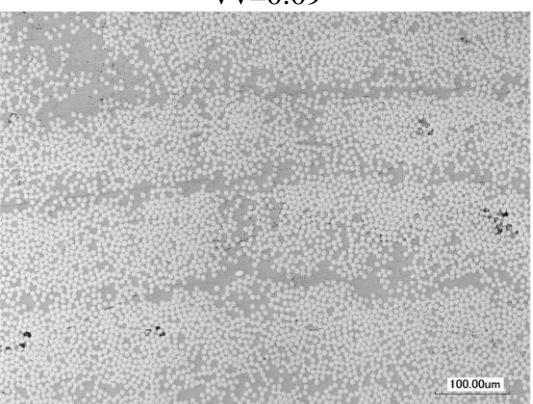
Edge sealed	Perimeter open to vacuum
Surface: 1-4 layers $V_v=0.41\%$ 	Surface: 1-4 layers $V_v=0.12\%$ 
Inside: 21-24 layers $V_v=9.04\%$ 	Inside: 21-24 layers $V_v=0.28\%$ 
Middle: 33-36 layers $V_v=10.51\%$ 	Middle: 33-36 layers $V_v=0.09\%$ 

Figure 4.9 Optical micrographs of the 72-layer laminates after processing ( $V_v$ : void content; dark black regions are voids).

The void content distribution through the thickness of edge sealed 72-layer laminate is plotted in Figure 4.11. A very low void content is seen in the layers close to the two surfaces, and much higher void content in the thickness center regions, which is in line with gas concentration profile due to pure diffusion with symmetric boundary conditions. Very large voids exist in the interface region between layers compared to the smaller sized voids within a single layer. The interlayer voids contribute significantly to the high void content in the interior layers as seen in Figure 4.7 and Figure 4.9. This may be because of the Thomson-Freundlich effect that gases tend to diffuse into large voids due to the relatively small surface tension on void boundary while small voids tends to diminish [50,101]. The void content result of edge sealed 72-layer laminate proves that the diffusion only mechanism is not effective in reducing void content using this experiment OVB process cycle.

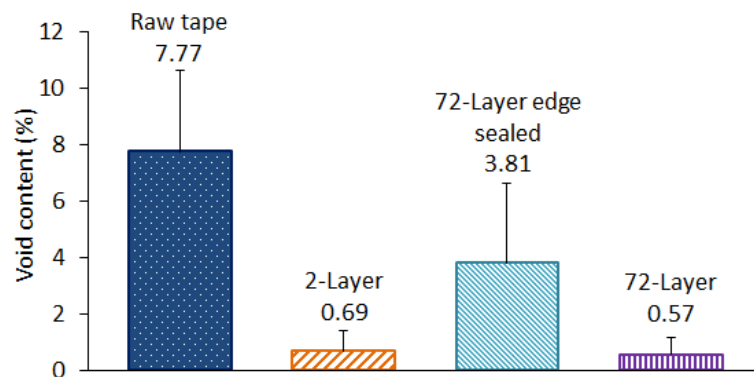


Figure 4.10 Average void contents of the processed laminates from more than 40 cross-sectional images along the width direction (more than 28 mm) in the center region of each laminate. Error bars are the standard deviation of the void content in all the images for each laminate. <1% void contents were obtained in 2-layer and 72-layer in the condition of open edges.

The 72-layer laminate with open edges reached void content of less than 1% (identical cycle to edge sealed laminate) and was equivalent to the 2-layer laminate. This proves that the permeable interface region is effective for void air evacuation. Furthermore, the diffusion time for air removal is based on the thickness of a single layer (49.2 s at 380 °C) versus on the entire laminate thickness (110 hrs at 380 °C). This simple experiment confirms that both mechanisms of single layer through-thickness diffusion and air flow through permeable interface gaps are active and required to achieve low void content during OVB processing of thick thermoplastic composite laminates.

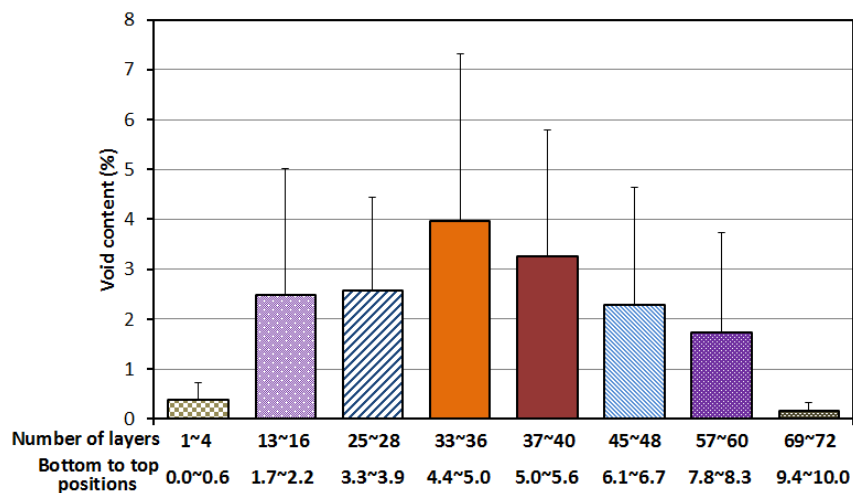


Figure 4.11 Void contents at different through thickness locations of the 72-layer edge sealed laminate. At each location, more than 40 cross-sectional images along the width direction (more than 28 mm) were examined. The error bars are the standard deviation of the void content in all the images for each through thickness location. Large error bars are due to the highly non-homogeneous void content along the width direction of the laminate.

Based on these experimental results one concludes that for the abbreviated process cycle and the size of the laminate used in this study, the volatiles in the inside layers (e.g. 21-36 layers) of the thick laminates with perimeter sealed require extremely long time to diffuse to the laminate surface through the thickness direction, resulting in very high void content at these locations for this process cycle. The same inside layers with perimeter venting to vacuum are essentially void free. The process cycle provides sufficient time for air to diffuse through a single layer and be evacuated through the permeable interlayers. The combination of mechanisms enables OVB processing of thick section AS4/PEEK laminates. Our experiments indicate that thick laminates with low void content are feasible with OVB processing since scaling layers are based on diffusion through a single layer tape thickness.

If air removal is purely governed by the diffusion mechanism as in the case when lateral edges of a part are sealed, the time required to evacuate the void air depends on the laminate thickness only and is independent of part in-plane dimensions. However, with a certain processing time, only laminates with thickness can reach 1% void content. The laminate thickness is largely limited by the processing time based on the diffusion mechanism only.

For the dual mechanism, the air removal time can be conservatively bounded as the summation of the diffusion time through a single layer and the flow time of void air evacuating to the vent location at the part perimeter. Diffusion time of a single layer to the resin softening point can be small, but flow times in the interface can be significant for parts with large in-plane dimensions and low interlayer permeability. It is very important to recognize that the dual mechanism is effective for laminates of any thickness and represents a major advantage of this approach. In contrast, the

through thickness diffusion mechanism is effective for parts of any inplane dimension but with very limited laminate thickness.

#### **4.6 Summary**

In this chapter, the viable mechanisms for void reduction in thermoplastic composite OVB processing were discussed. With only vacuum bag pressure, the driving force for air reduction can only be provided by reducing the internal pressure of voids through the removal of the void air. Two mechanisms for air removal were investigated for AS4/PEEK prepreg. In the case of edge perimeter sealed laminate, air removal is limited to diffusion through the entire laminate thickness, leading to part thickness limitations. In the case of edge perimeter open, air removal occurs through single layer diffusion and flows through a permeable interlayer created by the surface roughness of the prepreg. This combined mechanism route has no thickness limitations but inplane dimensions of the part in conjunction with the interlayer permeability govern the time needed for air removal. The two mechanisms were experimentally validated via OVB processing of essentially void free thick section laminates (72-layer with perimeter open to the vacuum). These results validated single layer diffusion followed by interlayer air evacuation as the key mechanism to achieve low void content in thick laminates via OVB processing. This mechanism points out the importance of the rough surfaces and interlayer permeability of thermoplastic prepreg tapes. In the next Chapter, non-isothermal models for diffusion and air flow will be established and provide more insight of the dual mechanism and the opportunity for optimization of processing cycles.

## Chapter 5

### MODELS FOR VOID AIR REMOVAL

#### 5.1 Introduction

The consolidation experiments in Chapter 4 demonstrated two mechanisms for void air removal: combined mechanism of void air diffusion through single layer prepreg followed by air flow through the interlayer region, and diffusion only mechanism through the thickness of prepreg stacks, as illustrated in Figure 5.1. Void air removal based on the combined mechanism is independent of the thickness of the laminate, and the processing time for air removal depends on the diffusion time from single layer prepreg and air flow time through the interlayer region to the part boundary. The processing time for void air removal via the diffusion only mechanism is governed by the thickness of the laminates. Air diffusing from voids to surrounding resin and the surfaces of the prepreg layer is a highly transient process depending on the processing cycles as discussed in Chapter 4 Session 4.3. Models based on the air removal mechanisms can provide in-depth understanding of the void air removal in the OVB processing and the effects of initial prepreg properties and processing conditions, and the opportunities for optimizing the process cycle.

Void dynamic models involving gas diffusion and nucleation were developed by Amon et al. [22] and Arefmanesh et al. [23] for bubble growth in viscous fluid in foaming process, Roychowdhury et al. [25] for volatile induced void formation in PEI resin, and Ledru et al. [27] for void growth in the processing of thermosetting composites. In all these models, Fickian diffusion equation is used to describe the

volatile diffusion process, and mass conservation equation at the void polymer or composite interface. No voids initially exist in the polymers or composites, and spherical voids are assumed. In this study, models for both air diffusion through the thickness of single layer prepreg and prepreg stacks and air flow through interlayer region are developed. The diffusion model has initial conditions of existing air voids in the prepreg tape and dissolved air in the composite region of prepreg. The temperature cycles in the consolidation experiments in Chapter 4 are applied to the model. The corresponding characteristic time for air removal will be obtained to further justify the proposed mechanism.

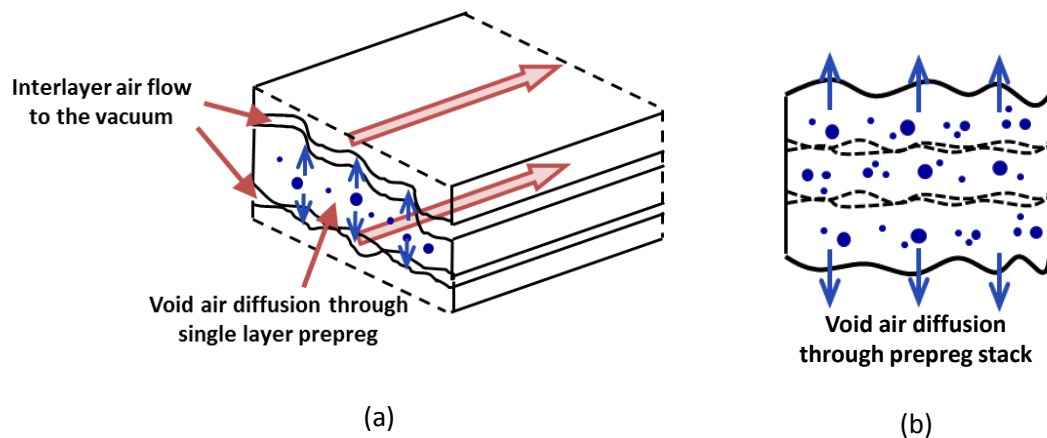


Figure 5.1 Schematic of void air removal mechanisms (a) void air diffusion through single layer prepreg followed by extraction through permeable interlayer regions, (b) void air diffusion through the thickness direction of a prepreg stack.

## **5.2 Model Set-up**

Based on the key mechanism for void air removal in the OVB processing of thermoplastic composites, models for air diffusion through single layer prepreg and air flow through interlayer region are developed separately. The air diffusion model for a single layer prepreg will be extended for prepreg stacks for the cases when the interlayer air flow is prohibited with sealed lateral edges of laminate stacks or extremely low air permeability of the interlayer regions.

### **5.2.1 Single Layer Air Diffusion Followed by Interlayer Air Flow**

#### **5.2.1.1 Non-isothermal Diffusion through Single Layer Prepreg**

In the thermoplastic prepreg tape, air molecules are partially trapped in the voids, and the rest are dissolved in the resin in the composite (fiber and matrix) region (Figure 5.2). Therefore, the through thickness diffusion model is composed of the composite domain and void domain. From statistical study of the void through thickness distribution, it is found that the void content is mainly distributed in the middle region of a prepreg layer. The model geometry is thus simplified by locating all voids in the center region of the prepreg tape as seen in Figure 5.3. With the application of vacuum before the thermal cycles in OVB processing, all the air in the interlayer region are evacuated (vacuum bag pressure and leaking are checked before processing). The air concentration at the surfaces of the tape is assumed 0 at all time. With this assumption, the diffusion is symmetric to the tape center, and air diffusion through half of the tape is solved in the model as illustrated in Figure 5.3.

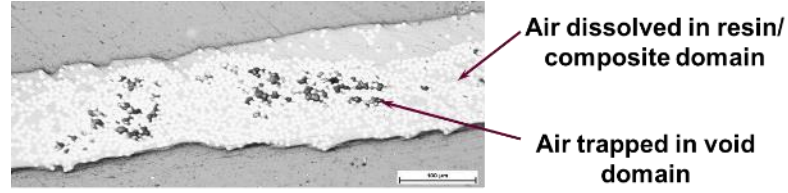


Figure 5.2 Air in voids and composite domains in the raw prepreg tape

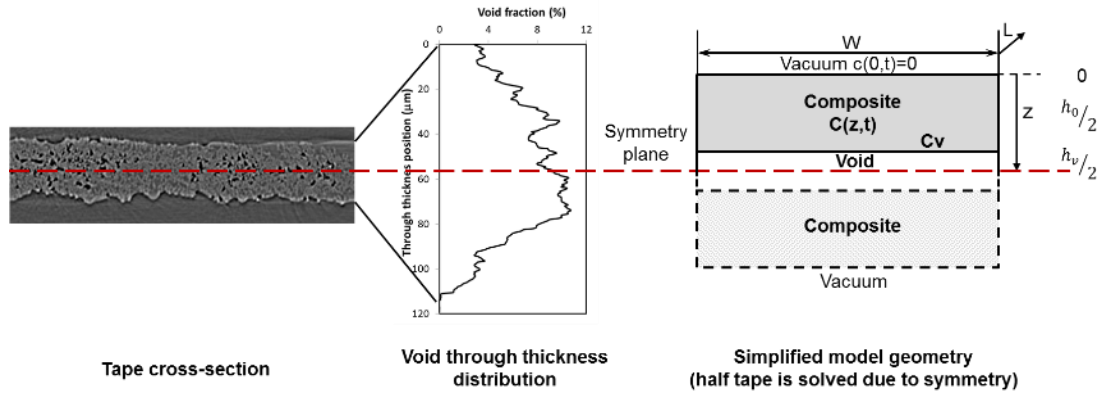


Figure 5.3 Simplified geometry for single layer diffusion model

In this model, through thickness diffusion of air molecules (79% N<sub>2</sub> and 21% O<sub>2</sub>) is calculated in composite domain. Void domain is a reservoir of air. And whether air goes into reservoir from the surrounding resin or goes out from the void depends on the concentration gradient at void boundary. Diffusion of air in composite domain follows 1-dimension Fick's second law:

$$\frac{\partial c_{c,g}(z,t)}{\partial t} = D_g(T(t)) \frac{\partial^2 c_{c,g}(z,t)}{\partial z^2} \quad (5.1)$$

Where  $c_c$  is the concentration in composite region; the subscript  $g$  denotes the volatile species (N<sub>2</sub> or O<sub>2</sub>).  $z$  is the position along the tape thickness and 0 at the tape surface.  $D_g(T(t))$  follows Equations E.7 and E.16 in Appendix E. Temperature  $T(t)$  is a

function of time for a processing cycle. The total diffusion length in composite domain is equal to half of the nominal tape thickness ( $h_0=0.18$  mm). The thickness of the void domain is calculated from the 2D void content  $V_{V0}$  (7.77%) and tape thickness:

$$\frac{h_v(0)}{2} = \frac{V_{V0} h_0}{2} \quad (5.2)$$

At the interface of composite and void domains (void boundary), mass conservation applies, i.e. the amount of air transport out from void domain is equal to that diffuse into the composite domain based on the mass conservation law. Therefore, at each time step  $\Delta t$ , the amount of gas transferred at the void boundary follows:

$$\Delta n_g(t) = q_g(t)\Delta t = -D_g(T(t)) \frac{\partial c_g(\frac{h}{2}, t)}{\partial z} \Delta t \quad (5.3)$$

Where  $q_g$  is the diffusion flux ( $\text{mol/m}^2 \text{ s}^{-1}$ ). The pressure  $P_v$  or volume  $V$  of the void domain follows ideal gas law:

$$P_v(t)V(t) = n(t)RT(t) \quad (5.4)$$

Where  $R$  is the gas constant. The void pressure  $P_v$  (Pa) is the sum of the partial pressure of  $\text{N}_2$  and  $\text{O}_2$ :

$$P_v(t) = P_{v_{N_2}}(t) + P_{v_{O_2}}(t) = [n_{N_2}(t) + n_{O_2}(t)] RT(t)/V(t) \quad (5.5)$$

Since this is a 1D model through the thickness direction of the tape, the other 2 dimensions are assumed to unit length. The void volume is represented by the void thickness as in Equation 5.2 with unit of m. Therefore, the amount of air in the void domain  $n_{N_2}(t)$  and  $n_{O_2}(t)$  are with the unit of  $\text{mol/m}^2$ .

The concentration of gases at void boundary follows Henry's Law:

$$c_{v_g}(t) = S_g(T(t)) P_{v_g}(t) \quad (5.6)$$

Where  $S_g$  is the Henry's gas law constant at temperature  $T$ , with a unit of  $\text{mol}/(\text{m}^3 \text{ Pa})$ . Since the prepreg tapes have been stored under ambient condition for a more than one

year, air dissolved in the resin and trapped in the voids reach equilibrium concentration under room temperature and atmosphere pressure. The initial condition in composite domain is:

$$c_{c-g}(z, 0) = S_g(298)P_g(z, 0) \quad (5.7)$$

Where the initial partial pressure for N<sub>2</sub> and O<sub>2</sub> are:

$$P_{N_2}(z, 0) = 0.79P_{atm} \quad (5.8)$$

$$P_{O_2}(z, 0) = 0.21P_{atm} \quad (5.9)$$

The initial amount of N<sub>2</sub> and O<sub>2</sub> in voids follows:

$$n_{N_2}(0) = 0.79 \frac{h_v(0)}{2} M(298K) \quad (5.10)$$

$$n_{O_2}(0) = 0.21 \frac{h_v(0)}{2} M(298K) \quad (5.11)$$

Where  $M(T)$  is number of mol of gas molecules per unit volume (mol/m<sup>3</sup>) and follows

$$M(T) = \frac{273}{T(K)} M_0 \quad (5.12)$$

And  $M_0$  is the number of mol gases per unit gas volume under 1atm pressure at 273K, 44.6 mol/m<sup>3</sup>. The gas concentration at the void boundary is given by:

$$C_{v_g}\left(\frac{h_0}{2}, 0\right) = S_g(298) P_{v-g}(0) \quad (5.13)$$

The partial pressure  $P_{v-g}(0)$  for N<sub>2</sub> and O<sub>2</sub> in the void domain follows equation 5.8 and 5.9 respectively. And  $S_g(298)$  for N<sub>2</sub> and O<sub>2</sub> is 1.92 mol/m<sup>3</sup> and 1.02 mol/m<sup>3</sup>, respectively.

Boundary condition at composite domain follows

$$c_c(0, t) = 0 \quad (5.14)$$

$$c_{c-g}\left(\frac{h_0}{2}, t\right) = c_{v_g}(t) \quad (5.15)$$

In void domain, two different boundary conditions apply to Equation 5.5. When temperature is below resin softening temperature (250-340 °C for semicrystalline PEEK [11]) the size of the voids  $h_v$  is assumed to be constant. Above this temperature, the pressure of the void domain equals to 1 atm at all time and the void size changes instantly based on ideal gas law with the assumption of resin flow over very small distance at void boundary.

Finite difference method is adopted to solve the partial differential equation of diffusion. All parameters are calculated for each time step  $\Delta t$ , and the upper bound for  $\Delta t$  is determined by the requirement of explicit finite difference scheme:

$$\frac{D\Delta t}{\Delta z^2} \leq \frac{1}{2} \quad (5.16)$$

All equations are programmed in LabVIEW 2015. A user interface model is developed integrating tape geometry and initial void content, processing cycle and vacuum level and the final amount of gas molecules in voids and void size. Therefore, one can apply the properties of other thermoplastic prepreg tapes, varies the processing conditions and predict the final void content in terms of void size or amount of void air.

### **5.2.1.2 Model for In-plane Interlayer Air Flow**

#### **5.2.1.2.1 General Model Set-up**

After diffusing out from single layer prepreg tape, it is assumed that all air molecules cumulate and fill in the interlayer cavities, and then flow out to the vacuum. In this model, the interlayer region between two prepreg layers is assumed to be in rectangular geometry as shown in Figure 5.4. Isothermal condition at the temperature that single layer diffusion process finishes is applied to the air evacuation through the

interlayer. With the fixed volume of the interlayer cavity and vacuum pressure at the edge ( $L_0$  position in Figure 5.4), the pressure in the cavity is a function of time and location ( $l$ ). Following Darcy's Law, the laminar air flow rate is given by

$$Q(l, t) = \frac{n(l, t)RT}{P(l, t)} = - \frac{Kh W dP(l, t)}{\mu(T) dl} \quad (5.17)$$

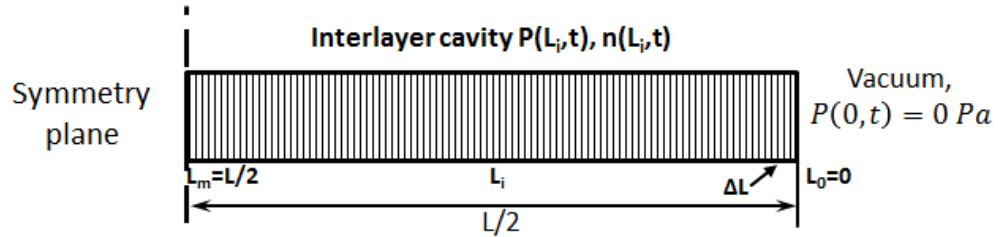


Figure 5.4 Schematic of air flow model in an interlayer cavity.  $L$  is the length of the interlayer cavity that air flow through; the transient flow is solved with finite difference method with element length of  $\Delta L$ , and  $m$  is the total number of elements.  $i$  denotes the  $i$ <sub>th</sub> number of element ( $i=1, \dots, m$ ) and the  $i$ <sub>th</sub> point along the panel length ( $i=0, \dots, m$ ).  $P(L_i, t)$  and  $n(L_i, t)$  are the pressure (Pa) and amount of molecules (mol/m) of air in the  $i$ <sub>th</sub> element.

To solve this transient problem, finite difference method was used and the interlayer region is divided into a number of sub-cavities (elements) as shown in Figure 5.4 and Eq.5.17 is satisfied for each element at each time step  $\Delta t$  in the following form:

$$\frac{\Delta n(L_{i-1}, t_k) RT}{P(L_i, t_k)} = - \frac{Kh (P(L_i, t_k) - P(L_{i-1}, t_{k-1}))}{\mu(T) \Delta L} \Delta t \quad (5.18)$$

Where,  $k$  is the number of time steps, starting from 1;  $T$  is the processing temperature when diffusion in the single layer finished. Mass conservation gives the total amount of gas in each element after  $t$ :

$$n(L_i, t_k) = n(L_i, t_{k-1}) - \Delta n(L_i, t_k) + \Delta n(L_{i+1}, t_k) \quad (5.19)$$

The new pressure in sub-cavity  $i$  at time  $t$  is:

$$P(L_i, t_k) = P(L_i, 0) \frac{n(L_i, t_k)}{n(L_i, 0)} \quad (5.20)$$

Where,  $n(L_i, 0)$  is the initial amount of gas in each sub-cavity (mol/m);

$$n(L_i, 0) = h_v M(T) \Delta L \quad (5.21)$$

The initial pressure in sub-cavity  $P(L_i, 0)$  is:

$$P(L_i, 0) = \frac{T}{298} \frac{V_V}{v_i} P_{atm} \quad (5.22)$$

Where,  $v_i$  is the content of interlayer space, and 20% was obtained from the surface roughness characterization in Chapter 3. The dynamic viscosity of air (Pa.s) as a function of temperature is given by

$$\mu(T) = c \frac{T^{1.5}}{T+S} \quad (5.23)$$

Where  $c$  and  $s$  are constants, and  $c=1.458 \text{ e-}6 \text{ Kg}/(\text{m s K}^{1/2})$ ,  $S=110.4 \text{ K}$  for air. [102]

#### 5.2.1.2.2 Klinkenberg Effect

During the OVB processing of thermoplastic composites, interlayer permeability reduces as the resin is softened at high temperature and after long time dwell (240°C under standard heating rate as measured in Chapter 3.). This is due to the reduction of the free space in the interlayer region. For gas flow in the porous media with small pore sizes, gas molecules may slip in the flow channels and the Klinkenberg may be considered. [82,83] Knudsen number is typically used to classify the flow regime. The Knudsen number for the interlayer region with different lay-up and temperature condition are estimated in Appendix G. And it is found that when the permeability thickness products are below the  $1\text{E-}17 \text{ m}^3$  which occurs for the 90°/90° interlayer when processing temperature is above 240 °C, slip flow may be applied.

With the Klinkenberg effect, the measured gas permeability  $K$  is linearly dependent on the intrinsic permeability of the porous media  $K_\infty$

$$K = K_\infty \left(1 + \frac{b}{P}\right) \quad (5.24)$$

Where  $P$  is the pressure of the gas, and  $b$  is the Klinkenberg parameter. Since the intrinsic permeability of a porous media essentially depends on the nature of the pore sizes and geometry, research efforts have been made on finding the relationship between  $b$  and  $K_\infty$ . Both experimental curve fitting and analytical derivation end up describing  $b$  as a power law function of  $K_\infty$ . [81,82,88,103,104] Civan [104] improved the formulation and methodology and obtained  $b$  for different gases as

$$b = 2.79 \times 10^3 \frac{\mu(T)}{\sqrt{M}} K_\infty^{-0.5} \quad (5.25)$$

Where  $M$  is the molecular mass of the gas with the unit of Kg/mol. For air at the room temperature at 1 atm,

$$b = 9.55 \times 10^{-3} K_\infty^{-0.5} \quad (5.26)$$

With the consideration of Klinkenberg parameter, by replacing  $K$  with Equation 5.24 in Equation 3.3 and 3.4 in Chapter 3, the relationship between intrinsic permeability thickness product  $K_\infty h$  and the measured  $Kh$  can be derived as (details in Appendix G)

$$Kh = K_\infty h \left(1 + \frac{2b}{P_{atm}}\right) \quad (5.27)$$

The Klinkenberg parameter  $b$  and  $K_\infty h$  are listed in Table G.3 in Appendix G. The ratio  $K_\infty h / Kh$  for 90°/90° interlayer at 300°C (with  $Kh$  of 7.89E-17 m<sup>3</sup>) shows the difference between  $K_\infty h$  and  $kh$  is within the variation of the measurement results (10%). This justifies our assumption to ignore the Klinkenberg effect in Chapter 3. However, in the transient model of interlayer air flow developed here, the Klinkenberg

effect can be more obvious as the gas pressure  $P$  reduces and enhance the local flow rate with the slip velocity. Therefore,  $K$  in Equation 5.17 and 5.18 are replaced with  $K_\infty$ , and gives

$$\frac{\Delta n(L_{i-1}, t_k) RT}{P(L_i, t_k)} = - \frac{K_\infty h \left(1 + \frac{b}{P(L_i, t_k)}\right) (P(L_i, t_k) - P(L_{i-1}, t_{k-1}))}{\mu(T) \Delta L} \Delta t \quad (5.29)$$

### 5.2.2 Through Thickness Diffusion in Prepreg Stacks

In the case of sealed lateral edges, interlayer air is trapped in the laminate. The removal of air in both inter- and intra-layer voids relies on diffusion through the thickness of a laminate. The model for single layer diffusion is extended to multilayer diffusion for laminates. Figure 5.5 illustrates the simplified geometry of the diffusion model of prepreg stacks with an example of a 3-layer laminate. The intralayer void domain is placed in the center region of one layer as in the single layer diffusion model, while the interlayer void domain is in between two layers. The interlayer void content is 20% based on 1 layer thickness obtained from tape surface roughness characterization and normalized with tape thickness in Chapter 1. The top and bottom surfaces of the laminate are exposed to vacuum, thus the diffusion is symmetric to the mid-plane of the laminate and solved through half of the laminate thickness in the multilayer diffusion model. The equations for mass conservation, ideal gas law, and Henry's law are applied to both intra- and inter-layer void domain which are void air sources region. The initial conditions and all boundary conditions in the model of single layer diffusion are applied to this multilayer diffusion model as well. LabVIEW is also used for programming this

model and integrating the inputs of material properties, processing conditions and final void air content.

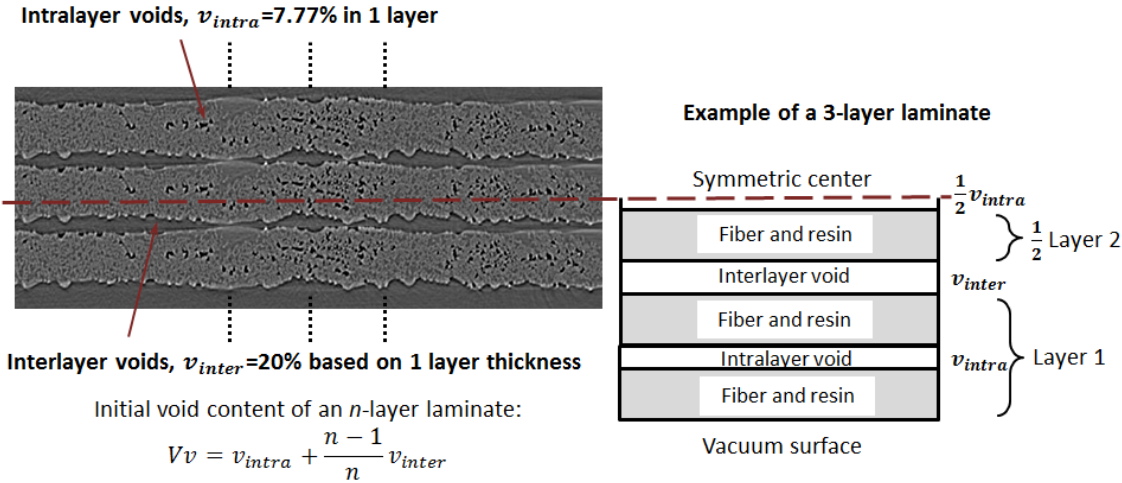


Figure 5.5 Simplified geometry for the model of diffusion through the thickness of prepreg stack with an example of a 3-layer laminate

### 5.3 Modeling Results for Consolidation Experiments

The void air removal in the 2 layer and 72-layer thick laminates in Chapter 4 are modeled. For the 2 layer and 72 layer laminates with perimeter open to vacuum, the models of diffusion through single layer prepreg and interlayer air flow are applied. For the 72 layer laminate with edge sealed condition, air removal is modeled through the diffusion through the thickness of prepreg stack. The bulk temperature profiles of 2-layer and 72-layer laminates presented in Chapter 4 Figure 4.5 are fitted into Gauss functions of time with the general equation below:

$$T(K) = f(t) = \sum_{i=1}^n a_i \times \exp\left(-\left(\frac{t-b_i}{c_i}\right)^2\right) \quad (5.30)$$

The fitting parameters n, a, b and c to achieve R-square > 0.9999 are shown in Table H.1 in Appendix H.

### 5.3.1 Air Removal in Laminates with Perimeter Open to Vacuum

#### 5.3.1.1 Results of Single Layer Diffusion

After the calculation, the evolution of the amount of air (sum of N<sub>2</sub> and O<sub>2</sub>) in the void domain of 2-layer and 72-layer laminate with perimeter open to vacuum were obtained and normalized with the original gas amount. The results are presented in Figure 5.6. The concentration gradient of N<sub>2</sub> in the composite domain in the single layer of the 72-layer laminate is showing in Figure 5.7. It is seen that at early stages of temperature ramping up (T < 110 °C in this cycle), air molecules dissolved in the resin diffuse in two directions: to the vacuum and into the void domain. In this stage, although the void pressure increases with temperature, the solubility of gases decreases with temperature, the concentration of gases at void boundary based on Henry's Law is still smaller than that in the surrounding resin. As the air in the resin continuously diffuse out to the vacuum, and concentration gradient in the composite domain is changed to one direction to the vacuum. The transient diffusion turns into steady state process (straight lines at temperature above 130 °C in Figure 5.7). And the concentration in the resin adjacent to void becomes smaller than at void boundary. This concentration gradient drives the void gases diffuse out into the adjacent composite region and eventually to the vacuum.

In this experimental processing cycle, the normalized amount of air in voids reached 0.01% of the initial amount after processing time of 74.3 min and 97.2 min,

corresponding to the temperature of 200°C and 197°C for 2-layer and 72-layer laminates, respectively as shown in Figure 5.6. These temperatures are way below the resin melting temperature, and the resin viscosity is still too high to close-up the interlayer gaps. From the characterization of interlayer permeability in OVB processing in Chapter 3, the permeability at these temperatures are still experimental measurable with our 1D flow set-up. The corresponding permeability thickness products are used in the calculation of air flow time in our interlayer air flow model in the Section 5.3.3.

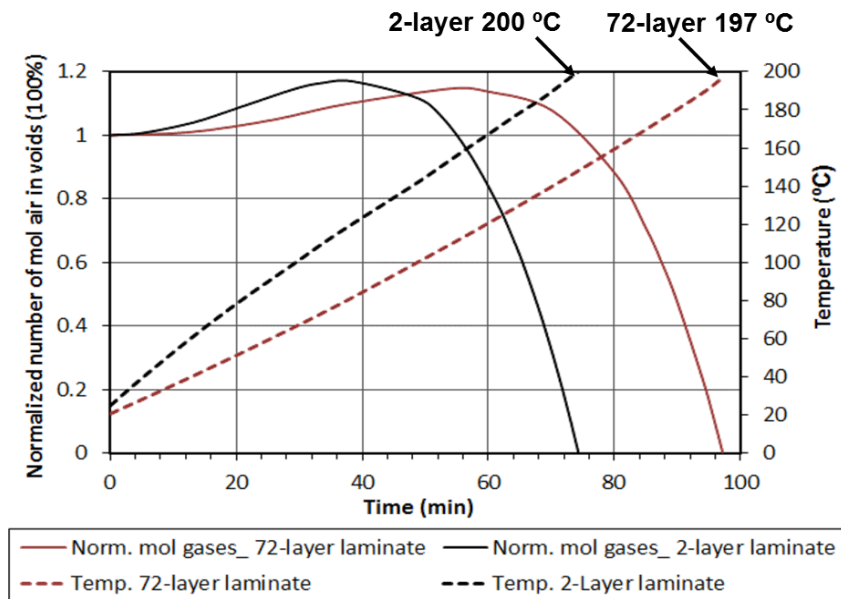


Figure 5.6 Evolution of number of moles of air normalized by the initial amount in voids in single layers of 2-layer and 72-layer laminates with perimeter open to vacuum, showing diffusion of single layer for thin and thick laminates completes at 200 °C and 197 °C during the heating ramps, respectively.

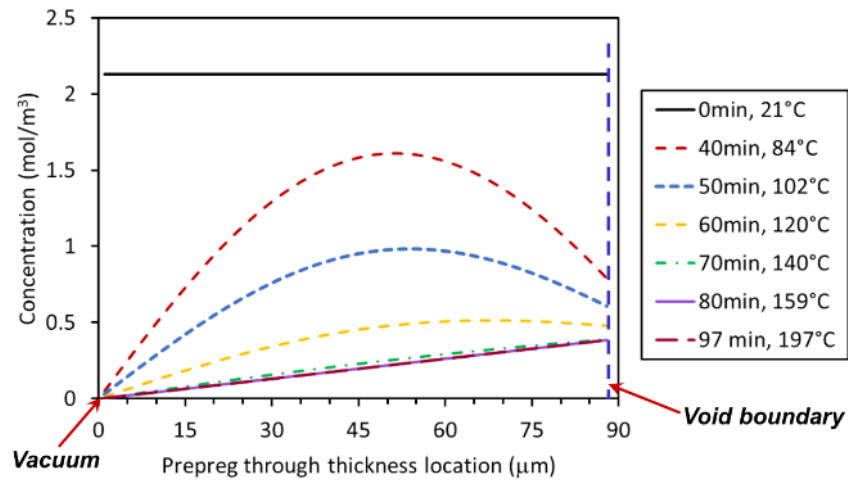


Figure 5.7 Concentration gradient of N<sub>2</sub> in the composite domain in the model of single layer diffusion during the heating ramp of 72-layer thick laminates

### 5.3.1.2 Characteristic Time for Interlayer Air Flow

Taking the cases of processed laminates, flow length is half of panel size due to the in plane symmetry of the panels,  $L = 0.15m$ . At temperature of 200 °C where 99.9% air in the voids has already diffused out from the single layer prepreg tape (calculated in Section 5.3.1), air viscosity is  $2.62 \times 10^{-5} Pa.s$ . From the measurement of interlayer permeability thickness products after different processing temperature in Chapter 3, the  $Kh$  values of  $1.8E-15 m^3$  and  $2.5 E-15 m^3$  (middle of the  $Kh$  at 170 °C and 240 °C) are used for 0°/0° and 0°/90° interlayer respectively. In order to obtain accurate results, small time step of  $10^{-9}s$  and 200 sub-cavities were used in the model. And the time to vent out 99.9% of the original amount of air is only 0.74 s and 0.55 s for 0°/0° and 0°/90° interlayers, respectively. With this extremely short flow time, air in the thick laminate in experiment can be removed before resin melted, resulting in almost void free void content.

### 5.3.2 Diffusion through Prepreg Stacks during Processing

For the laminate with lateral edges sealed in the OVB processing, void air removal can only rely on diffusion through the laminate thickness. With the Multilayer diffusion model in Section 5.2.2, applying the initial inter- and intra-layer void content shows in Figure 5.5, and the bulk temperature profile of 72-layer thick laminates, and resin softening temperature of 280 °C, three layers close to the surfaces of prepreg stack are void free after the processing cycle, which is comparable to the experimental result of about 7 void free surface layers shown in Chapter 4 (Figure 4.6). And overall 10% of the amount of air is removed after the processing cycle.

With the same temperature profile of the thick laminates in the consolidation experiment, a 5-layer laminate is predicted void free with the resin softening point of 280°C. The concentration profiles of N<sub>2</sub> in the composite domain of the layers during the temperature ramping are shown in Figure 5.8. It is seen that the concentration profile of the composite domain of inside half layers are the same due to the same conditions at the adjacent void boundaries. At the early stage of heating, the dissolved air in the composite domain diffuses into the two adjacent void domains as the solubility of in the composite domain decreases. This can also be seen in Figure 5.9 where the normalized number of mole of air in each void domain increases to be above 1 at temperature below 120 °C. The surface half layer next to the vacuum show similar behavior as in the single layer diffusion model. As the concentration gradient points in the direction of vacuum (120 °C in Figure 5.8 ½ layer 1), the air in the intralayer void domain of layer 1 in Figure 5.9 starts to diffuse out to the direction of the vacuum. At this time, the air in the composite domain of the inside layers keep diffusing in to the adjacent voids as shown in Figure 5.9. and approaching to steady state diffusion as the straight lines are shown at temperature above 160 °C in Figure

5.8. When the processing temperature is above 240°C, the concentration profile over the composite domain of the entire half laminates show gradient in the direction of vacuum and the air in all void domain are reducing as in Figure 5.9. It is seen that the air removal starts from the first void domain close to the vacuum, and then one by one towards the inside layers. Void air in the inside layers require more processing time or higher temperature during heating to diffuse out (360°C of the intralayer voids in layer 3 vs 280°C in layer 1 in Figure 5.9).

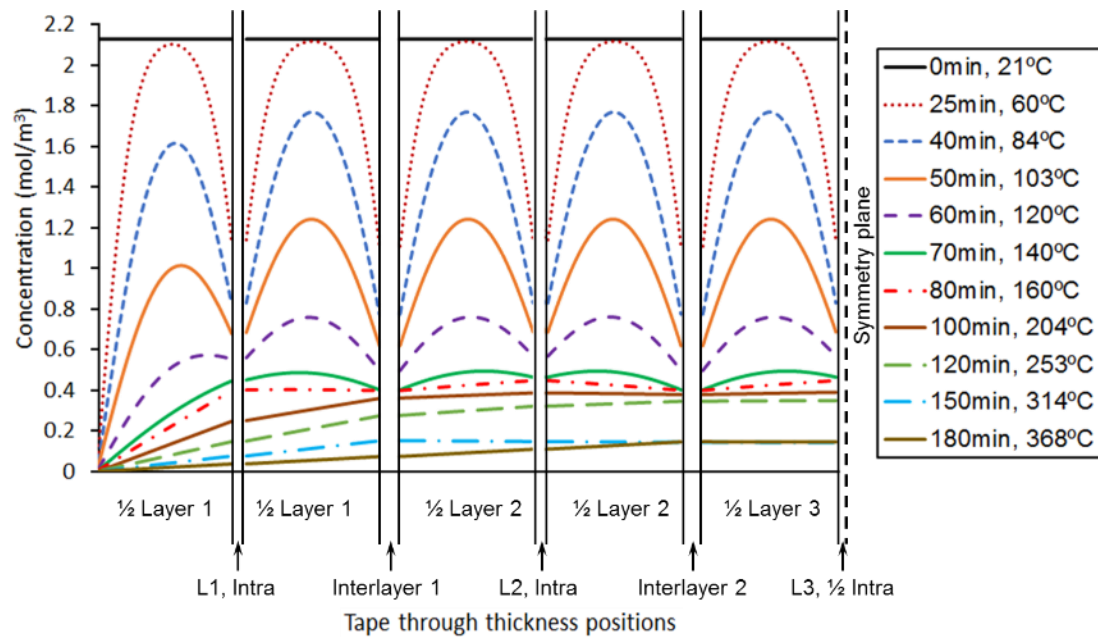


Figure 5.8 Concentration profile of N<sub>2</sub> in a 5-layer laminates during the heating ramp of consolidation experiment cycle for thick laminates

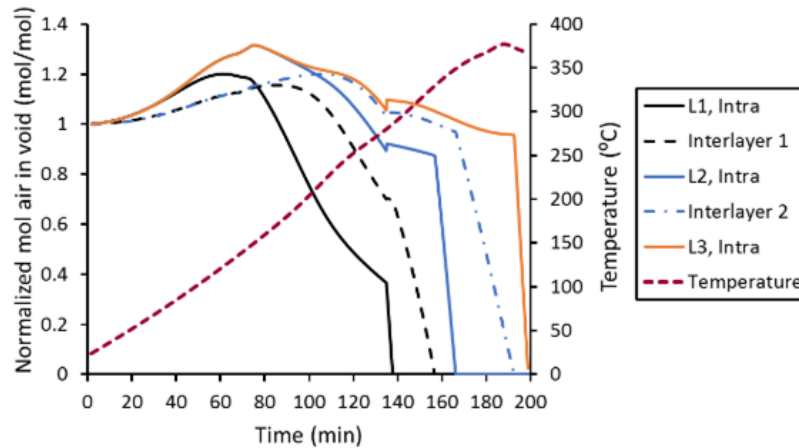


Figure 5.9 Normalized amount of air in each intra- and inter- layer void domain of a 5-layer laminate during the heating ramp of consolidation experiment for thick laminates

The evolution of the thickness of the void domains during heating is presented in Figure 5.10. Due to the higher void content in the interlayer region than inside the tape, void thickness of interlayer voids is higher than that of the intralayer voids. The thicknesses of all voids do not change before the resin softening point of 280°C. After 280°C, the void thickness changes instantly with the vacuum pressure as assumed in the model set-up, resulting in step changes of the void thickness shown in Figure 5.10. The void thickness then reduces with the reduction of the amount of air inside the voids, and gradually from the surface layers to the inside layers.

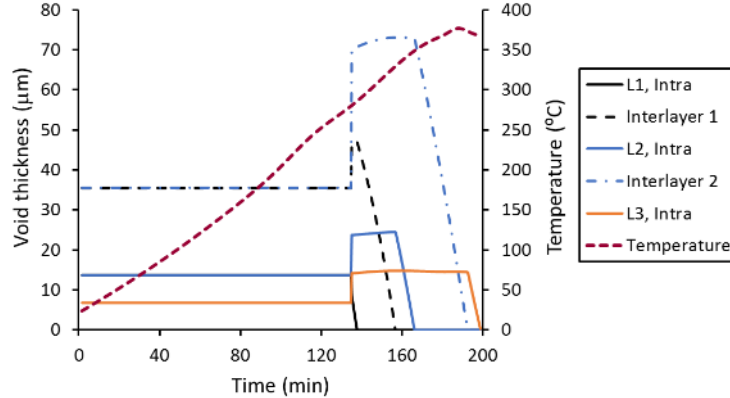


Figure 5.10 Thickness of each intra- and inter- layer void domain of a 5-layer laminate during the heating ramp of consolidation experiment for thick laminates

With the multilayer diffusion model, the diffusion times required to reach 1% void content in laminates having 1 to 72 layers (nominal total laminate thickness of 12.8 mm) at 380 °C are estimated and shown in Figure 5.11. Compared to the characteristic diffusion time required to remove 99% homogeneously distributed N<sub>2</sub> in the same laminate thickness, removing air in the intra- and inter-layer voids in the laminates require significantly longer time (109 hrs vs. 14 hrs). And the diffusion times are significantly higher than typical processing dwell times, i.e. exceeding 8 hours for parts thicker than 16 layers (2.8 mm). Nevertheless, the diffusion time for a single layer is small (77.8 seconds). With these results, we can conclude that for all practical applications, void reduction by diffusion mechanism alone is limited to thin laminates.

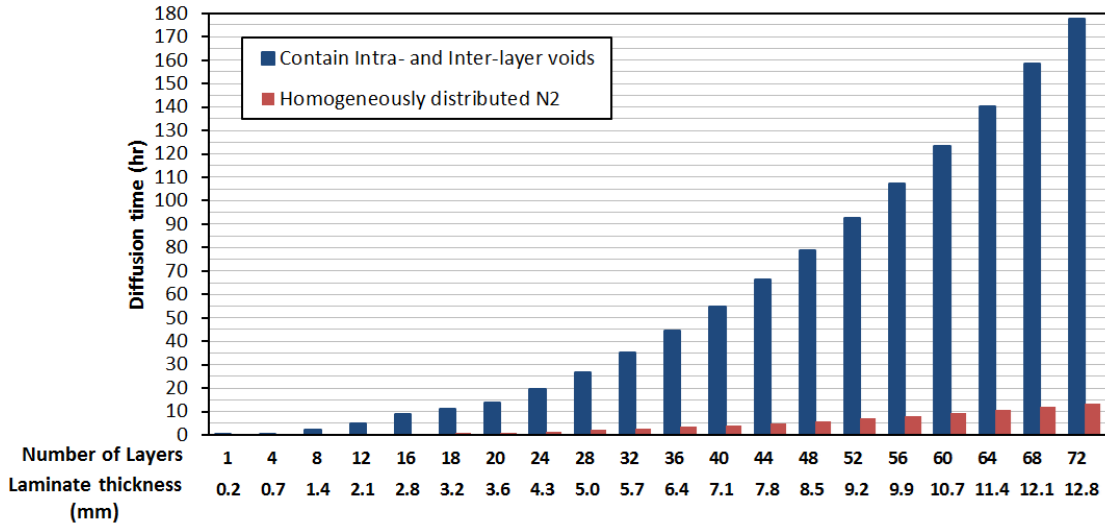


Figure 5.11 Diffusion time to achieve 1% void content in a laminate of the 1 to 72 - layer laminates. With the intra and interlayer voids inside of the laminates, the diffusion time required to remove air inside of the voids is much longer than that with homogeneously distributed N<sub>2</sub> and no voids in the tape

The above modeling results of air removal through thickness diffusion and interlayer air flow further validate that the combined mechanism of single layer diffusion and volatile flow through interlayer region can provide low void content of thick laminates in OVB processing as thin laminates.

#### 5.4 Summary

Non-isothermal gas diffusion model and interlayer air flow model are developed to simulate void air removal in the thermoplastic OVB processing. Models for single layer diffusion followed by interlayer air flow and multilayer diffusion can be applied to the laminates with lateral edges opened (allow interlayer air flow) and sealed (prohibit interlayer air flow), respectively. With the temperature profile in the consolidation experiments in Chapter 4, the single layer diffusion model predicts that

the 99% air diffuses out from voids at 200°C. Interlayer air model with the permeability input from Chapter 3 calculated extremely short air flow time for the experimental laminate size. Multilayer diffusion model predicts 4 void free surface layers for the 72-layer laminate under edges sealed condition, which is relatively conservative comparing to the experimental results of 7 layers. The modeling results analytically validated the key air removal mechanism of void air diffusing through the thickness of single diffusion and then flowing through the permeable interlayer region for thick section thermoplastic composites.

With the models, void air diffusion and flow can be investigated for various processing conditions and different sizes of the laminates. For a certain laminates, an optimized efficient and effective processing cycle may be designed from these models. Further parametric study and processing optimization will be introduced in Chapter 7. It is seen that the interlayer permeability during processing can significantly affect the air flow time. Although permeability is experimentally studied in Chapter 3, it is crucial to understand how the permeability could be affected with different processing condition, which will be investigated through the material behavior in the next chapter.

## Chapter 6

### MODEL FOR MATERIAL BEHAVIOR OF INTERLAYER REGION BEFORE RESIN MELT IN THE OVB PROCESSING

#### 6.1 Introduction

The characterization of interlayer air permeability in Chapter 3 shows that the reduction of permeability occurs with the increasing temperature and dwell times in the OVB processing below the melting point of the thermoplastic resin (PEEK in this work). The air removal models developed in Chapter 5 indicates that the permeability level during the processing may affect the void air removal and thus the void reduction during processing. Therefore, it is important to understand how the permeability could change with different processing conditions.

The reduction of the interlayer permeability is essentially from the reduction of interlayer free space, and relates to the development of the intimate contact between layers. The mechanism of intimate contact of thermoplastic composites has been investigated experimentally and analytically. [35,40,84,105–109] The models of intimate contact start with simplifying the geometry of the rough surfaces of the thermoplastic prepreg tapes with a distribution of rectangular elements [110], or a periodic array of identical rectangular elements [32,33,35,43,105,111], or using the fractal description of the rough surfaces [84,98,107,112]. However, all models are established based on the squeeze flow of the material which can only be applied to the processing temperature above resin melting point. Literatures have shown that the squeeze flow models can successfully predict the degree of intimate contact in the fast

speed processing such as ATP and filament winding. [20,31,33,34,106] In these processes, the heating rate can be as high as 200 °C/s (1.2E+4 °C/min) [113]. Therefore, the resin can be instantly melted and the development of intimate contact is dominated by the squeeze flow mechanism when resin is a fluid. In the OVB processing, the heating rate is typically 1 °C/min to 10 °C/min due to the heating mechanism and efficiency of the oven. The time required to reach the resin melting temperature for consolidation is significantly longer than in the ATP process. For PEEK resin, the processing time before reaching resin melting temperature of 340 °C can be in hours. When the temperature is above the glass transition and below the melting point, semi-crystalline polymers are in their rubbery state, and can subject to viscoelastic and viscoplastic deformation which are time and temperature dependent. Therefore, the mechanism for the reduction of interlayer permeability and interlayer free space below the resin melting point in the OVB processing is different from squeeze flow. The intimate contact model cannot be applied to the study of the evolution of interlayer region. In this Chapter, a material model based on the resin behavior is established for the non-isothermal condition in the OVB processing. The model results are compared to that from the measured interlayer permeability thickness products in Chapter 3. The materials behavior of the interlayer region is then discussed with the microstructure of the tape surface region and the surface characteristics of the tape from interlayers after processing. Prediction of the evolution of the interlayer region is attempted. The effect of the processing conditions to the evolution of the interlayer region is then discussed.

## 6.2 Related Mechanical Properties of PEEK resin

The modulus of PEEK at temperature range between -60 °C and 120 °C is about 3.5 GPa (with crystallinity of 35%), but reduced to an order magnitude smaller above glass transition temperature. [11,92]. Wang and Sun characterized the resin dominated transverse modulus of carbon PEEK composites under temperature up to 315 °C. [114,115] 50% loss of modulus was obtained after the resin glass transition, and the modulus is more than one order magnitude smaller at 315 °C than at room temperature. The temperature and strain rate dependent yield stress of PEEK resin has been observed experimentally[116–121]. EI-Qoubaa and Othman investigated the compressive yield stress of PEEK over the strain rate range of 1E-4/s to 1E+4/s and temperature range of -130 °C to 200 °C, and found that the yield stress sharply drops at the glass transition temperature, and the strain rate sensitivity increases with increasing strain rate. [116,117]

PEEK is subject to time and temperature dependent viscoelastic and viscoplastic creep deformation [91,122–125]. When the applied stress is smaller than the polymer yield stress, the modulus of the material degrades with time. Creep strain can be introduced into the material when a constant force or deadweight is applied. This strain is recoverable with time after the stress is removed. This behavior is a typical viscoelastic phenomenon and can be described with the viscoelastic constitutive models. The viscoelastic property of PEEK resin was characterized by several researchers with temperature up to 200 °C. [91,121,123,124,126–129] The principle of time-temperature superposition was applied to generate the master curve of the viscoelastic compliance. Arrhenius equation and Williams – Landel-Ferry equation were both used to fit the time –temperature shift factor. [119,126,127] Linear viscoelastic response at stress level smaller than 30 MPa at 90 °C was found by Xiao.

Sonmez and Hahn applied the linear viscoelastic constitutive model developed by Xiao on the analysis of stress distributions within the APC2 PEEK laminate. [130]. The creep strain observed from the viscoelastic response of PEEK is typically smaller than 1%. [131]

At stress levels higher than the yield stress of material, the time dependent creep deformation of material is permanent, which can be analyzed with viscoplastic models. The viscoplastic behaviors of PEEK and APC2 carbon PEEK composite at elevated temperature were investigated by Ha et al. The model for composite is developed based on the micromechanics theory integrating the linearly elastic response of the fibers and viscoplastic deformation of the resin. The viscoplastic constitutive model of PEEK resin adopted the von Mises criterion. The temperature dependent parameters of materials to fit the equations are from experimental measurements of PEEK resin at temperatures up to 177 °C. It is found that the viscoplastic creep behavior of APC2 composites is very sensitive to the applied load and the temperature. [123] Sun and coworkers investigated the elastic/viscoplastic properties of APC2 composites and developed constitutive model with the overstress function and the temperature dependent material constants from off- axis tension tests with temperature up to 315 °C.[115,132]

### **6.3 General Approach and Model set-up for Kh Prediction**

During the OVB processing, after the vacuum is applied, there is a constant force on top of the prepreg layers due to the atmosphere pressure outside of the vacuum bag, as shown in Figure 6.1. Similarly as in the intimate contact model with periodic array of identical rectangular elements [32,33,35], the interlayer region can be simplified into an array of N number of unit cells with the variation of the surface

roughness along the fiber direction ignored as shown in Figure 6.2. Under the force equilibrium, a constant force  $f$  is applied on each unit cell per unit length of the tape. The rectangle  $h_0 \times b_0$  represents the contact region of the surfaces, and  $h_0 \times w_0$  is the empty region that contributes to the interlayer permeability. Since the empty region of a unit cell does not sustain any load, the constant force  $f$  will act on the contact region  $b_0$ . Therefore, the initial local stress  $\sigma_0$  on  $b_0$  follows:

$$\sigma_0 = \frac{f}{b_0} = \frac{P_{atm}}{\frac{b_0}{L}} \quad (6.1)$$

Where  $\frac{b_0}{L}$  is defined to be the initial degree of intimate contact between layers in the intimate contact model. [32,33,35]

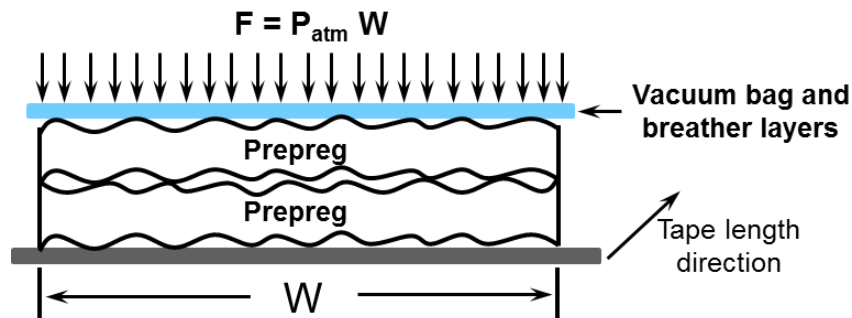


Figure 6.1 Constant force  $F$  per unit tape length applied through vacuum bag on top of the prepreg layers

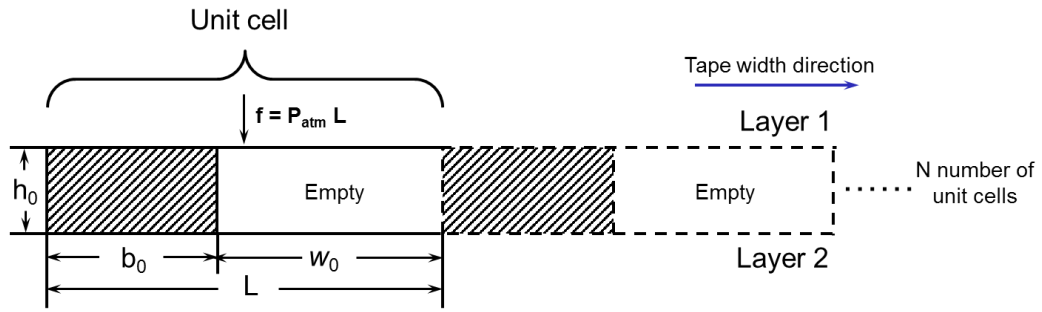


Figure 6.2 Simplified geometry and unit cell of the interlayer region along the tape width direction with a constant force  $f$  per unit length of the tape on each unit cell.

With the increasing time and temperature in the processing, the interlayer region height  $h$  reduces and  $b$  expands due to the Poisson's effect, as presented in Figure 6.3. Force equilibrium is maintained during the entire processing, therefore, we have

$$\sigma(T, t) b(T, t) = \sigma_0 b_0 = f \quad (6.2)$$

and

$$\sigma(T, t) = \frac{P_{atm}}{\frac{b(T, t)}{L}} \quad (6.3)$$

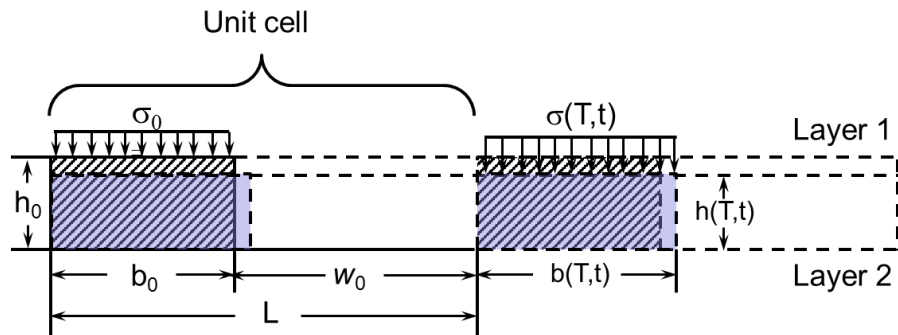


Figure 6.3 Unit cell of interlayer region before and after deformed with processing time and temperature

From the cross-sectional micro images of the AS4/APC2 prepreg tape (Figure 1.4 in Chapter 1 and Figure 3.1 in Chapter 3), it is seen that the thin rough surface layers contain resin pockets and is more resin rich compared to the inner body of the tape. The fiber content in the surface region is thus significantly lower than the nominal fiber content of the tape. Therefore, the material behavior model with the properties and material constants of resin will be adopted to obtain the strain of unit cell height  $\varepsilon_h$ .

Since the empty region in the unit cell contributes the interlayer permeability, the interlayer permeability thickness product  $Kh$  may be calculated. If a flat surface is placed on top of the prepreg tape, the interlayer geometry shows that  $w_0$  is significantly larger than  $h_0$  with the ratio of  $h_0/w_0$  in the order of 0.01. The initial contact area  $b_0$  and the degree of contact  $b_0/L$  is smaller than 1% (Figure G.1 in Appendix G). Therefore, the permeability thickness products of the interlayer region can be expressed as

$$Kh = \frac{h^3}{12} \quad (6.4)$$

With the  $Kh$  values measured in Chapter 3, the strain of  $h$  at different temperature and dwell times can be obtained and presented in Figure 6.4 for  $0^\circ/0^\circ$  and  $0^\circ/90^\circ$  interlayers. It is seen that although the strains of  $h$  of  $0^\circ/90^\circ$  interlayer are significantly smaller than those of  $0^\circ/0^\circ$  interlayer at temperature higher than  $170^\circ\text{C}$  and the dwell cycles, both interlayers show large permanent strains. There is no significant increase of the strain at temperature above  $170^\circ\text{C}$  for  $0^\circ/90^\circ$  interlayer and after 10 mins dwell at  $240^\circ\text{C}$  even after 8hrs dwell for  $0^\circ/0^\circ$  interlayer. This does not follow the time and temperature dependent behavior of the resin, and may be due to the elastic response of the fiber-fiber contact in the interlayer region. For the  $0^\circ/0^\circ$  interlayer, a higher strain

than the plateau strain is found at temperature of 300 °C. The DMA result of the prepreg tape in Figure 3.10 in Chapter 3 shows that the transition from rubbery plateau to fluid occurs at about 280 °C. Therefore, it is highly possible that this strain is due to the squeeze flow response of the interlayer region. Therefore, cut-off strains of 7.5% and 44% are obtained from the plateau strains of the 0°/90° and 0°/0° interlayers, respectively and applied to the resin behavior model.

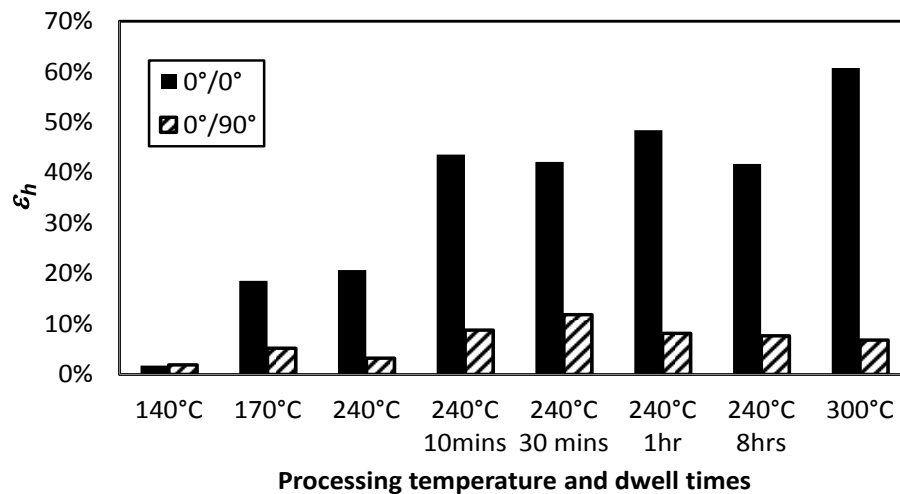


Figure 6.4 strain of  $h$  derived from measured  $Kh$  for 0°/0° and 0°/90° interlayers at elevated temperature and dwell time in OVB processing, showing large permanent strain and cut-off strains for both interlayers

The general approach for predicting  $Kh$  follows the flow diagram in Figure 6.5. With the selection of initial  $b_0/L$  ratio, initial stress  $\sigma_0$  can be obtained based on the force equilibrium. With the same time and temperature condition as the measured  $Kh$ , the strain curve of  $h$  can be obtained through resin behavior model, and compared to the strains  $\varepsilon_{h-layup}(T, t)$  calculated from the measured  $Kh$  for the lay-up. The

strain curve with best agreement determines the initial stress  $\sigma_{0-layup}$  for this lay-up. With the  $h_0$  obtained from measured  $Kh$  before processing,  $\sigma_{0-layup}$  and the resin behavior model, the  $Kh$  under any temperature condition could be predicted.

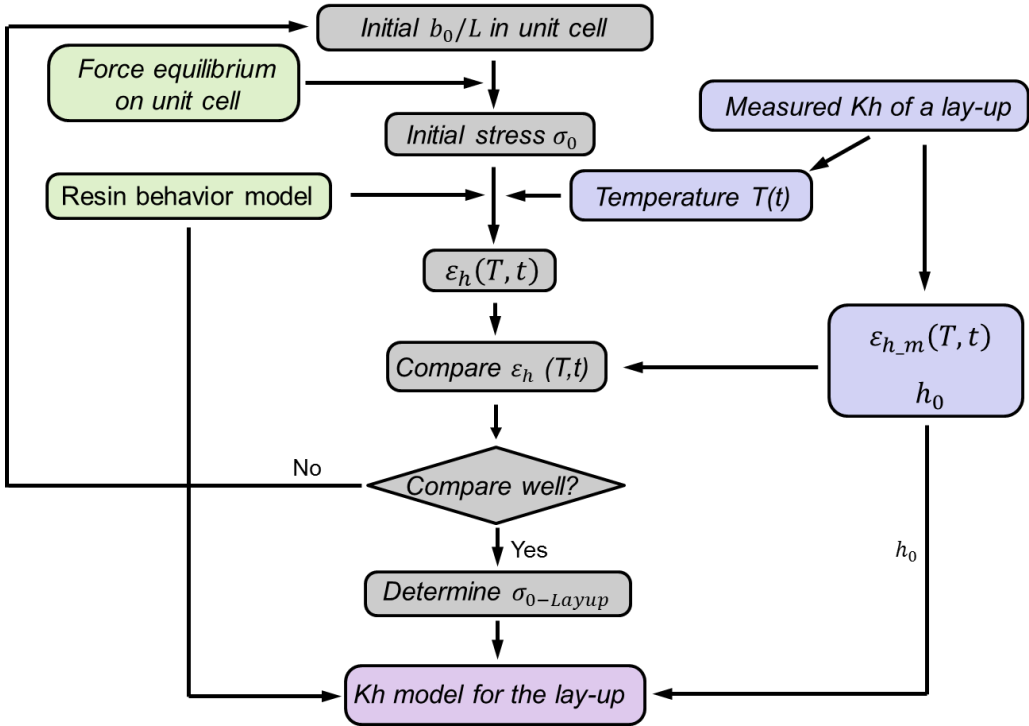


Figure 6.5 General approach to determine the model of  $Kh$  for a lay-up configuration

**6.4 Resin Behavior Model**

In this section, the model set-up for material response of the interlayer region during the processing cycle in the OVB processing will be presented. The strain of the height of the unit cell  $\epsilon_h(T, t)$  during processing can be composed by the instantaneous and reversible elastic strain  $\epsilon_e(T)$ , time dependent recoverable viscoelastic strain  $\epsilon_c(T, t)$  and permanent viscoplastic strain  $\epsilon_p(T, t)$ , as below

$$\varepsilon_h(T, t) = \varepsilon_e(T) + \varepsilon_c(T, t) + \varepsilon_p(T, t) \quad (6.5)$$

And the deformed  $h$  is

$$h(T, t) = h_0(1 - \varepsilon_h(T, t)) \quad (6.6)$$

As a result of Poisson effect,  $b$  expands as

$$b(T, t) = b_0(1 + \nu \varepsilon_h(T, t)) \quad (6.7)$$

Where  $\nu$  is the Poisson's ratio of PEEK resin with the value of 0.4 and 0.5 below and above glass transition temperature, respectively. [92][133]

Based on the force equilibrium in Equation 6.1, a  $\sigma_0$  can be obtained with an initial ratio of  $b_0/L$ . From Equation 6.2 and 6.7,  $\sigma(T, t)$  at any time and temperature can be obtained through

$$\sigma(T, t) = \sigma_0/(1 + \nu \varepsilon_h(T, t)) \quad (6.8)$$

Based on Ha's viscoplastic constitutive model [123], Von Mises criteria is adopted here to determine whether the time and temperature dependent material response should be viscoelastic or viscoplastic. Therefore, at an infinitesimal time step  $\Delta t$ , the strain  $\Delta\varepsilon_h$  follows

$$\Delta\varepsilon_h(T) = \begin{cases} \Delta\varepsilon_e(T) + \Delta\varepsilon_c(T) & (\sigma(T, t) \leq \sigma_y(T)) \\ \Delta\varepsilon_e(T) + \Delta\varepsilon_p(T) & (\sigma(T, t) > \sigma_y(T)) \end{cases} \quad (6.9)$$

Where  $\sigma$  is the stress on  $b$ , and  $\sigma_y(T)$  is the yield stress (threshold stress for viscoplastic deformation) of PEEK at temperature  $T$ , which significantly reduces with elevated temperature. In the OVB processing, after vacuum is applied, the initial stress  $\sigma_0$  applied on  $b$  depends on the initial contact area or the degree of intimate contact of the interlayer. As  $b$  expands with time and temperature, the stress  $\sigma_T$  on  $b$  decreases. The yield stress of resin  $\sigma_y(T)$  decreases with increasing temperature. When yield stress is reduced to be smaller than the local stress, viscoplastic deformation occurs.

The temperature dependent elastic strain and the change of elastic strain at each time step follow Equation 6.7 and 6.8

$$\varepsilon_e(T) = \sigma(T, t)/E(T) \quad (6.10)$$

$$\Delta\varepsilon_e(T) = \frac{\sigma(T_i, t_i)}{E(T_i)} - \frac{\sigma(T_{i-1}, t_{i-1})}{E(T_{i-1})} \quad (6.11)$$

Where  $i$  and  $i - 1$  are the current and previous time steps, and  $i$  is an integer from 1 to  $n$ .  $E(T_i)$  is the temperature dependent elastic modulus.

Linear viscoelastic response is assumed in this model. The viscoelastic strain induced by the variation of stress follows Boltzmann superposition principle which has a general form under isothermal condition as below

$$\varepsilon_c(t) = \int_{-\infty}^t D(t - \tau_n) d\sigma(\tau_n) \quad (6.12)$$

Where  $D(t)$  is the time dependent creep compliance,  $\tau_n$  is the time when  $d\sigma$  is applied. It can be also expressed with steps of stresses as

$$\varepsilon_c(t) = \sum_{i=1}^n \Delta\sigma_i D(t - t_i) \quad (6.13)$$

Where  $n$  is the number of the incremental steps. In the case of  $\Delta\sigma_n < 0$ , the viscoelastic strain due to  $\Delta\sigma$  starts to recover from time  $t_n$ . In order to include the temperature dependent creep compliance during the OVB processing cycle, the Equation 6.10 of Boltzmann superposition is extended for non-isothermal condition.

The viscoelastic strain at processing time  $t$  with corresponding temperature  $T$  is derived with incremental time step  $\Delta t$  in Appendix I, and given by

$$\varepsilon_c(T_n, t_n) = \sum_{i=1}^n \Delta\sigma_i [D(T_i, \Delta t) + \sum_{m=i+1}^n (D(T_m, (m - i + 1)\Delta t) - D(T_m, (m - i)\Delta t))] \quad (6.14)$$

The terms in the second summation operator in the Equation 6.11 are for the temperature effect of compliance at increasing time, and equal to 0 when  $n = 1$ . If constant temperature is applied, Equation 6.14 returns to the Equation 6.13. If both

temperature and stress is constant, Equation 6.14 recovers to the basic equation of linear viscoelasticity as below

$$\varepsilon_c(t) = \sigma D(t) \quad (6.15)$$

The change of elastic strain at each time step is also obtained (derivation is in Appendix I)

$$\Delta \varepsilon_{C_n}(T_n, t_n) = \sum_{i=1}^n (\Delta \sigma_i - \Delta \sigma_{i-1}) D(T_i, i \Delta t) \quad (6.16)$$

From the literature, it is seen that the successful description of viscoplastic behavior of materials depends on both the proper selection of model and the empirical fitting of material parameters to the model. The viscoplastic constitutive model developed by Ha and coworkers which provides good agreements with experimental results and includes the temperature dependent material parameters used in the model up to 177 °C is adopted for the viscoplastic deformation of the interlayer region. The one dimensional viscoelastic strain rate without hardening effect can be expressed as

$$\varepsilon_p(\dot{T}, t) = \sqrt{\frac{2}{3}} f(\xi(T, t)) \quad (6.17)$$

Where  $\xi(T, t)$  is the plastic potential,

$$\xi(T, t) = \frac{\sigma(T, t)}{\sigma_y(T)} - 1 \quad (6.18)$$

and  $f(\xi)$  is the plastic flow function in the following form

$$f(\xi(T, t)) = \begin{cases} 0 & \xi(T, t) \leq 0 \\ \frac{\xi(T, t)}{a_1(T)} + \frac{\xi(T, t)^g}{a_b(T)}, & \xi(T, t) > 0 \end{cases} \quad (6.19)$$

Where  $a_1(T)$ ,  $g$ , and  $a_b(T)$  are material parameters from literature [123]. The tensile and compressive stress-strain curves at different temperature up to 200 °C from the literature show no significant stress hardening effect is observed.[92,116,120,134]

Therefore, hardening effect is ignored in this model.

Therefore, the viscoplastic strain at each time step  $\Delta t$  can be obtained by

$$\Delta \varepsilon_p(T, t) = \Delta t \sqrt{\frac{2}{3}} \left[ \frac{\left( \frac{\sigma(T, t)}{\sigma_y(T)} - 1 \right)}{a_1(T)} + \frac{\left( \frac{\sigma(T, t)}{\sigma_y(T)} - 1 \right)^g}{a_b(T)} \right] \quad (6.20)$$

Once the overall strain  $\varepsilon_h(T, t)$  increases to the cut-off strain of the interlayer, the strain will not change with time and temperature based on the behavior of measured Kh of 0°/0° and 0°/90° interlayers.

## 6.5 Input of Material Properties and Parameters

In the literature, the temperature dependent elastic modulus of PEEK is reported with a maximum temperature of 177 °C. In order to cover the higher temperatures in the processing cycle, the transverse elastic modulus of unidirectional APC-2 composite measured by Wang and Sun [115] at elevated temperature up to 315 °C is used to derive the elastic modulus of PEEK resin. Since carbon fibers exhibit anisotropic behavior, Chamis equation for transverse modulus of a unidirectional lamina composed of anisotropic fibers in an isotropic matrix is adopted [135]

$$E_{22} = \frac{E_m}{1 - V_f \left( 1 - \frac{E_m}{E_{2f}} \right)} \quad (6.21)$$

Where  $E_{22}$  is the transverse modulus of a unidirectional laminate;  $E_m$  is the elastic modulus of the resin matrix,  $E_{2f}$  is the transverse modulus of the reinforcing fiber,  $V_f$  is the fiber volume fraction. Assuming the  $E_{2f}$  of carbon fiber is constant to be 13.25 GPa at the processing temperature range, and the fiber volume fraction is 60%, the modulus of PEEK in the composite is calculated. The modulus of PEEK is also affected by its crystallinity. In the consolidated APC2 composites, the crystallinity of PEEK resin is typically 35%. [92] However, in the raw prepreg tape, it is around 10.5%. [113] During the heating ramp in the processing, crystallization of PEEK in

the raw prepreg tape may occur at temperature above 180 °C, and the growth of the crystallinity largely depends on the heating rate of the cycle. [113] Since the deformation of PEEK at this temperature range may be dominated by the time dependent viscoelastic and viscoplastic response, the growth of crystallinity and its effect to the elastic modulus is ignored. Based on the relationship between the modulus and the crystallinity of PEEK obtained experimentally under room temperature by Talbott and Springer [136], a correction factor is applied to the derived PEEK modulus. The values of PEEK modulus are then fitted into a function of temperature as below

$$E(T) = \begin{cases} -1.74 \times 10^{-8} \text{Exp}(0.014 T) + 5.119 \text{Exp}(-1.656 \times 10^{-3} T) & (T \leq 442 K) \\ -4.608 \times 10^{-5} T^2 + 3.969 \times 10^{-2} T - 7.234 & (T > 442K) \end{cases} \quad (6.22)$$

The Elastic modulus of PEEK in the prepreg tape at elevated temperature is plotted in Figure 6.6.

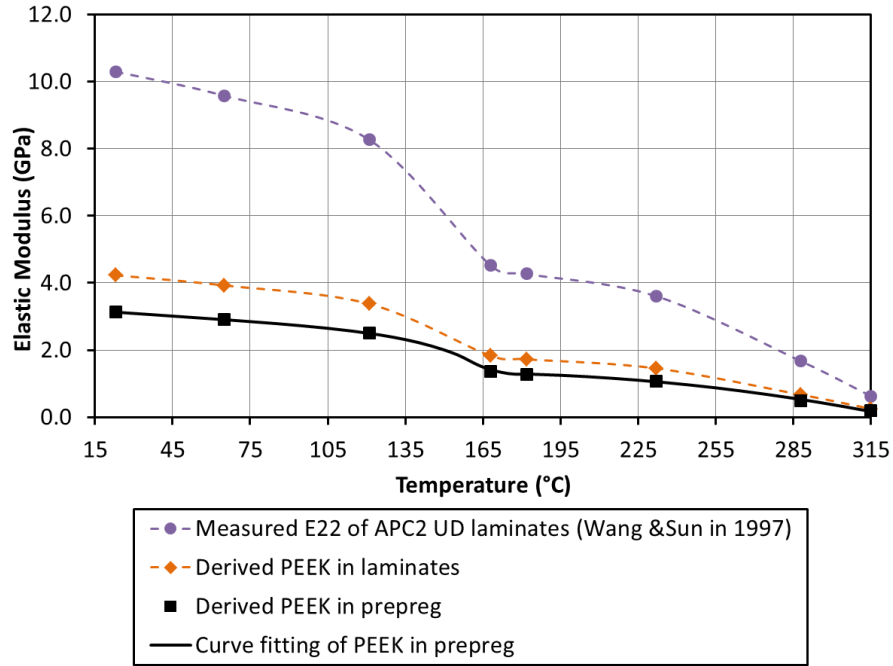


Figure 6.6 The Derived elastic modulus of PEEK in prepreg and consolidated laminates and measured transverse modulus  $E_{22}$  of APC2 unidirectional laminates at elevated temperature

The viscoelastic creep compliance and time-temperature shift factor of PEEK resin characterized at a maximum temperature of 177 °C in Xiao's work is used in this study. [126] Similarly as the elastic modulus, a correction factor for the low crystallinity in the prepreg tape than the measured consolidated laminates is applied to the original compliance function by Xiao, and gives the equation for creep compliance

$$D(T, t) = 1.24 \left( D_0 + \frac{D_\infty - D_0}{\left(1 + \frac{\tau_0 a_T(T)}{t}\right)^n} \right) \quad (6.23)$$

Where  $D_0$  and  $D_\infty$  are the initial compliance and the compliance at infinite time, respectively,  $\tau_0$  is the characteristic time parameter, and  $n$  is a material parameter.  $a_T(T)$  is the time – temperature shift factor and follow the Arrhenius function

$$\text{Log } a_T(T) = \frac{\Delta H}{2.3 R} \left( \frac{1}{T} - \frac{1}{T_0} \right) \quad (6.24)$$

Where  $\Delta H$  is the activation energy corresponding to the viscoelastic relaxation,  $R$  is the universal gas constant (1.98E-3 kcal/mol), and  $T_0$  is the reference temperature in K. The material parameters in Equation 6.23 and 6.24 are presented in Table 6.1.

Table 6.1 Material parameters in the viscoelastic compliance and time-temperature shift factor of PEEK in Equation 6.23 and 6.24.

$D_0$ (/GPa)	$D_\infty$ (GPa)	$\tau_0$ (s)	$n$	$T_0$ (K)	$\Delta H$ (kcal/mol)
0.256	1.614	1.608E+8	0.22	413	40.1 ( $T \leq T_0$ ) 261.5 ( $T_0 < T$ )

The temperature and time dependence of viscoelastic creep compliance of PEEK in prepreg are plotted in Figure 6.7 and 6.8, respectively. It is seen that at temperature below 120 °C, the creep compliance is nearly constant with increasing temperature and time, and increases significantly with time and temperature during the glass transition region (temperature of  $T_g \pm 25$  °C), and then reaches the second plateau at the resin rubbery region. At temperature higher than 170 °C, the creep compliance from Equation 6.23 and 6.24 is constant with time and temperature, which may not be realistic at temperature close to 300°C or for hours long. However, the large permanent strain of interlayer region above 170°C is mainly contributed by the viscoplastic deformation. Therefore, the viscoelastic creep compliance at high temperature may not affect the model calculation.

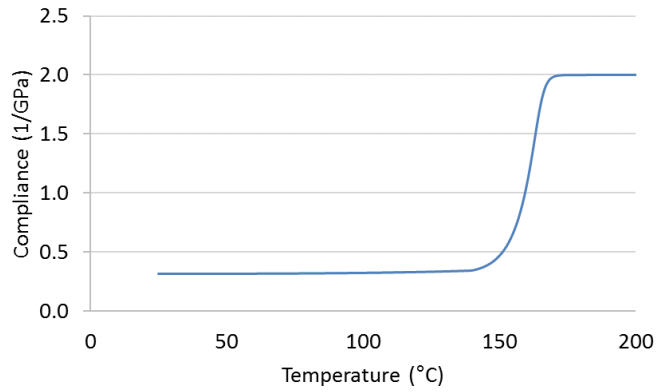


Figure 6.7 Viscoelastic creep compliance of PEEK in prepreg tape at temperature from 25 °C to 200 °C for  $t = 1$ s at each temperature plotted with Equation 6.23 and 6.24 with the material parameters from literature listed in Table 6.1.

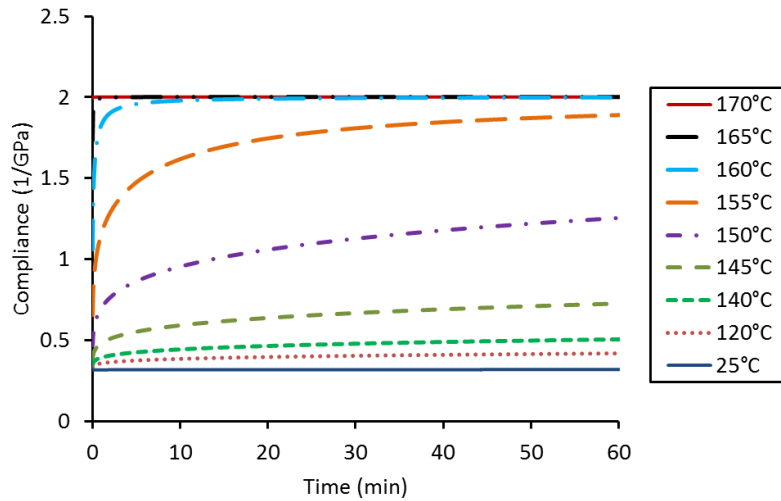


Figure 6.8 Time dependence of viscoelastic creep compliance of PEEK in prepreg tape at temperatures under isothermal condition plotted with Equation 6.23 and 6.24 with the material parameters from literature listed in Table 6.1.

Since the strain rate during the OVB processing is in the order of  $1E-4$  /s to  $1E-5$  /s, the temperature dependent yield stress (threshold stress for viscoplastic

deformation) measured under quasi-static loading condition by Ha et al. is employed. The temperature dependent material parameters used in the Equation 6.20 for the viscoelastic constitutive model follow a general equation

$$Y(T) = Y_0[1 + C_3 \tanh(C_2 \frac{C_1 T_g - T}{T_g})] \quad (6.25)$$

Where  $Y_0$ ,  $C_3$ ,  $C_2$ ,  $C_1$  for the corresponding material parameters are presented in Table 6.2.  $T_g$  is equal to 290 °F, and  $g$  in Equation 6.20 is 9.  $\sigma_y(T)$  is plotted in Figure 6.9.

Table 6.2 Temperature dependent material parameters in the viscoplastic model

Material parameters	$Y_0$	$C_3$	$C_2$	$C_1$
$\sigma_y(T)$ [MPa]	31.0	0.8	2.0	0.3
$a_1(T)$ [s]	7.2E+4	0.98	4.2	0.7
$a_b(T)$ [s]	2.1e+3	0.98	4.2	0.7

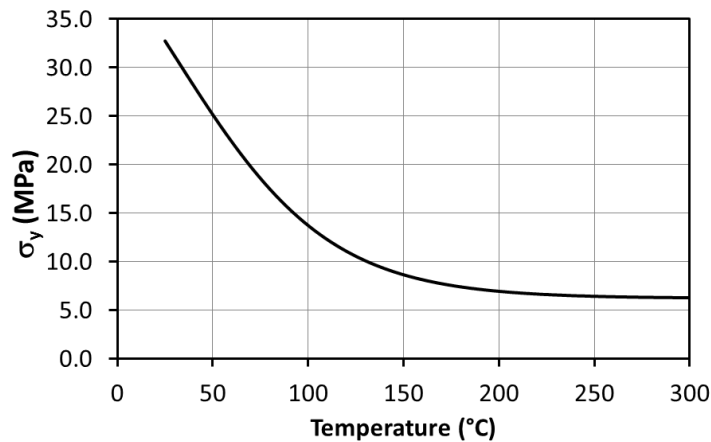


Figure 6.9 Temperature dependent yield stress (threshold stress for viscoplastic deformation) of PEEK used in the viscoplastic model

## 6.6 Results and Discussion of Material Behavior of Interlayer Region

### 6.6.1 General resin behavior

At a low stress level at all temperatures, the deformation of the height of unit cell  $h$  of the interlayer region is subjected to the viscoelastic behavior. The time dependent viscoelastic strain ( $\varepsilon_e(T) + \varepsilon_c(T)$ ) of  $h$  which represents the height of the interlayer unit cell in Figure 6.1 under a stress of 5 MPa (below yield stress) at temperature up to 165 °C is calculated with Equation 6.10 and 6.14 and plotted in Figure 6.10. The increasing strain with temperature at the time 0 is due to the reduction of elastic modulus of PEEK with temperature. At low temperature, the creep compliance is almost constant with time. Significant increase of the strain with time occurs after the onset of the glass transition. When temperature is approaching 165 °C, the compliance of the resin reaches the rubbery plateau. At higher temperature, the viscoelastic creep compliance may increase with time especially for long time period, which is not captured in this model due to the temperature range of the material parameters. Nevertheless, larger than 5% permanent strain of the height of the interlayer region at temperature above 170 °C (Figure 6.2) indicates that the deformation could be dominated by the elastic-viscoplastic response of the resin at higher temperature.

The elastic-viscoelastic strain depends on the local stress level during the processing as well, which is shown in Figure 6.11 where the strain values during temperature ramping with a heating rate of 2.8 °C/min under several constant stress (smaller than  $\sigma_y(T)$ ) are calculated. Less than 1% strain during the non-isothermal temperature ramping to 170 °C is obtained under constant stress of 5MPa. If the local

stress is high, the resin response during heating may switch from elastic-viscoelastic to elastic-viscoplastic due to the reduction of the yield stress with increasing temperature.

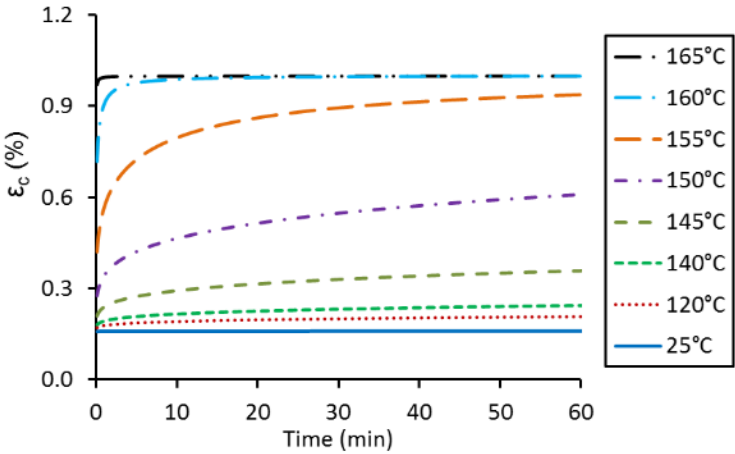


Figure 6.10 The elastic-viscoelastic strain of  $h$  under constant stress of 5 MPa at temperatures up to 165 °C from model calculation, showing increasing viscoelastic strain with temperature and time especially during the glass transition of the PEEK resin

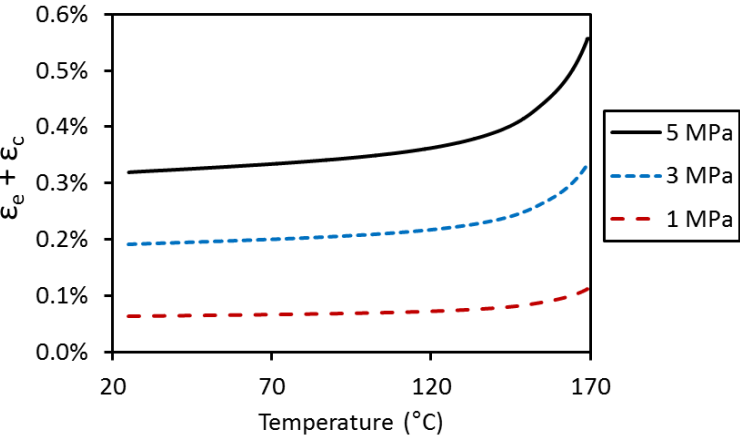


Figure 6.11 Elastic-viscoelastic strain of  $a$  during temperature ramp to 170 °C with a heating rate of 2.8 °C/min under the stress level of 1, 3, and 5 MPa from model calculation, showing the strain depends on the local stress of the interlayer region.

At high local stress level, the viscoplastic strain rate increases significantly with temperature and the  $\sigma/\sigma_y$  ratio. With the Equation 17-19, the viscoplastic strain rates under different  $\sigma/\sigma_y$  ratio with increasing temperature are calculated and presented in Figure 6.12. The plastic strain rate at low temperature can be in the order of  $10^{-5}/s$  -  $10^{-6}/s$  and increases to  $10^{-5}/s$  -  $10^{-3}/s$  at temperature above 250 °C. The strain rate can increase more than one order magnitude if the  $\sigma/\sigma_y$  ratio is increased from 1.2 to 1.8.

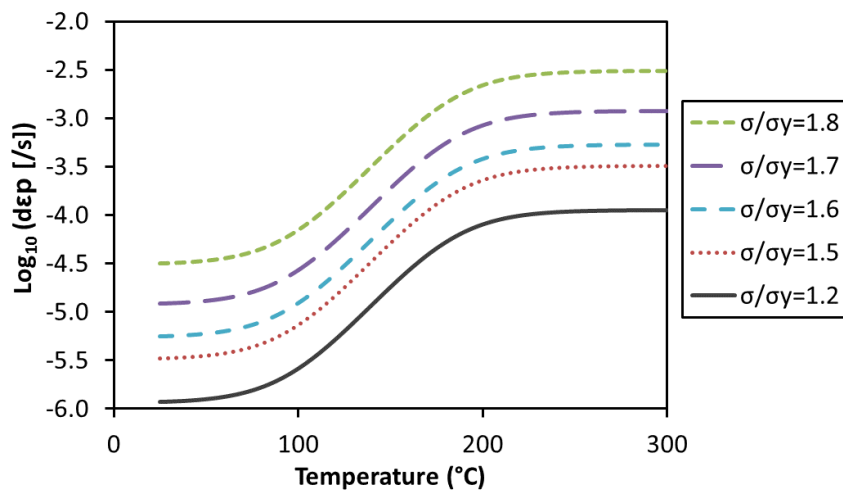


Figure 6.12 Viscoplastic strain rate with increasing temperature under different  $\sigma/\sigma_y$  ratio

From the above material behavior, it is seen that the overall strain of the interlayer region highly depends on the initial stress on the contact region between layers, which will be determined after comparing the strain calculated from measured  $kh$ .

### 6.6.2 Behavior of the interlayer region

The strains of the unit cell height  $h$  under different initial stress  $\sigma_0$  during the temperature ramping cycle with heating rate of  $2.8\text{ }^\circ\text{C}/\text{min}$  with the cut-off strains are obtained based on the resin behavior model, and compared with the strain calculated from the experimental measured  $Kh$  for of  $0^\circ/0^\circ$  and  $0^\circ/90^\circ$  interlayers in Figure 6.13 and 6.14, respectively. The evolution of the stress with different  $\sigma_0$  are also presented on the figures. It is seen that the temperature at the intercept stress of the  $\sigma$  and  $\sigma_y$  curves are the starting points of the elastic- viscoplastic response under different  $\sigma_0$ . The higher the  $\sigma_0$ , the earlier the resin deforms viscoplastically during the processing. The higher  $\sigma_0$ , the earlier the strain reaches cut-off strain. The strain curves that fits the experimental values for  $0^\circ/0^\circ$  and  $0^\circ/90^\circ$  interlayers best based on the least square method are with  $\sigma_0$  values of 11 MPa and 12 MPa, respectively.

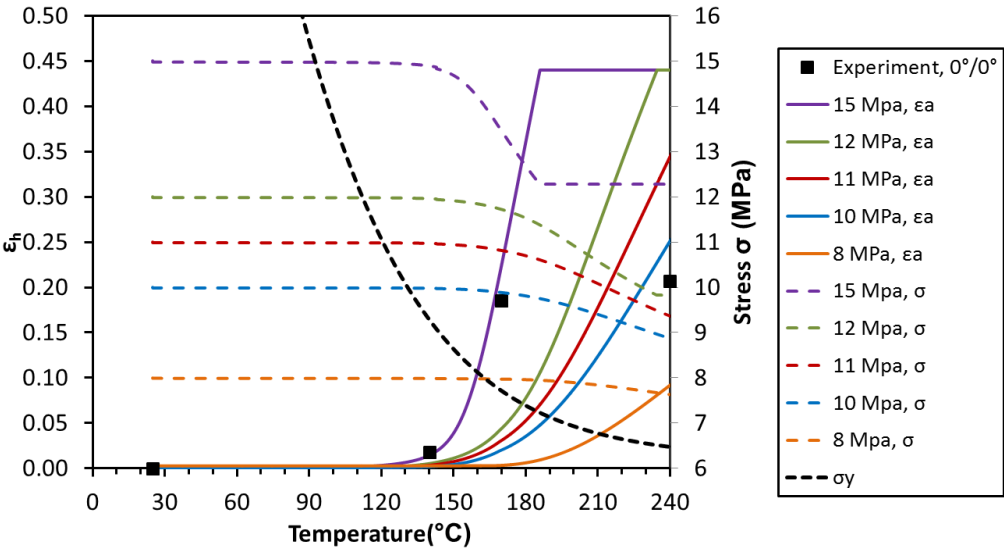


Figure 6.13 Comparison of  $\varepsilon_h$  from material response model under different initial stress and calculation from measured  $Kh$  during temperature ramp for  $0^\circ/0^\circ$  interlayer, showing the curve with  $\sigma_0 = 11\text{ MPa}$  fits the experimental results best

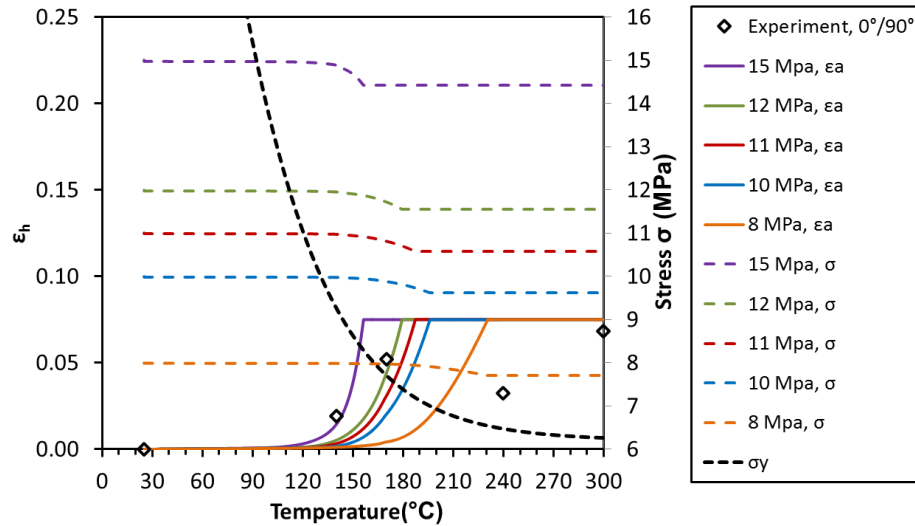


Figure 6.14 Comparison of  $\varepsilon_h$  from material response model under different initial stress and calculation from measured  $Kh$  during temperature ramp for  $0^\circ/90^\circ$  interlayer, showing the curve with  $\sigma_0 = 12 \text{ MPa}$  fits the experimental results best

For  $0^\circ/0^\circ$  interlayer, the comparison between modeled strain and experimental strain during the dwell cycle can be used to validate the determined  $\sigma_0$  from the temperature ramping cycle, which is presented in Figure 15. And the  $\sigma_0$  of 11 MPa does give the best fit, which also validates the material behavior model established in this study. It is noticed that the cut-off strain of  $0^\circ/90^\circ$  interlayers is achieved at  $180^\circ\text{C}$  before the dwell temperature of  $240^\circ\text{C}$  in experiment in the temperature ramping cycle. In this case. The strain curves comparing with measured values will automatically give the same  $\sigma_0$  of 12 MPa as seen in Figure 16.

Therefore, the  $\sigma_0$  of 11 MPa and 12 MPa are determined for  $0^\circ/0^\circ$  and  $0^\circ/90^\circ$  interlayers, corresponding to the initial  $b_0/L$  of 0.94% and 0.86%, respectively. At the cut-off strains, the corresponding stress for  $0^\circ/0^\circ$  and  $0^\circ/90^\circ$  are 9.03 MPa and 11.6 MPa, corresponding to the  $b/L$  ratios of 1.1% and 0.89%. It is seen that with all range of

strain, the ratio of  $b/L$  are very small for both interlayers, which also validate the usage of Equation 6.4.

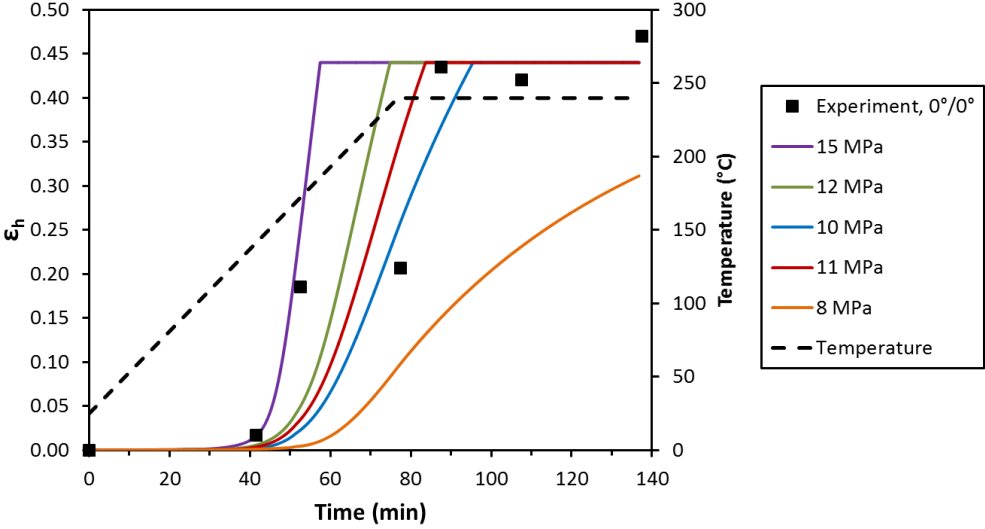


Figure 6.15 Comparison of  $\epsilon_h$  from material response model under different initial stress and calculation from measured  $Kh$  during temperature dwell cycle for  $0^\circ/0^\circ$  interlayer, showing the curve with  $\sigma_0 = 11 \text{ MPa}$  fits the experimental results best

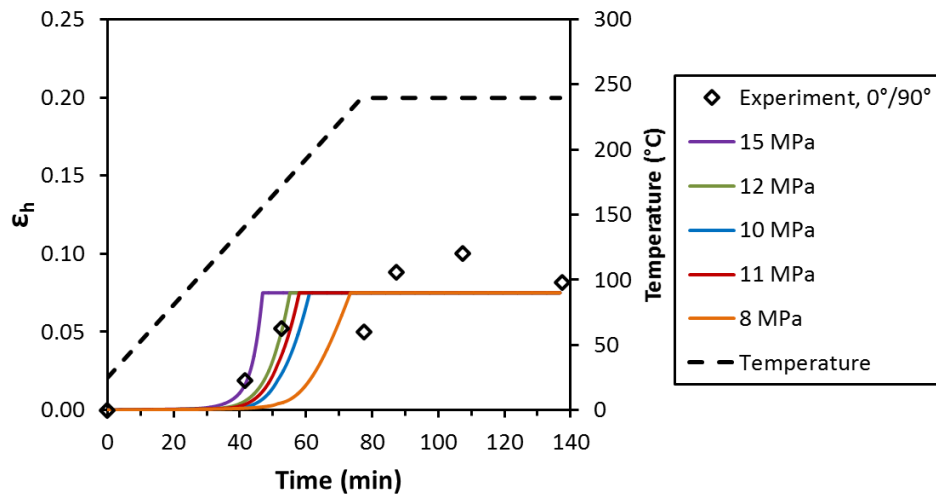


Figure 6.16 Comparison of  $\epsilon_h$  from material response model under different initial stress and calculation from measured  $Kh$  during temperature dwell cycle for  $0^\circ/90^\circ$  interlayer, showing the curve with  $\sigma_0 = 12 \text{ MPa}$  fits the experimental results best

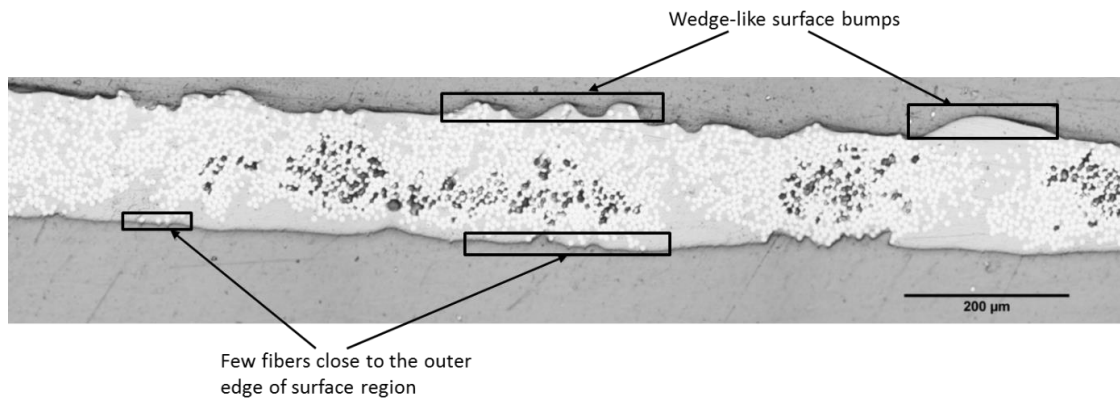


Figure 6.17 A typical cross-sectional micrograph of the AS4/APC2 tape with width of 1.35mm, showing wedge-like surface bumps, and few fibers locating close to the surface in the resin rich surface region.

Both  $0^\circ/0^\circ$  and  $0^\circ/90^\circ$  interlayers show the behavior of interlayer height reduction followed by plateau cut-off strain, but it occurs at different temperature in

the processing and at different strain levels. The invariable interlayer strain at elevated temperature and long-time dwell could be attributed to the fiber-fiber contacts at the interlayer region. The surface imprints perpendicular to the fiber direction on the tape from 0°/90° lay-up after processing in our previous study shows the evidence of fiber-fiber contacts (Chapter 3). Since the transverse modulus of carbon fiber is much higher than the modulus of the resin (15 times higher than PEEK resin at 240°C) and very stable with temperature (>400°C) [11], very limited strain can be introduced when fibers of the contact layers meet. Thus, the strain is constant with temperature. From Figure 6.17, it is seen that one side of the tape surface is more resin rich than the other, and the distance from the outer edge of the resin rich surface region to the main body of the tape where fibers are more homogeneously distributed is about 20 μm which is a few carbon fiber diameters thick. There are also few fibers located less than 3~4 μm to the edge of the tape surface. For 0°/90° interlayers, the orthogonal fiber-fiber contacts may form an in-plane network of the contact region where local high stress could be supported by the adjacent orthogonal contact of the rigid fibers, limit the strain reduction after the thin resin cover (3~4 μm) is compressed and the fibers at the surface of the layers meet. This can be indicated by the constant number of imprints on the tape surface from 0°/90° after 170 °C in our previous surface characterization (Chapter 3). In the case of 0°/0° interlayer, the fiber-fiber contacts are mostly along the fiber axial direction. With few fibers in the resin rich surface region, the transverse deformation is dominated by the resin properties until the fiber volume fraction reach a higher level and the fiber –fiber contact is closer to the main body of the tape. With Equation 6.4, the initial height  $h_0$  of the interlayer unit cell of the 0°/0° and 0°/90° interlayers are 34.8 μm and 32.9 μm, respectively. At the plateau strain of

44% and 7.5%, the deformation of the interlayer height is 15.3  $\mu\text{m}$  and 2.5  $\mu\text{m}$  for the  $0^\circ/0^\circ$  and  $0^\circ/90^\circ$  interlayers, respectively, which agrees well with the microstructure of the surface region of the tape.

From the above results, it is seen that the evolution of the interlayer region during the processing is initially dominated by the resin behavior, but significantly affected by the interlayer configuration and the forms of the fiber-fiber contacts after resin deformed. With the  $h_0$  from experimental results, the predicted and measured  $Kh$  for  $0^\circ/0^\circ$  and  $0^\circ/90^\circ$  interlayers are presented in Figure 6.18. When the temperature is closed to the resin melting point, resin turns into fluid and flows to fill the interlayer region following the squeeze flow mechanism.

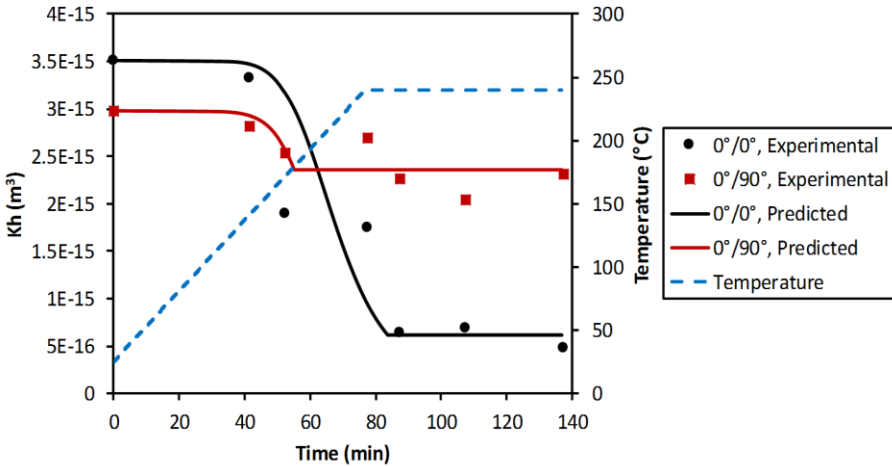


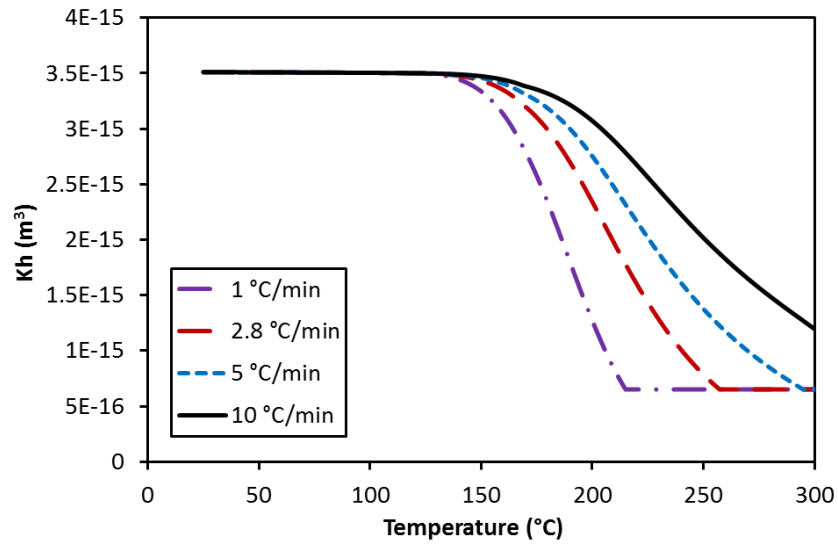
Figure 6.18 Predicted  $Kh$  of  $0^\circ/0^\circ$  and  $0^\circ/90^\circ$  interlayers by applying the initial  $h_0$  calculated from measured  $Kh$  with Equation 6.4 to the strain curves with  $\sigma_0 = 11 \text{ MPa}$  and  $\sigma_0 = 12 \text{ MPa}$ , respectively.

### 6.6.3 Effect of processing conditions to the interlayer permeability

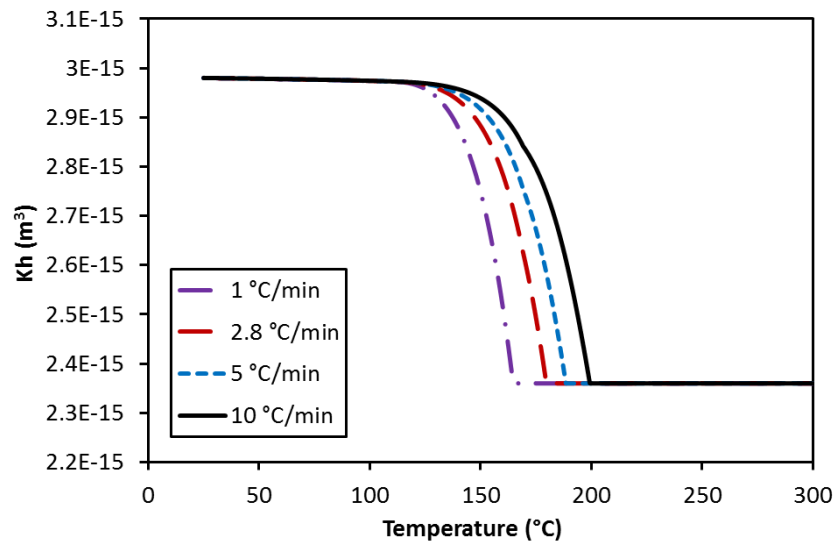
With the previously determined model for the  $Kh$  of  $0^\circ/0^\circ$  and  $0^\circ/90^\circ$  interlayers, the effect of heating cycles to the interlayer permeability in OVB processing can be studied.

Since heating rate can affect the total processing time, the effect of heating rate in the OVB processing to the  $Kh$  of  $0^\circ/0^\circ$  and  $0^\circ/90^\circ$  interlayers is presented in Figure 6.19. It is seen that less reduction of the permeability can be obtained with a higher heating rate at a same temperature for both  $0^\circ/0^\circ$  and  $0^\circ/90^\circ$  interlayers. In the relatively fast ramping, the time to reach a same temperature is shorter than with a slow heating rate. Thus, the time to develop the interlayer strain is reduced. The temperature to reach the plateau  $Kh$  increases with increasing heating rate.

To maintain the level of interlayer permeability, dwell cycles may be added in the heating ramps in the resin rubbery region. Figure 6.20 shows the evolution of  $Kh$  during cycles with different dwell temperature and same total processing time with a heating rate of  $5^\circ\text{C}/\text{min}$ . It is seen that lower temperature can better maintain the permeability with slower reduction rate during dwells (more gentle slope for the  $Kh$  curve of  $160^\circ\text{C}$  than  $220^\circ\text{C}$  after processing time of 30 mins for  $0^\circ/0^\circ$  interlayer in Figure 6.12 (a)), and significantly extends the processing time required to reach the plateau permeability, especially for the  $0^\circ/0^\circ$  interlayer.

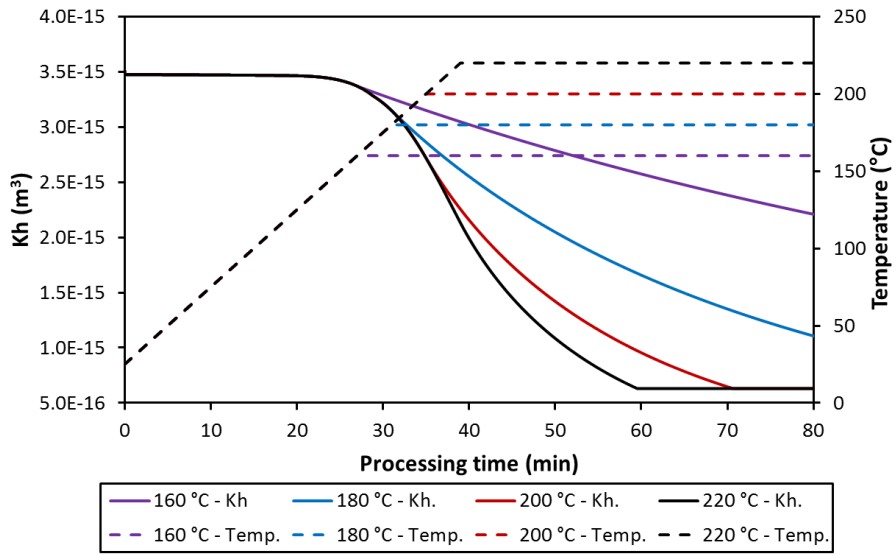


(a)

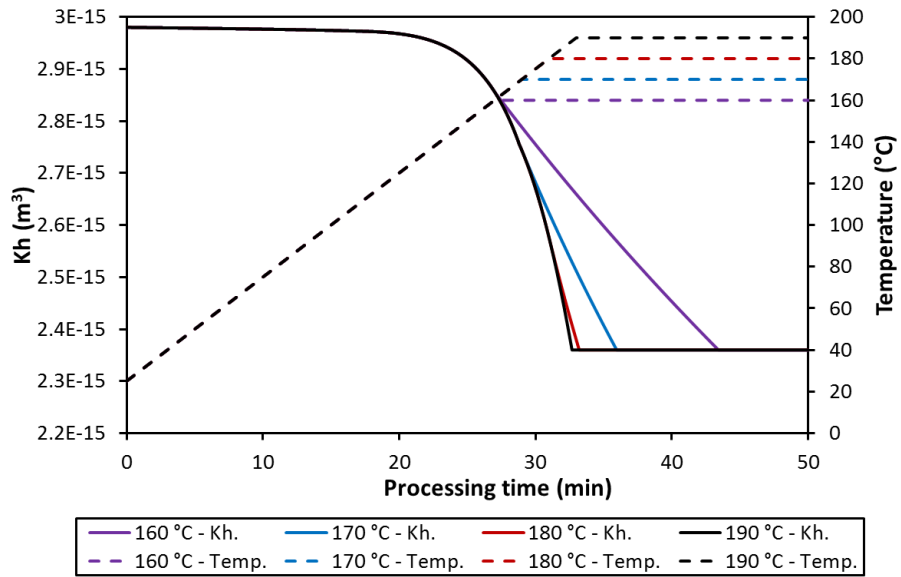


(b)

Figure 6.19 Evolution of interlayer permeability products  $Kh$  of (a)  $0^\circ/0^\circ$  and (b)  $0^\circ/90^\circ$  interlayers under different heating rate at elevated temperature, showing less reduction of interlayer permeability is obtained with relatively higher heating rate at a certain temperature before plateau  $Kh$



(a)



(b)

Figure 6.20 Evolution of interlayer permeability products  $Kh$  of (a)  $0^\circ/0^\circ$  and (b)  $0^\circ/90^\circ$  interlayers under different dwell cycles at elevated temperature with a heating rate of  $5^\circ\text{C}/\text{min}$ , showing less reduction of interlayer permeability can be achieved at same processing time with lower dwell temperature before plateau  $Kh$

## 6.7 Summary

In this chapter, the response of the interlayer region at the temperature below resin melting point during the OVB processing cycles is investigated. A model based on the time and temperature dependent elastic-viscoelastic-viscoplastic behavior of the PEEK resin is established to describe the deformation of the interlayer region under the non-isothermal processing condition. Depending on the local stress, material response may change from elastic-viscoelastic to elastic-viscoplastic. The viscoelastic response contributes strain smaller than 1%, and the large deformation are dominated by the viscoplastic response of the resin. The modeled strain under different initial stress are compared with the strain calculated from the measured interlayer permeability thickness products of 0°/0° and 0°/90° interlayers. The difference of the strain from resin model and experiments are discussed with the microstructure of the raw prepreg tape and the surface characteristics of the tapes from 0°/0° and 0°/90° interlayers after processing. It is found that the deformation of the interlayer is initially governed by the resin response. Fiber-fiber contacts at the interlayer region then supports the local stress and result in a strain plateau, preventing further deformation and reduction of the interlayer permeability with temperature and time, which occurs at different level of strain and stages of the processing for different lay-up configurations. The permeability of the 0°/0° and 0°/90° interlayers are then well predicted by selecting a proper initial stress and setting cut-off strains. It is shown that a relatively high heating rate and low temperature dwell cycle during the heating ramp can effectively impede the reduction of the interlayer permeability.

## **Chapter 7**

### **DESIGN AND OPTIMIZATION OF PROCESSING CYCLE OF THERMOPLASTIC OVB PROCESSING**

#### **7.1 Introduction**

Previously in Chapter 4 and Chapter 5, void volatile removal through the combined mechanism of air diffusion through the thickness of single layer thermoplastic prepreg and flow through the permeable interlayer region to the vacuum has been validated and modeled. In this chapter, the effect of initial void content in the raw prepreg tape, processing conditions including heating rate, dwell temperature and vacuum level, and part in-plane dimensions will be discussed through the parametric study of the models of diffusion and air flow. The design and optimization of the processing cycle for volatile removal will be discussed.

#### **7.2 Parametric Study of the Model of Single Layer Diffusion**

##### **7.2.1 Effect of Raw Tape Properties**

Different initial void contents in the tape contain different amount of void volatile that needs to be removed. During the non-isothermal heating ramps, the diffusion process for removing void air to reach 1% final void content may finish at higher temperature for higher initial void content. From Figure 7.1, it is seen that during a heating ramp with a rate of 2.8 °C/min, the diffusion process finishes at 27 °C lower and 9.6 mins earlier if the initial void content is reduced from 7.77% to 2%. However, if the initial void content is increased to 15%, a temperature of 20 °C higher

corresponding to 7.1 mins longer during the heating ramp is required. High initial void content may also require more time for resin to flow into the voids when temperature is above resin melting point. Therefore, low initial void content in the raw prepreg tape can always be a better starting point for void removal in the thermoplastic OVB processing.

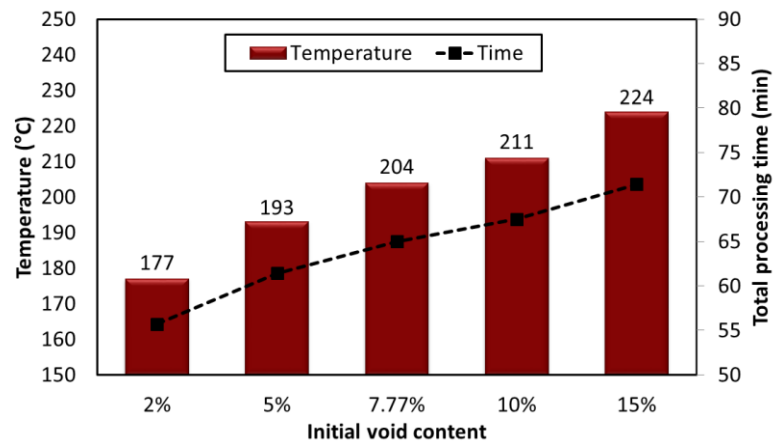


Figure 7.1 Temperature and processing time for removing the amount of void air to reach 1% void content through single layer diffusion with different initial void content with heating rate of 2.8 °C/min

### 7.2.2 Effect of Processing Conditions

The effect of heating rate to the temperature for removing 99.9% void air (N<sub>2</sub> and O<sub>2</sub> only) in the heating ramps with initial void content of 7.77% is presented in Figure 7.2. As the heating rate increases, the diffusion process completed at increasing temperatures, from 174 °C with 1 °C/min to 309 °C with 30 °C/min. However, the total processing time reduced significantly from about 149 min with 1 °C/min to 9 min with 30 °C/min. The heating rate in an oven is typically below 10 °C/min. Figure 7.2 shows that increasing the heating rate from the standard heating rate from 2.8 °C/min to 10

°C/min can save processing time of 40 mins for air removal through single layer diffusion. The effect of heating rate to the temperature gradient may be considered for thick laminates. Therefore, employing a relatively high heating rate with the consideration of the capability of the oven and part thickness can reduce the processing time for air diffusing from prepreg layers.

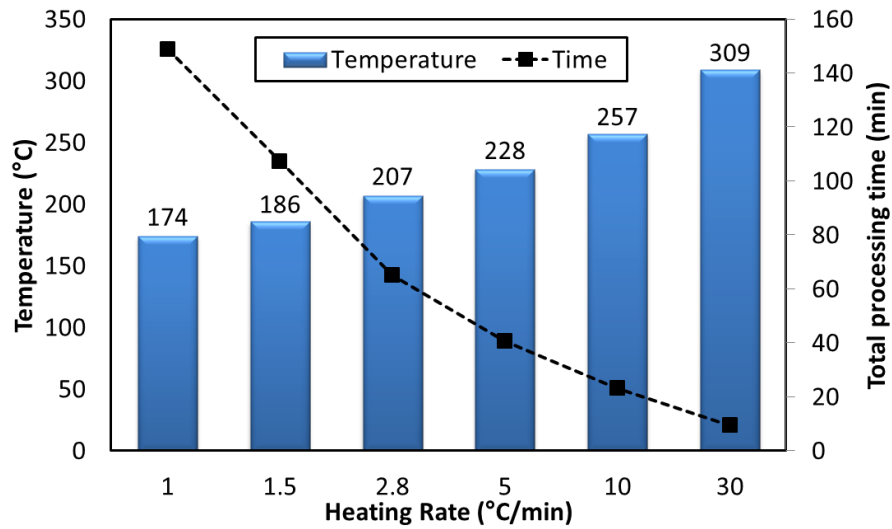


Figure 7.2 Temperature and processing time for removing 99.9% void volatiles through single layer diffusion during heating ramps with different heating rate with initial  $V_v=7.77\%$

If diffusion process finishes at a high temperature that the interlayer permeability reduces to a very low level, air removal through the interlayer air flow may not be effective. And air may still be trapped in the laminates, especially for thick sections. Therefore, low temperature dwell cycles may be added to the heating ramp to maintain the interlayer permeability for interlayer air flow. With the initial void content of 7.77% and heating rate of 2.8 °C/min, the processing time required for

diffusion with different dwell temperature from 140 °C to 200 °C is presented in Figure 7.3. It is seen that both the dwell time and total processing time reduced significantly when the temperature is above the glass transition temperature (143 °C). Although the dwell time significantly reduces as the dwell time increases, the total processing time for diffusion show no significant reduction at the temperature above 180 °C. Considering that time is also required to increase the temperature to the desired processing temperature for resin infusion, adding low temperature dwell for void volatile diffusion is not favorable to the optimization of total processing time.

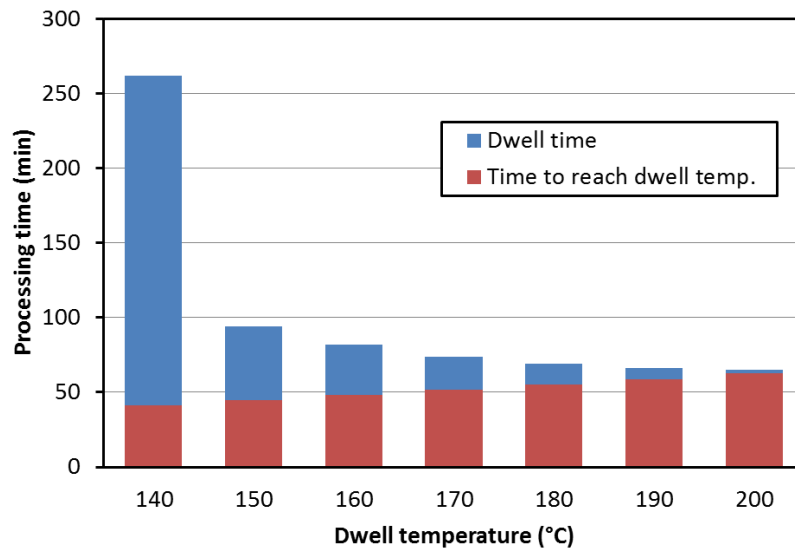


Figure 7.3 Total processing time required for removing 99.9% void volatiles through single layer diffusion at different dwell temperature with heating rate of 2.8 °C/min and initial  $V_v=7.77\%$

The vacuum level in the bag can also affect the temperature for diffusion completion. From Figure 7.4, it is seen that with the same heating rate of 2.8 °C/min

and initial void content of 7.77%, the diffusion completed at 19 °C higher under vacuum of 10 InHg than full vacuum, with a 7 more mins in the heating ramp. Lower vacuum level results in relatively higher concentration (Henry’s law) at the surface of the prepreg than full vacuum (30 InHg), leading to smaller concentration gradient from the inside to the surface of the prepreg. Therefore, at each temperature or time increments, the diffusion flux is smaller than under full vacuum condition. Thus the completion of diffusion process requires more time or higher temperature in the heating ramp. Besides, low vacuum level in the bag can significantly increase the time for resin flow to fill the voids. Therefore, in order to optimize the overall processing time, maintain a full vacuum in the bag is critical.

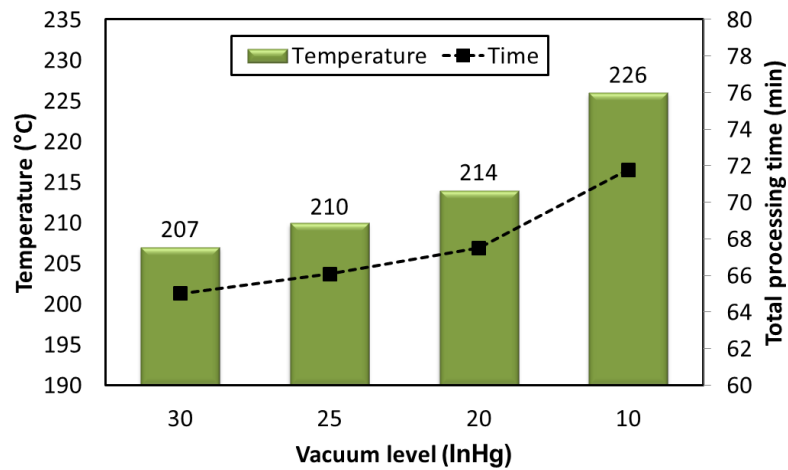


Figure 7.4 Temperature for removing 99.9% void volatiles through single layer diffusion with different vacuum levels with initial  $V_v=7.77\%$  and heating rate of  $2.8\text{ }^\circ\text{C}/\text{min}$

### 7.3 Parametric Study of the Air Flow Model through Permeable Interlayer Region

In the model of gas flow through the permeable interlayer region, it is assumed that all void air/volatiles are initially filled the interlayer region, then flowing out gradually. Therefore, different initial void content means different amount of volatiles to be evacuated. Therefore, the flow time required for volatile evacuation (pressure at the in-plane center is 500 Pa) depends on the initial void content. Figure 7.5 shows that for a part with in-plane dimension of 1 m, the air flow time increases with initial void content. This tendency is more obvious for lower permeabilities of the interlayer region.

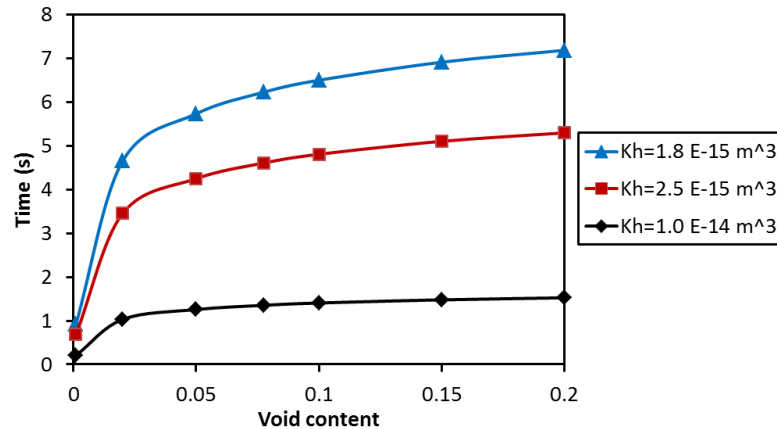


Figure 7.5 Air flow time with different initial void content in a part size of 1m.

Air evacuation time highly depends on the part in-plane dimension (flow length) and the interlayer permeability. The permeability thickness products of lay-ups before and after OVB processing measured from experiments ranges from  $8.0\text{E-}17 \text{ m}^3$  ( $90^\circ/90^\circ$  interlayer after 8 hrs dwell at  $240^\circ \text{C}$ ) to  $3.8 \text{E-}15 \text{ m}^3$  (raw tape  $0^\circ/15^\circ$ ) in

Chapter 3. The air evacuation time for part in-plane dimension up to 100 m are then estimated over the range of experimental  $Kh$  values and presented in Figure 7.6. It is seen that for a certain permeability parameter, the time required to evacuate void air increases with the part in-plane dimensions. From the series of curves with increasing permeability parameters, it is also seen that for a certain process time, larger permeability allows larger part size to be consolidated with OVB processing. With the  $Kh$  values of  $2.5 \text{ E-}15 \text{ m}^3$  and  $1.8 \text{ E-}15 \text{ m}^3$  from  $0^\circ/90^\circ$  and  $0^\circ/0^\circ$  interlayers at  $200^\circ\text{C}$ , part sizes that can be processed within an 8 hour processing time are up to 79 m and 68 m, respectively, which cover a wide range of parts. For larger part, the dual mechanism will require more time or higher permeable interfaces. For example, two curves with dashed lines having higher permeability thickness products than measured for the AS4/APC2 interlayer show that if the permeability parameter can be increased to  $1.0\text{E-}14 \text{ m}^3$ , the 100 m part can be consolidated within 4 hrs in OVB processing.

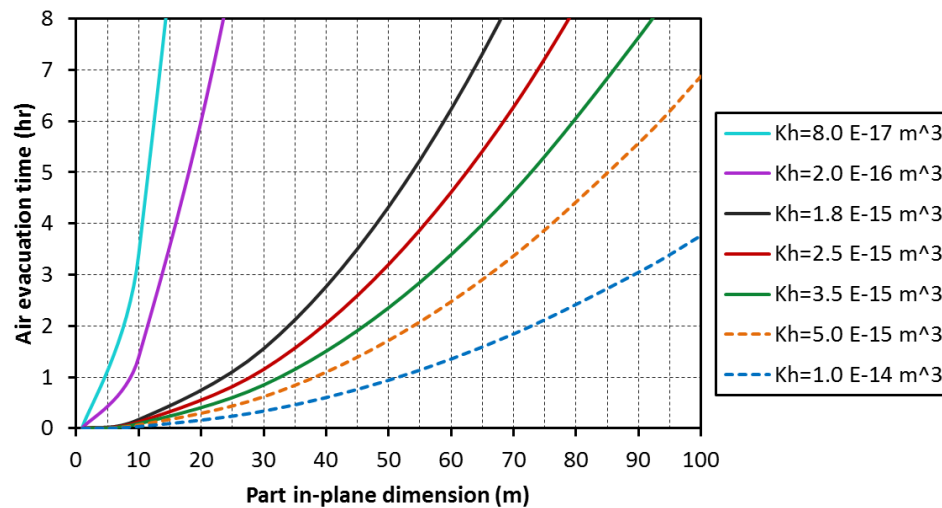


Figure 7.6 Air evacuation times for different part in-plane sizes under permeability thickness products of  $8.0\text{E-}16 \text{ m}^3$  to  $1\text{E-}14\text{m}^3$ . Laminates of any thickness can be OVB processed successfully.

#### **7.4 Discussion of Design and Optimization of the Processing Cycle**

To remove the void air in the thermoplastic composites in OVB processing, two mechanisms have been investigated in Chapter 4 and Chapter 5: (1) combined mechanism of void air diffusion from single layer prepreg followed by flow through the permeable interlayer region, (2) diffusion through the thickness of the prepreg stack mechanism only. Void air removal based on the combined mechanism is regardless of the thickness of the laminate, and the processing time for air removal depends on the diffusion time from single layer prepreg and air flow time. For a certain prepreg material, void air removal time is dominated by the air flow time especially for part with large in-plane dimensions. The processing time for void air removal via the diffusion only mechanism is governed by the thickness of the laminates. Therefore, one may choose the dominating mechanism for void air removal and design the processing cycle based on the dimensions of the thermoplastic composite parts.

With the model of interlayer air flow, the air evacuation time in AS4/APC2 laminate with a range of interlayer permeability and part in-plane dimensions can be calculated. For a certain air evacuation time, the maximum number of layers (or thickness) that air can be removed through diffusion only mechanism can be obtained from the model of diffusion through the thickness of prepreg stacks. Then a chart as Figure 7.7 can be prepared. The curves show the air evacuation time required for the corresponding part in-plane dimension and the interlayer air permeability. The maximum numbers of layers that can be evacuated through diffusion only mechanism at processing temperature of 380 °C correspond to the air evacuation time on the left Y axis are shown on the right. There are three basic ways to use this chart:

- a. With the known in-plane dimension and thickness, one may directly see which mechanism is more efficient on void air removal. Taking the part size of 35 m and the  $Kh$  of  $6.5 \text{ E-}16 \text{ m}^3$  (plateau  $Kh$  of  $0^\circ/0^\circ$  interlayer under  $240^\circ\text{C}$  in Chapter 3 and 6), air evacuation through the interlayer region takes 6 hours, corresponding to air diffusion through a 16 - layer laminate. (Case (a) in Figure 7.7). Therefore, if the laminate is less than 16 layers thick, diffusion only mechanism require shorter processing time than air flow through interlayer region.
- b. With a maximum allowable processing time (without heating and cooling ramps), the maximum void free part dimensions can be determined. For processing time of 4 hrs (case (b) in Figure 7.7), with the  $Kh$  of  $6.5 \text{ E-}16 \text{ m}^3$ , the maximum in-plane size of the part is 28 m. The max number of layers based on the diffusion mechanism is 13. If the length and number of layers of a part are within the allowable range, the mechanism for air removal can be determined based on the procedure in case (a).
- c. If the in-plane dimensions is larger than the calculated range, one may find the suitable interlayer permeability for void air removal in the allowable processing time, and design the dwell cycle based on the interlayer permeability level. As shown in Figure 7.7 case (c), with the maximum processing time of 4 hours, the  $Kh$  needs to be maintained higher than  $2.4 \text{ E-}15 \text{ m}^3$  for a part of 56 m during the processing.

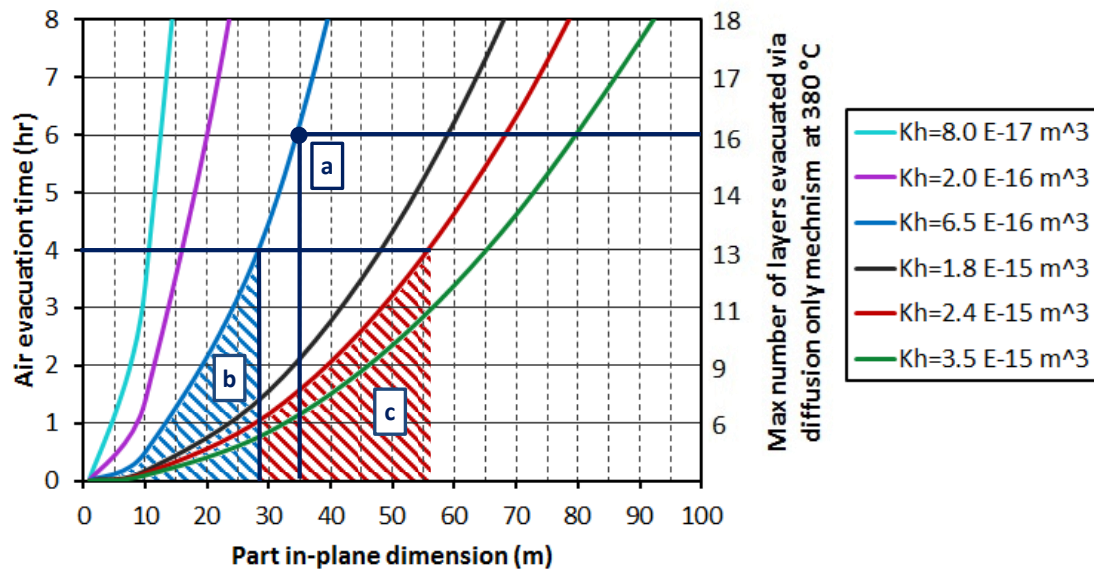


Figure 7.7 Chart for determination of the air removal strategy in OVB processing for AS4/APC2 laminates with initial  $V_v=7.77\%$  with (a) given part in-plane dimension and thickness (b) allowable processing time (c) allowable processing time and part-in plane dimension.

With the established models and the constructed chart (Figure 7.7), the strategy for void air removal can be conveniently determined for a thermoplastic composite part. If the diffusion only mechanism is chosen, processing cycle can be designed by adding a dwell period at  $380^\circ\text{C}$  for void reduction for AS4/APC2 laminates. For the combined mechanism, the air flow time in a part with known in-plane dimension is governed by the interlayer permeability during processing. With the materials behavior model for in Chapter 6, the interlayer permeability thickness products of  $0^\circ/90^\circ$  and  $0^\circ/0^\circ$  lay-ups in the OVB processing can be predicted.

The  $Kh$  of  $0^\circ/90^\circ$  and  $0^\circ/0^\circ$  lay-ups of the AS4/APC2 in the processing cycles with heating rate of  $5^\circ\text{C}/\text{min}$  and different dwell temperature up to a total processing time of 80 mins are shown in Figure 7.8 and 7.9, respectively. It is seen that the  $Kh$  values of  $0^\circ/90^\circ$  at the processing time when void air diffusion from single layer

completes are the plateau  $Kh$  of  $2.4 \text{ E-15 m}^3$  in all the cycles. [113] Therefore, the heating ramps can be designed with relatively high heating rate and the dwell period can be added to the temperature after single layer diffusion process completes. The dwell time can be calculated from the air flow model with the plateau permeability and the part in-plane dimension.

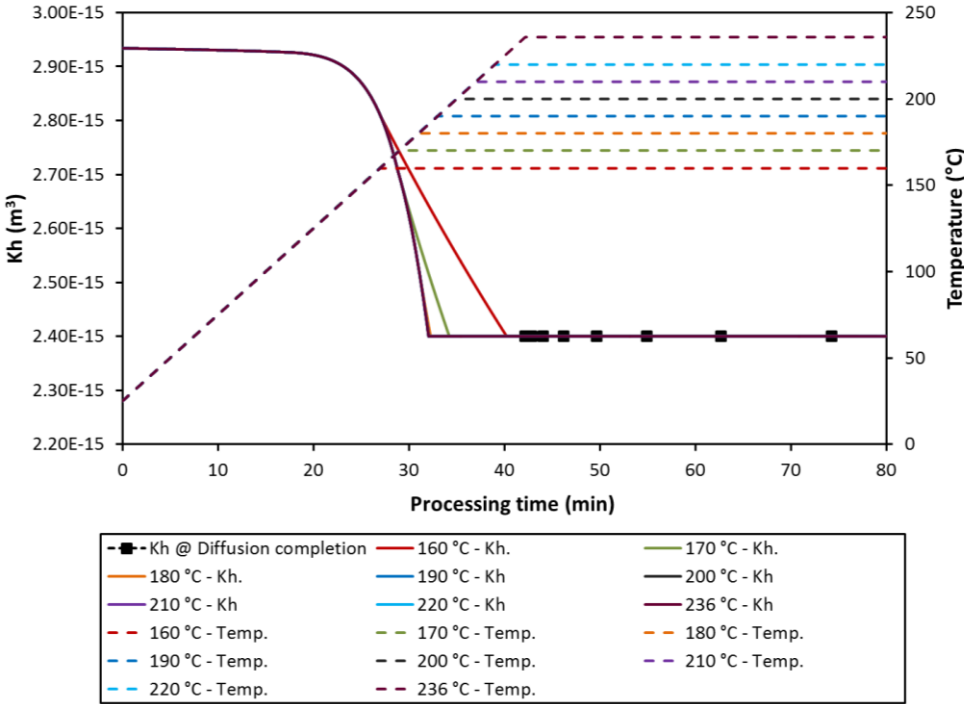


Figure 7.8 Interlayer permeability thickness products of  $0^\circ/90^\circ$  lay-up in the processing cycle with different dwell temperature and heating rate of  $5 \text{ }^\circ\text{C}/\text{min}$

The  $Kh$  values of  $0^\circ/0^\circ$  at the diffusion finishing time shown in Figure 7.9 reduces 24% from  $2.3\text{E-15 m}^3$  to  $1.7\text{E-15 m}^3$  as the dwell temperature increases from  $160 \text{ }^\circ\text{C}$  to  $190 \text{ }^\circ\text{C}$ , and almost invariant when dwell temperature is increased to  $236 \text{ }^\circ\text{C}$ .

The  $Kh$  values at diffusion completion time for all cycles are in the same order of magnitude and above  $1\text{E-}15 \text{ m}^3$ . The rate for the reduction of permeability during the dwell time increases with dwell temperature. The dwell time to reach the plateau  $Kh$  at  $160^\circ\text{C}$  is significantly longer than at  $236^\circ\text{C}$ , allowing air evacuation in larger part dimensions. For a part of 10 meters, 10 mins dwell time at temperature of  $200^\circ\text{C}$  can be added to the heating ramp for air removal. For a part of 50m, low temperature dwell at  $160^\circ\text{C}$  with a dwell time of more than 4 hrs may be added to the heating ramp.

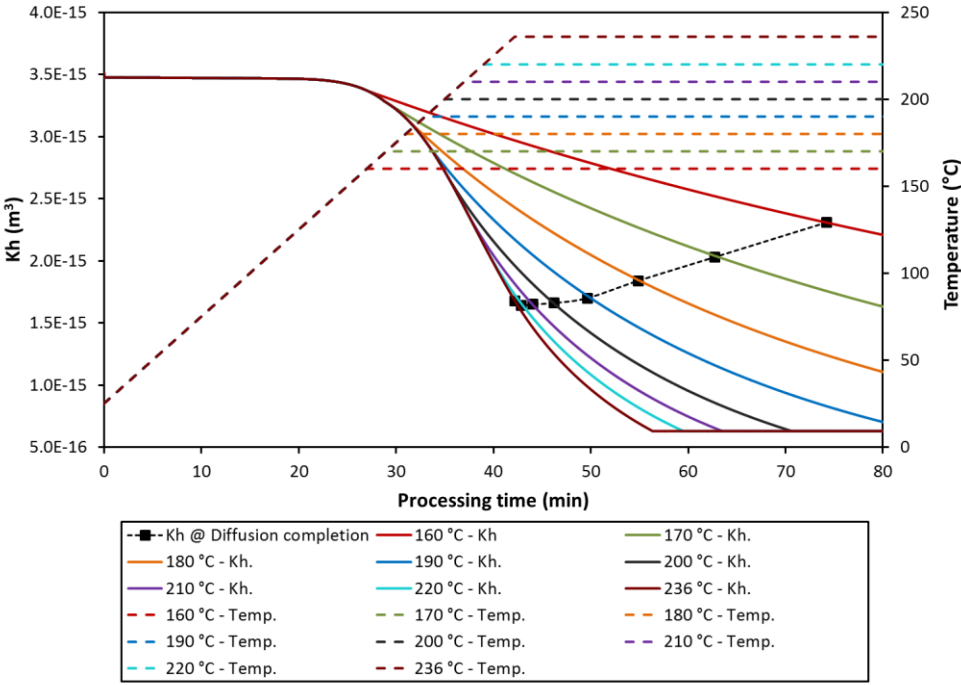


Figure 7.9 Interlayer permeability thickness products of  $0^\circ/0^\circ$  lay-up in the processing cycle with different dwell temperature and heating rate of  $5^\circ\text{C}/\text{min}$

From the previous parametric study, it is seen that low initial void content in the prepreg tape, full vacuum applied during the processing are favorable for air removal. Relatively high heating rate in the oven can significantly reduce the processing time for void air diffusing out from single layer prepreg tape with slightly increase of the diffusion complete temperature. The study of the material behavior of interlayer region shows that relatively high heating rate can decrease the reduction rate of the interlayer permeability in the resin rubbery region, allowing parts with larger in-plane dimensions to be processed (Chapter 6). For diffusion only mechanism, since the diffusion coefficient increases exponentially with temperature, high temperature dwell can provide high diffusion rate. Applying a heating rate to reach a desirable temperature for diffusion with shorter time can significantly reduce the overall processing time. Therefore, a relatively high heating rate could be beneficial for reducing the overall processing time for both mechanisms.

From the characterization of air permeability in Chapter 3, it is seen that the air permeability with a fixed interlayer included angle follows the rotation transformation matrix, which can also work at temperature since only the coordinate of interest changes. However, different interlayer included angle may have different behavior during the processing, as the different responses from  $0^\circ/0^\circ$  and  $0^\circ/90^\circ$  lay-ups. For the interlayer with cross-angles, the fiber/fiber contact limit the reduction of interlayer permeability at relatively higher level and early stage in the processing. Therefore, in the design of the laminate stacking sequences, block unidirectional lay-up is not favorable for void air removal and void reduction in the OVB processing.

## 7.5 Summary

Parametric study for the volatile removal in thermoplastic composites OVB processing was conducted based on the models for the combined mechanism and diffusion only mechanism in Chapter 5. It is seen that low initial void content in prepreg and high level of vacuum in the vacuum bag can reduce the processing time required for diffusion. A relatively high heating rate in the oven can significantly reduce the processing time for void air diffusion thorough single layer prepreg with slightly increasing of the temperature at which diffusion completes during the heating ramp. Time required for air evacuation in the interlayer region highly depends on the part in-plane dimensions or the flow length, and the level of interlayer air permeability in the processing. An air removal strategy chart can be constructed for selection of the dominating air removal mechanism for processing design and optimization based on the part in-plane dimensions and thickness and the allowable processing time. For thin parts with very large in-plane size, void air removal relying on diffusion through the laminate thickness in high temperature dwell cycle may reduce the processing time compared to the combined mechanism. The combined mechanism is more efficient for air removal in thick section laminates (>20 layers for AS4/APC2 laminates within 8 hrs processing window). The air flow time through the interlayer region of a part is governed by the interlayer permeability. Based on the evolution of the interlayer permeability during OVB processing, proper low temperature dwell cycle could be designed and added to the heating ramp to optimize the processing cycle. The models and results in this study provide important insights into the design and optimization of the OVB processing for the void air removal and void reduction in thermoplastic composites.

## Chapter 8

### SUMMARY AND FUTURE WORK

#### 8.1 Research Summary

A critical issue to evaluate the possibility for low cost OVB processing to replace the autoclave is the void reduction. The primary goal of this work is to explore the key mechanisms for void reduction and establish the processing method for thermoplastic composites with any size and thickness via OVB processing. In this research, the microstructure of voids in the thermoplastic prepreg is fully characterized in 3D instead of traditional 2D techniques. The 3D geometry of voids has been found. Void properties not only content but also length, equivalent diameter, and aspect ratio were studied statistically and described with suitable statistical distribution function. SRVE based on each void property representing the minimum size of the prepreg tape to be examined to obtain reliable property was determined. The statistical distribution functions can provide basics for modeling purposes. The methodology for analyzing the voids and relating the results to the void dynamics during the processing can be applied to other processing methods and other materials.

The rough surfaces of the prepreg tape were found to be an important feature of the thermoplastic prepreg tape which can provide highly permeable interlayer regions in prepreg stacks. The interlayer permeability of thermoplastic prepreg stacks was fully investigated with a novel experimental set-up based on 1D flow, which has not been studied before. The stacking sequence dependency of the interlayer permeability was obtained and it is proved the interlayer permeability tensor follows

the rotation transformation matrix for an included angle between two contact layers. The evolution of the interlayer permeability during the processing was also investigated experimentally. Theoretical model based on the time temperature dependent response of resin with the consideration of the fiber-fiber contact of the interlayer region was developed to describe the change of interlayer permeability during processing.

With the highly permeable interlayer region, the key mechanism for the removal of air in the voids that air diffusion through single layer prepreg followed by interlayer air flow through was validated by consolidation experiments of thick laminates in OVB processing. This mechanism also points out the importance of the interlayer permeability of the thermoplastic prepreg stacks. If the surfaces of the tape are smooth resulting low interlayer air permeability, void air removal may rely on the diffusion through the entire laminate thickness, leading to impractical processing time to achieve low void content thick laminate with the OVB process.

Analytical Models based on both the combined mechanism of single layer air diffusion followed by interlayer air flow and the diffusion through the thickness of the prepreg stacks only mechanism were developed. The models capture the details of the transient process of air diffusion and interlayer flow, further validates our proposed mechanism, and provides deep understanding of the mechanism for void air removal. With the models, the effect of initial void content in the prepreg, the processing conditions, and the part thickness and in-plane dimensions were investigated. And finally, the processing cycle can be designed and optimized for part with any thickness and in-plane dimensions.

## 8.2 Future Work

The void content in the thermoplastic prepreg sets the starting point for void reduction in the processing of the parts, and it is shown that the processing time can be reduced with low void content in the parametric study of this work. Therefore, it is very beneficial to have thermoplastic prepreg tape with low void content. The cost for producing low void content prepreg is very high now. So the impregnation technology on reducing the void content in the prepreg material efficiently without sacrificing the productivity and increasing the production cost of the thermoplastic prepreg tape can be investigated in future.

In this research, the interlayer permeability was shown to be an important mechanism to achieve low void content in thick thermoplastic laminates in OVB process, and largely affected by the microstructure of the surface layer of the prepreg tape. Promoting the interlayer permeability by designing and controlling the surface of the prepreg can be investigated. Increasing the height of the interlayer region can increase the permeability. Increasing the initial contact area can reduce the rate of the reduction of the interlayer permeability during processing with lower local stress. It is shown that fiber-fiber contact can limit the reduction of the interlayer permeability during processing. Enhancing the effect of fiber-fiber contact may be done by increasing the fiber volume fraction in the surface layers of the prepreg. However, this may result in lack of bonding between layers. Therefore, there might be an optimal resin thickness that provides a good balance of bonding and fiber-fiber contact. Another future investigation may be on changing the microstructure of the entire thermoplastic prepreg tape to provide permeability in the through –thickness direction and in-plane direction in single layer of the tape.

In this research, the interlayer permeability was monitored after the processing and was related to the resin behavior through model work and the investigation on the microstructure of the tape. Techniques to monitor the interlayer thickness change and measure the interlayer permeability at elevated temperature can provide better understanding for the evolution of the interlayer permeability.

The modeling of the interlayer permeability may be done with FEM. The evolution of the interlayer geometry may be modeled with real tape surface or interlayer profiles and time temperature dependent resin constitutive models. The deformed interlayer geometry may be input into a fluid dynamics model for the simulation of air flow to predict the interlayer permeability. In the squeeze flow intimate contact model, the initial degree of contact of more than 0.29 is reported [33,35]. However, in this research, it is seen that the initial contact is in the order of 0.01. The difference between the two is mainly due to the development of intimate contact at temperature below the resin melting. The FEM resin constitution model will provide the first step model of the development of intimate contact during the processing that is not included in the intimate contact model developed based on squeeze flow mechanism before. This model will complete the model for the development of intimate contact for the entire processing cycle.

For the thermoplastic composite ATP process, research efforts were mostly spend on obtaining fully consolidated part right after the ATP process. However, post consolidation with autoclave is commonly used to achieve low void content. OVB processing may replace the autoclave for the post processing to reduce the processing cost. However, if voids are trapped in the laminates after ATP process and the interlayer regions of the laminates are not permeable enough for void air evacuation,

the time required to reduce void air relying on diffusion through the thickness direction can be extremely long and not practical for thick parts. In order to activate the mechanism of interlayer air flow, ATP process may be controlled to provide enough bonding of the layers but still leave permeable interlayer regions for the air evacuation in the OVB process. And the experimental set-up for the interlayer permeability measurement designed in this dissertation may be used to characterize the interlayer permeability for the prepreg stack after ATP process. Then, the relationship between ATP processing condition and the interlayer permeability can be obtained, and eventually used for the optimization of the two step process of ATP followed by OVB process.

Process models developed in this research are individual models based on each mechanism. The temperature gradient through the thickness direction of the laminates was not considered in the models. Future work on integrating all the models and take more details into account such as the temperature gradient, or distributed voids in the laminates can provide better simulation for the void reduction in the processing.

Experimental work to further validate and evaluate the applicability of the processing models may be conducted with different processing conditions such as partial vacuum, positive pressure, heating rates, and the dimension of the parts.

## REFERENCES

- [1] Vaidya UK, Chawla KK. Processing of fibre reinforced thermoplastic composites. *Int Mater Rev* 2008;53:185–218.
- [2] Lystrup A, Andersen TL. Autoclave consolidation of fibre composites with a high temperature thermoplastic matrix. *J Mater Process Technol* 1998;77:80–5.
- [3] Fernandez I, Blas F, Frovel A. Autoclave forming of thermoplastic composite parts. *J Mater Process Technol* 2003;143:266–9.
- [4] Miller A, Gibson AG. Impregnation techniques for thermoplastic matrix composites. *Polym Polym Compos* 1996;4:459–81.
- [5] Bates PJ, Zou XP. Polymer melt impregnation of glass roving. *Int J Polym Process* 2002;4.
- [6] Cogswell FN, Staniland PA. Method of producing fibre-reinforced composition. 4,541,884, 1985.
- [7] Cogswell FN, Cowen G, Nield E, Turner RM. Process for making fibre reinforced products. 4,783,349, 1988.
- [8] Texier A, Davist RM, Lyon KR, Gungor A, Mcgrath JE, Marand H, et al. Fabrication of PEEK / carbon fibre composites by aqueous suspension prepregging \* 1993;34:896–906.
- [9] Wood JR, Bader MG. Void control for polymer-matrix composites (1): Theoretical and experimental methods for determining the growth and collapse of gas bubbles. *Compos Manuf* 1994;5:139–47.
- [10] Santulli C, Brooks R, Rudd CD, Long a. C. Influence of microstructural voids on the mechanical and impact properties in commingled E-glass/polypropylene thermoplastic composites. *Proc Inst Mech Eng Part L J Mater Des Appl* 2002;216:85–100.
- [11] Cogswell FN. Thermoplastic aromatic polymer composites : a study of the structure, processing, and properties of carbon fibre reinforced polyetheretherketone and related materials. Oxford [England]; Boston:

Butterworth-Heinemann; 1992.

- [12] Roychowdhury S. Consolidation in filament winding of thermoplastic matrix composites. Master's Thesis, Univ Delaware, Newark, 19716 n.d.
- [13] Olson BD, Gillespie JW, Bogetti TA, Lamontia MA. The effects and non-destructive evaluation of defects in thermoplastic compression-loaded composite cylinders. *J Thermoplast Compos Mater* 1995;8:109–36.
- [14] Boey FYC, Lye SWW. VOID REDUCTION IN AUTOCLAVE PROCESSING OF THERMOSET COMPOSITES .1. HIGH-PRESSURE EFFECTS ON VOID REDUCTION. *Composites* 1992;23:261–265 ST-VOID REDUCTION IN AUTOCLAVE PROCESSI.
- [15] Grunenfelder LK, Nutt SR. Void formation in composite prepregs – Effect of dissolved moisture. *Compos Sci Technol* 2010;70:2304–9.
- [16] Gu YZ, Li M, Zhang ZG, Sun ZJ. Void Formation Model and Measuring Method of Void Formation Condition During Hot Pressing Process. *Polym Compos* 2010;31:1562–1571 ST-Void Formation Model and Measuring.
- [17] Advani S, Sozer E, Mishnaevsky L. *Process Modeling in Composites Manufacturing*. vol. 56. 2003.
- [18] Hou M, Ye L, Mai YW. Manufacturing process and mechanical properties of thermoplastic composite components. *J Mater Process Technol* 1997;63:334–8.
- [19] Gennaro R, Montagna F, Maffezzoli a., Fracasso F, Fracasso S. On-line Consolidation of Commingled Polypropylene/Glass Roving During Filament Winding. *J Thermoplast Compos Mater* 2011;24:789–804.
- [20] Lamontia MA, Funck SB, Gruber MB, Cope RD, Waibel BJ, Gopez NM. Manufacturing flat and cylindrical laminates and built up structure using automated thermoplastic tape laying, fiber placement, and filament winding. *Sampe J* 2003;39:30–8.
- [21] Lamontia MA, Gruber MB. Remaining developments required for comercializing in situ thermoplastic ATP. *SAMPE 2007 - Balt MD* 2007:15.
- [22] AMON M, DENSON C. A STUDY OF THE DYNAMICS OF FOAM GROWTH - ANALYSIS OF THE GROWTH OF CLOSELY SPACED SPHERICAL BUBBLES. *Polym Eng Sci* 1984;24:1026–34.
- [23] Arefmanesh A, Advani SG, Dvani S, Michaelides E. A numerical study of

- bubble-growth during low-pressure structural foam molding process. *Polym Eng Sci* 1990;30:1330–7.
- [24] Arefmanesh A. Numerical and Experimental Study of Bubble Growth in Highly Viscous Fluids 1991.
- [25] Roychowdhury S. Void formation and growth in amorphous thermoplastic polymeric materials. University of Delaware, 1995.
- [26] Roychowdhury S, Gillespie JW, Advani SG. Volatile-induced void formation in amorphous thermoplastic polymeric materials: I. Modeling and parametric studies. *J Compos Mater* 2001;35:340–66.
- [27] Ledru Y, Bernhart G, Piquet R, Schmidt F, Michel L. Coupled visco-mechanical and diffusion void growth modelling during composite curing. *Compos Sci Technol* 2010;70:2139–45.
- [28] Boey FYC, Lye SW. Void reduction in autoclave processing of thermoset composites Part 2 : Void reduction in a microwave curing process. *Composites* 1992;23:266–70.
- [29] Denault J, Canada C, Dumouchel M, Division A. Consolidation process of PEEK / carbon composite for aerospace applications. *Adv Perform Mater* 1998;5:83–96.
- [30] Carpenter CE, Colton JS. On-Line Consolidation Mechanisms in Thermoplastic Filament Winding. *Polym Compos* 1994;15.
- [31] Pitchumani R, Ranganathan S, Don RC, Gillespie JW, Lamontia MA. Analysis of transport phenomena governing interfacial bonding and void dynamics during thermoplastic tow-placement. *Int J Heat Mass Transf* 1996;39:1883–97.
- [32] LEE W, SPRINGER G. A MODEL OF THE MANUFACTURING PROCESS OF THERMOPLASTIC MATRIX COMPOSITES. *J Compos Mater* 1987;21.
- [33] MANTELL S, SPRINGER G. MANUFACTURING PROCESS MODELS FOR THERMOPLASTIC COMPOSITES. *J Compos Mater* 1992;26.
- [34] Pitchumani R, Gillespie JW, Lamontia MA. Design and optimization of a thermoplastic tow-placement process with in-situ consolidation. *J Compos Mater* 1997;31:243–75.
- [35] Tierney J, Gillespie JW. Modeling of in situ strength development for the thermoplastic composite tow placement process. *J Compos Mater*

2006;40:1487–506.

- [36] Tierney J. MATERIAL QUALITY DEVELOPMENT DURING THE AUTOMATED TOW Placement Process. PhD Thesis, Univ Delaware 2003.
- [37] Ranganathan S, Advani SG, Lamontia MA. A nonisothermal process model for consolidation and void reduction during in-situ tow placement of thermoplastic composites. *J Compos Mater* 1995;29:1040–62.
- [38] Ranganathan S, Advani SG. A model for consolidation and void reduction during thermoplastic tow placement. *25th Int SANPE Tech Conf* 1993:630–41.
- [39] Tierney J, Gillespie JW. Modeling of heat transfer and void dynamics for the thermoplastic composite tow-placement process. *J Compos Mater* 2003;37:1745–68.
- [40] Tierney J. Process Modeling of Thermoplastic Composites and Its Applications THE AUTOMATED TOW PLACEMENT. EADS Visit 2006.
- [41] Khan MA, Mitschang P, Schledjewski R. Tracing the void content development and identification of its effecting parameters during in situ consolidation of thermoplastic tape material. *Polym Polym Compos* 2010;18:1–15.
- [42] Lamontia MA, Bruber M., Tierney J, Gillespie JW, Jensen B., Cano RJ. In situ thermoplastic ATP needs flat tapes and tows with few voids. *SAMPE Eur.*, 2009.
- [43] Lamontia MA, Gruber MB, Tierney J, Gillespie Jr. JW, Jensen BJ, Cano RJ. Modeling the Accudyne Thermoplastic In Situ ATP Process. *30th Int. SAMPE Eur. Conf. Paris*, 2009.
- [44] Lamontia MA, Gruber MB, Systems A, Drive S, Tierney J, Gillespie JW. Modeling the Accudyne thermoplastic in situ ATP process. *SAMPE 2009, Porte Versailles, Paris, Fr. March 23-25, 2009.*
- [45] Gruber MB, Lockwood IZ, Dolan TL, Funck SB, Tierney J, Simacek P, et al. THERMOPLASTIC IN SITU PLACEMENT REQUIRES BETTER IMPREGNATED TAPES AND TOWS. *SAMPE 2012 - Balt., n.d.*
- [46] Simacek P, Advani SG, Gruber M, Jensen B. A non local void filling model to describe its dynamics during processing. *Compos Part A Appl Sci Manuf* 2013;46:154–65.

- [47] Kardos JL, Dudukovic MP, Dave R. VOID GROWTH AND RESIN TRANSPORT DURING PROCESSING OF THERMOSETTING - MATRIX COMPOSITES. *Adv Polym Sci* 1986;80:102–123 ST-VOID GROWTH AND RESIN TRANSPORT DURI.
- [48] Vaxman A, Narkis M, Siegmann A, Kenig S. VOID FORMATION IN SHORT-FIBER THERMOPLASTIC COMPOSITES. *Polym Compos* 1989;10:449–453 ST-VOID FORMATION IN SHORT-FIBER THERMO.
- [49] Leterrier Y, Gsell C. Formation and Elimination of Voids During the Processing of Thermoplastic Matrix Composites. *Polym Compos* 1994;15:101–5.
- [50] Muric-Nesic J, Compston P, Stachurski ZH. On the void reduction mechanisms in vibration assisted consolidation of fibre reinforced polymer composites. *Compos Part A Appl Sci Manuf* 2011;42:320–7.
- [51] Nam J, Sefefus JC. Gas permeation and viscoelastic deformation of prepregs in composite manufacturing processes. *Polym Compos* 1995;1:370–377.
- [52] Shim S, Seferis JC. Thermal and Air Permeation Properties of a Carbon Fiber / Toughened Epoxy Based Prepreg System. *J Appl Polym Sci* 1997;65:5–16.
- [53] Tavares SS, Michaud V, Månson J -a. E. Assessment of semi-impregnated fabrics in honeycomb sandwich structures. *Compos Part A Appl Sci Manuf* 2010;41:8–15.
- [54] Tavares SS, Caillet-Bois N, Michaud V, Månson J -a. E. Non-autoclave processing of honeycomb sandwich structures: Skin through thickness air permeability during cure. *Compos Part A Appl Sci Manuf* 2010;41:646–52.
- [55] Tavares SS, Michaud V, Månson J -a. E. Through thickness air permeability of prepregs during cure. *Compos Part A Appl Sci Manuf* 2009;40:1587–96.
- [56] Xin C, Li M, Gu Y, Li Y, Zhang Z. Measurement and analysis on in-plane and through-thickness air permeation of fiber/resin prepreg. *J Reinf Plast Compos* 2011;30:1467–79.
- [57] Juska TD, Musser BS, Jordan BP, Hall JC. Oven cacuum bBag (OVB) prepreg fabrication infusion processing. *SAMPE J* 2009 2009;45:22–36.
- [58] Santulli C, Gil RG, Long AC, Clifford MJ. Void content measurements in commingled E-glass/polypropylene composites using image analysis from optical micrographs. *Sci Eng Compos Mater* 2002;10:77–90.

- [59] Wolfrath J, Michaud V, Manson J. Deconsolidation in glass mat thermoplastics: Influence of the initial fibre/matrix configuration. *Compos Sci Technol* 2005;65:1601–8.
- [60] Spowart JE. The 3-D analysis of discontinuously reinforced aluminum composite microstructures. *J Mater* 2006;58:29–33.
- [61] Spowart JE. Automated serial sectioning for 3-D analysis of microstructures. *Scr Mater* 2006;55:5–10.
- [62] Fujisaki K, Yokota H, Furushiro N, Komatani S, Ohzawa S, Sato Y, et al. Three-dimensional microscopic elemental analysis using an automated high-precision serial sectioning system. *Microsc Microanal* 2011;17:246–51.
- [63] Awaja F, Nguyen M, Zhang S, Arhatari B. The investigation of inner structural damage of UV and heat degraded polymer composites using X-ray micro CT. *Compos Part A Appl Sci Manuf* 2011;42:408–18.
- [64] Centea T, Hubert P. Measuring the impregnation of an out-of-autoclave prepreg by micro-CT. *Compos Sci Technol* 2011;71:593–9.
- [65] Enfedaque A, Molina-Aldareguia JM, Galvez F, Gonzalez C, Llorca J. Effect of glass fiber hybridization on the behavior under impact of woven carbon fiber/epoxy laminates. *J Compos Mater* 2010;44:3051–68.
- [66] Hernandez S, Sket F, Molina-Aldareguia JM, Gonzalez C, Llorca J. Effect of curing cycle on void distribution and interlaminar shear strength in polymer-matrix composites. *Compos Sci Technol* 2011;71:1331–41.
- [67] Kim KJ, Yu WR, Lee JS, Gao L, Thostenson ET, Chou TW, et al. Damage characterization of 3D braided composites using carbon nanotube-based in situ sensing. *Compos Part A Appl Sci Manuf* 2010;41:1531–7.
- [68] Tiseanu I, Tsitrone E, Kreter A, Craciunescu T, Loarer T, Pegourie B, et al. X-ray micro-tomography studies on carbon based composite materials for porosity network characterization. *Fusion Eng Des* 2011;86:1646–51.
- [69] Scheck C, Zupan M. Ductile fracture evaluated through micro-computed X-ray tomography. *Scr Mater* 2011;65:1041–4.
- [70] Spowart JE. Automated serial sectioning for 3-D analysis of microstructures. *Scr Mater* 2006;55:5–10.
- [71] Shan Z, Gokhale AM. Representative volume element for non-uniform

2002;24:361–79.

- [72] Grufman C, Ellyin F. Numerical modelling of damage susceptibility of an inhomogeneous representative material volume element of polymer composites. *Compos Sci Technol* 2008;68:650–7.
- [73] Trias D, Costa J, Turon A, Hurtado J. Determination of the critical size of a statistical representative volume element (SRVE) for carbon reinforced polymers☆. *Acta Mater* 2006;54:3471–84.
- [74] Zangenberg J, Brøndsted P. Determination of the minimum size of a statistical representative volume element from a fibre-reinforced composite based on point pattern statistics. *Scr Mater* 2013;68:503–5.
- [75] Spanos PD, Kotsos A. A multiscale Monte Carlo finite element method for determining mechanical properties of polymer nanocomposites. *Probabilistic Eng Mech* 2008;23:456–70.
- [76] Chen XL, Liu YJ. Square representative volume elements for evaluating the effective material properties of carbon nanotube-based composites. *Comput Mater Sci* 2004;29:1–11.
- [77] Jafari A, Khatibi AA, Mashhadi MM. Comprehensive investigation on hierarchical multiscale homogenization using Representative Volume Element for piezoelectric nanocomposites. *Compos Part B Eng* 2011;42:553–61.
- [78] Scholz S, Gillespie JW, Heider D. Measurement of transverse permeability using gaseous and liquid flow. *Compos Part A Appl Sci Manuf* 2007;38:2034–40.
- [79] Marcus H. Permeability of a sample of an anisotropic porous medium. *J Geophys Res* 1962;67:5215–25.
- [80] Zhang D, Heider D, Gillespie, John W. J. Volatile removal during out of autoclave processing of high performance thermoplastic composites. *CAMX - 2014, Orlando, 13-16 Oct., 2014*, p. 14.
- [81] Ziarani AS, Aguilera R. Knudsen's Permeability Correction for Tight Porous Media. *Transp Porous Media* 2012;91:239–60.
- [82] Wu Y, Pruess K, Persoff P, Division ES, Berkeley L. Gas flow in porous media with Klinkenberg effects. *Transp Porous Media* 1998;32:117–37.
- [83] Levy A, Kratz J, Hubert P. Air evacuation during vacuum bag only prepreg

processing of honeycomb sandwich structures: In-plane air extraction prior to cure. *Compos Part A Appl Sci Manuf* 2015;68:365–76.

- [84] Yang F, Pitchumani R. Fractal description of interlaminar contact development during thermoplastic composites processing. *J Reinf Plast Compos* 2001;20:536–46.
- [85] Faulder D. Decline curve analysis of vapor-dominated reservoirs. 15. US Dep. Energy's Geotherm. Progr. Rev. San Fr. CA (United States), 24-26 Mar 1997, 1997.
- [86] Daprat G, Ramey H, Cincoley H. A method to determine the permeability thickness product for a naturally fractured reservoir. *J Pet Technol* 1982;34:1364–70.
- [87] Centea T, Grunenfelder LK, Nutt SR. A review of out-of-autoclave prepregs - Material properties, process phenomena, and manufacturing considerations. *Compos Part A Appl Sci Manuf* 2015;70:132–54.
- [88] Cender T a., Simacek P, Davis S, Advani SG, Advani DSG. Gas Evacuation From Partially Saturated Woven Fiber Laminates. *Transp Porous Media* 2016;115:1–18.
- [89] Van Krevelen DW, TE Nijenhuis K. *Properties of polymers*. 4th ed. Radarweg 29, PO Box 211, 1000 AE Amsterdam, The Netherlands: Elsevier B.V.; 2009.
- [90] Mark JE. *Polymer data handbook*. Oxford University Press, Inc.; 1999.
- [91] Xiao X. Studies of the viscoelastic behaviour of a thermoplastic resin composite. *Compos Sci Technol* 1989;34:163–82.
- [92] A comprehensive review of the materials properties of VICTREX® PEEK™ high performance polymer. [www.victrex.com](http://www.victrex.com) n.d.
- [93] Ciora RJ, Magill JH. Rolltruded poly(Aryl Ether Ether Ketone) (PEEK) for membrane applications. *Sep Sci Technol* 1997;32:899–923.
- [94] Zhang D, Heider D, Advani SG, Gillespie, John W. J, Gillespie JW. Out of autoclave consolidation of voids in continuous fiber reinforced thermoplastic composites. SAMPE 2013 - Long Beach, CA, 6-9 May, 2013, n.d., p. 16.
- [95] Zhang D, Heider D, Gillespie, John W. J. Determination of void statistics and statistical representative volume elements in carbon fiber-reinforced thermoplastic prepregs. *J Thermoplast Compos Mater* 2015.

- [96] Paul DR, Dibenedetto AT. Diffusion in amorphous polymers. *Polymer (Guildf)* 1965;44:17–44.
- [97] Wang D, Jiang W, Gao H, Jiang Z. Diffusion and swelling of carbon dioxide in amorphous poly(ether ether ketone)s. *J Memb Sci* 2006;281:203–10.
- [98] Yang F, Pitchumani R. A fractal Cantor set based description of interlaminar contact evolution during thermoplastic composites processing. *J Mater Sci* 2001;36:4661–71.
- [99] Bologna S, G DR, Spagnoli G. Sorption / desorption of carbon dioxide into amorphous and semicrystalline PEEK films. *ISASF 2008, Barcelona, n.d.*, p. 1–6.
- [100] Zhang D, Levy A, Gillespie JW. On the void consolidation mechanisms of continuous fiber reinforced thermoplastic composites. *SAMPE 2012-Baltimore, MD, 2012*, p. 16.
- [101] Paul A. *Chemistry of Glasses*. Second. 29 West 35th Street, New York, NY 10001: Chapman and Hall; 1990.
- [102] Dixon JC. Appendix B-Properties of Air. *Shock Absorber Handb*. 2nd ed., West Sussex, England: John Wiley & Sons, Ltd; 2007, p. 375–8.
- [103] Firouzi M, Alnoaimi K, Kovscek A, Wilcox J. Klinkenberg effect on predicting and measuring helium permeability in gas shales. *Int J Coal Geol* 2014;123:62–8.
- [104] Civan F. Effective correlation of apparent gas permeability in tight porous media. *Transp Porous Media* 2010;82:375–84.
- [105] Levy A, Heider D, Tierney J, Gillespie JW. Inter-layer thermal contact resistance evolution with the degree of intimate contact in the processing of thermoplastic composite laminates. *J Compos Mater* 2013;48:491–503.
- [106] Mantell SC, Qiuling Wang, Springer GS. Processing Thermoplastic Composites in a Press and by Tape Laying--Experimental Results. *J Compos Mater* 1992;26:2378–401.
- [107] F. Yang, Pitchumani R. Nonisothermal Healing and Interlaminar Bond Strength Evolution During Thermoplastic Matrix Composites Processing. *Polym Compos* 2003;24:263–78.
- [108] Stokes-Griffin CM, Compston P, Matuszyk TI, Cardew-Hall MJ. Thermal

- modelling of the laser-assisted thermoplastic tape placement process. *J Thermoplast Compos Mater* 2013;28:1445–62.
- [109] Hou M, Ye L, Lee H, Mai Y. Manufacture of a carbon-fabric-reinforced polyetherimide (CF/PEI) composite material. *Compos Sci Technol* 1998;58:181–90.
- [110] Dara PH, Loos AC. *Thermoplastic Matrix Composite Processing Model*. 1985.
- [111] Sonmez FO, Akbulut M. Process optimization of tape placement for thermoplastic composites. *Compos Part a-Applied Sci Manuf* 2007;38:2013–2023 ST–Process optimization of tape place.
- [112] Borodich FM, Mosolov AB. Fractal roughness in contact problems. *J Appl Math Mech* 1992;56:681–90.
- [113] Tierney JJ, Gillespie Jr. JW. Crystallization kinetics behavior of PEEK based composites exposed to high heating and cooling rates. *Compos Part A Appl Sci Manuf* 2004;35:547–58.
- [114] Sun CT, Yoon KJ. Characterization of elastic-plastic behavior of AS4/PEEK thermoplastic composite for temperature variation. *J Compos Mater* 1991;25:1297–313.
- [115] Wang C, Sun CT. Experimental characterization of constitutive models for PEEK thermoplastic composite at heating stage during forming. *J Compos Mater* 1997;31:1480–506.
- [116] El-Qoubaa Z, Othman R. Strain rate sensitivity of polyetheretherketone's compressive yield stress at low and high temperatures. *Mech Mater* 2016;95:15–27.
- [117] El-Qoubaa Z, Othman R. Characterization and modeling of the strain rate sensitivity of polyetheretherketone's compressive yield stress. *Mater Des* 2015;66:336–45.
- [118] Chen F, Ou H, Lu B, Long H. A constitutive model of polyether-ether-ketone (PEEK). *J Mech Behav Biomed Mater* 2016;53:427–33.
- [119] Kawai M, Masuko Y, Kawase Y, Negishi R. Micromechanical analysis of the  $\sigma$ -axis rate-dependent inelastic behavior of unidirectional AS4 = PEEK at high temperature 2001;43:2069–90.
- [120] Rae PJ, Brown EN, Orler EB. The mechanical properties of poly(ether-ether-

- ketone) (PEEK) with emphasis on the large compressive strain response. *Polymer (Guildf)* 2007;48:598–615.
- [121] Jones DP, Leach DC, Moore DR. Mechanical properties of poly (ether-ether-ketone) for engineering applications. *Polymer (Guildf)* 1985;26:1385–93.
- [122] Maksimov R, Kubat J. Time and Temperature Dependent Deformation of Poly(Ether Ether Ketone) PEEK. *Mech Compos Mater* 1997;33:517–25.
- [123] Ha SK, Wang Q, Chang F-K. Modeling the viscoplastic behavior of fiber-reinforced thermoplastic matrix composites at elevated temperatures. *J Compos Mater* 1991;25:334–74.
- [124] Damore A, Pompo A, Netti P, Masi E, Nicolais L. Non-Linear Viscoelastic Behavior of PEEK-Based Composites 1993;12:327–40.
- [125] Wang C, Sun C. Experimental characterization of constitutive models for PEEK thermoplastic composite at heating stage during forming. *J Compos Mater* 1997;31:1481–506.
- [126] Xiao XR, Hiel CC, Cardon AH. Characterization and modeling of nonlinear viscoelastic response of PEEK resin and PEEK composites. *Compos Eng* 1994;4:681–702.
- [127] Amore AD, Pompo A, Nicolais L. Viscoelastic Effects in Poly ( Ether Ether Ketone ) ( PEEK ) and PEEK-Based Composites 1991;41:303–25.
- [128] Vieille B, Albouy W, Taleb L. Viscoelastic viscoplastic model for aeronautical thermoplastic laminates at high temperature: Validation on high stress gradient structures. *Compos Part B Eng* 2016;90:278–86.
- [129] Drozdov AD. A model for the viscoelastic behavior of polymers at finite strains. *Int J Solids Struct* 1998;68:2315–47.
- [130] Sonmez FO, Hahn HT. Thermoviscoelastic analysis of the thermoplastic composite tape placement process. *J Thermoplast Compos Mater* 1997;10:381–414.
- [131] Chapman BM. Linear superposition of viscoelastic responses in nonequilibrium systems. *J Appl Polym Sci* 1974;18:3523–36.
- [132] Gates TS, Sun CT. Elastic/viscoplastic constitutive model for fiber reinforced thermoplastic composites. *AIAA J* 1991;29:457–63.
- [133] Collantes ER, Gahimer T, Welsh WJ. Evaluation of computational chemistry

approaches for predicting the properties of polyimides. *Comput Theor Polym Sci* 1996;6:29–40.

- [134] Yuan M, Galloway JA, Hoffman RJ, Bhatt S. Influence of Molecular Weight on Rheological, Thermal, and Mechanical Properties of PEEK. *Polym Eng Sci* 2011;51:94–102.
- [135] Chou T-W. *Microstructural design of fiber composites*. 1st ed. Cambridge, UK: Cambridge University Press; 1992.
- [136] Talbott MF, Springer GS, Berglund LA. The Effects of Crystallinity on the Mechanical Properties of PEEK Polymer and Graphite Fiber Reinforced PEEK. *J Compos Mater* 1987;21:1056–81.
- [137] Kirsch VA, Kirsch AA. Deposition of Aerosol Nanoparticles in Model Fibrous Filters. In: Agranovski I, editor. *AerosolsScience Technol*. 1st ed., Weinheim, Germany: Wiley-VCH; 2010, p. 285.
- [138] Wu S. Interfacial and surface tensions of polymers. *JMacromolecular Sci Rev Macromol Chem Phys* 1074;C 10:1–73.
- [139] Solid surface energy data (SFE) for common polymers n.d.
- [140] Advani SG, Sozer EM. *Process Modeling in Composites Manufacturing*. vol. 56. 2003.

## Appendix A

### COMPARISON ON VOID STATISTICS BETWEEN X-RAY MICRO-CT AND OPTICAL MICROSCOPY

#### A.1 Method for sample preparation and optical microscopy inspection

Prepreg samples were cut from different area of prepreg tape, embedded in epoxy resin, and polished down with Al<sub>2</sub>O<sub>3</sub> particles of 3μm in diameter. The cross-sections of the polished samples were observed with Nikon ECLIPS LV100 at 200× magnification. Images were taken with a resolution of 0.48μm/pixel. The width of prepreg (across the fiber direction) in each image is 0.64mm. 89 images from 8 prepreg samples were analyzed for voids. Single images were processed with Image J to obtain void content, void through thickness distribution, and void equivalent diameter. Then the distribution including average values were obtained through a statistical approach. The detailed image processing method and statistical procedures adopted is provided in Figure A.1.

#### A.2 2D Results Comparison

3D information of AS4/APC2 prepreg was obtained after micro CT scanning of 10 samples under 0.74μm/pixel. Since 2D micrographs of the cross-section of prepreg were generated from micro-CT, the 2D results can be used to compare with results from optical microscopy. The micro-CT 2D average void content was obtained by averaging the 2D void content of all the cross-sectional images of each sample and

then the 10 samples. It is seen from Figure A.2 that the 3D average void content value is slightly lower than the 2D micro-CT results (5.97% vs. 6.15%), but within the inherent variation between 2D and 3D, and can be considered equivalent. Consequently, the 2D cross-sections from micro-CT provide accurate void content information. The 3D micro-CT results reveal the 3D rod-like void geometry in the prepreg. In Figure A.2, both the 2D and 3D void content from micro-CT scans are found to be less than the 2D optical microscopy result. The difference can be attributed to the higher resolution optical microscopy capturing a larger number of small diameter voids that are below the micro-CT resolution.

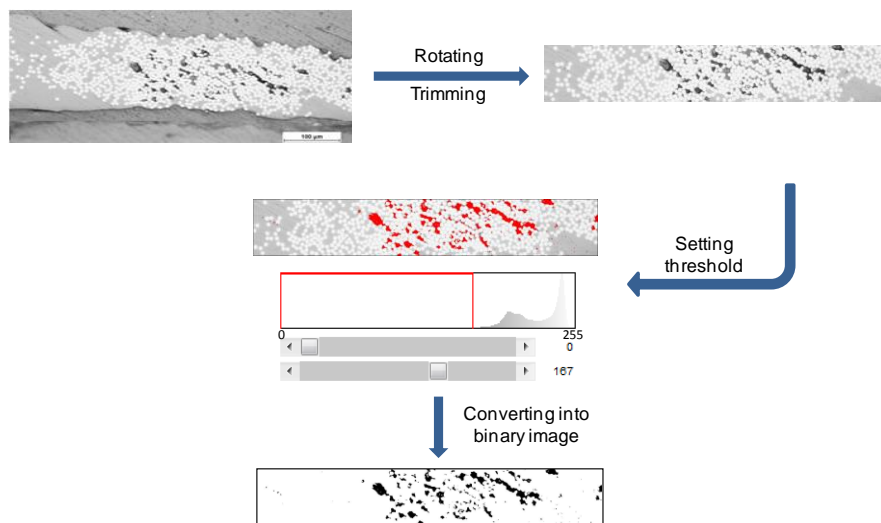


Figure A.1 Basic procedures for image processing

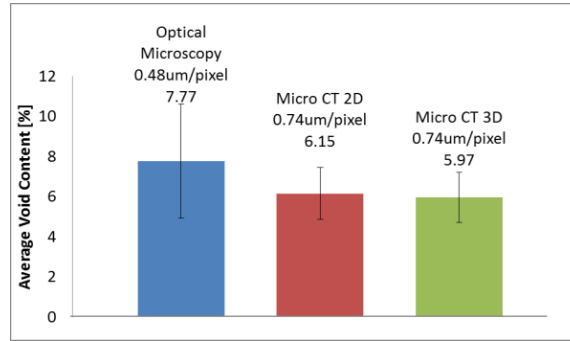


Figure A.2 2D and 3D average void content of prepreg tape

Comparing the 2D micro-CT and optical microscopy, the void equivalent diameter and the number density were analyzed, and the void size distributions per mm tape across the fiber direction are shown in Figure A.3. It is seen that voids with equivalent diameter in the range of  $3.5\mu\text{m}$  to  $24.5\mu\text{m}$  are similar in both the micro-CT 2D and optical microscopy methods. The major difference between the results is the number of voids smaller than  $3.5\mu\text{m}$ . More specifically, no void with equivalent diameter smaller than  $0.7\mu\text{m}$  was detected with micro-CT and a much smaller number of voids with  $d < 1.5\mu\text{m}$  were detected with micro-CT compare to the higher resolution optical microscopy. This is mainly due to the slightly lower resolution of micro-CT compared to the optical microscopy. In this case, the voids with equivalent diameter smaller than 1 pixel size were not detected. This likely explains the differences in void content measurements in Figure A.2.

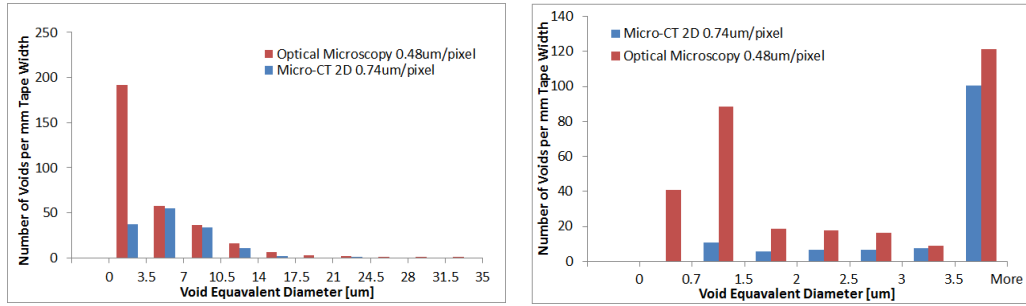


Figure A.3 Comparison of void equivalent diameter distribution per mm tape across the fiber direction

## **Appendix B**

### **DETERMINATION OF MICRO-CT RESOLUTIONS FOR VOID INSPECTION**

In order to obtain accurate results of void length, content, equivalent diameter and number densities within relatively large sample volume in minimum scanning time,  $\mu$ -CT scanning resolution to be used should be determined. One sample of 2.1 mm (width)  $\times$  1.8 mm (length)  $\times$  0.18 mm was scanned under 0.74  $\mu\text{m}/\text{pixel}$ , 1.48  $\mu\text{m}/\text{pixel}$  and 2.96  $\mu\text{m}/\text{pixel}$  with different image size of 4000  $\times$  2096, 2000  $\times$  1048, and 1000  $\times$  524 pixels, respectively. The effect of resolution on void volume and dimensions were studied.

#### **B.1 Effect of Scanning Resolution on Void Content**

Voids were extracted from the three scans and shown in Figure B.1. The total void volume and content of this sample under 1.48  $\mu\text{m}/\text{pixel}$  is comparable to the results under 0.74  $\mu\text{m}/\text{pixel}$ . Comparing to the void content from 0.74  $\mu\text{m}/\text{pixel}$  scan, the error for the scans of 1.48  $\mu\text{m}/\text{pixel}$  and 2.96  $\mu\text{m}/\text{pixel}$  are 8.9% and 19.2% respectively. It is also seen that small voids are not detected in the scan under 2.96 $\mu\text{m}/\text{pixel}$ .

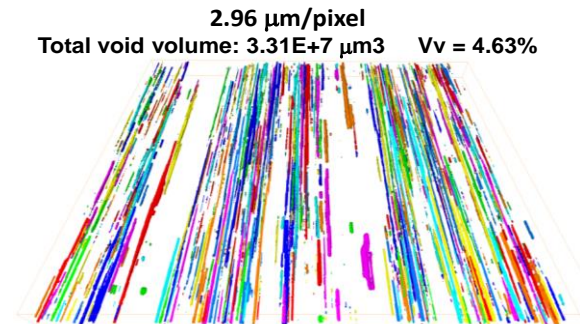
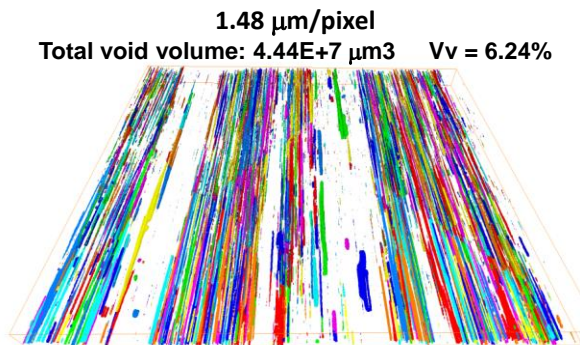
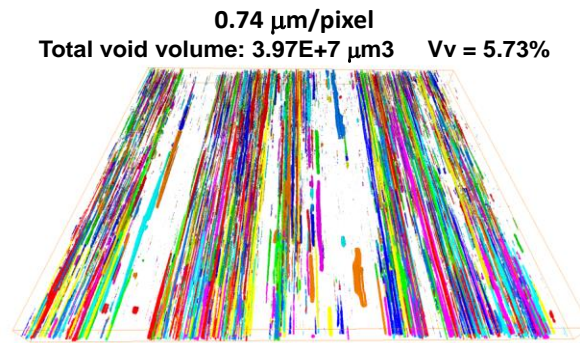


Figure B.1 Voids in the sample scanned with different resolutions of  $\mu\text{-CT}$ .

## B.2 Effect of scanning resolution on void length

The quantitative results of void length in the sample under different scanning resolutions are presented in Figure B.2. The major difference from scanning resolutions is the number of void with length below 400  $\mu\text{m}$  (i.e. 430 in highest resolution vs. 150 in lowest resolution). Many of the voids in this length range have smaller diameters that cannot be detected with lower resolutions. For the long voids with length  $> 800\mu\text{m}$ , no significant difference was found from the distributions. Voids with length equal to sample length of 1.8 mm were found in all three scans. In the length range of 400  $\mu\text{m}$  to 800  $\mu\text{m}$ , 1.48  $\mu\text{m}/\text{pixel}$  result contains more voids than the other two settings and is likely due to coalesce of the rod-like voids in close proximity.

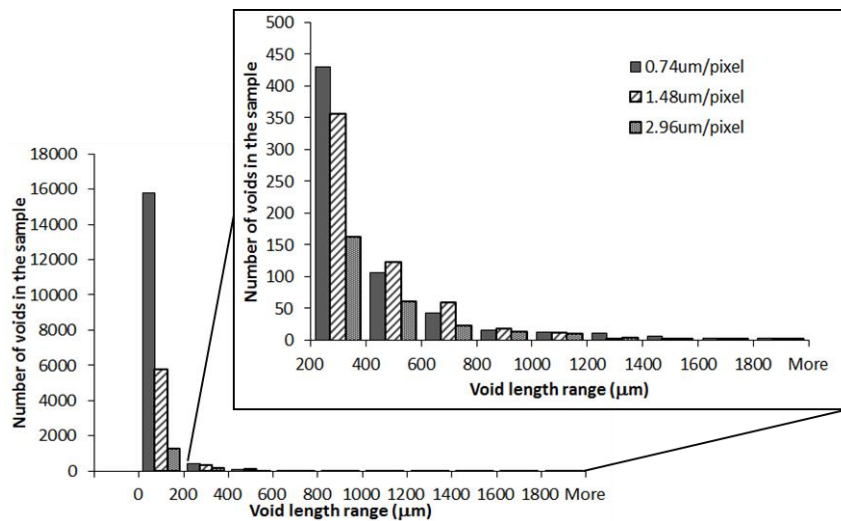


Figure B.2 Number of voids in different length ranges in a sample of 2.1 mm  $\times$  1.8 mm  $\times$  0.18 mm under different scanning resolution.

### B.3 Effect of scanning resolution on void equivalent diameter

Since voids may have varying cross section size along the axial direction, equivalent diameter of each void were calculated from its volume and length by assuming they are cylindrical. The number of voids in void equivalent diameter ranges with different resolution is shown in Figure B.3. It is seen that the number of voids that have diameter smaller than  $3.5 \mu\text{m}$  are significantly reduced when the resolution is reduced. More voids were found in lower resolution scans with diameter larger than  $7 \mu\text{m}$ . It is noticed that maximum and minimum detectable void equivalent diameter increases as the resolution decreases. The errors for maximum equivalent diameters compared to the highest resolution base line are 11% and 16% for  $1.48 \mu\text{m}/\text{pixel}$  and  $2.96 \mu\text{m}/\text{pixel}$  scanning results.

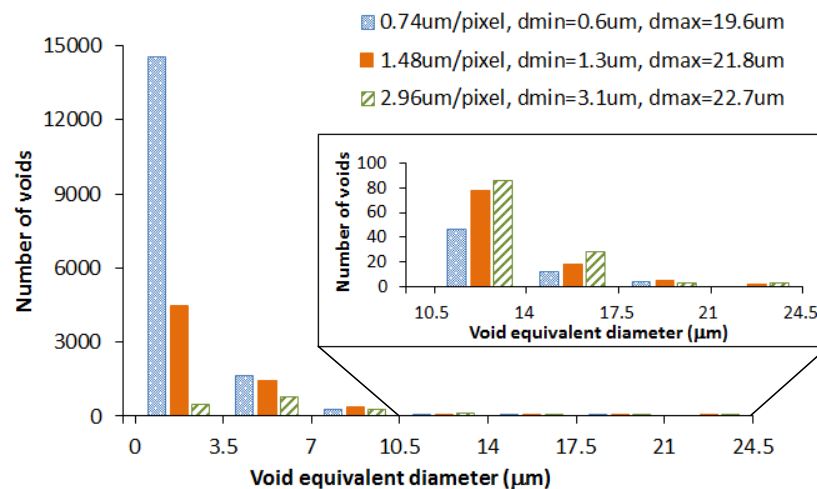


Figure B.3 Number of voids in different equivalent diameter ranges in a sample of  $2.1 \text{ mm} \times 1.8 \text{ mm} \times 0.18 \text{ mm}$  under different scanning resolution

From the above comparison, the highest resolution of 0.74  $\mu\text{m}/\text{pixel}$  can provide most accuracy for overall void volume, content, diameter and number density. 1.48  $\mu\text{m}/\text{pixel}$  provides reasonable accuracy for void content (<10% variation). 2.96  $\mu\text{m}/\text{pixel}$  is not recommended for the study of micro voids properties in this thermoplastic prepreg since it is losing too much void information. Comparing with the resolution of 0.74  $\mu\text{m}/\text{pixel}$ , the inspection time with 1.48  $\mu\text{m}/\text{pixel}$  is much shorter (3.5 hrs vs. 10 hrs for sample length of 3.8 mm) and reasonable for relatively large total sample volume.

## Appendix C

### Determination of Settings for Tape Surface Characterization with Confocal Microscope

#### C.1 Definitions of Surface Roughness Parameters

The definitions of the surface roughness parameter in the thesis are introduced as below and the schematics are presented in Figure C.1

Arithmetic mean roughness  $R_a$ : Arithmetic average of the absolute values of the roughness profile ordinates.

RMS roughness  $R_q$ : Root mean square average of the roughness profile ordinates.

Cross point average  $R_z$ : Vertical distance between the highest peak and the deepest valley within a sampling length

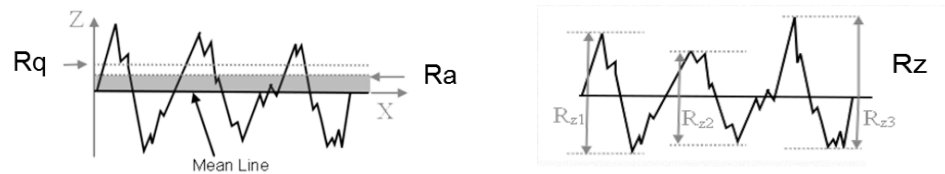


Figure C.1 Schematics of surface roughness parameters  $R_a$ ,  $R_q$ , and  $R_z$

#### C.2 Selection of Surface Scanning Parameters

In order to find out the proper scanning set-up for the surface characterization of the prepreg tape, six settings with different magnifications, image sizes, resolutions and z pitches are examined and listed in Table C.1.

Table C.1 Scanning Settings

	Setting 1	Setting 2	Setting 3	Setting 4	Setting 5	Setting 6
Magnification	400		200		50	
Object Lens Magnification	20		10		2.5	
Image size (pixel × pixel)	1024 × 768		2048 × 1536		2048 × 1536	
X-Y Resolution (nm/pixel)	2754.2		2765.6		5681.8	
Z pitch (um)	0.5	1	2	4	32	64

Settings 1 to 4 have same X-Y resolution, but different moving range of the laser. With higher magnification in Setting 1 and 2, the image field is smaller than lower magnification. Therefore, to scan the same total area of sample, more time is needed for these two settings. Similarly, the scanning time for setting 5 and setting 6 with the magnification of 50 will scan fastest for the same sample area among the 6 settings. A tape sample of 25mm (width) × 0.8mm (length) was scanned with the six settings. The laser intensity image of a portion of the sample is shown in Figure C.1. The surface roughness results are compared in Table C.2. It is seen that results from

setting 3 and setting 4 compares well with those from higher magnification, and results setting 5 and setting 6 are way off and not acceptable. Further considering the scanning time for different settings, setting 4 was selected to scan the tape surfaces with reduced noise in z direction and high X-Y resolution.



Figure C.2 Laser intensity image of the tape sample (from scanning setting 4)

Table C.2 Roughness results after surface scanning with the six settings

	Area surface roughness			3 line roughness								
				Line 1			Line 2			Line 3		
	Ra (um)	Rq (um)	Rz (um)	Ra (um)	Rq (um)	Rz (um)	Ra (um)	Rq (um)	Rz (um)	Ra (um)	Rq (um)	Rz (um)
S1	9.1	11.33	83.9	9	11.21	71.85	9.15	11.39	70.85	9.01	11.23	69.08
S2	9.15	11.41	81.84	9.08	11.32	64.28	9.2	11.47	64.81	9.05	11.3	62.39
S3	9.46	11.83	87.24	9.37	11.75	74.89	9.63	12	67.12	9.45	11.77	63.48
<b>S4</b>	<b>9.33</b>	<b>11.65</b>	<b>81.04</b>	<b>9.19</b>	<b>11.51</b>	<b>64.8</b>	<b>9.55</b>	<b>11.87</b>	<b>69.17</b>	<b>9.18</b>	<b>11.44</b>	<b>68.62</b>
S5	31.5	42.79	730.4	31.26	42.64	425.57	30.3	44.12	627.45	31.27	42.29	372.73
S6	31.87	43.64	707.05	32.8	45.11	472.66	31.87	42.69	522.79	33.5	46.16	482.83

## Appendix D

### Calculation of Characteristic time for Voids Escaping through Buoyancy

Force balance of the voids in composite follows Newton's Law:

$$F_b - F_d = 0 \quad (D.1)$$

Buoyancy Force

$$F_b = V\rho_l g \quad (D.2)$$

$\rho_l$  is the density of the fluid,  $g$  is the acceleration due to gravity

Stokes' Law, drag force for a cylindrical needle with very large ratio of length to radius can be approximated to be [137]:

$$F_d = \frac{4\pi\mu v L}{(2-Ln Re)} \quad (D.3)$$

Reynolds number:

$$Re = \frac{\rho}{\mu} D_h v \quad (D.4)$$

Where:  $\mu$  is the viscosity of the fluid;

$$\mu = 132.95 \text{ Exp} \left[ \frac{2969K}{T[K]} \right] \quad (D.5)$$

At processing temperature of 380°C,  $\mu = 12540 \text{ Pa}\cdot\text{s}$

$D_h$  is the hydraulic diameter of the particles;  $v$  is the steady state velocity of the rising void;  $L$  is the length of the particle

From Chapter 2, it is seen the voids are in cylindrical shape. The largest diameter of 14  $\mu\text{m}$  and length of 1 mm from 99% voids are used in this calculation.  $g$

is  $9.8 \text{ m/s}$ ,  $\rho_l$  is  $1320 \text{ Kg/m}^3$ ; the calculated steady state velocity for the void to move up is:

$$v = 4.8 \times 10^{-10} \text{ m/s} \quad (\text{D.6})$$

Time to reach surface 0.15mm apart

$$t = \frac{0.15 \times 10^{-3}}{v \cdot 3600} = 86.8 \text{ hrs} \quad (\text{D.7})$$

## Appendix E

### Solubility and Diffusion Coefficient of O2 and N2 in APC2 Composites

The temperature dependence solubility and diffusion coefficient for a gas in a polymer system can be expressed by a Van't Hoff-Arrhenius equation [89]:

$$S(T) = S_0 \text{Exp}\left(-\frac{\Delta H_s}{RT}\right) \quad (\text{E.1})$$

$$D(T) = D_0 \text{Exp}\left(-\frac{E_D}{RT}\right) \quad (\text{E.2})$$

Where  $\Delta H_s$  is molar heat of sorption,  $E_D$  is the activation energy of diffusion, R is the gas constant, T is temperature in Kelvin.

The solubility and diffusion coefficient of N<sub>2</sub> and H<sub>2</sub>O in amorphous PEEK were measured by Ciora and Magill. And the  $\Delta H_s$ ,  $S_0$ ,  $E_D$ , and  $D_0$  were obtained and shown in the Table E.1.

Table E.1  $S_0$ ,  $D_0$ ,  $\Delta H_s$ , and  $E_D$  of N<sub>2</sub> and H<sub>2</sub>O in amorphous PEEK [93]

	N <sub>2</sub>		H <sub>2</sub> O
	<T <sub>g</sub>	>T <sub>g</sub>	
$S_0$ [m <sup>3</sup> /m <sup>3</sup> Pa <sup>-1</sup> ]	3.89e-09	1.26e-07	2.77e-09
$\Delta H_s$ [KJ/mol]	-15.3	-3.5	-34.3
$D_0$ [m <sup>2</sup> /s]	2.33e-06	2.84e-04	6.74e-05
$E_D$ [KJ/mol]	41.3	57.4	45.8

Assuming gas molecules do not dissolve into or diffuse through the crystallized region of PEEK and fiber region in the prepreg, the solubility and

diffusion coefficient in prepreg material can be estimated from those in amorphous resin as below:

$$S = S_a(1 - x_c)V_m \quad (\text{E.3})$$

$$D = D_a(1 - x_c)V_m \quad (\text{E.4})$$

Where  $S_a$  and  $D_a$  are the solubility and diffusion coefficient in the amorphous polymers.  $x_c$  is the crystallinity of resin,  $V_m$  is the resin volume fraction of the prepreg tape.

With 10.5% crystallinity of the PEEK [36] in the prepreg tape and 35% resin volume, the solubility ( $\text{m}^3/\text{m}^3 \text{ Pa}^{-1}$ ) and diffusion coefficient ( $\text{m}^2/\text{s}$ ) of  $\text{N}_2$  and  $\text{H}_2\text{O}$  in the prepreg tape are as below:

$$S_{\text{N}_2}(T) = \begin{cases} 1.23 \times 10^{-9} \text{Exp} \left[ \frac{1840}{T} \right] & (T < T_g) \\ 3.96 \times 10^{-8} \text{Exp} \left[ \frac{421}{T} \right] & (T \geq T_g) \end{cases} \quad (\text{E.5})$$

$$S_{\text{H}_2\text{O}}(T) = 8.72 \times 10^{-10} \text{Exp} \left[ \frac{4125}{T} \right] \quad (\text{E.6})$$

$$D_{\text{N}_2}(T) = \begin{cases} 7.34 \times 10^{-7} \text{Exp} \left[ -\frac{4968}{T} \right] & (T < T_g) \\ 8.95 \times 10^{-5} \text{Exp} \left[ -\frac{6904}{T} \right] & (T \geq T_g) \end{cases} \quad (\text{E.7})$$

$$D_{\text{H}_2\text{O}}(T) = 2.12 \times 10^{-5} \text{Exp} \left[ -\frac{5509}{T} \right] \quad (\text{E.8})$$

For simple gases like  $\text{N}_2$  and  $\text{O}_2$ , no polar bonds tie the gas molecules to the polymers, the variations of solubility of a given gas in different polymers do not show large variations. However, the nature of the gas such as the potential energy and the potential length plays a significant role to the solubility. From a survey of 20 polymers, it is shown the solubility of  $\text{O}_2$  is two time of that of  $\text{N}_2$  in the same polymer at room temperature.[89] Therefore, it is estimated that:

$$S_{\text{O}_2}(298\text{K}) = 2 S_{\text{N}_2}(298\text{K}) \quad (\text{E.9})$$

Van Amerongen found  $\Delta H_s$  depends on the boiling points or the Kennard-Jones temperature ( $\frac{\varepsilon}{k}$ ) of the gas with the following equation [89]:

$$\frac{\Delta H_s}{R} = \begin{cases} 500 - 10 \frac{\varepsilon}{k}, & (\text{glassy polymers}) \\ 1000 - 10 \frac{\varepsilon}{k}, & (\text{rubbers elastomers}) \end{cases} \quad (\text{E.10})$$

Also, for rubbers,

$$\text{Log } S_0 = -5.5 - 0.005 \frac{\varepsilon}{k} \quad (\text{E.11})$$

With  $\frac{\varepsilon}{k}$  of O<sub>2</sub> to be 107 K [89], the solubility of O<sub>2</sub> in prepreg tape can be estimated from Equation E.3, E.9-E.11 as below:

$$S_{O_2}(T) = \begin{cases} 1.74 \times 10^{-7} \text{Exp} \left[ \frac{570}{T} \right] & (T < T_g) \\ 3.23 \times 10^{-7} \text{Exp} \left[ \frac{70}{T} \right] & (T \geq T_g) \end{cases} \quad (\text{E.12})$$

The activation energy of diffusion  $E_D$  can be assumed to be proportional to second power of collision diameter ( $\sigma_x$ ) of the gas. [89]

$$\frac{E_D}{R} = (\sigma_x / \sigma_{N_2})^2 p \quad (\text{E.13})$$

$p$  equals  $\frac{E_D}{R}$  in Equation E.5 if the gas is N<sub>2</sub>. With  $(\sigma_{O_2} / \sigma_{N_2})^2$  to be 0.83, the  $\frac{E_D}{R}$  of O<sub>2</sub> can be obtained.

Initial parameter  $D_0$  ( $m^2/s$ ) follows [89]:

$$\text{Log } (D_0) = \begin{cases} 0.001 \frac{E_D}{R} - 9.0 \pm 0.8, & (\text{glassy polymers}) \\ 0.001 \frac{E_D}{R} - 8.0 \pm 0.4, & (\text{rubbers elastomers}) \end{cases} \quad (\text{E.14})$$

If directly insert  $\frac{E_D}{R}$  of O<sub>2</sub> into the above equation, variation can be large. From the measured results of N<sub>2</sub>, the following equation is used to obtain  $D_0$  of O<sub>2</sub> in PEEK:

$$\text{Log } (D_{0N_2} / D_{0O_2}) = 0.001 \left( \frac{E_{DN_2}}{R} - \frac{E_{DO_2}}{R} \right) \quad (\text{E.15})$$

The diffusion coefficient of O<sub>2</sub> in the prepreg tape is derived with Equations E.13-E.15 and follows:

$$D_{O_2}(T) = \begin{cases} 1.05 \times 10^{-7} \text{Exp} \left[ -\frac{4123}{T} \right] & (T < T_g) \\ 6.0 \times 10^{-6} \text{Exp} \left[ -\frac{5730}{T} \right] & (T \geq T_g) \end{cases} \quad (\text{E.16})$$

For the solubility, the following equation will be applied to change the unit into mol/m<sup>3</sup> for Henry's gas law constant for the diffusion model in Chapter 5.

$$M(T) = \frac{273}{T(K)} M_0 \quad (\text{E.17})$$

Where  $M(T)$  is number of mol of gas molecules per unit volume (mol/m<sup>3</sup>) at temperature T.

## Appendix F

### ESTIMATION OF SUPER-SATURATION RATIO AND PROBABILITY OF NUCLEATION OF AIR DISSOLVED IN THE COMPOSITE DOMAIN OF PREPREG TAPE

Following the Henry's Law, the saturation concentration of a gas in resin is:

$$C_s = S_g(T)P \quad (\text{F.1})$$

Where  $C_s$  is the saturation concentration of gas under vapor pressure  $P$ , and  $S_g(T)$  is the solubility of the gas in polymer at temperature  $T$ .

Super-saturation ratio is:

$$a = \frac{C_g}{C_s} - 1 \quad (\text{F.2})$$

Where  $C_g$  is the actual concentration of the gas.

Assuming that air molecules dissolved in the tape are in equilibrium under room temperature and atmosphere pressure before OVB processing, the initial concentration of  $N_2$  and  $O_2$  can be obtained from equations E.5, E.6. With the 40% relative humidity in ambient condition, the water vapor pressure is 1180 Pa. The initial concentration of  $H_2O$  can be calculated from equation E.12. With the application of vacuum in the processing, the absolute pressure is 2 atm. If assuming the amount of gases in the resin during processing do not change, the supersaturation ratios of  $N_2$ ,  $O_2$ , and  $H_2O$  during temperature ramping of the processing are plotted in Figure F.1.

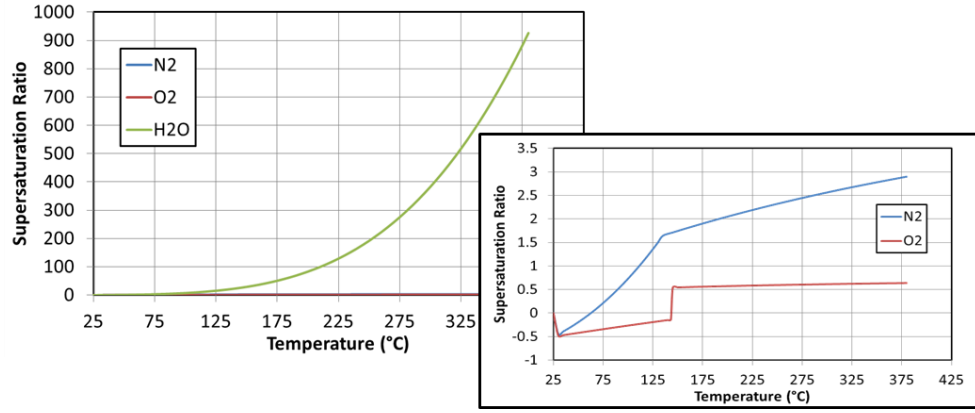


Figure F.1 Supersaturation ratios of N<sub>2</sub>, and O<sub>2</sub> during temperature ramping in OVB processing

According to the classic nucleation theory, the probability of forming new nuclei or nucleation rate (number of nuclei/s m<sup>-3</sup>) follows:

$$J(T) = M(T) \left( \frac{2\sigma(T)}{\pi m} \right)^{\frac{1}{2}} \text{Exp} \left( - \frac{16\pi\sigma(T)^3}{3KT(Pv(T)-Pl)^2} \right) = A \text{Exp}(-B) \quad (\text{F.3})$$

Where  $M(T)$  is the number of molecules in unit volume in gas phase:

$$M(T) = \frac{273(K)1}{0.0224*T(K)} \times 6.022 \times 10^{23} \quad (\text{F.4})$$

$\sigma(T)$  is the surface tension of PEEK resin with unit of N/m, and decreases 5e-05 N/m per K [138,139]:

$$\sigma(T) = 0.042 - 0.05/1000 * (T - 298) \quad (\text{F.5})$$

$m$  (Kg) is the mass of a molecule;  $K$  is Boltzmann constant (1.38e-23 m<sup>2</sup>Kg s<sup>-2</sup>K<sup>-1</sup>);

$Pv(T)$  is the vapour pressure which can be calculated from Henry's Law:

$$Pv(T) = \frac{S_g(298)*Patm}{S_g(T)} = \frac{C_g(298)}{S_g(T)} \quad (\text{F.6})$$

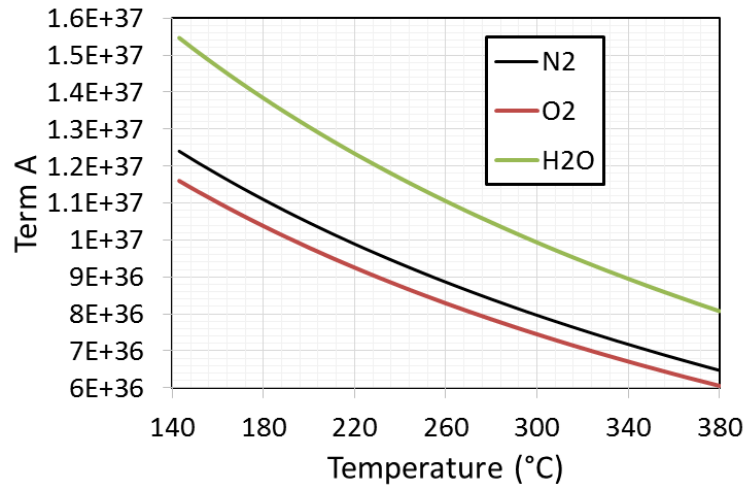
$Pl$  is the pressure of the gas in surrounding medium. The absolute pressure on the laminate is 2 atm. By assuming the composition of air at high temperature is the same

as room temperature,  $P_l$  for  $N_2$  and  $O_2$  are 1.58 atm and 0.42 atm respectively. The saturation vapor pressure for moisture at high temperature is estimated through Buck Equation:

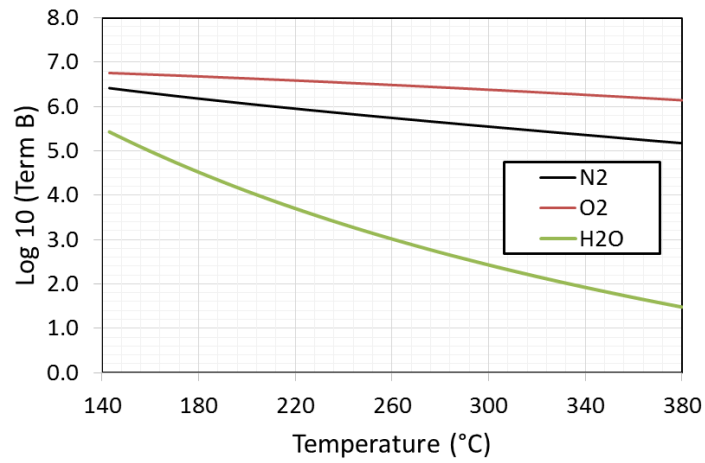
$$P_{H_2O} (KPa) = 0.611 \text{ Exp} \left( \left( 18.678 - \frac{T(^{\circ}C)}{234.5} \right) \left( \frac{T(^{\circ}C)}{257.14 + T(^{\circ}C)} \right) \right) \quad (F.7)$$

And the absolute moisture pressure in the medium is 2 times of the pressure calculated from equation F.7 for all temperatures.

With all the inputs above, the term A and term B with increasing temperature for the gases are presented in Figure F.2. With the highest vapor pressure at the temperature of 380 °C, the probability to observe a nucleus for  $N_2$  and  $O_2$  are extremely low ( $3.89 \times 10^{(-5e4)}$  and  $4.95 \times 10^{(-2e7)}$  for a sample size of 1 m<sup>3</sup> volume and time of 10000 s for  $N_2$  and  $O_2$  respectively). Calculation shows when temperature is above 340 °C, the nucleation rate for moisture is 4 nuclei /m<sup>3</sup>/s which is still very low. Diffusion process occurs after vacuum is applied during the processing. It is highly possible that the moisture molecules diffuses out during the processing before reaching 340 °C. The local vapor pressure of moisture can be even lower than the current calculation. The probability of creating new nuclei is very low. Therefore nucleation due to moisture is ignored.



(a)



(b)

Figure F.2 Term A and Term B of the nucleation rates of N<sub>2</sub>, O<sub>2</sub> and H<sub>2</sub>O with increasing temperature in OVB processing.

## Appendix G

### KUNDSSEN NUMBER, FLOW REGIMES AND KLINKENBERG PARAMETERS FOR INTERLAYER AIR FLOW

#### G.1 Knudsen Number and Flow Regime

Knudsen number ( $Kn$ ) is a dimensionless parameter that is commonly used to classify flow regimes when dealing with gaseous flow in fine porous media. And the flow regimes based on different range of Knudsen number can be seen in Table G.1.[81]

Table G.1 Knudsen number and flow regimes

Knudsen number	Flow regime	Model to be applied
$Kn < 0.01$	Viscous (Continuum) flow	Darcy's equation for laminar flow
$0.01 < Kn < 0.1$	Slip flow	Darcy's equation with klinkenberg correction
$0.1 < Kn < 10$	Transition flow	Darcy's law with Knudsen's correction, or Burnett's equation with slip boundary conditions
$Kn > 10$	Knudsen's (Free molecular) flow	Knudsen's diffusion equation

Knudsen number can be calculated through

$$Kn = \lambda/r \quad (G.1)$$

Where  $\lambda$  is the molecular mean free path, and is 68 nm for air at room temperature;  $r$  is the pore radius. For the interlayer region of the thermoplastic prepreg, it is very

difficult to obtain  $r$  from surface characterization. However,  $r$  may be estimated from measured permeability products. By simplifying the interlayer region into a rectangular duct, the permeability of the duct should follow [140]

$$K = \frac{a^2}{12} \left[ 1 - \frac{192}{\pi^5} \frac{a}{w} \sum_{i=1,3,5,\dots}^{\infty} \frac{\tanh\left(\frac{i\pi w}{2a}\right)}{i^5} \right] \quad (\text{G.2})$$

Where  $a$  and  $w$  are the height and width of the rectangular duct respectively. And  $a$  can be assumed as  $2r$ . If a flat plate sits on top of the tape surface, the ratio of  $a/w$  can be in the order of 0.01 as seen in the Figure G.1. Therefore, the second term in the bracket of Equation G.2 can be ignored for permeability. Therefore, the permeability thickness product is expressed as

$$Kh = Ka = \frac{a^3}{12} \quad (\text{G.3})$$

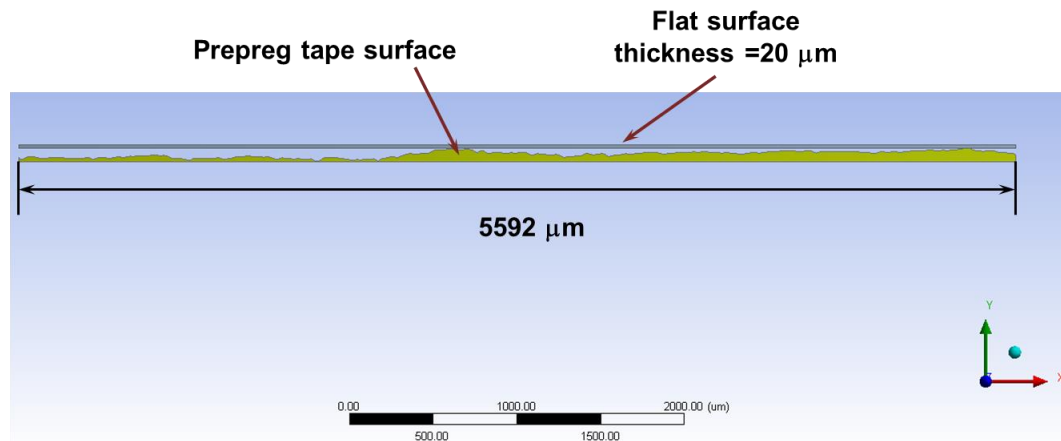


Figure G.1 Prepreg tape surface in contact with a flat surface showing the ratio of interlayer region height and width of porous channels can be in the order of 0.01

$a$  and  $Kn$  calculated from the  $Kh$  values representing the whole range of measurement results in Chapter 3 are listed in Table G.2. It is seen that when measured  $Kh$  reduces from the order of  $1e-16 \text{ m}^3$  to  $1 e-17 \text{ m}^3$ , the flow regime switches from viscose flow to slip flow and Klinkenberg effect becomes significant.

Table G.2  $K$ ,  $r$  and  $Kn$  estimated from the measured  $Kh$

Interlayer	$Kh \text{ (m}^3\text{)}$	$K \text{ (m}^2\text{)}$	$r = \frac{a}{2} \text{ (}\mu\text{m)}$	$Kn$
0°/0° @ RT	3.51E-15	1.01E-10	17.4	0.004
0°/90° @ RT	2.98E-15	9.05E-11	16.5	0.004
60°/90° @ RT	1.10E-15	4.65E-11	11.8	0.006
90°/90° @ RT	3.04E-16	1.97E-11	7.7	0.009
90°/90° @ 240°C	1.88E-16	1.43E-11	6.6	0.010
90°/90° @ 300°C	7.89E-17	8.04E-12	4.9	0.014

## G.2 Klinkenberg Effect

The measured gas permeability  $K$  is linearly dependent on the intrinsic permeability of the porous media  $K_\infty$  with Klinkenberg parameter  $b$  as below

$$K = K_\infty \left(1 + \frac{b}{P}\right) \quad (\text{G.4})$$

In the 1D steady state flow measurement of interlayer permeability thickness products, Equation G.4 can be inserted into the Darcy's equation

$$Q = - \frac{K_\infty \left(1 + \frac{b}{P}\right) h \times W}{\mu} \frac{dP}{dx} = \frac{\dot{n}RT}{P} \quad (\text{G.5})$$

With the consideration of compressibility of air, rearranging Equation G.5 and integrating both side for  $P$  and  $x$ , we obtain

$$\int_{P_1}^{P_0} (P + b) dP = -\frac{\dot{n}RT \mu}{K_{\infty}h W} \int_{x_1}^{x_0} dx \quad (G.6)$$

$$\dot{n}RT = \frac{K_{\infty}h W [(P_0^2 - P_1^2) + 2b(P_0 - P_1)]}{2 \mu L} \quad (G.7)$$

With  $P_0 = P_{atm}$ ,  $P_1 = 0$ , air pressure at the flow meter side equals to  $P_{atm}$ , the measured flow rate turns into

$$Q = \frac{\dot{n}RT}{P_{atm}} = \frac{K_{\infty}h (1 + \frac{2b}{P_{atm}}) W P_{atm}}{2 \mu L} \quad (G.8)$$

Therefore, the relationship between  $K_{\infty}h$  and the measured  $Kh$  is obtained

$$Kh = K_{\infty}h (1 + \frac{2b}{P_{atm}}) \quad (G.9)$$

From Civan's work, Kinkenberg parameter can be expressed as a power law function of  $K_{\infty}$ . For air under room temperature and 1 atm pressure,

$$b = 9.55 \times 10^{-3} K_{\infty}^{-0.5} \quad (G.10)$$

With Equation G.3, G.9 and G.10,  $K_{\infty}$  and the ratio  $K_{\infty}h/Kh$  for the interlayer listed in Table G.2 are calculated and presented in Table G.3

Table G.3  $b$ ,  $K_{\infty}h$  and  $K_{\infty}h/Kh$  for some measured interlayer in Chapter 3

Interlayer	$Kh$ (m <sup>3</sup> )	$b$	$K_{\infty}h$	$K_{\infty}h/Kh$
0°/0° @ RT	3.51E-15	951	3.45E-15	98.2%
0°/90° @ RT	2.98E-15	1004	2.92E-15	98.1%
60°/90° @ RT	1.10E-15	1400	1.07E-15	97.3%
90°/90° @ RT	3.04E-16	2149	2.92E-16	95.9%
90°/90° @ 240°C	1.88E-16	2522	1.79E-16	95.3%
90°/90° @ 300°C	7.89E-17	3369	7.40E-17	93.8%

## Appendix H

### FITTING PARAMETERS FOR TEMPERATURE PROFILES MEASURED IN CONSOLIDATION EXPERIMENTS

Temperature profile in the consolidation experiments in Chapter 4 Figure 5.4 can be fitted into Gauss functions of time with the general equation below:

$$T(K) = f(t) = \sum_{i=1}^n a_i \times \exp\left(-\left(\frac{t-b_i}{c_i}\right)^2\right) \quad (\text{H.1})$$

The number of terms n, and fitting parameters, a, b and c to achieve R-square > 0.9999 are shown in Table H.1 and used in the single layer diffusion model in Chapter 5.

Table H.1 Fitting parameters of Gauss functions for temperature profiles used for non-isothermal diffusion analysis

Fitting parameters		Consolidation Cycles	
		2-layer	72-layer
Term n			
1	a1	9.319	6.806
	b1	9231	11280
	c1	339.7	341
2	a2	42.16	9.932
	b2	9529	7014
	c2	1745	1019
3	a3	73.17	27.96
	b3	168.6	10460
	c3	3457	2034
4	a4	2.307	22.4
	b4	12190	12460
	c4	981.3	2541
5	a5	573.2	459.9
	b5	9169	12300
	c5	9365	18050
6	a6	2.816E+08	143.5
	b6	1.857E+05	11570
	c6	43970	6277

## Appendix I

### DERIVATION OF NON-ISOTHERMAL VISCOELASTIC CONSTITUTIVE EQUATION

In the model of material behavior of interlayer region during the OVB processing, the stress and time – temperature dependent creep compliance of the viscoelastic response may change continuously. The viscoelastic constitutive equation is derived with incremental time step  $\Delta t$  as below.

At step 1, number of step  $n = 1$ , the corresponding temperature is  $T_1$ , processing time  $t_1 = n \Delta t = \Delta t$ , applied stress is  $\Delta\sigma_1$ , and the creep strain is

$$\varepsilon_c(T_1, t_1) = \Delta\sigma_1 D(T_1, \Delta t) \quad (\text{I.1})$$

At step 2, number of step  $n = 2$ , the corresponding temperature is  $T_2$ , processing time  $t_1 = 2 \Delta t$ , applied stress is  $\Delta\sigma_1 + \Delta\sigma_2$ , and the creep strain is

$$\varepsilon_c(T_2, t_2) = \Delta\sigma_1 [D(T_1, \Delta t) + (D(T_2, 2\Delta t) - D(T_2, \Delta t))] + \Delta\sigma_2 D(T_2, \Delta t) \quad (\text{I.2})$$

The change of strain is

$$\Delta\varepsilon_c(T_2, t_2) = \Delta\sigma_1 D(T_2, 2\Delta t) + (\Delta\sigma_2 - \Delta\sigma_1) D(T_2, \Delta t) \quad (\text{I.3})$$

At step 3, number of step  $n = 3$ , the corresponding temperature is  $T_3$ , processing time  $t_1 = 3 \Delta t$ , applied stress is  $\Delta\sigma_1 + \Delta\sigma_2 + \Delta\sigma_3$ , and the creep strain is

$$\varepsilon_c(T_3, t_3) = \Delta\sigma_1 [D(T_1, \Delta t) + (D(T_2, 2\Delta t) - D(T_2, \Delta t)) + (D(T_3, 3\Delta t) - D(T_3, 2\Delta t))] + \Delta\sigma_2 [D(T_2, \Delta t) + D(T_3, 2\Delta t) - D(T_3, \Delta t)] + \Delta\sigma_3 [D(T_3, \Delta t)] \quad (\text{I.4})$$

The change of strain of this step is

$$\Delta\varepsilon_c(T_3, t_3) = \Delta\sigma_1 D(T_3, 3\Delta t) + (\Delta\sigma_2 - \Delta\sigma_1) D(T_3, 2\Delta t) + (\Delta\sigma_3 - \Delta\sigma_2) D(T_3, \Delta t) \quad (\text{I.5})$$

To generalized the equations I.1, I.2 and I.4, the total creep strain is

$$\varepsilon_c(T_n, t_n) = \sum_{i=1}^n \Delta\sigma_i [D(T_i, \Delta t) + \sum_{m=i+1}^n (D(T_m, (m-i+1)\Delta t) - D(T_m, (m-i)\Delta t))] \quad (\text{I.6})$$

And from equations I.3 and I.5, the change of creep strain at each time step is generalized into

$$\Delta\varepsilon_{c_n}(T_n, t_n) = \sum_{i=1}^n (\Delta\sigma_i - \Delta\sigma_{i-1}) D(T_i, i\Delta t) \quad (\text{I.7})$$

# Appendix J

## PERMISSIONS

7/26/2017

Journal Author Archiving Policies and Re-Use | SAGE Publications Inc

[Find My Rep](#) | [Login](#) | [Contact](#)



Search: keyword, title  
Search

Cart 0

### Journal Author Archiving Policies and Re-Use

- [Authors Re-Using Their Own Work](#)
  - [Gold Open Access and SAGE Choice](#)
  - [Green Open Access](#)
  - [Green Open Access Journal Exceptions](#)
- [Author Co-ops](#)
- [Permissions Clearance](#)

#### Authors Re-Using Their Own Work

SAGE Journal authors are able to re-use their Contribution in certain circumstances without requiring permission from SAGE. It is important to check your signed Contributor Agreement and/or the submission guidelines for the Journal to which you submitted your Contribution to review the journal's policy regarding author re-use.

##### Gold Open Access and SAGE Choice

If you wish to re-use an Open Access Contribution published under a Creative Commons License, please see [Re-use of Open Access Content](#) for more information.

##### Green Open Access: SAGE's archiving policy

Most SAGE journals are published under SAGE's Green Open Access policy, which allows you, as author, to re-use your Contribution as indicated below. For a list of titles that are exceptions to this policy, please scroll down to the bottom of the page.

##### Green Open Access policy:

- You may share the version of the Contribution you submitted to the journal (version 1) anywhere at any time.
- Once the Contribution has been accepted for publication, you may post the accepted version (version 2) of the Contribution on your own personal website, your department's website or the repository of your Institution without any restrictions.
- You may not post the accepted version (version 2) of the Contribution in any repository other than those listed above (i.e. you may not deposit in the repository of another Institution or a subject repository) until 12 months after first publication of the Contribution in the journal.
- You may use the published Contribution (version 3) for your own teaching needs or to supply on an individual basis to research colleagues, provided that such supply is not for commercial purposes.
- You may use the published Contribution (version 3) in a book authored or edited by you at any time after publication in the journal. This does not apply to books where you are contributing a chapter to a book authored or edited by someone else.
- You may not post the published Contribution (version 3) on a website or in a repository without permission from SAGE.

When posting or reusing your Contribution under this policy, appropriate credit must be given to the SAGE journal where the Contribution has been published, as the original source of the content, as follows: Author(s), Article Title, Journal Title (Journal Volume Number and Issue Number) pp. xx-xx. Copyright © [year] (Copyright Holder). Reprinted by permission of SAGE Publications. Additionally, please provide a link to the appropriate DOI for the published version of the Contribution on the SAGE Journals website (<http://journals.sagepub.com>).

The chart below includes common requests and an explanation of which 'version' of the article can be used in each circumstance. If the table below indicates that permission is required, please see the instructions for requesting permission at [Journals Permissions](#).

I WANT TO:	CLEARED PERMISSION	REQUIRES PERMISSION
------------	--------------------	---------------------

include up to one full article in my unpublished dissertation or thesisVersion 3

supply my article to my students or use the article for teaching purposesVersion 3

supply my article to a research colleague at an academic institutionVersion 3

supply my article to a commercial organization for republication, distribution or a web postingX

upload my article to my Institution repository or department websiteVersion 2

upload my article to a repository NOT affiliated with my Institution, 12 months after publicationVersion 2

republish my article in a book I am writing or editingVersion 3

contribute my article to a book edited or written by someone elseX

VERSION OF CONTRIBUTION	DEFINITION
-------------------------	------------

Version 1original submission to the journal (before peer review)

Version 2original submission to the journal with your revisions after peer review, often the version accepted by the editor (author accepted manuscript)

Version 3copy-edited and typeset proofs and the final published version

[back to top](#)

#### Green Open Access Journal Exceptions

The following titles are exceptions to our Green Open Access policy. For the terms of re-use of Contributions published in these titles, please review the author re-use terms contained within your Contributor Agreement.

If you have further questions regarding the following titles, please contact the Permissions team at [permissions@sagepub.com](mailto:permissions@sagepub.com).

- *Administrative Science Quarterly*
- *California Management Review*
- *Foot & Ankle International*
- *Journal of Dental Research*
- *Otolaryngology–Head and Neck Surgery*

If you have further questions regarding the following titles, please contact the Permissions team at [permissions@sagepub.co.uk](mailto:permissions@sagepub.co.uk).

- *The British Journal of Politics and International Relations*
- *European Heart Journal: Acute Cardiovascular Care*
- *European Journal of Cardiovascular Nursing*
- *European Journal of Preventive Cardiology*
- *Political Studies Review*
- *Political Studies*
- *Political Insight*
- *Politics*

#### Author Copies

If you are the corresponding author of a Contribution, you will receive an e-print of your Contribution. Please see our [Author e-prints policy](#) for more information.

It is not SAGE's policy to provide PDFs of the published Contribution (version 3) for posting on servers or depositing in institutional repositories.

However, you may update your own version of the article (version 1 or version 2) to reflect substantive changes to the content made during production and convert that article into PDF form.

[back to top](#)

#### Permissions Clearance

For advice on how to clear permission for material contained within a Contribution you intend to *submit for publication* in a SAGE Journal, please visit our Author Gateway [Copyright and Permissions FAQs](#).